WAVE BREAKING AND WIND-FORCED WAVES IN SHALLOW WATER

by

Shigeaki TSUTSUI

March 1984

WAVE BREAKING AND WIND-FORCED WAVES IN SHALLOW WATER

by

Shigeaki TSUTSUI

Submitted in partial fulfillment of
the requirements for the degree of
DOCTOR OF ENGINEERING
at
KYOTO UNIVERSITY
Kyoto, Japan
March 1984

ABSTRACT

This dissertation is relevant both to various breaking conditions for progressive gravity waves and to wave motion generated by strong wind in shallow water. First, there is an analytical description of breaking phenomena for two types of wave breaking of irrotational motion, with and without wind effects. Secondly, there are laboratory experiments on wave breaking to study possible internal breaking conditions. Finally, there is an analysis of wave motion caused by strong wind, where large scale "carrier" wind waves are termed the "wind-forced waves".

As to the breaking of progressive gravity waves without wind effects, a breaking model is developed to discover what kind of mathematical equation could describe the whole wave history from non-breaking to symmetric "peaking" of wave crests, such as Stokes' crested configuration. The breaking model is developed from the usual basic equations for wave motion with use of the reductive perturbation method and Thom's catastrophe theory. It is shown that the wave profile is smooth but as the wave approaches the maximum steepness, it has a sharp curvature at the crest becoming angled rather than rounded at just breaking. Hydraulic properties, such as the breaking inception, also comfirm the validity of the model.

If there are wind effects, surface drift in a vortical wind-drift layer formed at an air-sea interface, generated by the exertion of the wind, can be determined based on intrinsic equations, derived from the Navier-Stokes equations of motion with boundary layer approximations. The breaking inception in the presence of surface drift is formulated in reference to the shear stress exerting on the wave surface and to the Rankine-Stokes breaking condition. At just breaking, the shear stress changes sign becoming

negative in the leeward side of the wave crest. Then, spilling regions may be formed from the water there tumbling forward.

Premonitory phenomena in breaking waves are also investigated experimentally based on the imbalance in the partition of wave energies, leading to internal breaking conditions. The potential energy of waves begins to decrease in front of the breaking point, causing a sharp increase in kinetic energy which becomes prominent in the partition of wave energies. They, finally, lead waves to an unstable state, where the waves may break.

The governing equations for the wind-forced waves generated by strong wind are derived from the Navier-Stokes equations of motion through the perturbation method with shallow water assumptions. They are a generalization of the Korteweg-deVries-Burgers equation including all physical and mathematical terms to be accounted for, such as nonlinearity and dispersion of waves, dissipation in water, wind stresses, and friction at the sea bottom. The hydraulic quantities are expressed in relation to the wind stresses. In the equilibrium state of the internal and external forces, the wind-forced waves could occur and result in cnoidal wave trains. They accompany wind-induced currents and could become asymmetric if the bottom friction is reasonably great. The pressure, namely, Burgers' term, has a significant role in generation of the wind-forced waves as does the shear stress. The chief characteristics of the wind-forced waves are verified in comparison with experimental and field data.

ACKNOWLEDGEMENTS

The author's thanks are offered to Professor Yoshito TSUCHIYA, Disaster Prevention Research Institute, Kyoto University, for his continual supervision and stimulative fruitful discussion during the course of this research and for a critical reading of the manuscript; to Professor Hiroshi MITSUI, Department of Civil Engineering, Faculty of Engineering, Tokushima University, for his invariable encouragement; to the colleagues of the Disaster Prevention Research Institute, Kyoto University, for their assistance during the laboratory experiments and their permission to use the field data at Ogata coast; and also to all his colleagues in the Department of Civil Engineering, Faculty of Engineering, University of the Ryukyus. But his greatest debt is to Keiko TSUTSUI, to whom this work is dedicated.

The support has been partially provided by a Grant-in-Aid for Scientific Research of the Ministry of Education, Science and Culture in 1978 (No.375298), 1979(No.475404), and 1980(No.575338).

CONTENTS

CHAPTER 1

INTRODUCTION

An accurate knowledge of the behaviour of water waves, especially the wave breaking on a beach as the last stage of wave history, is often essential in coastal engineering, such as for the design of nearshore structures and for the prediction of sand movements on a beach. As a result, many efforts have been made to clarify the breaking mechanism. Because of this central position of wave breaking in coastal phenomena, it seems necessary to try to understand precisely some of the mechanisms of wave breaking and related phenomena.

The threads to be woven into the fabric of this dissertation are primarily three. There is, first, the breaking of irrotational progressive waves. In mathematical wave theory, this wave form is assumed to remain symmetric as the amplitude increases, until the wave of maximum height for the given wave period and water depth is reached. This type of breaking is thought to be governed by the relation between the wave velocity and water particle velocity at the wave crest or by the radius of convergence of the mathematical theory. It may be, however, argued that this breaking condition is actually due to a small scale phenomenon occuring locally. Secondly, there is the breaking of progressive waves in the presence of wind-induced surface drift. If additional energy is transferred to a sharp-crested wave, the wave should break first at the wave crest. The complex process of the wind-wave interaction can lead to breaking caused by energy transfer through a turbulent boundary layer formed at and just below the wave surface. Ocean surface waves are formed by the superposition of many wave trains of different direction and frequency. Short gravity waves

riding on large-scale "carrier" waves play an important role in production of surface drift. Finally, there is an investigation of large-scale waves generated by strong wind.

The problem of breaking of steady progressive surface waves is one of the oldest in the literature of mathematical fluid mechanics and one of the most important in coastal engineering. Pioneers of theoretical fluid mechanics, Airy[1], Stokes[2),3)], Rayleigh[4], and others, chiefly considered the elementary properties of surface waves in terms of a perfect fluid theory, based on the assumptions that the wave slopes were small or that particle accelerations were negligible compared with gravity, which led to wave motions that were either sinusoidal or cnoidal in form. However, such assumptions are not valid for waves of great steepness. By a simple argument, Stokes[2),3)] gave a local solution which stated that the highest free surface wave would break with a sharp-crested angle of 120°. About fifty years later, Michell[5] expanded Stokes' method to numerically calculate the periodic wave profile of greatest height for water of infinite depth and found the limiting height to be attained at (wave height)/(wave length) = 0.142, while Nekrasov[6] demonstrated that these wave profiles could be expressed by an integral equation. Following him, Krasovskii[7] certified that Nekrasov's integral equation included Stokes' limiting wave. As proved by Levi-Civita[8] and Struick[9], by reformulating the problem for waves on water of finite depth, series expansions similar to Stokes' do converge for sufficiently small amplitudes. However, they did not give the maximum radius of convergence.

Since Stokes' argument, several valuable solutions for maximum waves have been obtained by imposing his limiting configuration with the angle of 120°. For instance, Yamada[10),11)] and Yamada and Shiotani[12] calculated the limiting wave profiles of solitary and periodic waves. While Lenau[13] and Longuet-Higgins[14] introduced the method of conformal mapping to obtain the

wave profile of the solitary wave. Byatt-Smith[15] also derived an exact integral equation for the solitary wave. However, as proposed by Grant[16] and Norman[17], by investigating the free surface condition[18], the index of singularity at the wave crest is irrational, and though Stokes' limiting configuration can be attained by waves of the greatest possible height, waves with crest angle values smaller than Stokes' can also break.

Recently, the computer-aided continuation of Stokes' expansion have been carried out by Schwartz[19], Longuet-Higgins and Fenton[20], Cokelet[21], Williams[22], and others. Schwartz discovered first that Stokes' expansion never converges beyond a certain wave steepness smaller than the maximum. Schwartz's calculation also indicates that most waves in deep water will break with sharp-crested angles of nearly 90° and that waves with angles of about 120° are restricted to the almost highest waves; this means that the singularity at the wave crest plays a significant role in wave breaking. In addition, Longuet-Higgins and Fenton for the solitary wave, Longuet-Higgins for deep water waves, and Cokelet and Williams for waves on water of finite depth, all discovered that many characteristics of gravity waves, such as wave velocity, energy, and momentum, do take on maximum values before the wave of greatest amplitude is reached. Furthermore, as suggested by Longuet-Higgins and Cokelet[23] in the calculation of the time-dependent, free surface flow, water near the wave crest of an irrotational wave surges forward, so the breaking can occur at a wave amplitude substantially smaller than Stokes' limiting configuration and, furthermore, the energy density becomes locally high when the wave enters the breaking region.

Although these computer-aided numerical calculations may be regarded as exact solutions and that they show that both asymmetric breaking and symmetric peaking are accounted for in the equations of the exact potential theory, may one conclude that these analyses are suitable for insight into the actual breaking phenomenon? In addition, one could ask what kind of

mathematical equation could generate wave forms both for non-breaking waves as well as for the limiting configurations? This is a side of the problem of wave breaking to which we will address ourselves in Chapter 2.

With regard to this, Seliger[24] and Whitham[25] proposed an integro-differential equation with the Fourier integral combining full linear dispersion with long wave nonlinearity; the Fourier integral fills the role of the dispersion term and behaves like Dirac's δ-function. This equation reduces to the Korteweg-deVries equation[26] in shallow water approximations. Seliger was able to show with this equation that a sufficiently asymmetric hump would break in a manner analogous to gas dynamics. However, an analytically exact solution of this model equation is hardly obtainable.

The variational principle for irrotational wave motion established by Luke[27] shows that the Lagrangian is the integral of the dynamical boundary condition at the free surface. This principle, therefore, assures the existence of the Hamiltonian as a conservative quantity of wave motion, which may be capable of expressing the wave profiles of both non-breaking waves and waves with sharp-crested angles.

While it is well known that as a wave approaches the breaking point, it steepens causing the velocity field to vary. The recent discoveries mentioned above also indicate that near the breaking point the energy balance in the wave surely has some effect on the breaking phenomenon; that is, there may exist an internal breaking condition for progressive waves which is dependent upon the individual characteristics of a wave. This is another side of wave breaking investigated experimentally in the present work. The results are presented in Chapter 3.

The complex energy transfer from wind to waves can yet lead to other type of breaking mechanism. When wind blows over a wavy surface, a vortical wind-drift layer may be generated at the air-sea interface; if the wind speed becomes great, the formation of a spilling region ahead of the wave

crest occurs likely as "white caps" or "white horses". The effects of this wind-induced surface drift on wave breaking have been considered significant, but the quantitative evaluation has been yet to be carried out.

Energy transfer is fundamental in the analysis for wind-generated waves. Most previous work relevant to this investigation has in fact been directly concerned with questions how the action of wind may give rise to waves. In one of the earliest attempts at solving this problem, Jeffreys[28),29)] postulated an expression introducing the sheltering coefficient. Jeffreys' theory makes use of the principle that an already existing wave train will grow if the wind supplies energy to it at a rate greater than that of viscous dissipation in water, but his theory provides no estimation for the sheltering coefficient. Internal effects and tangential stress due to the wind are also neglected, and the only property of the normal pressure distribution, needed for his calculation of average energy supply, is the Fourier component in phase with the wave slope. Jeffreys' theory was for a long time held in doubt since experimental estimations of the sheltering coefficient gave values much too small to explain the wave growth. However, about thirty years later, Miles[30)] calculated the induced pressure component in phase with the wave slope; even when there is no separation of air flow, sufficiently large values of the sheltering coefficient can occur when there is a critical point away from the wave surface in a region of the velocity profile where the curvature is negatively large. Miles[31),32),33)] extended his theory, with further contributions by Benjamin[34),35)] and Lighthill[36)], and others. In a careful and detailed analysis by Benjamin[34)], it was found that the surface pressure varies in phase with the wave slope and the shear stress changes sign becoming negative on the leeward side; that is, the stresses distribute in much the same way as if the leeward slopes of the wave were sheltered. For instance, the pressure distribution often has a substantial component in phase with

the wave slope, just as if a wake were formed behind each wave crest. Of course, actual separation effects of air flow were outside the scope of their analyses which were applicable only to short waves.

These developments constituted a great advance, and it became evident that the energy flux across the surface to waves is associated both with the pressure in phase with the wave slope and with the shear stress in phase with the wave elevation[37]. In these analyses, air flow was regarded as quasi-laminar, although diffusive effects of turbulence are more realistic. Many investigators[37] have, since, attempted to evaluate the effects of turbulence. The recent calculation by Gent and Taylor[38] shows that if the wave surface can be presumed to be rough, variations in surface roughness with respect to the phase of waves substantially modify the energy flux to the waves. Therefore, short waves, such as ripples riding on a long wave, probably cause variations in surface stress.

In connection with the surface drift, Stewart[39] realized the importance of wind effects intuitively, and his theory was revised by Longuet-Higgins[40]. They assumed stress distributions similar to those of Miles and Benjamin. The essence of their analyses is that the greatest acceleration in the wind-drift layer occurs where the shear stress is greatest and that the minimum speed and maximum drift layer thickness attain $\pi/2$ later in phase, behind the shear stress, that is, the leeward side of the wave crest. These results are, of course, basically identical to those of Miles and Benjamin. By simple but stimulative analyses, Banner and Phillips[41] and Phillips and Banner[42] evaluated the surface drift distribution with respect to the phase of waves more quantitatively, based on the vorticity balance in the wind-drift layer and on the neglect of viscous effects. Banner and Melville[43] also certified their analyses experimentally. They termed this small scale wave breaking affected by wind the "incipient breaking". The results can be summarized as follows: Surface

drift at the wave crest becomes prominent, at the same time, the maximum wave height without breaking diminishes rapidly with the increase in surface drift, and when the surface drift vanishes, the point of incipient breaking corresponds to Stokes' limiting form with sharp-crested angle of 120°. As they pointed out themselves, however, because the viscous effect in the wind-drift layer is neglected, underestimation of surface drift should be expected; and, furthermore, the normal distribution of the surface drift in the wind-drift layer is no longer evaluated at all. Therefore, this model for incipient breaking offers no information with regard to the wind-stresses. This will be taken up in Chapter 2.

At this point, one may wonder if steady, wind-generated waves of large-scale are indeed possible? Such waves sometimes occur in shallow water in an equilibrium state between external forces, such as wind-stresses, bottom friction, and dissipation or damping in water, and they would accompany wind-induced currents. Therefore, a one-dimensional analysis of wave motion may be useful for suitably taking into account the effects of external forces. Such an analysis can be derived by integrating across a water depth and the resultant equations of motion should involve the effects of nonlinearity, dispersion, and external forces.

One of the recent remarkable developments in nonlinear wave theory is the discovery of explicit, exact solutions for various canonical equations, such as the Korteweg-deVries[44], Sine-Gordon[45], and Schrödinger[46] equations, based on the inverse scattering method[47]. The Korteweg-deVries equation is, of course, one of the simplest prototypes, that combines nonlinearity and dispersion. In this respect, it is analogous to the Burgers equation[48], which also combines nonlinearity with diffusion. It is, therefore, natural for the present research to begin with the Korteweg-deVries-type equation.

The well-known representative equation, which combines the nonlinearity

and bottom friction in an open channel flow, leads to the cnoidal wave or bore solutions on moderate channel slopes and to roll waves on a sufficiently steep channel slope. The first discussion of the effect of bottom friction on cnoidal waves entering still water may have been by Sandover and Zienkiewicz[49] in terms of Chézy's law. That of roll waves was originally by Thomas[50] and Dressler[51] with an appropriate jump condition. The first quantitative discussion on the effects of bottom friction and dispersion, on the other hand, appears to have been done by Byatt-Smith[52] to show that a steady undular bore is possible. In addition, diffusion or damping in water combined with both nonlinearity and dispersion was discussed by Johnson[53] in the analysis of the undular bore; that is, he dealt with the Korteweg-deVries-Burgers equation. These previous analyses do not take into account any of the effects of internal or external forces. It is, thus, clear that further research into the problem involving all effects is required for the oscillatory wave motion generated by wind. This will be developed in Chapter 4.

In concluding this chapter the organization of the present work can be described as follows:

Chapter 2 investigates two kinds of breaking conditions for progressive gravity waves. The first kind of wave beaking is for purely irrotational motion. The customary basic equations of motion are transformed into the Hamiltonian systems through the variational principle. Accordingly, the Hamiltonian exists as a conservative quantity of wave motion. A breaking model is proposed by transforming the Hamiltonian into a suitable form based on Thom's catastrophe theory[54]. This model equation coincides with the Korteweg-deVries equation in the lowest order of approximations and can describe the periodic(cnoidal) and solitary waves. For limiting waves, the wave crest ceases to be rounded and becomes angled, with angles slightly less than that of Stokes and Grant. However, the water particle velocity

and the wave velocity are fairly close together at just breaking.

The second kind is wave breaking in the presence of wind-induced surface drift. The governing equation for the normal distribution of surface drift in the wind-drift layer is derived from the Navier-Stokes equations of motion with the aid of boundary layer approximations. The breaking inception is given with reference to surface drift. Changes in the normal distribution of surface drift in the wind drift layer with respect to the phase of waves are evaluated in terms of the underlying velocity field which is, in essence, irrotational. The shear stress and drift layer thickness are proportional to the inverse of the square root of the Reynolds number as in the boundary layer theory. The shear stress and surface drift change sign and become negative further on the leeward side of the wave crest, indicating a tendency toward a reversal of the surface drift, and the resultant pressure has the effect of suction near the wave crest.

Chapter 3 describes experimentally the characteristics of wave behaviour on a sufficiently mild slope and discusses an internal breaking condition. The energy balance in progressive waves is investigated, based on the conservation law of energy flux, and partition laws of wave energies are formulated. Potential energy being only one of the easily estimatable wave energy properties, its changes over the slope are evaluated and a sharp decrease is seen when a wave approaches the breaking point. At the same time, the kinetic energy increases rapidly. Therefore, waves would break due to this unstable state of the energy balance.

In Chapter 4 the wave motion generated by strong wind is described. These waves will be termed the "wind-forced waves". To suitably take in the effects of all external forces, a one-dimensional analysis similar to that for storm surges is adopted. The formulation of the problem set up in preceding sections leads to the governing equation, which is a generaliza-

tion of the Korteweg-deVries-Burgers-type equation with the bottom friction term given by Chézy's law. A steady state solution, accompaning wind-induced currents, is constructed with use of the method of averaging. The cnoidal wave solution is found to be stable from the analysis, based on the linear stability theory as is usual in nonlinear oscillations. The most stable wave motion is also defined by introducing the physical motion. Furthermore, wind stresses exerting on the wind-forced waves are determined in relation to the friction at the sea bottom and Reynolds number, and the shear stress at just breaking in the presence of surface drift is decided using the results in Chapter 2. Wave profiles of the wind-forced waves become asymmetric when the dissipation at the sea bottom is great. This asymmetry is caused by the phase shift derived from the averaging process. Both the average velocity and shear stress distribute with respect to the phase of waves showing profiles similar to wave profiles. The pressure has a significant role in generation of the wind-forced waves as does the shear stress, acting like a positive external force. The primary properties of the wind-forced waves are verified in comparison with some experimental and field data.

Chapter 5, finally, gives the conclusion summarizing the results in each chapter.

References

1) Airy,G.B.: Tides and waves, *In* Encyclopedia Metoropolitan, London, 1845.
2) Stokes,G.G.: On the theory of oscillatory waves, Trans. Camb. Phil. Soc., Vol.8, 1847, pp.441-455.
3) Stokes,G.G.: Supplement to a paper on the theory of oscillatory waves, Mathematical and Physical Papers, Vol.1, Camb. Univ. Press, 1880, pp.314-326.
4) Rayleigh,L.: On waves, Phil. Mag., Ser.1, 1876, pp.257-279.
5) Michell,A.G.M.: The highest waves in water, Phil. Mag., Ser.5, Vol.36, 1893, pp.430-437.
6) Nekrasov,A.I.: On waves of permanent type I, Izv. Ivanovo-Voznesensk, Politekhn. Inst., Vol.3, 1921, pp.52-65.
7) Krasovskii,Yu,P.: On the theory of steady-state waves of finite ampli-

tude, Zh. Vych. Mat., Vol.1, No.5, 1961, pp.836-855.
8) Levi-Civita,T.: Détermination rigoureuse des ondes permanentes d'ampleur finie, Math. Ann., Vol.93, 1925, pp.264-314.
9) Struick,D.J.: Détermination rigoureuse des ondes irrotationelles periodiques dans un canal à profondeur finie, Math. Ann., Vol.95, 1926, pp.595-634.
10) Yamada,H.: Highest waves of permanent type on the surface of deep water, Rep. Res. Inst. Appl. Mech., Kyushu Univ., Vol.5, 1957, pp.37-52.
11) Yamada,H.: On the highest solitary wave, Rep. Res. Inst. Appl. Mech., Kyushu Univ., Vol.5, 1957, pp.53-67.
12) Yamada,H. and T.Shiotani: On the highest water waves of permanent type, Bull. Disas. Prev. Res. Inst., Kyoto Univ., Vol.18, Part 2, No.135, 1968, pp.1-21.
13) Lenau,C.W.: The solitary waves of maximum amplitude, Jour. Fluid Mech., Vol.26, 1966, pp.309-320.
14) Longuet-Higgins,M.S: On the form of the highest progressive and standing waves in deep water, Proc. Roy. Soc. Lond., A.331, 1973, pp.445-456.
15) Byatt-Smith,J.G.S.: An exact integral equation for steady surface waves, Proc. Roy. Soc. Lond., A.315, 1970, pp.405-418.
16) Grant,M.A.: The singularity at the crest of a finite amplitude progressive Stokes waves, Jour. Fluid Mech., Vol.59, 1973, pp.257-262.
17) Norman,A.C.: Expansions for the shape of maximum amplitude Stokes waves, Jour. Fluid Mech., Vol.66, 1974, pp.261-265.
18) Laitone,E.V.: The second order approximation to cnoidal and solitary waves, Jour. Fluid Mech., Vol.9, 1960, pp.430-440.
19) Schwartz,L.W.: Computer extension and analytic continuation of Stokes' expansion for gravity waves, Jour. Fluid Mech., Vol.62, 1974, pp.553-578.
20) Longuet-Higgins,M.S. and J.D.Fenton: On the mass, momentum, energy and circulation of a solitary wave. II, Proc. Roy. Soc. Lond., A.340, 1974, pp.471-493.
21) Cokelet,E.D.: Steep gravity waves in water of arbitrary uniform depth, Proc. Roy. Soc. Lond., A.286, 1977, pp.183-230.
22) Williams,J.M.: Limiting gravity waves in water of finite depth, Phil. Trans. Roy. Soc. Lond., A.302, 1981, pp.139-188.
23) Longuet-Higgins,M.S. and E.D.Cokelet: The deformation of steep surface waves on water.I, A numerical method of computation, Proc. Roy. Soc. Lond., A.350, 1976, pp.1-26.
24) Seliger,R.: A note on breaking waves, Proc. Roy. Soc. Lond., A.303, 1968, pp.493-496.
25) Whitham,G.B.: Variational methods and applications to water waves, Proc. Roy. Soc. Lond., A.299, 1967, pp.6-25.
26) Korteweg,D.J. and G.deVries: On the change of form of long waves advancing in a rectangular channel, and on a new type of long stationary waves, Phil. Mag., Ser.39, 1895, pp.422-443.
27) Luke,J.C.: A variational principle for a fluid with a free surface, Jour. Fluid Mech., Vol.27, 1967, pp.395-397.
28) Jeffreys,H.: On the formation of waves by wind, Proc. Roy. Soc. Lond., A.107, 1924, pp.189-206.
29) Jeffreys,H.: On the formation of waves by wind.II, Proc. Roy. Soc. Lond., A.110, 1925, pp.341-347.
30) Miles,J.W.: On the generation of surface waves by shear flows, Jour. Fluid Mech., Vol.3, 1957, pp.185-204.
31) Miles,J.W.: On the generation of surface waves by shear flows. Part 2, Jour. Fluid Mech., Vol.6, 1959, pp.568-582.

32) Miles,J.W.: On the generation of surface waves by shear flows. Part 3, Jour. Fluid Mech., Vol.6, 1959, pp.583-598.
33) Miles,J.W.: On the generation of surface waves by shear flows. Part 4, Jour. Fluid Mech., Vol.13, 1962, pp.433-448.
34) Benjamin,T.B.: Shearing flow over a wavy boundary, Jour. Fluid Mech., Vol.6, 1959, pp.161-205.
35) Benjamin,T.B.: Effects of a flexible boundary on hydrodynamic stability, Jour. Fluid Mech., Vol.9, 1960, pp.513-532.
36) Lighthill,M.J.: Physical interpretation of the mathematical theory of wave generation by wind, Jour. Fluid Mech., Vol.14, 1962, pp.385-398.
37) *See* Phillips,O.M.: The Dynamics of the Upper Ocean, 2nd Ed., Camb. Univ. Press, 1977, 337p.
38) Gent,P.R. and P.A.Taylor,: A numerical model of the air flow above water waves, Jour. Fluid Mech., Vol.77, 1976, pp.105-128.
39) Stewart,R.W.: Mechanics of the air-sea interface, Phys. Fluids, Suppl., Vol.10, 1967, S47-S55.
40) Longuet-Higgins,M.S.: Action of a variable stress at the surface of water waves, Phys. Fluids, Vol.12, 1969, pp.737-740.
41) Banner,M.L. and O.M.Phillips: On the incipient breaking of small scale waves, Jour. Fluid Mech., Vol.65, 1974, pp.647-656.
42) Phillips,O.M. and M.L.Banner: Wave breaking in the presence of wind drift and swell, Jour. Fluid Mech., Vol.66, 1974, pp.625-640.
43) Banner,M.L. and W.K.Melville: On the separation of air flow over water waves, Jour. Fluid Mech., Vol.77, 1976, pp.825-842.
44) Gardner,C.S., J.M.Greene, M.D.Kruskal, and R.M.Miura: Method for solving the Korteweg-deVries equation, Phys. Rev. Lett., Vol.19, 1967, pp.1095-1097.
45) Perring,J.K. and T.H.R.Skyrme: A model unified field equation, Nucl. Phys., Vol.31, 1962, pp.550-555.
46) Zakharov,V.E. and A.B.Shabat: Exact theory of two-dimensional self-focusing and one-dimensional self-modulation of waves in nonlinear media, Soviet Physics, J.E.T.P., Vol.34, 1972, pp.62-69.
47) Lax,P.D: Integrals of nonlinear equations of evolution and solitary waves, Comm. Appl. Math., Vol.21, 1968, pp.467-490.
48) Burgers,J.M.: A mathematical model illustrating the theory of turbulence, Adv. Appl. Mech., Vol.1, 1948, pp.171-199.
49) Sandover,J.A. and O.C.Zienkiewicz: La Houille Branch, Vol.17, Grenoble, France, 1962, p.443.
50) Thomas,H.A.: The propagation of waves in steep prismatic conduits, Proc. Hyd. Conf. Univ. Iowa Studies in Engrg., Bull.20, No.397, 1940, pp.214-229.
51) Dressler,R.F: Mathmatical solution of the problem of roll waves in inclined open channels, Comm. Pure Appl. Math., Vol.2, 1949, pp.149-194.
52) Byatt-Smith,J.G.B.: Effects of empirical dissipation terms in the solution of the undular bore, Quart. Appl. Math., 1971, pp.499-515.
53) Johnson,R.S.: Shallow water waves on a viscous fluid-The undular bore, Phys. Fluids, Vol.15, 1972, pp.1693-1699.
54) Thom,R.: Structural Stability and Morphogenesis, (Trans. by Fowler,D.H. and C.H.Waddington), Benjamin, Massachusetts, 1975, 348p.

CHAPTER 2

BREAKING CONDITIONS FOR PROGRESSIVE WAVES OF PERMANENT TYPE

2.1 Introduction

This chapter discusses theoretically two types of breaking conditions for progressive waves, that is, wave breaking under the assumption of irrotationality of motion without wind effects and wave breaking in the presence of surface drift generated by the exertion of wind.

For irrotational gravity waves, the transient breaking of large scale waves in a uniform or nearly uniform water depth is generally believed to occur when the wave profile steepens and reaches to the limiting configuration of Stokes[1),2)] and Michell[3)], characterized by the sharp crest with an included angle of 120°, and at the same time the wave velocity and water particle velocity at the wave crest approach equality, which is the Rankine-Stokes breaking condition[1)]. Many usual analyses of wave breaking have been based on this condition. However, in applying the finite amplitude wave theories, when the velocities are equal, the crested angle of the limiting configuration is never generated, i.e. the wave surface remains smooth. The reason is chiefly attributed to the lack of order of approximations in the perturbation procedure. Nevertheless, the basic equations for wave motion surely should contain the solutions with peaking, too. Therefore, it is worth analyzing the systems and formulating solutions which can express the whole wave history from smooth wave profiles to peaking.

Section 2.2 proposes a breaking model for waves of permanent type. The variational principle established by Luke[4)] shows that the Lagrangian is

the integral of the nonlinear dynamical boundary condition at the wave surface. The integral surface for the wave motion, therefore, exists as a conservative quantity and is suitable for driving characteristics of the wave solution, rendering a transformation from the Lagrangian to Hamiltonian systems possible. The Hamiltonian of the fourth order approximation is obtained from a wave equation expressed by only the water surface displacement, noting that the Hamiltonian is the Taylor approximation of the solution which corresponds to the Korteweg-deVries equation[5] in the lowest order of approximations. Based on the classification theorem by Thom[6] for a surface with singular points, the Hamiltonian can be further converted into the needed energy surface. The resultant model shows that the cnoidal wave solution can exibit the peaking of the limiting configuration and nearly satisfy equality of the velocities at just breaking.

On the other hand, when wind blows over a wavy surface, a vortical wind-drift layer appears to be dominant at and just below the wave surface, and soon the wave begins to break at the wave crest, often as "white caps" or "white horses". Sections 2.3 and 2.4 deal with this surface drift which may chiefly govern the wave breaking by wind.

Small scale wave breaking has been discussed by Banner and Phillips, and others[7),8),9)]. Their analyses show that, neglecting viscous effects, the surface drift at the wave crest increases to several times that at the mean water level and that the maximum wave height reached without breaking diminishes rapidly with this increase. To the incipient breaking of waves are applied the finite amplitude wave theories in order to evaluate the distribution of surface drift with respect to the phase of waves and the breaking inception under the effective wind. Here comes in question the relation between wind stresses and surface drift. However, their analyses are insufficient in regard to this relation due to the omission of the viscous effects. When the duration and speed of the wind become reasonably

great compared with the wave motion, the viscous effects are no longer negligible.

From this standpoint, the normal distribution of surface drift in the vortical wind-drift layer is evaluated based on intrinsic equations[10] derived from the Navier-Stokes equations of motion with boundary layer approximations. The wind stresses at just breaking, such as shear stress and pressure, are determined with use of the breaking condition of Rankine-Stokes' type. The surface drift distributes in much the same way as if the leeward side of the wave crest were sheltered, so when the effect of the shear stress becomes great compared with the pressure, the downward side of the wave crest may tumble forward in the usually understood sense.

Section 2.5 summarizes the preceding results obtained from the theoretical investigations in this chapter.

2.2 A Breaking Model for Progressive Waves of Permanent Type

(1) Wave Equation in Shallow Water

When a perturbation method is applied to the basic equations for wave motion, periodicity is usually assumed for both the wave profile and the velocity potential. This assumption restrains the fluid motion *a priori*, so the wave motion cannot be formulated without using physical conditions, such as Stokes' first and second definitions for the wave velocity[11]. In this section, following Tsuchiya and Yasuda's developments[12),13)], periodicity is assumed for the wave profile, but not for the water particle velocity, and a basic equation for breaking waves expressed by only the water surface displacement is proposed.

Consider two-dimensional surface waves propagating on water of uniform depth h with constant density ρ, under the influence of gravity g. Assuming

that the fluid is inviscid and incompressible and that the motion is irrotational, there exists velocity potential. A coordinate origin is set up at the sea bottom, the x^*-axis being taken horizontally and z^*-axis, vertically upward as illustrated in **Fig. 2.1.** Positive x^* is taken to be the same direction of wave propagation. Non-dimensional variables are defined as

$$\phi = \phi^*/h\sqrt{gh}, \quad (x,z) = (x^*,z^*)/h, \quad t = t^*\sqrt{g/h}, \quad \tilde{\zeta} = \zeta^*/h, \qquad (2.1)$$

where the asterisk denotes a dimensional variable, and ϕ^* is the velocity potential, ζ^* the water surface displacement, and t^* the time. The basic equations are, thus,

$$\left.\begin{aligned} &\nabla^2\phi = 0, \\ &\phi_t + (1/2)(\phi_x^2+\phi_z^2)+z-1 = 0 \qquad \text{at } z = \tilde{\zeta}, \\ &\tilde{\zeta}_t+\tilde{\zeta}_x\phi_x-\phi_z = 0 \qquad \text{at } z = \tilde{\zeta}, \\ &\phi_z = 0 \qquad \text{at } z = 0, \end{aligned}\right\} \qquad (2.2)$$

where ∇^2 is the Laplacian and the subscripts denote partial derivatives.

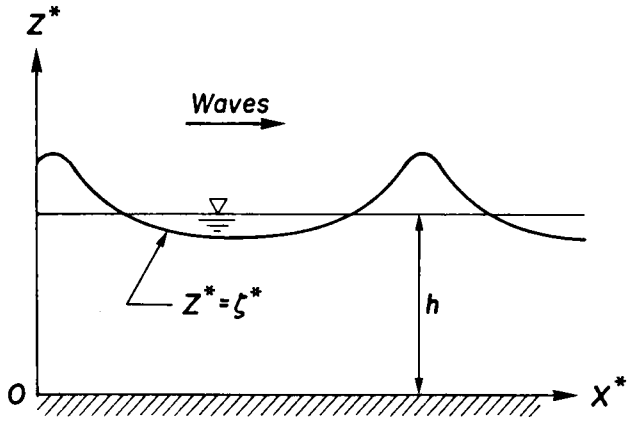

Fig. 2.1 Coordinate system.

The second and third of Eq. (2.2) are the dynamical and kinematic boundary conditions, respectively. The variational principle[4] for Eq. (2.2) is

$$\delta\int\int_R \mathfrak{L}\, dxdt = 0, \quad \mathfrak{L} = -\int_0^{\tilde{\zeta}} \{\phi_t + (1/2)(\phi_x^2+\phi_z^2)+z-1\}\, dz, \qquad (2.3)$$

where $\mathfrak{L}$ is the Lagrangian and R an arbitrary region in the (x,t) space.

The first, third, and fourth of Eq. (2.2) are derived from the variation $\delta\phi$, and the second, from the variation $\delta\tilde{\zeta}$. The significance of Eq. (2.3) is that the basic equations are the stationary conditions for the functional.

Now introduce Gardner-Morikawa's transformation[14]

$$\xi = \varepsilon^{1/2}(x - t), \quad \tau = \varepsilon^{3/2}t, \quad z = z, \tag{2.4}$$

and take perturbations for the water surface displacement and velocity potential as

$$\tilde{\zeta}(x,t) = 1+\varepsilon\zeta_1(\xi,\tau)+\varepsilon^2\zeta_2(\xi,\tau)+\varepsilon^3\zeta_3(\xi,\tau)+\ldots, \tag{2.5}$$

$$\phi(x,z,t) = \varepsilon^{1/2}\{\ \phi_1(\xi,z,\tau)+\varepsilon\phi_2(\xi,z,\tau)+\varepsilon^2\phi_3(\xi,z,\tau)+\ldots\ \}, \tag{2.6}$$

where ε is a small parameter. The boundary conditions for a function $f(x,z,t)$ at the wave surface $z = \tilde{\zeta}$ can be expanded in the Taylor series around $z = 1$ such that

$$f(x,\tilde{\zeta},t) = f(\xi,1,\tau)+(\tilde{\zeta}-1)f_z(\xi,1,\tau)+(1/2!)(\tilde{\zeta}-1)^2f_{zz}(\xi,1,\tau)+\ldots \tag{2.7}$$

By inserting Eqs. (2.4), (2.5), and (2.6) into the basic eqations (2.2), the lowest order equations of approximations become

$$\left.\begin{aligned} &\phi_{1zz} = 0, \\ &\zeta_1-\phi_{1\xi} = -(1/2)\phi_{1z}^2 \qquad \text{at } z = 1, \\ &\phi_{1z} = 0 \qquad \text{at } z = 1, \\ &\phi_{1z} = 0 \qquad \text{at } z = 0. \end{aligned}\right\} \tag{2.8}$$

From the first of Eq. (2.8) $\phi = C_1z + C_2$, where C_1 and C_2 are arbitrary functions of ξ and τ, arising from the integration. From the fourth condition of Eq. (2.8) $C_1 = 0$. The second and third of Eq. (2.8), then, lead to

$$\phi_{1\xi} = \zeta_1, \quad \phi_1 = C_2(\xi,\tau). \tag{2.9}$$

Since ϕ_1 is independent of z in the first order approximation, the horizontal component of water particle velocities distributes uniformly throughout the water depth.

The second order approximations are

$$\left.\begin{aligned} &\phi_{2zz} = -\phi_{1\xi\xi}, \\ &\zeta_2 - \phi_{2\xi} = -\phi_{1\tau} - (1/2)\phi_{1\xi}^2 \qquad \text{at } z = 1, \\ &\phi_{2z} = -\zeta_{1\xi} \qquad \text{at } z = 1, \\ &\phi_{2z} = 0 \qquad \text{at } z = 0. \end{aligned}\right\} \tag{2.10}$$

With the aid of Eq. (2.9), the first of Eq. (2.10) integrates to

$$\phi_2 = -(1/2)z^2\zeta_{1\xi} + C_4(\xi,\tau), \tag{2.11}$$

where the kinematic boundary condition at $z = 1$ and the condition at $z = 0$ have been used. From the dynamical boundary condition, C_4 becomes

$$C_{4\xi} = C_{2\tau} + \zeta_2 + (1/2)\zeta_1^2 + (1/2)\zeta_{1\xi\xi}. \tag{2.12}$$

To obtain the wave equation, third order approximations are required:

$$\left.\begin{aligned} &\phi_{3zz} = -\phi_{2\xi\xi}, \\ &\zeta_3 - \phi_{3\xi} = -(1/2)\phi_{2z}^2 - \phi_{1\xi}\phi_{2\xi} - \phi_{2\tau} + \zeta_1\phi_{2\xi z} \qquad \text{at } z = 1, \\ &\phi_{3z} = -\zeta_{2\xi} - \zeta_1\phi_{2zz} + \zeta_{1\xi}\phi_{1\xi} + \zeta_{1\tau} \qquad \text{at } z = 1, \\ &\phi_{3z} = 0 \qquad \text{at } z = 0. \end{aligned}\right\} \tag{2.13}$$

The velocity potential ϕ_3 easily integrates to

$$\phi_3 = (1/24)z^4\zeta_{1\xi\xi\xi} - (1/2)z^2C_{4\xi\xi} + C_6(\xi,\tau), \tag{2.14}$$

and C_6 is given by

$$\begin{aligned} C_{6\xi} = {} & C_{4\tau} + \zeta_1 C_{2\tau} + \zeta_3 + \zeta_1\zeta_2 + (1/2)\zeta_{2\xi\xi} \\ & + (1/2)\zeta_1^3 + \zeta_{1\xi}^2 + (3/2)\zeta_1\zeta_{1\xi\xi} + (5/24)\zeta_{1\xi\xi\xi\xi}. \end{aligned} \tag{2.15}$$

The kinematic boundary condition, the third of Eq. (2.13), gives the wave equation for ζ_1,

$$\zeta_{1\tau} + (3/2)\zeta_1\zeta_{1\xi} + (1/6)\zeta_{1\xi\xi\xi} = 0, \tag{2.16}$$

by eliminating ϕ_1, ϕ_2, ϕ_3, ζ_2, and C_4. This equation is the well-known Korteweg-deVries equation[5].

For the fourth order terms the same pattern is followed. The basic equations are

$$\left.\begin{aligned} &\phi_{4zz} = -\phi_{3\xi\xi}, \\ &\zeta_4 - \phi_{4\xi} = \zeta_2\phi_{2\xi z} + (1/2)\zeta_1^2\phi_{2\xi zz} + \zeta_1\phi_{3\xi z} - \phi_{3\tau} - \zeta_1\phi_{2\tau z} - (1/2)\phi_{2\xi}^2 \\ &\qquad\qquad - \phi_{1\xi}\phi_{3\xi} - \zeta_1\phi_{1\xi}\phi_{2\xi z} - \zeta_1\phi_{2z}\phi_{2zz} - \phi_{2z}\phi_{3z} \qquad \text{at } z = 1, \end{aligned}\right\} \tag{2.17}$$

$$\left.\begin{aligned}\phi_{4z} &= -\zeta_{3\xi}-\zeta_2\phi_{2zz}-(1/2)\zeta_1{}^2\phi_{2zzz}-\zeta_1\phi_{3zz}\\ &\quad+\zeta_{1\xi}\phi_{2\xi}+\zeta_{2\xi}\phi_{1\xi}+\zeta_{2\tau} \qquad \text{at } z=1,\\ \phi_{4z} &= 0 \qquad \text{at } z=0,\end{aligned}\right\}$$

and the velocity potential ϕ_4 and function C_6 can be expressed as

$$\phi_4 = -(1/720)\,z^6\zeta_{1\xi\xi\xi\xi\xi\xi}+(1/24)z^4C_{4\xi\xi\xi\xi}-(1/2)z^2C_{6\xi\xi}+C_8(\xi,\tau), \tag{2.18}$$

$$\begin{aligned}C_{8\xi} &= C_{6\tau}+\zeta_1C_{6\xi}+(1/2)C_{6\xi\xi\xi}+(1/2)C_{4\xi}{}^2+(1/2)\zeta_1C_{4\xi\xi\xi}+\zeta_{1\xi}C_{4\xi\xi}\\ &\quad-(1/2)\zeta_{1\xi\xi}C_{4\xi}-(1/2)C_{4\xi\xi\tau}-(1/24)C_{4\xi\xi\xi\xi\xi}+\zeta_4+\zeta_2\zeta_{1\xi\xi}+\zeta_1\zeta_{1\xi}{}^2\\ &\quad-(1/2)\zeta_1{}^2\zeta_{1\xi\xi}-\zeta_1\zeta_{1\xi\tau}-(1/8)\zeta_1\zeta_{1\xi\xi\xi\xi}+(1/8)\zeta_{1\xi\xi}{}^2-(1/6)\zeta_{1\xi}\zeta_{1\xi\xi\xi}\\ &\quad+(1/24)\zeta_{1\xi\xi\xi\tau}+(1/720)\zeta_{1\xi\xi\xi\xi\xi\xi}.\end{aligned} \tag{2.19}$$

The wave equation for ζ_2 is similarly determined from the kinematic boundary condition:

$$\zeta_{2\tau}+(3/2)(\zeta_1\zeta_2)_\xi+(1/6)\zeta_{2\xi\xi\xi} = -F_1, \tag{2.20}$$

where

$$\begin{aligned}F_1 &= (1/15)\zeta_{1\xi\xi\xi\xi\xi}+(2/3)\zeta_1\zeta_{1\xi\xi\xi}+(3/2)\zeta_{1\xi}\zeta_{1\xi\xi}+(3/2)\zeta_1{}^2\zeta_{1\xi}\\ &\quad+(1/6)\zeta_{1\xi\xi\tau}+(3/2)\zeta_1\zeta_{1\tau}+\zeta_{1\xi}C_{2\tau}+(1/2)C_{2\tau\tau}.\end{aligned} \tag{2.21}$$

When a similar procedure is carried out up to the order of $\varepsilon^{11/2}$ to obtain the wave equations for ζ_3 and ζ_4, the velocity potential ϕ_5 and function C_{10} are given by

$$\begin{aligned}\phi_5 &= (1/40320)z^8\zeta_{1\xi\xi\xi\xi\xi\xi\xi\xi}-(1/720)z^6C_{4\xi\xi\xi\xi\xi\xi}\\ &\quad+(1/24)z^4C_{6\xi\xi\xi\xi}-(1/2)z^2C_{8\xi\xi}+C_{10}(\xi,\tau),\end{aligned} \tag{2.22}$$

$$\begin{aligned}C_{10\xi} &= C_{8\tau}+\zeta_1C_{8\xi}+(1/2)C_{8\xi\xi\xi}+C_{4\xi}C_{6\xi}-(1/2)\zeta_{1\xi\xi}C_{6\xi}+\zeta_{1\xi}C_{6\xi\xi}-(1/2)C_{6\xi\xi\tau}\\ &\quad+(1/2)\zeta_1C_{6\xi\xi\xi}-(1/24)C_{6\xi\xi\xi\xi\xi}-(1/2)C_{4\xi}C_{4\xi\xi\xi}+(1/24)\zeta_{1\xi\xi\xi\xi}C_{4\xi}\\ &\quad-\zeta_1\zeta_{1\xi\xi}C_{4\xi}+2\zeta_1\zeta_{1\xi}C_{4\xi\xi}+\zeta_2C_{4\xi\xi\xi}-(1/6)\zeta_{1\xi\xi\xi}C_{4\xi\xi}+(1/2)C_{4\xi\xi}{}^2\\ &\quad-(1/2)\zeta_1{}^2C_{4\xi\xi\xi}+(1/4)\zeta_{1\xi\xi}C_{4\xi\xi\xi}-\zeta_1C_{4\xi\xi\tau}-(1/6)\zeta_{1\xi}C_{4\xi\xi\xi\xi}\\ &\quad-(1/8)\zeta_1C_{4\xi\xi\xi\xi\xi}+(1/24)C_{4\xi\xi\xi\xi\tau}+(1/720)C_{4\xi\xi\xi\xi\xi\xi}+\zeta_5+\zeta_3\zeta_{1\xi\xi}\\ &\quad+\zeta_2\zeta_{1\xi}{}^2-\zeta_2\zeta_{1\xi\tau}-(1/6)\zeta_2\zeta_{1\xi\xi\xi\xi}+(1/2)(\zeta_1\zeta_{1\xi})^2-(1/2)\zeta_1{}^3\zeta_{1\xi\xi}\\ &\quad+(1/2)\zeta_1\zeta_{1\xi}{}^2-(1/2)\zeta_1{}^2\zeta_{1\xi\tau}+(1/72)\zeta_{1\xi\xi\xi}{}^2-(1/12)\zeta_1{}^2\zeta_{1\xi\xi\xi\xi}\\ &\quad-(2/3)\zeta_1\zeta_{1\xi}\zeta_{1\xi\xi\xi}+(1/6)\zeta_1\zeta_{1\xi\xi\xi\tau}+(1/144)\zeta_1\zeta_{1\xi\xi\xi\xi\xi}\\ &\quad+(1/120)\zeta_{1\xi}\zeta_{1\xi\xi\xi\xi\xi}-(1/48)\zeta_{1\xi\xi}\zeta_{1\xi\xi\xi}-(1/720)\zeta_{1\xi\xi\xi\xi\xi\tau}\\ &\quad-(1/40320)\zeta_{1\xi\xi\xi\xi\xi\xi\xi}.\end{aligned} \tag{2.23}$$

The third and fourth order wave equations are also given as

$$\zeta_{3\tau}+(3/2)\{\zeta_1\zeta_3+(1/2)\zeta_2^2\}_\xi+(1/6)\zeta_{3\xi\xi\xi} = -F_2, \tag{2.24}$$

$$\zeta_{4\tau}+(3/2)(\zeta_1\zeta_4+\zeta_2\zeta_3)_\xi+(1/6)\zeta_{4\xi\xi\xi} = -F_3, \tag{2.25}$$

where

$$\begin{aligned}
F_2 = {} & (1/15)\zeta_{2\xi\xi\xi\xi\xi}+(2/3)\zeta_1\zeta_{2\xi\xi\xi}+(2/3)\zeta_{1\xi\xi\xi}\zeta_2+(3/2)\zeta_{1\xi}\zeta_{2\xi\xi} \\
& +(3/2)\zeta_{1\xi\xi}\zeta_{2\xi}+(3/2)\zeta_1^2\zeta_{2\xi}+3\,\zeta_1\zeta_{1\xi}\zeta_2+(1/6)\zeta_{2\xi\xi\tau} \\
& +(3/2)\zeta_1\zeta_{2\tau}+(3/2)\zeta_2\zeta_{1\tau}+\zeta_{1\xi}C_{4\tau}+\zeta_{2\xi}C_{2\tau}+(1/2)\zeta_{4\tau\tau} \\
& +(17/630)\zeta_{1\xi\xi\xi\xi\xi\xi\xi}+(2/5)\zeta_1\zeta_{1\xi\xi\xi\xi\xi}+(4/3)\zeta_{1\xi}\zeta_{1\xi\xi\xi\xi}+2\,\zeta_{1\xi\xi}\zeta_{1\xi\xi\xi} \\
& +(15/2)\zeta_1\zeta_{1\xi}\zeta_{1\xi\xi}+(5/4)\zeta_1^2\zeta_{1\xi\xi\xi}+(5/2)\zeta_{1\xi}^3+(9/4)\zeta_1^3\zeta_{1\xi} \\
& +(1/15)\zeta_{1\xi\xi\xi\xi\tau}+(5/3)\zeta_{1\xi\xi\xi}\zeta_{1\tau}+(5/6)\zeta_1\zeta_{1\xi\xi\tau}+(4/3)\zeta_{1\xi}\zeta_{1\xi\tau} \\
& +3\,\zeta_1^2\zeta_{1\tau}+(1/6)\zeta_{1\xi\xi\xi}C_{2\tau}+(5/2)\zeta_1\zeta_{1\xi}C_{2\tau}-(1/12)\zeta_{1\xi\tau\tau}+\zeta_{1\tau}C_{2\tau} \\
& +(3/2)\zeta_1C_{2\tau\tau},
\end{aligned} \tag{2.26}$$

$$\begin{aligned}
F_3 = {} & (1/15)\zeta_{3\xi\xi\xi\xi\xi}+(2/3)\zeta_1\zeta_{3\xi\xi\xi}+(2/3)\zeta_2\zeta_{2\xi\xi\xi}+(2/3)\zeta_3\zeta_{1\xi\xi\xi} \\
& +(3/2)\zeta_{1\xi}\zeta_{3\xi\xi}+(3/2)\zeta_{2\xi}\zeta_{2\xi\xi}+(3/2)\zeta_{3\xi}\zeta_{1\xi\xi}+(3/2)\zeta_1^2\zeta_{3\xi} \\
& +(3/2)\zeta_2^2\zeta_{1\xi}+3\,\zeta_1\zeta_2\zeta_{2\xi}+3\,\zeta_1\zeta_{1\xi}\zeta_3+(1/6)\zeta_{3\xi\xi\tau}+(3/2)\zeta_1\zeta_{3\tau} \\
& +(3/2)\zeta_2\zeta_{2\tau}+(3/2)\zeta_3\zeta_{1\tau}+\zeta_{1\xi}C_{6\tau}+\zeta_{2\xi}C_{4\tau}+\zeta_{3\xi}C_{2\tau}+(1/2)C_{6\tau\tau} \\
& +(17/630)\zeta_{2\xi\xi\xi\xi\xi\xi\xi}+(2/5)\zeta_2\zeta_{1\xi\xi\xi\xi\xi}+(2/5)\zeta_1\zeta_{2\xi\xi\xi\xi\xi}+(4/3)\zeta_{2\xi}\zeta_{1\xi\xi\xi\xi} \\
& +(4/3)\zeta_{1\xi}\zeta_{2\xi\xi\xi\xi}+2\,\zeta_{1\xi\xi}\zeta_{2\xi\xi\xi}+2\,\zeta_{2\xi\xi}\zeta_{1\xi\xi\xi}+(15/2)\zeta_1\zeta_{1\xi}\zeta_{2\xi\xi} \\
& +(15/2)\zeta_1\zeta_{1\xi\xi}\zeta_{2\xi}+(15/2)\zeta_{1\xi}\zeta_{1\xi\xi}\zeta_2+(5/4)\zeta_1^2\zeta_{2\xi\xi\xi}+(5/2)\zeta_1\zeta_2\zeta_{1\xi\xi\xi} \\
& +(15/2)(\zeta_{1\xi})^2\zeta_{2\xi}+(9/4)\zeta_1^3\zeta_{2\xi}+(27/4)\zeta_1^2\zeta_2\zeta_{1\xi}+(1/15)\zeta_{2\xi\xi\xi\xi\tau} \\
& +(5/3)\zeta_{2\xi\xi}\zeta_{1\tau}+(5/3)\zeta_{1\xi\xi}\zeta_{2\tau}+(5/6)\zeta_1\zeta_{2\xi\xi\tau}+(5/6)\zeta_2\zeta_{1\xi\xi\tau} \\
& +(4/3)\zeta_{2\xi}\zeta_{1\xi\tau}+(4/3)\zeta_{1\xi}\zeta_{2\xi\tau}+3\,\zeta_1^2\zeta_{2\tau}+6\,\zeta_1\zeta_2\zeta_{1\tau}+(1/6)\zeta_{1\xi\xi\xi}C_{4\tau} \\
& +(1/6)\zeta_{2\xi\xi\xi}C_{2\tau}+(5/2)\zeta_1\zeta_{1\xi}C_{4\tau}+(5/2)\zeta_2\zeta_{1\xi}C_{2\tau}+(5/2)\zeta_1\zeta_{2\xi}C_{2\tau} \\
& -(1/12)\zeta_{2\xi\tau\tau}+\zeta_{1\tau}C_{4\tau}+\zeta_{2\tau}C_{2\tau}+(3/2)\zeta_1C_{4\tau\tau}+(3/2)\zeta_2C_{2\tau\tau} \\
& +(31/2835)\zeta_{1\xi\xi\xi\xi\xi\xi\xi\xi\xi}+(68/315)\zeta_1\zeta_{1\xi\xi\xi\xi\xi\xi\xi}+(17/18)\zeta_{1\xi}\zeta_{1\xi\xi\xi\xi\xi\xi} \\
& +(61/30)\zeta_{1\xi\xi}\zeta_{1\xi\xi\xi\xi\xi}+(53/18)\zeta_{1\xi\xi\xi}\zeta_{1\xi\xi\xi\xi}+(26/3)\zeta_1\zeta_{1\xi}\zeta_{1\xi\xi\xi\xi} \\
& +14\,\zeta_1\zeta_{1\xi\xi}\zeta_{1\xi\xi\xi}+(151/12)\zeta_{1\xi}^2\zeta_{1\xi\xi\xi}+16\,\zeta_{1\xi}\zeta_{1\xi\xi}^2+(87/4)\zeta_1^2\zeta_{1\xi}\zeta_{1\xi\xi} \\
& +(65/4)\zeta_1\zeta_{1\xi}^3+(11/6)\zeta_1^3\zeta_{1\xi\xi\xi}+(11/10)\zeta_1^2\zeta_{1\xi\xi\xi\xi\xi}+(15/4)\zeta_1^4\zeta_{1\xi} \\
& +(17/630)\zeta_{1\xi\xi\xi\xi\xi\xi\tau}+(7/15)\zeta_1\zeta_{1\xi\xi\xi\xi\tau}+(167/120)\zeta_{1\xi}\zeta_{1\xi\xi\xi\tau}
\end{aligned}$$

$$+ (12/5)\zeta_{1\xi\xi}\zeta_{1\xi\xi\tau} + (16/15)\zeta_{1\tau}\zeta_{1\xi\xi\xi\xi} + (131/60)\zeta_{1\xi\tau}\zeta_{1\xi\xi\xi}$$
$$+ (13/6)\zeta_1^2\zeta_{1\xi\xi\tau} + (121/12)\zeta_1\zeta_{1\xi}\zeta_{1\xi\tau} + (61/6)\zeta_1\zeta_{1\tau}\zeta_{1\xi\xi} + 9\,\zeta_{1\tau}\zeta_{1\xi}^2$$
$$+ 6\,\zeta_1^3\zeta_{1\tau} - (3/80)\zeta_{1\xi\xi\xi\tau\tau} - (1/2)\zeta_1\zeta_{1\xi\tau\tau} + (4/3)\zeta_{1\tau}\zeta_{1\xi\tau}$$
$$+ (5/4)\zeta_{1\xi}\zeta_{1\tau\tau} - (1/12)\zeta_{1\tau\tau\tau} + (1/15)\zeta_{1\xi\xi\xi\xi\xi}C_{2\tau} + \zeta_1\zeta_{1\xi\xi\xi}C_{2\tau}$$
$$+ (7/2)\zeta_{1\xi}\zeta_{1\xi\xi}C_{2\tau} + (1/3)\zeta_{1\xi\xi\tau}C_{2\tau} + 6\,\zeta_1^2\zeta_{1\xi}C_{2\tau} + 5\,\zeta_1\zeta_{1\tau}C_{2\tau}$$
$$+ (7/6)\zeta_{1\xi\xi}C_{2\tau\tau} + 3\,\zeta_1^2C_{2\tau\tau} + \zeta_{1\xi}C_{2\tau}^2 + C_{2\tau}C_{2\tau\tau}. \qquad (2.27)$$

Odd terms C_j $(j = 1,3,5,\ldots)$ vanish from the boundary condition at $z = 0$, but even terms C_j $(j = 2,4,6,\ldots)$ must be treated as non-zero functions because of the non-periodicity for the water particle velocity. If both sides of Eqs. (2.16), (2.20), (2.24), and (2.25) are summed up respectively with the aid of

$$\zeta = \zeta_1 + \varepsilon\zeta_2 + \varepsilon^2\zeta_3 + \varepsilon^3\zeta_4 + \ldots, \qquad (2.28)$$

$$\Omega = C_2 + \varepsilon C_4 + \varepsilon^2 C_6 + \varepsilon^3 C_8 + \ldots, \qquad (2.29)$$

the wave equation expressed by only the water surface displacement is given by

$$\zeta_\tau + (3/2)\zeta\zeta_\xi + (1/6)\zeta_{\xi\xi\xi} = -\varepsilon F_1 - \varepsilon^2 F_2 - \varepsilon^3 F_3 - \ldots, \qquad (2.30)$$

with

$$F_1 = (1/15)\zeta_{\xi\xi\xi\xi\xi} + (2/3)\zeta\zeta_{\xi\xi\xi} + (3/2)\zeta_\xi\zeta_{\xi\xi} + (3/2)\zeta^2\zeta_\xi$$
$$+ (1/6)\zeta_{\xi\xi\tau} + (3/2)\zeta\zeta_\tau + \zeta_\xi\Omega_\tau + (1/2)\Omega_{\tau\tau}, \qquad (2.31.1)$$

$$F_2 = (17/630)\zeta_{\xi\xi\xi\xi\xi\xi\xi} + (2/5)\zeta\zeta_{\xi\xi\xi\xi\xi} + (4/3)\zeta_\xi\zeta_{\xi\xi\xi\xi} + 2\,\zeta_{\xi\xi}\zeta_{\xi\xi\xi}$$
$$+ (15/2)\zeta\zeta_\xi\zeta_{\xi\xi} + (5/4)\zeta^2\zeta_{\xi\xi\xi\xi} + (5/2)\zeta_\xi^3 + (9/4)\zeta^3\zeta_\xi$$
$$+ (1/15)\zeta_{\xi\xi\xi\xi\xi\tau} + (5/3)\zeta_{\xi\xi\xi}\zeta_\tau + (4/3)\zeta_\xi\zeta_{\xi\tau} + (5/6)\zeta\zeta_{\xi\xi\tau} + 3\,\zeta^2\zeta_\tau$$
$$- (1/12)\zeta_{\xi\tau\tau} + (1/6)\zeta_{\xi\xi\xi}\Omega_\tau + (5/2)\zeta\zeta_\xi\Omega_\tau + \zeta_\tau\Omega_\tau + (3/2)\zeta\Omega_{\tau\tau}, \qquad (2.31.2)$$

$$F_3 = (31/2835)\zeta_{\xi\xi\xi\xi\xi\xi\xi\xi\xi} + (68/315)\zeta\zeta_{\xi\xi\xi\xi\xi\xi\xi} + (17/18)\zeta_\xi\zeta_{\xi\xi\xi\xi\xi\xi}$$
$$+ (61/30)\zeta_{\xi\xi}\zeta_{\xi\xi\xi\xi\xi} + (53/18)\zeta_{\xi\xi\xi}\zeta_{\xi\xi\xi\xi} + (26/3)\zeta\zeta_\xi\zeta_{\xi\xi\xi\xi}$$
$$+ 14\,\zeta\zeta_{\xi\xi}\zeta_{\xi\xi\xi} + (151/12)\zeta_\xi^2\zeta_{\xi\xi\xi} + 16\,\zeta_\xi\zeta_{\xi\xi}^2 + (87/4)\zeta^2\zeta_\xi\zeta_{\xi\xi}$$
$$+ (65/4)\zeta\zeta_\xi^3 + (11/6)\zeta^3\zeta_{\xi\xi\xi} + (11/10)\zeta^2\zeta_{\xi\xi\xi\xi\xi} + (15/4)\zeta^4\zeta_\xi$$
$$+ (17/630)\zeta_{\xi\xi\xi\xi\xi\xi\tau} + (7/15)\zeta\zeta_{\xi\xi\xi\xi\tau} + (167/120)\zeta_\xi\zeta_{\xi\xi\xi\tau}$$
$$+ (12/5)\zeta_{\xi\xi}\zeta_{\xi\xi\tau} + (16/15)\zeta_\tau\zeta_{\xi\xi\xi\xi} + (131/60)\zeta_{\xi\tau}\zeta_{\xi\xi\xi} + (13/6)\zeta^2\zeta_{\xi\xi\tau}$$

$$+ (121/12)\zeta\zeta_\xi\zeta_{\xi\tau} + (61/6)\zeta\zeta_\tau\zeta_{\xi\xi} + 9\,\zeta_\tau\zeta_\xi^2 + 6\,\zeta^3\zeta_\tau - (3/80)\zeta_{\xi\xi\xi\tau\tau}$$
$$- (1/2)\zeta\zeta_{\xi\tau\tau} + (4/3)\zeta_\tau\zeta_{\xi\tau} + (5/4)\zeta_\xi\zeta_{\tau\tau} - (1/12)\zeta_{\tau\tau\tau}$$
$$+ (1/15)\zeta_{\xi\xi\xi\xi\xi}\Omega_\tau + \zeta\zeta_{\xi\xi\xi}\Omega_\tau + (7/2)\zeta_\xi\zeta_{\xi\xi}\Omega_\tau + (1/3)\zeta_{\xi\xi\tau}\Omega_\tau + 6\,\zeta^2\zeta_\xi\Omega_\tau$$
$$+ 5\,\zeta\zeta_\tau\Omega_\tau + (7/6)\zeta_{\xi\xi}\Omega_{\tau\tau} + 3\,\zeta^2\Omega_{\tau\tau} + \zeta_\xi\Omega_\tau^2 + \Omega_\tau\Omega_{\tau\tau}, \qquad (2.31.3)$$

and

$$\Omega_\xi = \zeta + \varepsilon\{\ \Omega_\tau + (1/2)\zeta^2 + (1/2)\zeta_{\xi\xi}\ \}$$
$$+ \varepsilon^2\{\ \zeta\Omega_\tau + (1/2)\zeta^3 + \zeta_\xi^2 + (3/2)\zeta\zeta_{\xi\xi} + (5/24)\zeta_{\xi\xi\xi\xi}\ \}$$
$$+ \varepsilon^3\{\ (1/2)\Omega_\tau^2 + (3/2)\zeta^2\Omega_\tau + (1/2)\zeta_{\xi\xi}\Omega_\tau + 2\zeta_\xi\zeta_\tau + (5/8)\zeta^4$$
$$+ (9/4)\zeta^2\zeta_{\xi\xi} + 5\zeta\zeta_\xi^2 + (13/8)\zeta_{\xi\xi}^2 + (8/3)\zeta_\xi\zeta_{\xi\xi\xi}$$
$$+ (25/24)\zeta\zeta_{\xi\xi\xi\xi} + (61/720)\zeta_{\xi\xi\xi\xi\xi\xi}\ \}$$
$$+ \ldots\ldots \qquad (2.32)$$

When $\varepsilon = 0$, Eq. (2.30) coincides with the Korteweg-deVries equation.

Now consider the waves of permanent type, for which it should be held that

$$d\xi/d\tau = c_0 + \varepsilon c_1 + \varepsilon^2 c_2 + \varepsilon^3 c_3 + \ldots = \text{const.} = c^*, \qquad (2.33)$$

where c^*, say, is a correction term for the wave velocity. Furthermore, introduce a frame of reference moving with the wave,

$$\theta = \xi - c^*\tau. \qquad (2.34)$$

Therefore, the wave equation for waves of permanent type in shallow water finally becomes the ordinary differential equation with respect to θ:

$$-c^*\zeta_\theta + (3/2)\zeta\zeta_\theta + (1/6)\zeta_{\theta\theta\theta} = -\varepsilon F_1 - \varepsilon^2 F_2 - \varepsilon^3 F_3 - \ldots, \qquad (2.35)$$

where

$$F_1 = (1/15)\zeta_{\theta\theta\theta\theta\theta} + (2/3)\zeta\zeta_{\theta\theta\theta} + (3/2)\zeta_\theta\zeta_{\theta\theta} + (3/2)\zeta^2\zeta_\theta$$
$$- (1/6)c^*\zeta_{\theta\theta\theta} - (5/2)c^*\zeta\zeta_\theta + (1/2)c^{*2}\zeta_\theta, \qquad (2.36.1)$$

$$F_2 = (17/630)\zeta_{\theta\theta\theta\theta\theta\theta\theta} + (2/5)\zeta\zeta_{\theta\theta\theta\theta\theta} + (4/3)\zeta_\theta\zeta_{\theta\theta\theta\theta} + 2\,\zeta_{\theta\theta}\zeta_{\theta\theta\theta}$$
$$+ (15/2)\zeta\zeta_\theta\zeta_{\theta\theta} + (5/4)\zeta^2\zeta_{\theta\theta\theta} + (5/2)\zeta_\theta^3 + (9/4)\zeta^3\zeta_\theta$$
$$- (1/15)c^*\zeta_{\theta\theta\theta\theta\theta} - c^*\zeta\zeta_{\theta\theta\theta} - (7/2)c^*\zeta_\theta\zeta_{\theta\theta} - 6\,c^*\zeta^2\zeta_\theta$$
$$+ (1/6)c^{*2}\zeta_{\theta\theta\theta} + 4\,c^{*2}\zeta\zeta_\theta - (1/2)c^{*3}\zeta_\theta, \qquad (2.36.2)$$

$$F_3 = (31/2835)\zeta_{\theta\theta\theta\theta\theta\theta\theta\theta\theta} + (68/315)\zeta\zeta_{\theta\theta\theta\theta\theta\theta\theta} + (17/18)\zeta_\theta\zeta_{\theta\theta\theta\theta\theta}$$

$$+(61/30)\zeta_{\theta\theta}\zeta_{\theta\theta\theta\theta}+(53/18)\zeta_{\theta\theta\theta}\zeta_{\theta\theta\theta}+(26/3)\zeta\zeta_{\theta}\zeta_{\theta\theta\theta}$$
$$+14\,\zeta\zeta_{\theta\theta}\zeta_{\theta\theta\theta}+(151/12)\zeta_{\theta}^{2}\zeta_{\theta\theta\theta}+16\,\zeta_{\theta}\zeta_{\theta\theta}^{2}+(87/4)\zeta^{2}\zeta_{\theta}\zeta_{\theta\theta}$$
$$+(65/4)\zeta\zeta_{\theta}^{3}+(11/6)\zeta^{3}\zeta_{\theta\theta\theta}+(11/10)\zeta^{2}\zeta_{\theta\theta\theta\theta}+(15/4)\zeta^{4}\zeta_{\theta}$$
$$-(17/630)c^{*}\zeta_{\theta\theta\theta\theta\theta\theta}-(8/15)c^{*}\zeta\zeta_{\theta\theta\theta\theta}-(8/3)c^{*}\zeta_{\theta}\zeta_{\theta\theta\theta}$$
$$-(14/3)c^{*}\zeta_{\theta\theta}\zeta_{\theta\theta\theta}-(13/4)c^{*}\zeta^{2}\zeta_{\theta\theta\theta}-(53/2)c^{*}\zeta\zeta_{\theta}\zeta_{\theta\theta}-10\,c^{*}\zeta_{\theta}^{3}$$
$$-(55/4)c^{*}\zeta^{3}\zeta_{\theta}+(1/15)c^{*2}\zeta_{\theta\theta\theta\theta\theta}+(3/2)c^{*2}\zeta\zeta_{\theta\theta\theta}+(13/2)c^{*2}\zeta_{\theta}\zeta_{\theta\theta}$$
$$+(63/4)c^{*2}\zeta^{2}\zeta_{\theta}-(1/6)c^{*3}\zeta_{\theta\theta\theta}-6\,c^{*3}\zeta\zeta_{\theta}+(1/2)c^{*4}\zeta_{\theta}, \qquad (2.36.3)$$

and

$$\Omega_{\theta} = \zeta+\varepsilon\{-c^{*}\zeta+(1/2)\zeta^{2}+(1/2)\zeta_{\theta\theta}\}$$
$$+\varepsilon^{2}\{c^{*2}\zeta-(3/2)c^{*}\zeta^{2}-(1/2)c^{*}\zeta_{\theta\theta}+(1/2)\zeta^{3}$$
$$+\zeta_{\theta}^{2}+(3/2)\zeta\zeta_{\theta\theta}+(5/24)\zeta_{\theta\theta\theta\theta}\}$$
$$+\varepsilon^{3}\{-c^{*3}\zeta+3\,c^{*2}\zeta^{2}+(1/2)c^{*2}\zeta_{\theta\theta}-(5/2)c^{*}\zeta^{3}-3\,c^{*}\zeta_{\theta}^{2}$$
$$-(5/2)c^{*}\zeta\zeta_{\theta\theta}-(5/24)c^{*}\zeta_{\theta\theta\theta\theta}+(5/8)\zeta^{4}+(9/4)\zeta^{2}\zeta_{\theta\theta}$$
$$+5\,\zeta\zeta_{\theta}^{2}+(13/8)\zeta_{\theta\theta}^{2}+(8/3)\zeta_{\theta}\zeta_{\theta\theta\theta}+(25/24)\zeta\zeta_{\theta\theta\theta\theta}$$
$$+(61/720)\zeta_{\theta\theta\theta\theta\theta\theta}\}$$
$$+\ldots\ldots \qquad (2.37)$$

(2) Variational Formulation

First, Eq. (2.35) is transformed into a form suitable for variational formulation. With the aid of Eqs. (2.28) and (2.33), the two lowest order equations are

$$-c_{0}\zeta_{1\theta}+(3/2)\zeta_{1}\zeta_{1\theta}+(1/6)\zeta_{1\theta\theta\theta}=0, \qquad (2.38)$$

and

$$-c_{0}\zeta_{2\theta}-c_{1}\zeta_{1\theta}+(3/2)(\zeta_{1}\zeta_{2})_{\theta}+(1/6)\zeta_{2\theta\theta\theta}$$
$$=-(1/15)\zeta_{1\theta\theta\theta\theta\theta}-(2/3)\zeta_{1}\zeta_{1\theta\theta\theta}-(3/2)\zeta_{1\theta}\zeta_{1\theta\theta}-(3/2)\zeta_{1}^{2}\zeta_{1\theta}$$
$$+(1/6)c_{0}\zeta_{1\theta\theta\theta}+(5/2)c_{0}\zeta_{1}\zeta_{1\theta}-(1/2)c_{0}^{2}\zeta_{1\theta}. \qquad (2.39)$$

The higher order derivatives $\zeta_{1\theta\theta\theta\theta}$ and $\zeta_{1\theta\theta\theta}$ in Eq. (2.39) can be eliminated by Eq. (2.38), hence

$$-c_0\zeta_{2\theta}-c_1\zeta_{1\theta}+(3/2)(\zeta_1\zeta_2)_\theta+(1/6)\zeta_{2\theta\theta\theta}$$
$$=(3/10)\zeta_{1\theta}\zeta_{1\theta\theta}-(9/10)\zeta_1{}^2\zeta_{1\theta}+(21/5)c_0\zeta_1\zeta_{1\theta}-(19/10)c_0{}^2\zeta_{1\theta}. \quad (2.40)$$

By accomplishing similar transformations for Eq. (2.35) and by adding together both sides of the resultant equations, such as Eqs. (2.38) and (2.40), Eq. (2.35) becomes

$$\begin{aligned}
&-c^*\zeta_\theta+(3/2)\zeta\zeta_\theta+(1/6)\zeta_{\theta\theta\theta}\\
&=\varepsilon\{(3/20)\zeta_\theta{}^2-(3/10)\zeta^3+(21/10)c^*\zeta^2-(19/10)c^{*2}\zeta\}_\theta\\
&+\varepsilon^2\{-(149/700)\zeta^2\zeta_{\theta\theta}+(13/35)\zeta\zeta_\theta{}^2-(36/175)c^*\zeta_\theta{}^2-(5967/2800)\zeta^4\\
&\quad+(1971/350)c^*\zeta^3-(4869/700)c^{*2}\zeta^2+(576/175)c^{*3}\zeta\}_\theta\\
&+\varepsilon^3\{(1157/3500)\zeta_\theta{}^2\zeta_{\theta\theta}-(151/2625)\zeta^3\zeta_{\theta\theta}+(229/350)c^*\zeta^2\zeta_{\theta\theta}\\
&\quad+(10123/7000)\zeta^2\zeta_\theta{}^2-(4241/1750)c^*\zeta\zeta_\theta{}^2+(546/875)c^{*2}\zeta_\theta{}^2\\
&\quad-(8541/3500)\zeta^5+(54003/3500)c^*\zeta^4-(87141/3500)c^{*2}\zeta^3\\
&\quad+(3117/175)c^{*3}\zeta^2-(947/175)c^{*4}\zeta\}_\theta\\
&+\cdots\cdots
\end{aligned} \quad (2.41)$$

There is no variational principle for this equation as it stands, so that some potential representations are required. The simplest choice is

$$\zeta=\varphi_\xi=\varphi_\theta, \qquad \chi=\varphi_{\xi\xi}=\varphi_{\theta\theta}, \quad (2.42)$$

as pointed out by Whitham[15]. Therefore, Eq. (2.41) is expressed as

$$\begin{aligned}
&-c^*\varphi_{\theta\theta}+(3/2)\varphi_\theta\varphi_{\theta\theta}+(1/6)\chi_{\theta\theta}\\
&=\varepsilon\{(3/20)\varphi_{\theta\theta}{}^2-(3/10)\varphi_\theta{}^3+(21/10)c^*\varphi_\theta{}^2-(19/10)c^{*2}\varphi_\theta\}_\theta\\
&+\varepsilon^2\{-(149/700)\varphi_\theta{}^2\varphi_{\theta\theta\theta}+(13/35)\varphi_\theta\varphi_{\theta\theta}{}^2-(36/175)c^*\varphi_{\theta\theta}{}^2-(5967/2800)\varphi_\theta{}^4\\
&\quad+(1971/350)c^*\varphi_\theta{}^3-(4869/700)c^{*2}\varphi_\theta{}^2+(576/175)c^{*3}\varphi_\theta\}_\theta\\
&+\varepsilon^3\{(1157/3500)\varphi_{\theta\theta}{}^2\varphi_{\theta\theta\theta}-(151/2625)\varphi_\theta{}^3\varphi_{\theta\theta\theta}+(229/350)c^*\varphi_\theta{}^2\varphi_{\theta\theta\theta}\\
&\quad+(10123/7000)\varphi_\theta{}^2\varphi_{\theta\theta}{}^2-(4241/1750)c^*\varphi_\theta\varphi_{\theta\theta}{}^2+(546/875)c^{*2}\varphi_{\theta\theta}{}^2\\
&\quad-(8541/3500)\varphi_\theta{}^5+(54003/3500)c^*\varphi_\theta{}^4-(87141/3500)c^{*2}\varphi_\theta{}^3\\
&\quad+(3117/175)c^{*3}\varphi_\theta{}^2-(947/175)c^{*4}\varphi_\theta\}_\theta\\
&+\cdots\cdots
\end{aligned} \quad (2.43)$$

It will be sufficient to consider the wave motion described by the variational principle

$$\delta\int\int \mathfrak{L}(\chi,\chi_\theta,\varphi_\theta,\varphi_{\theta\theta})\,d\theta\,d\theta = 0 \tag{2.44}$$

for the pair of Eqs. (2.42) and (2.43) because Eq. (2.43) integrates onece to give the third derivative $\varphi_{\theta\theta\theta}$, then this term in the right-hand side of Eq. (2.43) can be eliminated. The variational equations are

$$\frac{\partial\mathfrak{L}}{\partial\chi} - \frac{d}{d\theta}\frac{\partial\mathfrak{L}}{\partial\chi_\theta} = 0, \qquad \frac{d}{d\theta}\frac{\partial\mathfrak{L}}{\partial\varphi_\theta} - \frac{d^2}{d\theta^2}\frac{\partial\mathfrak{L}}{\partial\varphi_{\theta\theta}} = 0. \tag{2.45}$$

These equations can be integrated approximately as follows: from Eq. (2.42) and the first of Eq. (2.45), the Lagrangian takes the form

$$\mathfrak{L} = -(1/6)\chi_\theta\varphi_\theta - (1/12)\chi^2 + \mathfrak{L}^*(\varphi_\theta,\varphi_{\theta\theta}) \tag{2.46}$$

with the correction term $\mathfrak{L}^*$ which follows from the differential equation

$$\begin{aligned}
D\mathfrak{L}^* &= c^*\varphi_\theta - (3/4)\varphi_\theta^2 \\
&+\varepsilon\,[\ (3/20)\varphi_{\theta\theta}^2 - (3/10)\varphi_\theta^3 + (21/10)c^*\varphi_\theta^2 - (19/10)c^{*2}\varphi_\theta\ ] \\
&+\varepsilon^2[\ (13/35)\varphi_\theta\varphi_{\theta\theta}^2 - (36/175)c^*\varphi_{\theta\theta}^2 - (657/560)\varphi_\theta^4 \\
&\quad + (762/175)c^*\varphi_\theta^3 - (4869/700)c^{*2}\varphi_\theta^2 + (576/175)c^{*3}\varphi_\theta \\
&\quad - (447/350)B_0\varphi_\theta^2\ ] \\
&+\varepsilon^3[\ -(1631/7000)\varphi_\theta^2\varphi_{\theta\theta}^2 - (77/175)c^*\varphi_\theta\varphi_{\theta\theta}^2 + (546/875)c^{*2}\varphi_{\theta\theta}^2 \\
&\quad - (6294/3500)\varphi_\theta^5 + (33103/3500)c^*\varphi_\theta^4 - (64908/3500)c^{*2}\varphi_\theta^3 \\
&\quad + (3117/175)c^{*3}\varphi_\theta^2 - (947/175)c^{*4}\varphi_\theta \\
&\quad + B_0\{(3471/1750)\varphi_{\theta\theta}^2 - (302/875)\varphi_\theta^3 + (687/175)c^*\varphi_\theta^2\}\ ] \\
&+ \ldots\ldots,
\end{aligned} \tag{2.47}$$

where B_0 is an integral constant to be determined later, arising in elimination of the third derivative $\varphi_{\theta\theta\theta}$. D is also the differential operator

$$D = \frac{\partial}{\partial\varphi_\theta} - \frac{d}{d\theta}\frac{\partial}{\partial\varphi_{\theta\theta}}. \tag{2.48}$$

The assumptions that

$$\mathfrak{L}^* = \mathfrak{L}^*_1 = (\alpha_1\varphi_\theta + \beta_1\varphi_\theta^2 + \gamma_1\varphi_\theta^3)\varphi_{\theta\theta}^2 + G_1(\varphi_\theta) + \mathfrak{L}^*_2(\varphi_\theta,\varphi_{\theta\theta}), \tag{2.49}$$

$$\begin{aligned}
G_1(\varphi_\theta) &= (1/2)c^*\varphi_\theta^2 - (1/4)\varphi_\theta^3 \\
&\quad +\varepsilon\,[\ -(3/40)\varphi_\theta^4 + (7/10)c^*\varphi_\theta^3 - (19/20)c^{*2}\varphi_\theta^2\ ]
\end{aligned}$$

$$+\varepsilon^2\{\ -(657/2800)\varphi_\theta{}^5+(762/700)c^*\varphi_\theta{}^4-(1623/700)c^{*2}\varphi_\theta{}^3$$
$$+(288/175)c^{*3}\varphi_\theta{}^2-(149/350)B_0\varphi_\theta{}^3\ \}$$
$$+\varepsilon^3\{\ -(1049/3500)\varphi_\theta{}^6+(33103/17500)c^*\varphi_\theta{}^5$$
$$-(16227/3500)c^{*2}\varphi_\theta{}^4+(1039/175)c^{*3}\varphi_\theta{}^3-(947/350)c^{*4}\varphi_\theta{}^2$$
$$+B_0\{-(151/1750)\varphi_\theta{}^4+(229/175)c^*\varphi_\theta{}^3\}\ \}$$
$$+\ .\ .\ .\ .\ . \tag{2.50}$$

lead the coefficients α_1, β_1, and γ_1 to

$$\left.\begin{aligned}\alpha_1 &= -(3/20)\varepsilon+(36/175)\varepsilon^2c^*-(546/875)\varepsilon^3c^{*2}-(3471/1750)\varepsilon^2B_0,\\ \beta_1 &= -(13/70)\varepsilon^2+(11/50)\varepsilon^3c^*,\\ \gamma_1 &= (1631/21000)\varepsilon^3.\end{aligned}\right\} \tag{2.51}$$

The equation for $\mathfrak{L}^*_2$ in the next order approximation is

$$D\mathfrak{L}^*_2 = \varepsilon\{\ (27/20)\varphi_\theta{}^3-(9/5)c^*\varphi_\theta{}^2-(9/5)B_0\varphi_\theta\ \}$$
$$+\varepsilon^2\{\ -(27/100)\varphi_\theta\varphi_{\theta\theta}{}^2+(387/175)\varphi_\theta{}^4-(2751/350)c^*\varphi_\theta{}^3$$
$$+(2061/350)c^{*2}\varphi_\theta{}^2+B_0\{-(78/35)\varphi_\theta{}^2+(432/175)c^*\varphi_\theta\}\ \}$$
$$+\varepsilon^3\{\ -(351/350)\varphi_\theta{}^2\varphi_{\theta\theta}{}^2+(648/875)c^*\varphi_\theta\varphi_{\theta\theta}{}^2+(29139/14000)\varphi_\theta{}^5$$
$$-(12518/875)c^*\varphi_\theta{}^4+(105681/3500)c^{*2}\varphi_\theta{}^3-(3168/175)c^{*3}\varphi_\theta{}^2$$
$$+B_0\{(36893/1750)\varphi_\theta{}^3-(18516/875)c^*\varphi_\theta{}^2-(6552/875)c^{*2}\varphi_\theta\}$$
$$-(20826/875)B_0{}^2\varphi_\theta\ \}$$
$$+\ .\ .\ .\ .\ . \tag{2.52}$$

This method of successive approximation can reduce the lowest order term of ε in the right-hand side of the differential equation as was done in deriving Eq. (2.52) from Eq. (2.47). The Lagrangian $\mathfrak{L}^*$ in the order of ε^3 can be finally approximated by

$$\mathfrak{L}^* = -(1/4)\varphi_\theta{}^3+(1/2)c^*\varphi_\theta{}^2$$
$$+\varepsilon\{\ -(3/20)\varphi_\theta\varphi_{\theta\theta}{}^2+(21/80)\varphi_\theta{}^4+(1/10)c^*\varphi_\theta{}^3-(19/20)c^{*2}\varphi_\theta{}^2$$
$$-(9/10)B_0\varphi_\theta{}^2\ \}$$
$$+\varepsilon^2\{\ -(71/1400)\varphi_\theta{}^2\varphi_{\theta\theta}{}^2+(36/175)c^*\varphi_\theta\varphi_{\theta\theta}{}^2-(99/2800)\varphi_\theta{}^5$$
$$-(33/70)c^*\varphi_\theta{}^4-(249/700)c^{*2}\varphi_\theta{}^3+(288/175)c^{*3}\varphi_\theta{}^2$$
$$-B_0\{(22/35)\varphi_\theta{}^3-(216/175)c^*\varphi_\theta{}^2\}\ \}$$

$$
\begin{aligned}
&+\varepsilon^3\,[\ (139/420)\varphi_\theta{}^3\varphi_{\theta\theta}{}^2-(263/1750)c^*\varphi_\theta{}^2\varphi_{\theta\theta}{}^2-(546/875)c^{*2}\varphi_\theta\varphi_{\theta\theta}{}^2\\
&\quad-(331/800)\varphi_\theta{}^6+(862/875)c^*\varphi_\theta{}^5+(903/875)c^{*2}\varphi_\theta{}^4\\
&\quad-(17/175)c^{*3}\varphi_\theta{}^3-(947/350)c^{*4}\varphi_\theta{}^2\\
&\quad-B_0\,\{\,(3471/1750)\varphi_\theta\varphi_{\theta\theta}{}^2-(5201/875)\varphi_\theta{}^4\\
&\qquad+(6323/875)c^*\varphi_\theta{}^3+(3276/875)c^{*2}\varphi_\theta{}^2\}\\
&\quad-(10413/875)B_0{}^2\varphi_\theta{}^2\ \,]\\
&+\cdots\cdots
\end{aligned}
\tag{2.53}
$$

(3) Hamiltonian

Since the dynamical system at this stage is for a potential field under gravity, one can transform it into a Hamiltonian system. If the momentums for χ_θ, φ_θ, and $\varphi_{\theta\theta}$ are conjugated as p, q, and r, respectively, the canonical transformations are

$$
\left.
\begin{aligned}
p &= \partial\mathfrak{L}/\partial\chi_\theta = -(1/6)\varphi_\theta,\\
q &= \partial\mathfrak{L}/\partial\varphi_\theta = -(1/6)\chi_\theta+\partial\mathfrak{L}^*/\partial\varphi_\theta,\\
r &= \partial\mathfrak{L}/\partial\varphi_{\theta\theta} = \partial\mathfrak{L}^*/\partial\varphi_{\theta\theta}.
\end{aligned}
\right\}
\tag{2.54}
$$

The Hamiltonian is, thus, given by

$$
\begin{aligned}
\mathfrak{K} &= p\,\chi_\theta + q\,\varphi_\theta + r\,\varphi_{\theta\theta} - \mathfrak{L}\\
&= (1/4)\varphi_\theta{}^3-(1/2)c^*\varphi_\theta{}^2+q\varphi_\theta+(1/12)\chi^2\\
&\quad+\varepsilon\,[\ -(3/20)\varphi_\theta\varphi_{\theta\theta}{}^2-(21/80)\varphi_\theta{}^4-(1/10)c^*\varphi_\theta{}^3+(19/20)c^{*2}\varphi_\theta{}^2\\
&\qquad+(9/10)B_0\varphi_\theta{}^2\ \,]\\
&\quad+\varepsilon^2\,[\ -(71/1400)\varphi_\theta{}^2\varphi_{\theta\theta}{}^2+(36/175)c^*\varphi_\theta\varphi_{\theta\theta}{}^2+(99/2800)\varphi_\theta{}^5\\
&\qquad+(33/70)c^*\varphi_\theta{}^4+(249/700)c^{*2}\varphi_\theta{}^3-(288/175)c^{*3}\varphi_\theta{}^2\\
&\qquad+B_0\,\{\,(22/35)\varphi_\theta{}^3-(216/175)c^*\varphi_\theta{}^2\}\ \,]\\
&\quad+\varepsilon^3\,[\ (139/420)\varphi_\theta{}^3\varphi_{\theta\theta}{}^2-(263/1750)c^*\varphi_\theta{}^2\varphi_{\theta\theta}{}^2-(546/875)c^{*2}\varphi_\theta\varphi_{\theta\theta}{}^2\\
&\qquad+(331/800)\varphi_\theta{}^6-(862/875)c^*\varphi_\theta{}^5-(903/875)c^{*2}\varphi_\theta{}^4\\
&\qquad+(17/175)c^{*3}\varphi_\theta{}^3+(947/350)c^{*4}\varphi_\theta{}^2\\
&\qquad-B_0\,\{\,(3471/1750)\varphi_\theta\varphi_{\theta\theta}{}^2+(5201/875)\varphi_\theta{}^4
\end{aligned}
$$

$$- (6323/875)c^{*}\varphi_{\theta}^{3} - (3276/875)c^{*2}\varphi_{\theta}^{2}\}$$

$$+ (10413/875)B_0^{2}\varphi_{\theta}^{2} \ ]$$

$$+ \ldots\ldots \tag{2.55}$$

Hamilton's canonical equations are

$$\left.\begin{aligned} d\chi/d\theta &= \partial\mathcal{K}/\partial p, & d\varphi/d\theta &= \partial\mathcal{K}/\partial q, \\ d\varphi_{\theta}/d\theta &= \partial\mathcal{K}/\partial r, & dp/d\theta &= -\partial\mathcal{K}/\partial\chi, \\ dq/d\theta &= -\partial\mathcal{K}/\partial\varphi = 0, & dr/d\theta &= -\partial\mathcal{K}/\partial\varphi_{\theta}. \end{aligned}\right\} \tag{2.56}$$

The fifth of Eq. (2.56) gives q = const., and since Eq. (2.55) does not explicitly contain the variable θ, Eq. (2.55) is an integral(energy) surface. On the other hand, Eq. (2.55) has to coincide with the Korteweg-deVries equation in the lowest order, so that the constant $B_0 = -q$. By changing back to two variables ζ and ζ_{θ}, the Hamiltonian (2.55) can be consequently expressed as

$$\begin{aligned}
\varepsilon^{3}\mathcal{K} = \varepsilon^{3}\zeta^{3}\,[\ & \{(1/4) - (1/10)\varepsilon c^{*} + (249/700)\varepsilon^{2}c^{*2} + (17/175)\varepsilon^{3}c^{*3} + \ldots\} \\
& - \{(22/35) + (6323/875)\varepsilon c^{*} + \ldots\}\,\varepsilon^{2}q \\
& - \{(21/80) - (33/70)\varepsilon c^{*} + (903/875)\varepsilon^{2}c^{*2} + \ldots\}\,\varepsilon\zeta \\
& + \{(5201/875) + \ldots\}\,\varepsilon^{2}q\cdot\varepsilon\zeta \\
& + \{(99/2800) - (862/875)\varepsilon c^{*} + \ldots\}\,\varepsilon^{2}\zeta^{2} \\
& + \{(331/800) + \ldots\}\,\varepsilon^{3}\zeta^{3} + \ldots\ldots\ ] \\
- \varepsilon^{2}\zeta^{2}\,[\ & \{(1/2) - (19/20)\varepsilon c^{*} + (288/175)\varepsilon^{2}c^{*2} - (947/350)\varepsilon^{3}c^{*3} + \ldots\}\,\varepsilon c^{*} \\
& + \{(9/10) - (216/175)\varepsilon c^{*} + (3276/875)\varepsilon^{2}c^{*2} + \ldots\}\,\varepsilon^{2}q \\
& - \{(10413/875) + \ldots\}\,(\varepsilon^{2}q)^{2} \ ] \\
+ \varepsilon^{2}q\cdot\varepsilon\zeta & \\
+ \varepsilon^{3}\zeta_{\theta}^{2}\,[\ & (1/12) - \{(3/20) - (36/175)\varepsilon c^{*} + (546/875)\varepsilon^{2}c^{*2} + \ldots\}\,\varepsilon\zeta \\
& + \{(3471/1750) + \ldots\}\,\varepsilon^{2}q\cdot\varepsilon\zeta \\
& - \{(71/1400) + (263/1750)\varepsilon c^{*} + \ldots\}\,\varepsilon^{2}\zeta^{2} \\
& + \{(139/420) + \ldots\}\,\varepsilon^{3}\zeta^{3} - \ldots\ldots\ ]\,.
\end{aligned} \tag{2.57}$$

(4) Breaking Model

Eq. (2.57) is the approximate solution of basic equations (2.2) and also is the first integral for the Korteweg-deVries equation in the lowest order, where the energy surface is expressed by the cubic function of the variable ζ and by the quadratic function of ζ_θ. It is important that the coefficient of ζ_θ^2 have a positive root and that this root be the singular point of the first integral and, therefore, correspond to the singular point in the wave form which should occur at the crest of the breaking wave. In the usual nonlinear wave theory based on the perturbation method, this singularity is removed into non-homogeneous terms as in the right-hand side of Eq. (2.30), so that it does not play an important role. A new concept is, therefore, neccessary to discuss wave breaking resulting from this singularity.

According to the catastrophe theory[6], which is a classification theorem of singular points on a three-dimensional manifold, the types of singular points on a surface V represented by a cubic function of two variables X and Y are classified into two types

$$V_i = X^3 \pm XY^2 + a_i Y^2 + b_i X + c_i Y, \qquad i = 1,2, \tag{2.58}$$

where a_i, b_i, and c_i are parameters. Positive and negative signs correspond to hyperbolic and elliptic umbilics, respectively. By equating $(X,Y) = (\zeta,\zeta_\theta)$ and by evaluating the coefficients of ζ^3 and $\zeta\zeta_\theta^2$, it becomes clear that Eq. (2.57) corresponds to the elliptic umbilic, that is, the energy surface should be interpreted as the Taylor expansion around a singular point[16]. If Eq. (2.57) can be transformed into the form of Eq. (2.58), which would mean that the lowest order(essential) singularity is reserved and others due to the higher power series are removed, the resultant equation could be expected to express the breaking of waves.

Now, the coefficients of ζ^3 and ζ_θ^2 contain the variable $\varepsilon\zeta$, parameters

εc^* and $\varepsilon^2 q$; and, moreover, there is a relation between them. When $\zeta_\theta{}^2 = 0$, the most significant information is obtained, i.e. for the solitary wave this gives the relation between the wave height and wave velocity. Therefore, $\varepsilon\zeta$ and its powers in the coefficients of ζ^3 and $\zeta\zeta_\theta{}^2$ can be replaced by εc^* and $\varepsilon^2 q$, provided that when $\zeta_\theta{}^2 = 0$, $|\varepsilon^2 q| \ll 0$ and $|\varepsilon^3 \mathcal{H}| \ll 0$ for shallow water waves, that is, the terms in higher powers of $\varepsilon\zeta$ are thrown-back to lower powers. The resultant Hamiltonian is

$$\begin{aligned}
\varepsilon^3\mathcal{H} = \varepsilon^3\zeta^3 \Big[& \{(1/4)-(5/8)\varepsilon c^*+(9/8)\varepsilon^2 c^{*2}-(2821/1400)\varepsilon^3 c^{*3}+\ldots\} \\
& -\{(2203/1400)-(2497/1000)\varepsilon c^*+\ldots\}\,\varepsilon^2 q \Big] \\
-\varepsilon^2\zeta^2 \Big[& \{(1/2)-(19/20)\varepsilon c^*+(288/175)\varepsilon^2 c^{*2} \\
& -(947/350)\varepsilon^3 c^{*3}+\ldots\}\,\varepsilon c^* \\
& +\{(9/10)-(216/175)\varepsilon c^*+(3276/875)\varepsilon^2 c^{*2}-\ldots\}\,\varepsilon^2 q \\
& -\{(10413/875)+\ldots\}\,(\varepsilon^2 q)^2 \Big] \\
& +\varepsilon^2 q\cdot\varepsilon\zeta \\
& +\varepsilon^3\zeta_\theta{}^2 \Big[(1/12)-\{(3/20)-(73/700)\varepsilon c^*-(3553/10500)\varepsilon^2 c^{*2}-\ldots \\
& \qquad -(6303/3500)\varepsilon^2 q+\ldots\}\,\varepsilon\zeta \Big] .
\end{aligned} \tag{2.59}$$

Hydraulic quantities, non-dimensionalized by the water depth h and the gravity g as in Eq. (2.1), are given as follows: the water surface displacement, wave velocity, and frame of reference moving with the wave are

$$\eta = \varepsilon\zeta, \qquad c = 1+\varepsilon c^*, \qquad X = x-ct, \tag{2.60}$$

respectively. Then, Eq. (2.59) becomes

$$(a_0-\eta)(d\eta/dX)^2 = a_1\cdot(a_4 - a_3\,\eta + a_2\,\eta^2 - \eta^3), \tag{2.61}$$

with

$$\left.\begin{aligned}
a_0(\varepsilon c^*) &= (5/9)+(73/189)\varepsilon c^*+(6040/3969)\varepsilon^2 c^{*2}+\ldots \\
&\quad +\{(2101/315)+\ldots\}\,\varepsilon^2 q, \\
a_1(\varepsilon c^*) &= 12\,a_0(\varepsilon c^*)\cdot P(\varepsilon c^*), \\
a_2(\varepsilon c^*) &= \Big[\{(1/2)-(19/20)\varepsilon c^*+(288/175)\varepsilon^2 c^{*2} \\
&\quad -(947/350)\varepsilon^3 c^{*3}+\ldots\}\,\varepsilon c^* \\
&\quad +\{(9/10)-(216/175)\varepsilon c^*+(3276/875)\varepsilon^2 c^{*2}+\ldots\}\,\varepsilon^2 q
\end{aligned}\right\} \tag{2.62}$$

$$
\begin{aligned}
&\quad - \{ (10413/875) + \ldots \} (\varepsilon^2 q)^2 \ ] / P(\varepsilon c^*), \\
a_3(\varepsilon c^*) &= \varepsilon^2 q / P(\varepsilon c^*), \\
a_4(\varepsilon c^*) &= \varepsilon^3 \mathcal{K} / P(\varepsilon c^*), \\
P(\varepsilon c^*) &= (1/4) - (5/8)\varepsilon c^* + (9/8)\varepsilon^2 c^{*2} - (2821/1400)\varepsilon^3 c^{*3} + \ldots \\
&\quad - \{ (2203/1400) - (2497/1000)\varepsilon c^* + \ldots \} \varepsilon^2 q.
\end{aligned}
$$

Eq. (2.61) is the basic equation for wave breaking. When $\eta = 0$, $(d\eta/dX)^2$ must be real, so $\varepsilon^3 \mathcal{K} \geqq 0$. For periodic waves, one of the roots of the cubic equation in the right-hand side of Eq. (2.61) must be positive and the others negative, and in addition the positive one must be smaller than the root of the coefficient of $(d\eta/dX)^2$. Let these roots be η_1, $-\eta_2$, $-\eta_3$, and η_4; $\eta_4 \geqq \eta_1 \geqq 0$, $\eta_3 \geqq \eta_2 \geqq 0$, respectively. **Fig. 2.2** illustrates the relation between these roots. Therefore, Eq. (2.61) becomes

$$
(\alpha \, d\eta/dX)^2 = \frac{(\eta_1 - \eta)(\eta_2 + \eta)(\eta_3 + \eta)}{(\eta_4 - \eta)}, \tag{2.63}
$$

with

$$
\begin{aligned}
\alpha^2 &= 1/a_1(\varepsilon c^*), \\
\eta_4 &= a_0(\varepsilon c^*), \\
a_2(\varepsilon c^*) &= \eta_1 - \eta_2 - \eta_3, \\
a_3(\varepsilon c^*) &= -\eta_1\eta_2 + \eta_2\eta_3 - \eta_3\eta_1, \\
a_4(\varepsilon c^*) &= \eta_1\eta_2\eta_3,
\end{aligned}
\tag{2.64}
$$

and integrates to give the wave profile for periodic waves

$$
\begin{aligned}
\eta &= -\eta_2 + (\eta_1 + \eta_2) \frac{\mathrm{cn}^2 \upsilon}{1 - k^2 \mathrm{sn}^2\gamma \, \mathrm{sn}^2 \upsilon}, \\
|X| &= 2\alpha\beta \left\{ \upsilon \cdot \mathrm{dn}^2\gamma + \frac{\mathrm{sn}\gamma \, \mathrm{dn}\gamma}{\mathrm{cn}\gamma} \Pi(\upsilon, \gamma) \right\},
\end{aligned}
\tag{2.65}
$$

with

$$
\begin{aligned}
k^2 &= \{ (\eta_1 + \eta_2)(\eta_4 + \eta_3) \} / \{ (\eta_4 + \eta_2)(\eta_1 + \eta_3) \} \leqq 1, \\
\mathrm{sn}^2\gamma &= (\eta_1 + \eta_3)/(\eta_4 + \eta_3) \leqq 1, \\
k^2 \mathrm{sn}^2\gamma &= \mu^2/\beta^2, \\
\beta^2 &= (\eta_4 + \eta_2)/(\eta_1 + \eta_3), \\
\mu^2 &= (\eta_1 + \eta_2)/(\eta_1 + \eta_3) \leqq 1,
\end{aligned}
\tag{2.66}
$$

where sn, cn, and dn are the Jacobian elliptic functions of the first, second, and third kinds, respectively, k is the modulus, and $\Pi(\upsilon,\gamma)$ the incomplete elliptic integral of the third kind, defined by

$$\Pi(\upsilon,\gamma) = k^2 \mathrm{sn}\gamma\, \mathrm{cn}\gamma\, \mathrm{dn}\gamma \int_0^{\upsilon} \frac{\mathrm{sn}^2\upsilon}{1-k^2\mathrm{sn}^2\gamma\, \mathrm{sn}^2\upsilon}\, \mathrm{d}\upsilon. \tag{2.67}$$

The wave height is given by

$$H = \eta_1 + \eta_2, \tag{2.68}$$

and the wave length is decided as follows: when $\eta = \eta_1$ and $-\eta_2$, $\upsilon = 0$ and K, respectively, then

$$L = 2\,|X|_{\upsilon=K} = 4\alpha\beta K \left\{ \mathrm{dn}^2\gamma + \frac{\mathrm{sn}\gamma\, \mathrm{dn}\gamma}{\mathrm{cn}\gamma} Z(\gamma) \right\}, \tag{2.69}$$

where $Z(\upsilon)$ is the incomplete elliptic integral of the second kind, defined by

$$Z(\upsilon) = \int_0^{\upsilon} \left\{ \mathrm{dn}^2\upsilon - \frac{E}{K} \right\} \mathrm{d}\upsilon, \tag{2.70}$$

and K and E are the complete elliptic integrals of the first and second kinds, respectively.

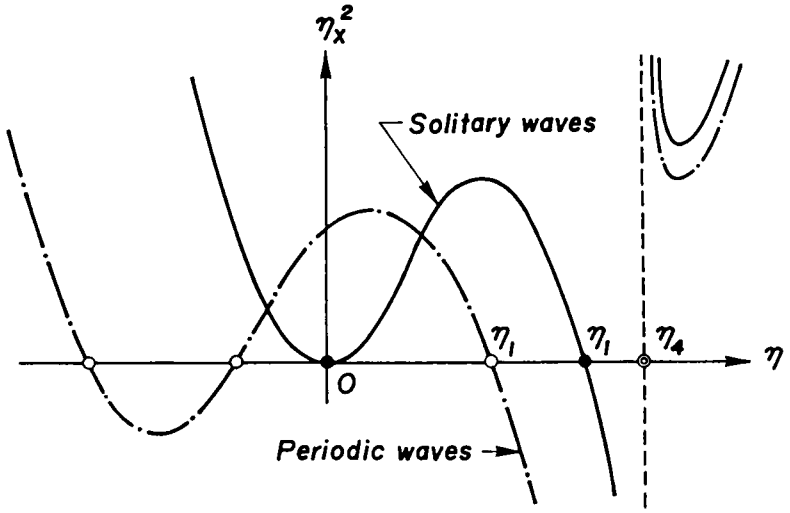

Fig. 2.2 Relation between the roots of the basic equation for wave breaking.

The conservative condition of mass

$$(1/L)\int_0^L \eta \, dx = 0 \tag{2.71}$$

gives the trough depth, defined as the distance from the mean water level to the wave trough,

$$\eta_2 = 2\alpha\beta\frac{H}{L}\left\{\frac{\mathrm{dn}\gamma}{\mathrm{cn}\gamma}\right\}^2\left[\frac{E}{k^2}+\left\{2-\mathrm{sn}^2\gamma-\frac{1}{k^2}\right\}K\right.$$

$$\left.+\frac{\mathrm{sn}\gamma}{\mathrm{cn}\gamma\,\mathrm{dn}\gamma}\left\{2-\mathrm{sn}^2\gamma-\frac{1}{k^2\mathrm{sn}^2\gamma}\right\}K\cdot Z(\gamma)\right]. \tag{2.72}$$

In these equations there are two basic families of variables. The first family is the wave height H and wave length L or wave period T. The second family is the seven quantities η_1, η_2, η_3, η_4, εc^*, $\varepsilon^2 q$, and $\varepsilon^3 \mathcal{K}$. Corresponding equations are the seven equations of the second to fifth of Eq. (2.64), and Eqs. (2.68), (2.69), and (2.72). The waves, therefore, exist as the two-parameter family of wave height and wave length or wave period, so that the hydraulic quantities relating to the wave profiles can be formulated with no use of the physical condition, such as Stokes' first or second definition for the wave velocity, as mentioned before.

(5) Occurrence of Wave Breaking

This section shows how the basic equation (2.63) constructs wave breaking. **Fig. 2.2** illustrates the relation between η and $(d\eta/dX)^2$. The root of the coefficient of $(d\eta/dX)^2$, η_4, is a singular point of the energy surface. When a wave breaks, the greatest root of the right-hand side of Eq. (2.61), η_1, approaches this singular point, i.e. $\eta_1 \to \eta_4$. In this critical state the singularity is apparently removed, so that the breaking of the wave can occur. Grant[17] has pointed out that previous theoretical investigations on wave breaking assume that the singular point of a wave in

the physical plane is in the upper region of the wave crest and moves down to the wave crest just before breaking. These circumstances are in accordance with each other. Seliger's model[18),19)] for wave breaking, which is the integro-differential equation with the Fourier kernel of the phase velocity for linear waves, takes the same standpoint on the singularity as the present theory.

Fig. 2.3 shows contour lines of equi-energy level on energy surfaces for the solitary wave. The broken lines indicate contour lines of a lower energy level than the surroundings. Stable regions are the shaded areas enclosed by the solution curves. There are three saddle points marked by solid circles on the energy surface. The saddle point at the coordinate origin corresponds to the point of infinity in the solitary wave phase. When $\eta_1 \rightarrow \eta_4$, the other two saddle points lie on the solution curve, and these points also correspond to the wave crest at just breaking. But when the wave breaks, the three saddle points lie in the equi-energy level, the critical state, indicating that the energy is about to overflow from the energy potential well. This may be equivalent to the phenomenon of wave breaking. **Fig. 2.4** also shows contour lines of equi-energy level on an energy surface for a periodic wave at just breaking. The general aspect of the energy surface is the same as for the solitary wave with the difference that one saddle point in phase with $d\eta/dX = 0$ is in the external unstable region.

For both solitary and periodic waves the trajectories pass two of the saddle points at just breaking. However, it is well-known in the theory of dynamical systems that there is no trajectory which links saddle points; therefore, the breaking wave profiles should show them to be in the limiting state to which waves approach.

Fig. 2.5 illustrates the energy surfaces for the Korteweg-deVries equation, hyperbolic and elliptic umbilics, respectively. The energy

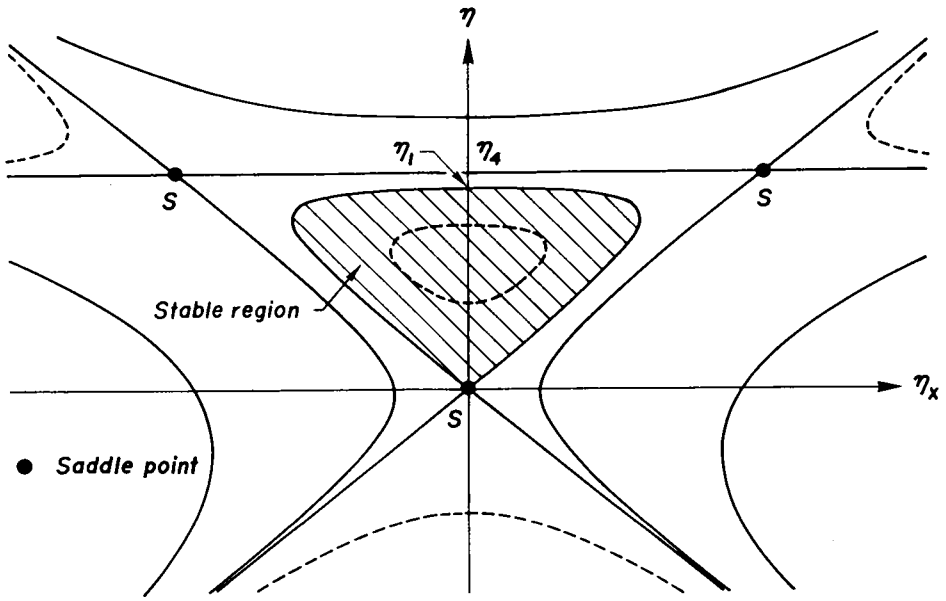

(1) Non-breaking

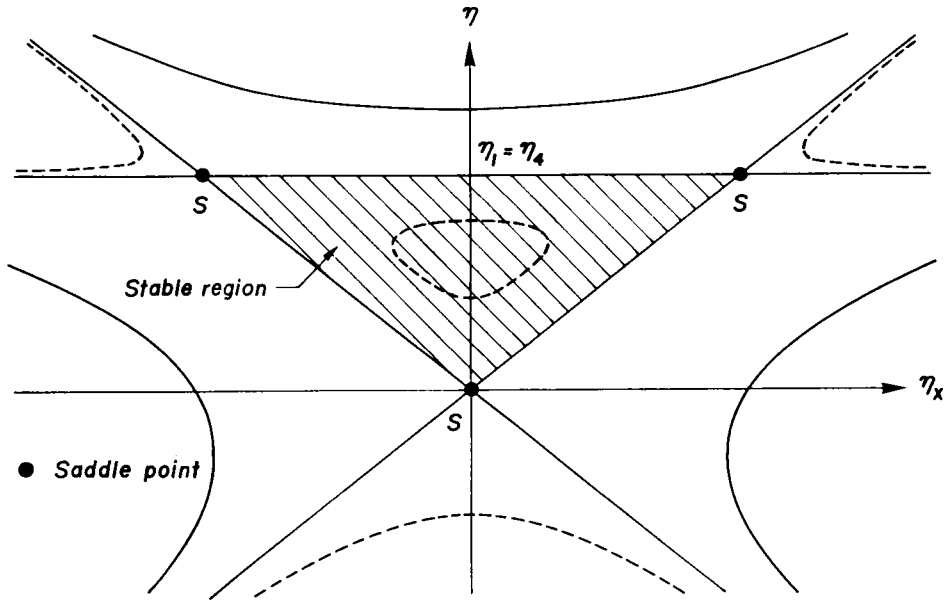

(2) Just breaking

Fig. 2.3 Schematic diagrams of contour lines of equi-energy level on energy surfaces for the solitary wave.

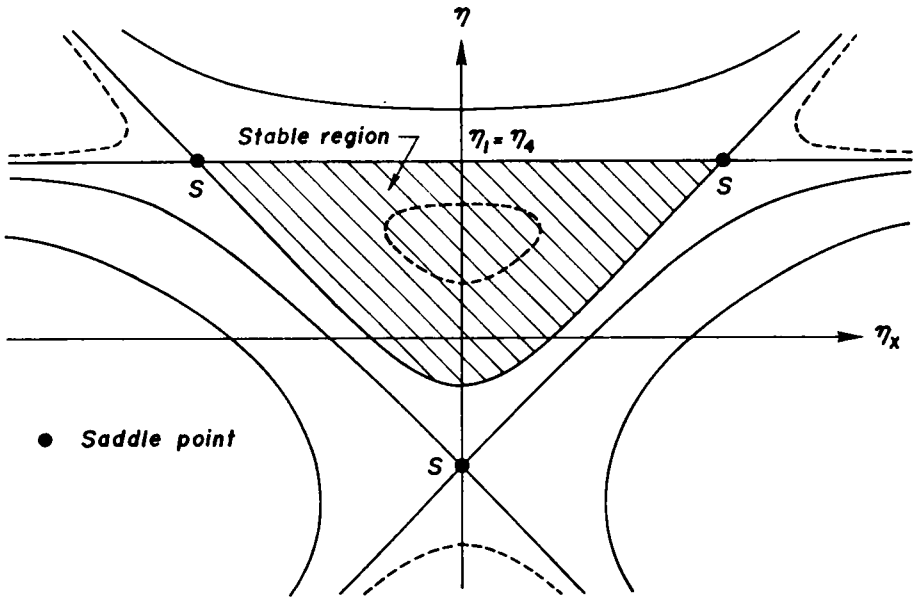

Just breaking

Fig. 2.4 Schematic diagram of contour lines of equi-energy level on an energy surface for a periodic wave.

surfaces for the Korteweg-deVries equation and hyperbolic umbilic are found to be homeomorphic, while those for the solitary wave at just breaking and the elliptic umbilic are also homeomorphic. The energy surfaces for periodic waves at just breaking are intermediate ones as seen from **Fig. 2.3** to **Fig. 2.5**. The wave breaking is surely affected by this transition from the hyperbolic to elliptic umbilics due to the existence of the singular point on the energy surface.

For breaking waves, $\eta_1 \rightarrow \eta_4$, then the wave profile, wave length, and trough depth become, respectively,

$$\left.\begin{aligned} \eta_b &= -\eta_2 + H_b \{\cosh\upsilon - (1/\mu)\sinh\upsilon\}^2, \\ |X| &= 2\alpha\upsilon, \qquad H_b = \eta_1 + \eta_2, \end{aligned}\right\} \tag{2.73}$$

$$L_b = 2\alpha \ln\{(1+\mu)/(1-\mu)\}, \tag{2.74}$$

$$\eta_2 = -\eta_3 + 4(\alpha/\mu)(H_b/L_b), \tag{2.75}$$

where the subscript b denotes quantities at just breaking. The maximum

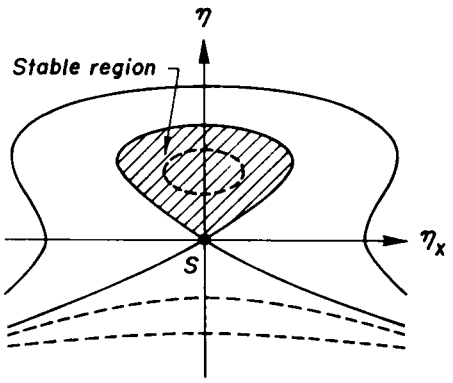

(1) Korteweg-deVries equation

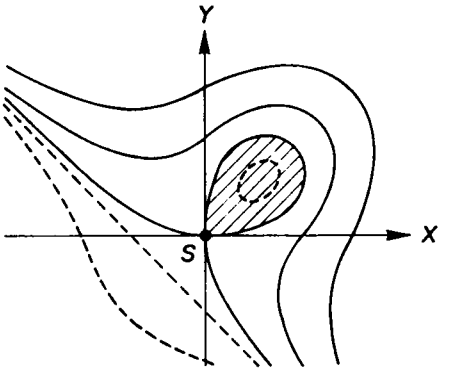

(2) Hyperbolic umbilic

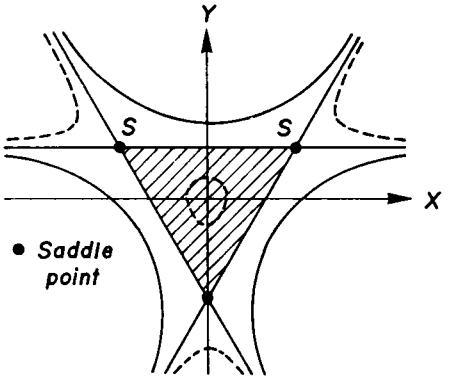

(3) Elliptic umbilic

Fig. 2.5 Schematic diagrams of contour lines of equi-energy level on energy surfaces for the Korteweg-deVries equation, hyperbolic and elliptic umbilics.

crest height η_4, defined as the length from the mean depth of water to the wave crest, that is, the root of coefficient of $(d\eta/dX)^2$, is

$$\eta_4 = (5/9)+(73/189)\varepsilon c^*+(6040/3969)\varepsilon^2 c^{*2}+(2101/315)\varepsilon^2 q+\ldots \quad (2.76)$$

This is the upper bound for crest heights, therefore, gives the breaking condition. The breaking angle is also given by

$$\omega = \pi-2\tan^{-1}\{H_b/(\alpha\mu)\}\ . \quad (2.77)$$

(6) Discussion

a. Solitary wave

The extreme case of the solitary wave is provided by $k^2 = 1$, $L = L_b = \infty$, and $\eta_2 = \eta_3 = 0$. The relation between the wave height and wave velocity is obtained by setting $(d\eta/dX)^2 = \varepsilon^2 q = \varepsilon^3 \mathcal{K} = 0$ in Eq. (2.61), then

$$H = 2\varepsilon c^* \cdot \frac{1-(19/10)\varepsilon c^*+(576/175)\varepsilon^2 c^{*2}-(947/175)\varepsilon^3 c^{*3}+\ldots}{1-(5/2)\varepsilon c^*+(9/2)\varepsilon^2 c^{*2}-(2821/350)\varepsilon^3 c^{*3}+\ldots}. \quad (2.78)$$

The breaking condition is

$$\eta_4 = (5/9)+(73/189)\varepsilon c^*+(6040/3969)\varepsilon^2 c^{*2}+\ldots \quad (2.79)$$

The solitary wave breaks at the point where the wave height - wave velocity curve, Eq. (2.78), intersects the breaking condition curve, Eq. (2.79). On the other hand, the breaking condition derived from the boundary conditions at the wave surface is

$$H = c^2/2. \quad (2.80)$$

The maximum values for the solitary wave are given in **Table 2.1** together with previous results[13),20),21),22),23),24),25),26),27),30)].

Fig. 2.6 shows the changes in wave height with respect to the wave velocity given by Eq. (2.78). Longuet-Higgins and Fenton's value[27)] is shown by an open circle. Fenton's ninth order solution[25)] is also shown by the heavy, broken line. In the others, solid and broken lines show the

Table 2.1 Physical properties of the highest waves.

Authors	H	c
McCowan(1894)	0.78	1.249
Yamada(1957)	0.828	1.287
Lenau(1966)	0.827	1.286
Byatt-Smith(1970)	0.86	1.311
Strelkoff(1971)	0.85	1.304
Fenton(1972)	0.85	1.304
Longuet-Higgins(1974)	0.8296	1.288
Longuet-Higgins and Fenton(1974)	0.827	1.286
Tsuchiya and Yasuda(1974)	0.846	1.364
Williams(1981)	0.8332	1.2909
Breaking model	0.814	1.304

breaking conditions (2.79) and (2.80), respectively. Furthermore, representative values of the maximum wave height and the corresponding wave velocity, given in **Table 2.1**, are also in the figure.

Eq. (2.78) agrees well with Fenton's ninth order solution over the whole range of wave velocity. On the other hand, the curve by Longuet-Higgins and Fenton takes on the multi-valued profile and its curvature sharply changes near the breaking point. These properties have been recently found for finite amplitude waves by some authors[28),29),30)] and recognized as important characteristics of waves.

Now, for some discussion on these properties, the inversion of Eq. (2.78) is

$$\varepsilon c^* = \frac{H}{2} \cdot \frac{1-(5/4)H+(3/2)H^2-(2543/1400)H^3+\ldots}{1-(19/20)H+(1551/1400)H^2-(17807/14000)H^3+\ldots}, \qquad (2.81)$$

and the expansion in a power series becomes

$$\varepsilon c^* = (1/2)H-(3/20)H^2+(3/56)H^3-(309/5600)H^4+\ldots \qquad (2.82)$$

Fenton's equation for the wave velocity

$$c^2 = (1+\varepsilon c^*)^2 = \sum_{n=0}^{9} A_n (H)^n \tag{2.83}$$

is also expanded as

$$\varepsilon c^* = 0.5H - 0.15H^2 + 0.053571H^3 - 0.055179H^4 + 0.019866H^5 - 0.034284H^6 + 0.009655H^7 - 0.027688H^8 + 0.007258H^9 - \ldots \tag{2.84}$$

Fig. 2.7 shows the comparison of Eq. (2.81) to Eq. (2.84) with Longuet-Higgins and Fenton's value. In the figure, the variable n indicates the adoption of n terms in both the denominator and numerator of Eq. (2.81). The power series approximation (2.82) coincides with Eq. (2.84) to the fourth order, which is the maximum order of approximations in the present theory. It is found that when the order of approximations increases, Eq. (2.81) may approach Longuet-Higgins and Fenton's curve, but the degree of convergence may be slow. This shows that the relation between the wave height and wave velocity sensitively depends on whether the wave velocity is an independent variable or not. Remembering that Longuet-Higgins and Fenton's results were determined by the Padé approximation for the same equation as Eq. (2.83), Eq. (2.81) may take on the multi-valued property. Therefore, the discrepancy is chiefly caused by the lack of higher order terms.

The breaking condition (2.79) gives slightly fewer values than Eq. (2.80) near the breaking point. However, the maximum wave height and wave velocity in the present work agree fairly closely with the others as seen in **Table 2.1.**

The wave profile for the solitary wave is expressed by

$$\left.\begin{aligned} \eta &= H\frac{\operatorname{sech}^2 \upsilon}{1-(1/\beta^2)\tanh^2\upsilon}, \\ |X| &= 2\alpha\beta\left\{\upsilon-(1/\beta)\ln\sqrt{(\beta+\tanh\upsilon)/(\beta-\tanh\upsilon)}\right\}, \end{aligned}\right\} \tag{2.85}$$

and the breaking wave profile is given by

$$\eta_b = H_b \exp(-|X|/\alpha). \tag{2.86}$$

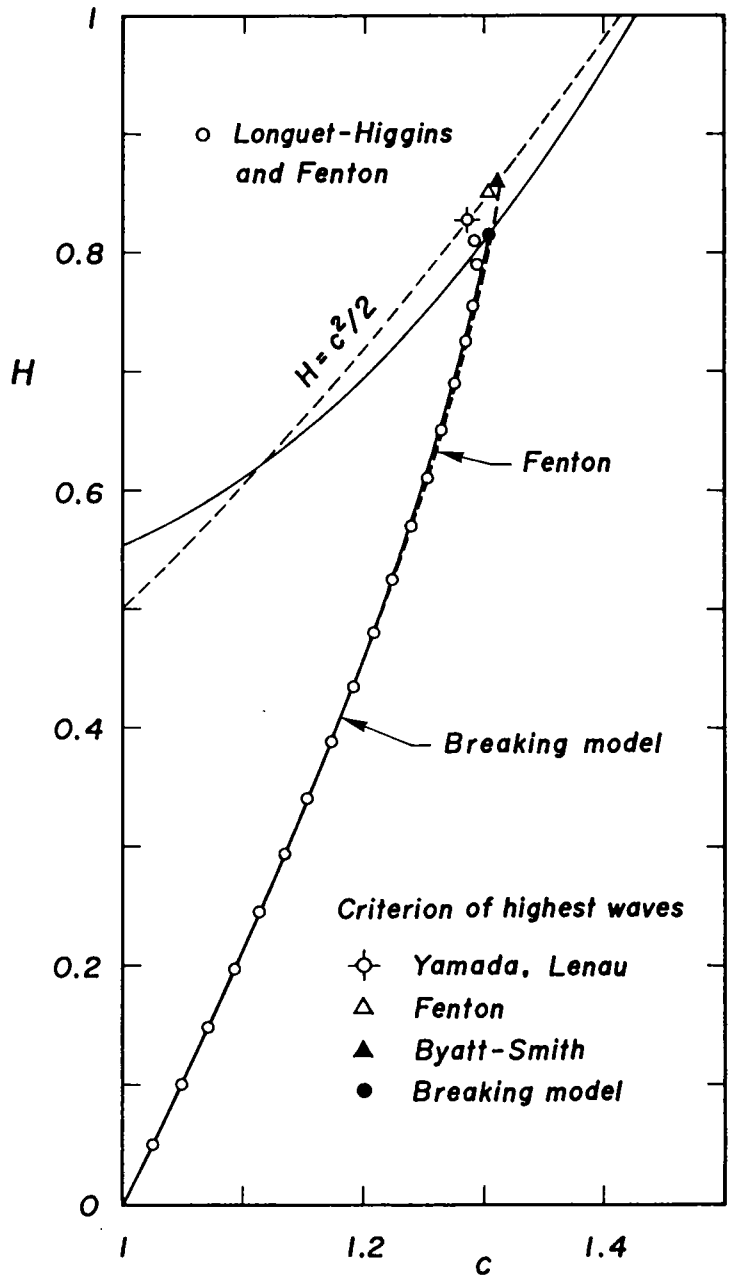

Fig. 2.6 Changes in wave height and in breaking condition for the solitary wave.

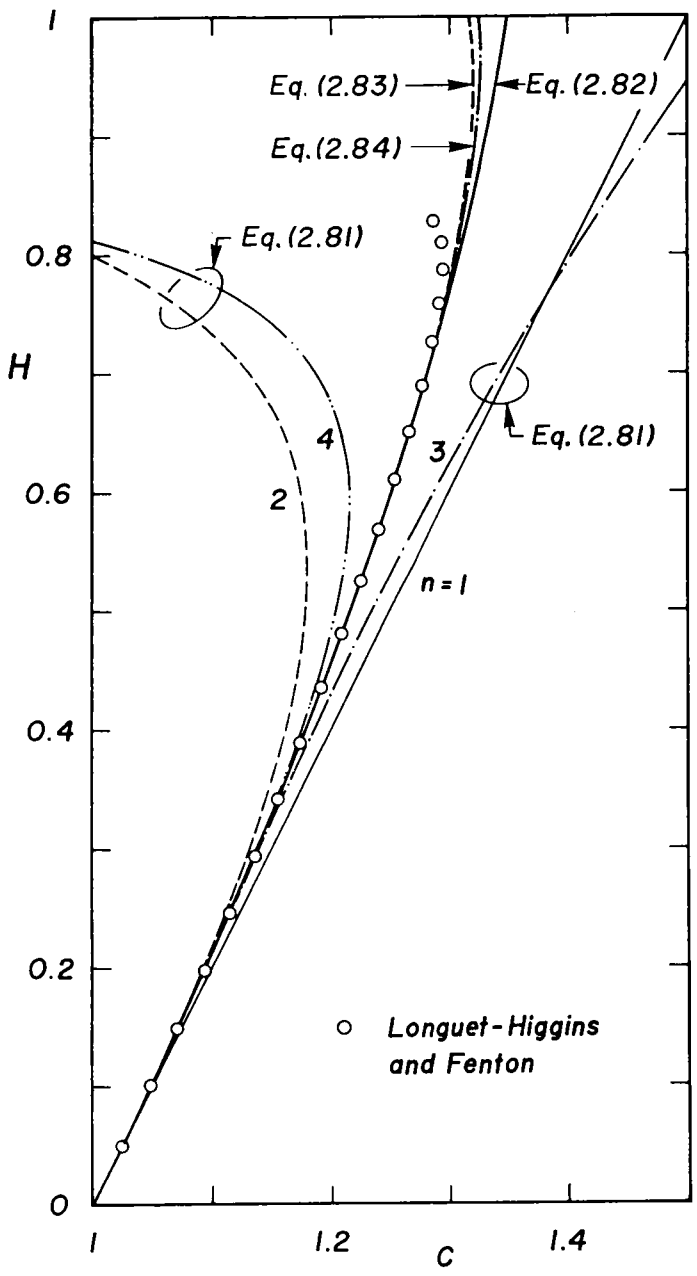

Fig. 2.7 Comparison of wave height-wave velocity curves for the solitary wave with Longuet-Higgins and Fenton's value.

Fig. 2.8 shows wave profiles for the solitary wave approaching the breaking wave profile with an angled crest. **Fig. 2.9** gives the comparison of wave profiles with various wave heights, for which Bayatt-Smith[23] has compared his theoretical results with Fenton's. Bayatt-Smith's profiles, although not plotted in the figure, are indistinguishable from Fenton's ninth order solution. In the figure, wave profiles based on Grimshaw's third order approximation[31] and Tsuchiya and Yasuda's third order approximation (NC-3)[13] obtained for the limiting case of the cnoidal wave are also plotted. The wave profiles in the present work are slimmer than the others and differences between wave profiles are nearly constant even for great values of wave height near the breaking point because the breaking angle is 100.4° which is less than Stokes' angle of 120°. Notice that the cuspidal profile at just breaking cannot be obtained by Fenton's ninth order approximation for lack of more higher order terms. For instance, Schwartz[28] worked generally to the order of 48 but only to the order of 117 for the deep water waves, while Cokelet[29] worked throughout to the order of 110.

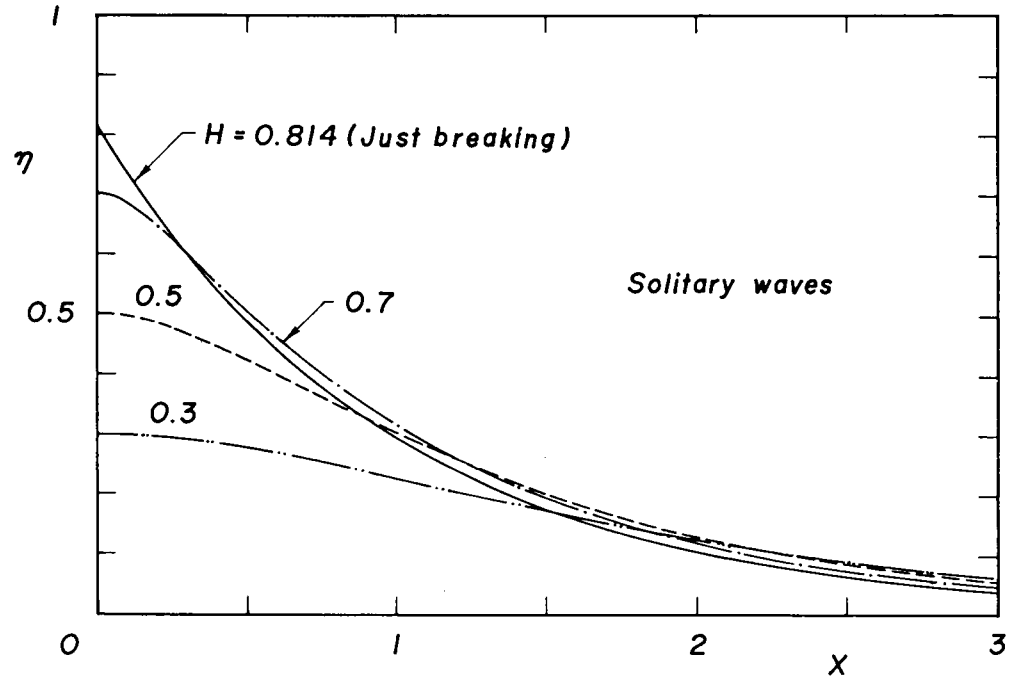

Fig. 2.8 Wave profiles for the solitary wave.

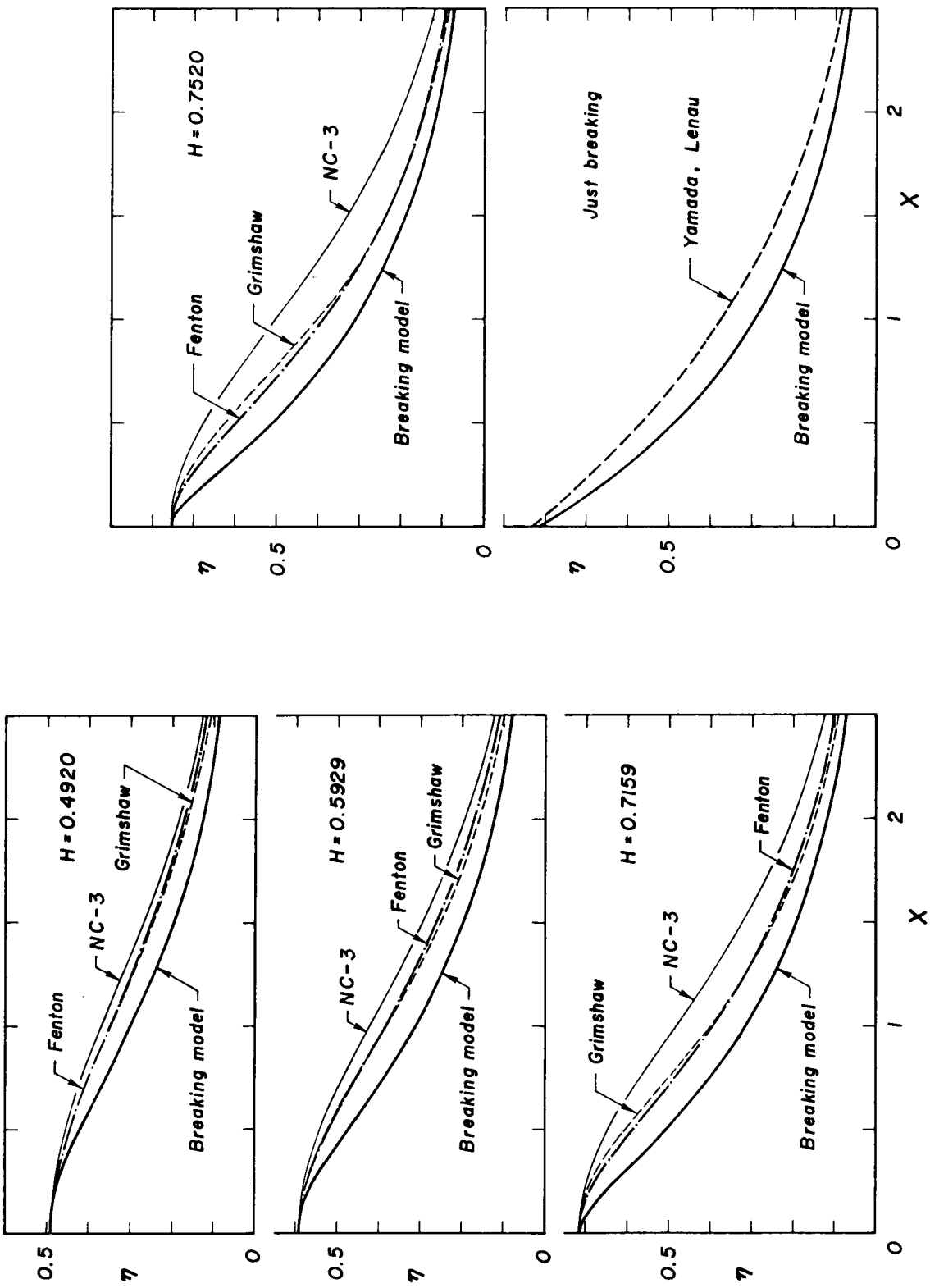

Fig. 2.9 Comparison of wave profiles for the solitary wave.

b. Periodic waves

Wave properties for periodic waves are discussed here in comparison with those based on the Stokes wave theory of third order approximation (**S-3**)[32], the Quasi-Stokes wave theory of fourth order approximation (**QS-4**)[12], and also the cnoidal wave theory (**NC-3**)[13], the last two being developed by the reductive perturbation method.

Fig. 2.10 shows wave profiles for periodic waves of the dimensionless wave period T = 20 with various wave heights H, which approach the breaking wave profile with an angled crest. Some comparisons of these wave profiles for various T and H are shown in **Fig. 2.11**. Wave profiles based on the breaking model are slimmer than the others as was the case with the solitary wave.

Figs. 2.12, 2.13, and **2.14** respectively show the changes in wave height, in wave velocity, and in crest height at just breaking with respect to the dimensionless wave period T. The curves based on the three wave theories above are obtained by the adoption of the Rankine-Stokes breaking condition[1]. The values in Figs. **2.12** and **2.13** are for the solitary wave. The differences of breaking wave height between the breaking model and other theories are nearly constant. The reason results chiefly from the discrepancy in values of wave height for the solitary wave. The wave velocities for values of T greater than 25 are slightly less than those for cnoidal waves, while for small T the breaking model has wave velocities about 15 % greater than the others do, in spite of smaller values for breaking wave heights. Similarly, the crest heights at just breaking are also greater.

The breaking angle of finite amplitude waves is shown in **Fig. 2.15**. The solitary wave at the maximum wave height has a crested angle of 100.4°. **Fig. 2.15** suggests that breaking angles are nearly constant for dimensionless wave periods greater than 15 and sharply increase to 180° for the

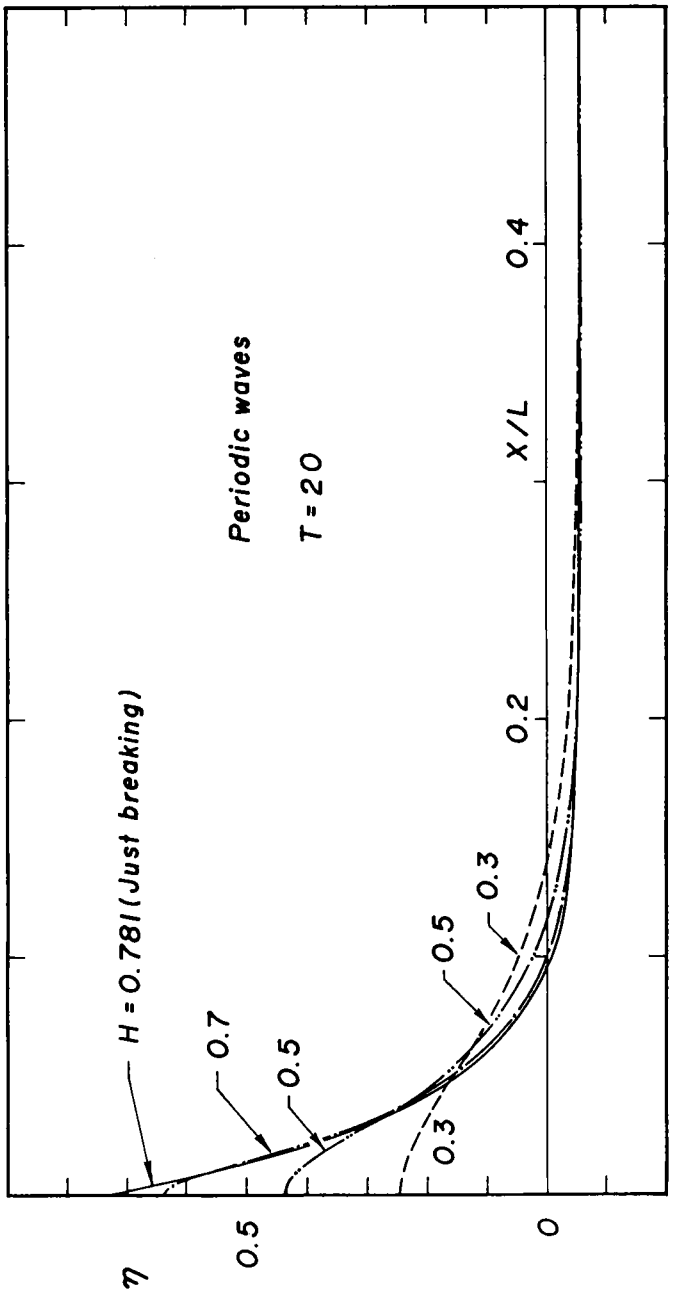

Fig. 2.10 Example of wave profiles for periodic waves.

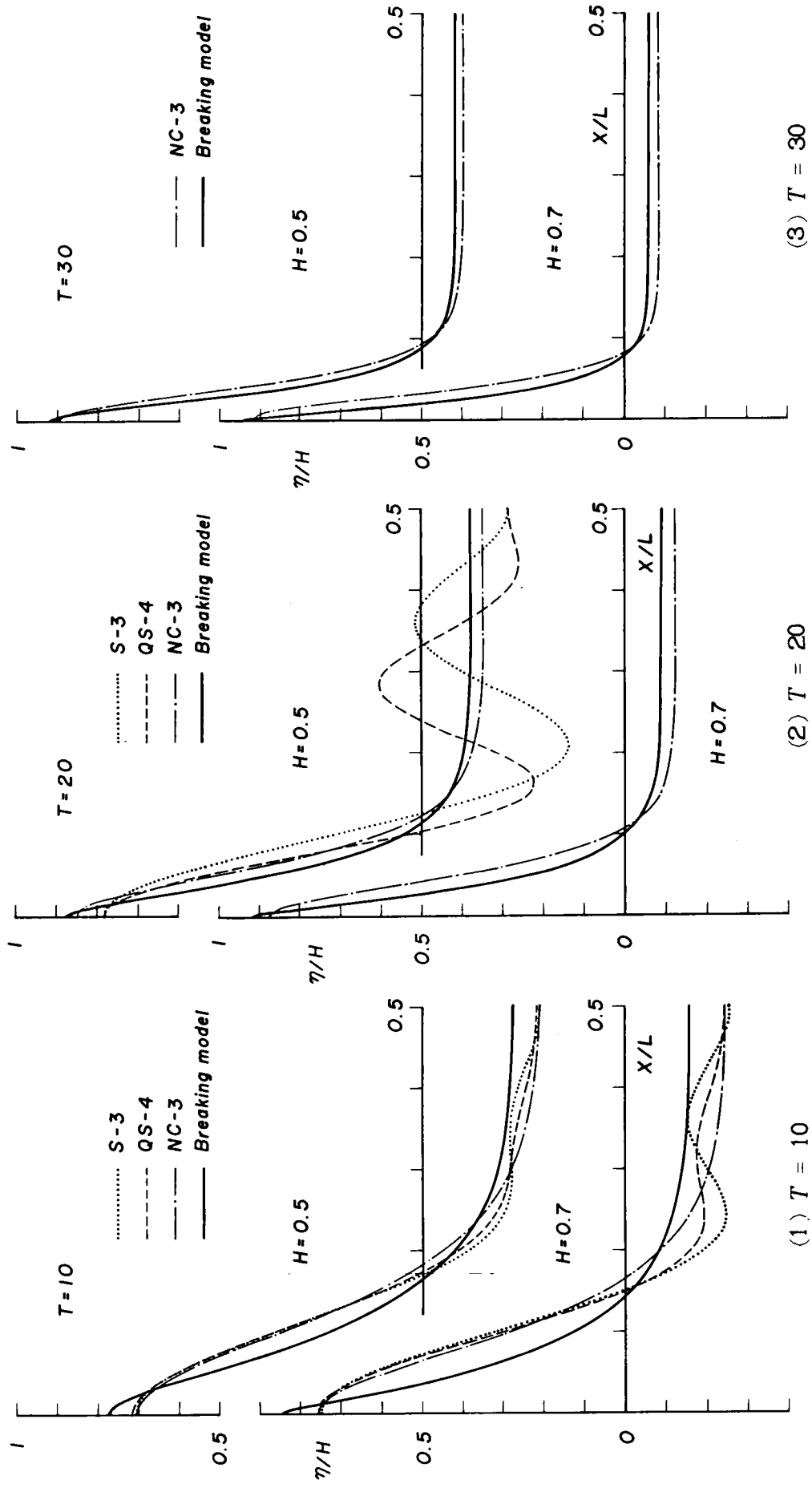

Fig. 2.11 Some comparisons of wave profiles for periodic waves.

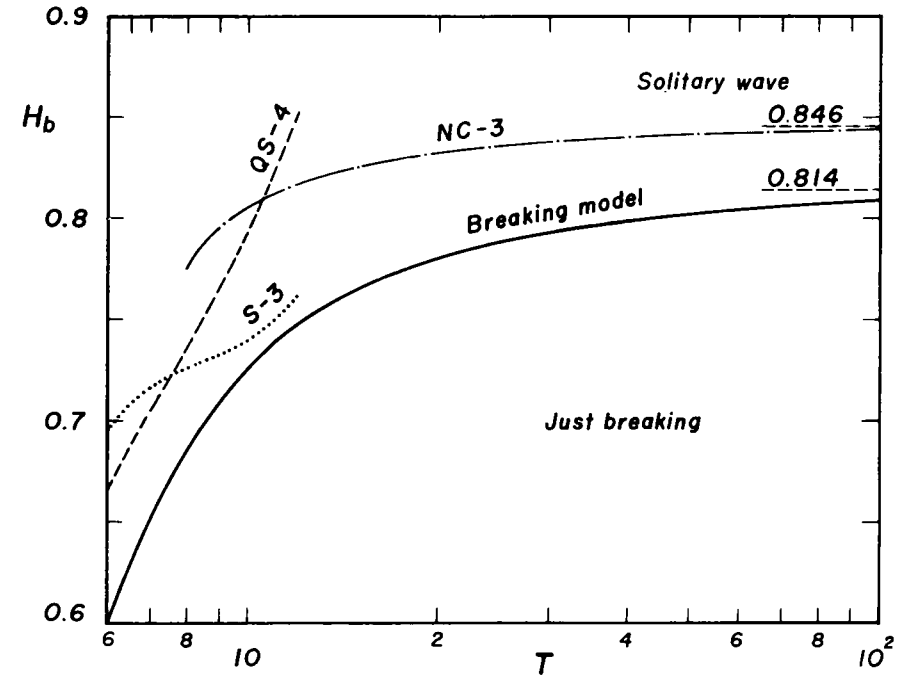

Fig. 2.12 Changes in wave height at just breaking.

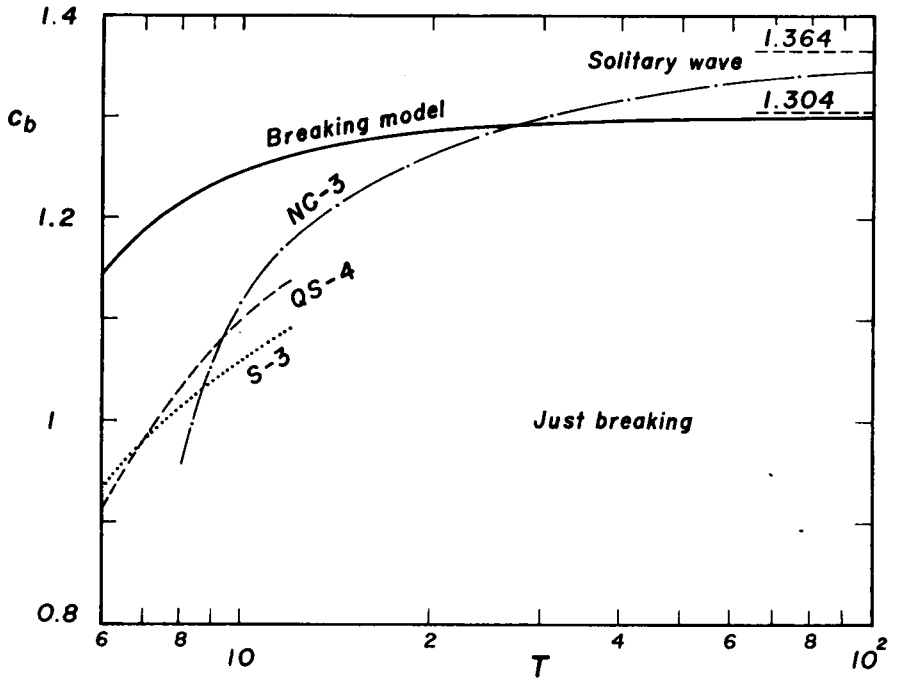

Fig. 2.13 Changes in wave velocity at just breaking.

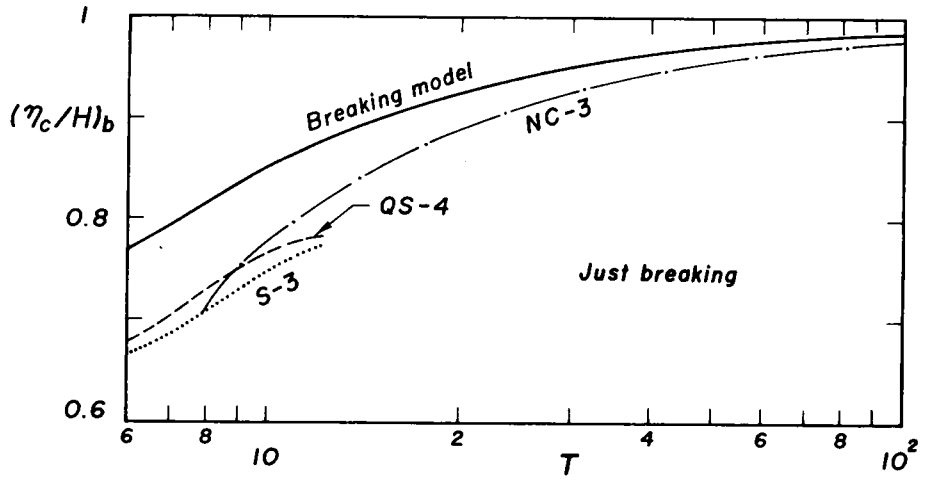

Fig. 2.14 Changes in crest height at just breaking.

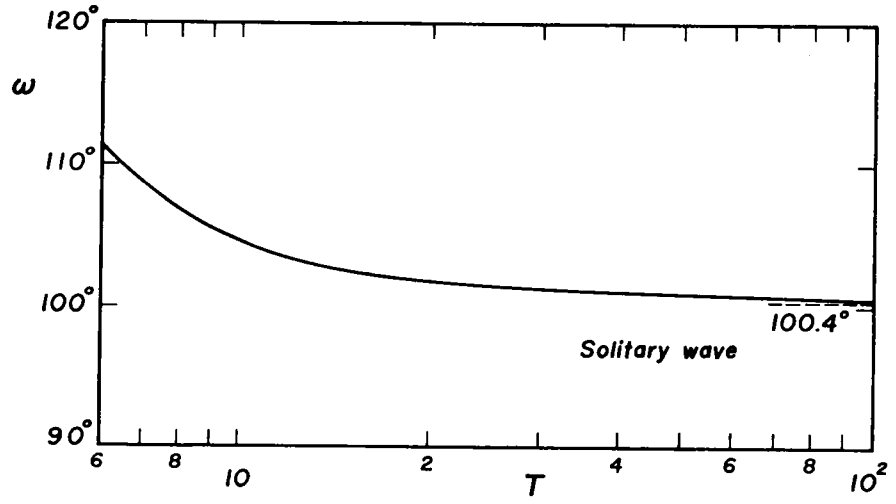

Fig. 2.15 Changes in breaking angle at just breaking.

smallest wave period, that is, no wave.

Fig. 2.16 shows a comparison of various breaking inceptions[12),13),33),34)]. The breaking model agrees closely with other breaking inceptions over the whole range of $1/L_b < 0.18$ because the discrepancies in wave height and in wave velocity seen in **Figs. 2.12** and **2.13** have apparently vanished due to the adoption of the representation H_b/L_b.

A similar comparison of the changes in wave velocity and in crest height for the smaller values of wave height H = 0.7 and 0.5 are given in **Figs. 2.17** and **2.18**, respectively. Wave velocities based on the breaking model, as before, take on greater values than the others for small T, but the attention must be paid to the fact that the corresponding wave heights are much closer to the breaking wave heights than the others as seen in **Fig. 2.12**. **Fig. 2.18** also shows that the crest heights are higher than those obtained from previous theories.

The breaking model, as discussed above, gives longer period waves whose crest heights and wave velocities are a little greater. The reasons stem from the formulation procedure of the breaking model described in Section 2.2(4), the assumption that $\varepsilon^2 q \ll 1$ and $\varepsilon^3 \mathcal{K} \ll 1$ when $d\eta/dX = 0$, and from the lack of higher order terms.

Finally, we turn to a discussion on the water particle velocity. There exists a singular point in the equation for the wave profile as seen in Eq. (2.65), and this equation cannot be expanded in a power series. Therefore, the proper expression for the water particle velocity is still unknown. This is a disadvantage of the breaking model. Nevertheless, the chief difficulty in the wave theory is that an unknown wave profile is contained in the boundary conditions at the free surface, and if the wave profile is known *a priori*, physical quantities, such as water particle velocity, mass flux, and wave energy, can be determined as an external boundary value problem. For an approximate solution for this problem, the use of the stream function theory[35] possesses manifold advantages. According to this theory, the wave profile and the horizontal and vertical components of water particle velocities can be expressed, respectively, in the present notation, as

$$\eta = (1/c)\left[\varphi_0 - \sum_{n=4,6,\ldots}^{N-1} \sinh(n-2)\pi \frac{h+\eta}{L}\right.$$

$$\times\left\{X_n\cos(n-2)\pi\frac{x_1}{L}+X_{n+1}\sin(n-2)\pi\frac{x_1}{L}\right\}\Bigg], \qquad (2.87)$$

$$u = -\sum_{n=4,6,\ldots}^{N-1}(n-2)\frac{\pi}{L}\cosh(n-2)\pi\frac{h+z}{L}$$

$$\times\left\{X_n\cos(n-2)\pi\frac{x_1}{L}+X_{n+1}\sin(n-2)\pi\frac{x_1}{L}\right\}, \qquad (2.88)$$

$$w = -\sum_{n=4,6,\ldots}^{N-1}(n-2)\frac{\pi}{L}\sinh(n-2)\pi\frac{h+z}{L}$$

$$\times\left\{X_n\sin(n-2)\pi\frac{x_1}{L}-X_{n+1}\cos(n-2)\pi\frac{x_1}{L}\right\}, \qquad (2.89)$$

where $x_1 = x - ct$, N is an odd number, φ_0 is the stream function at the wave surface, and X_j are coefficients of the Fourier series. If the wave surface η, wave period T, and wave velocity c are given, the Fourier coefficients X_j and the value of the stream function φ_0 must satisfy the kinematic boundary condition by means of the least square approximation. The degree of satisfaction is evaluated by the standard deviation

$$\sigma_1 = \sqrt{E_1}, \quad E_1 = (1/I)\sum_{i=1}^{I}(\eta_i-\eta_{mi})^2, \qquad (2.90)$$

in which the subscript i is a phase index for a sequence consisting of I values and m indicates a measured quantity. The dynamical boundary condition at the wave surface is

$$(1/2)\{(u-c)^2+w^2\}+\eta = \text{const.} = Q, \text{ say.} \qquad (2.91)$$

The gross error for this boundary condition is similarly evaluated by the standard deviation

$$\left.\begin{aligned}\sigma_2 &= \sqrt{E_2}, \quad E_2 = (1/I)\sum_{i=1}^{I}(\bar{Q}-Q_i)^2,\\ \bar{Q} &= (1/I)\sum_{i=1}^{I}Q_i, \quad Q_i = \eta_{mi}+(1/2)\{(u_i-c)^2+w_i^2\},\end{aligned}\right\} \qquad (2.92)$$

where Q_i are Bernoulli's constants at the wave surface. On the other hand,

the dynamical boundary condition in the present theory, the second of Eq. (2.2), becomes

$$(1/2)\{(u-c)^2+w^2\}+\eta = (1/2)c^2 \tag{2.93}$$

at the wave surface, that is, an arbitrary function of time t is included in the potential ϕ_t. Here exists the difference in the definition for the dynamical boundary conditions between the two wave theories, Eqs. (2.91) and (2.93). The function $\overline{Q}-(1/2)c^2$ is, then, an index of the accuracy of the approximation for this boundary condition based on the stream function theory.

Fig. 2.19 shows the changes in $\overline{Q}-(1/2)c^2$ with respect to the wave height for T = 10, 20, and 30, where the kinematic boundary condition is satisfied to the order of $\sigma_1 < 10^{-5}$ for the sequence of I = 128. The figure indicates that Eqs. (2.88) and (2.89) can estimate water particle velocities satisfying the dynamical boundary condition within an error of 1 %. **Fig. 2.20** shows the relations between the wave height and both the horizontal component of water particle velocities at the wave crest u_c and the wave velocity. This figure can be used to examine the Rankine-Stokes breaking condition. Open circles are evaluated values of the wave velocity based on the breaking model as well as those of the water particle velocity at wave crests based on the stream function theory. The solid circles are quantities at just breaking. Broken lines are extrapolation curves using Lagrange's interpolation polynomial. **Fig. 2.21** is the enlargement of **Fig. 2.20**. The water particle velocities u_c approach the breaking point asymptotically, although the values are about a few percent less than the wave velocities at just breaking. **Figs. 2.20** and **2.21** suggest that the breaking model with peaking has the property of $u_c \rightarrow c$ at just breaking, that is, the Rankine-Stokes breaking condition holds.

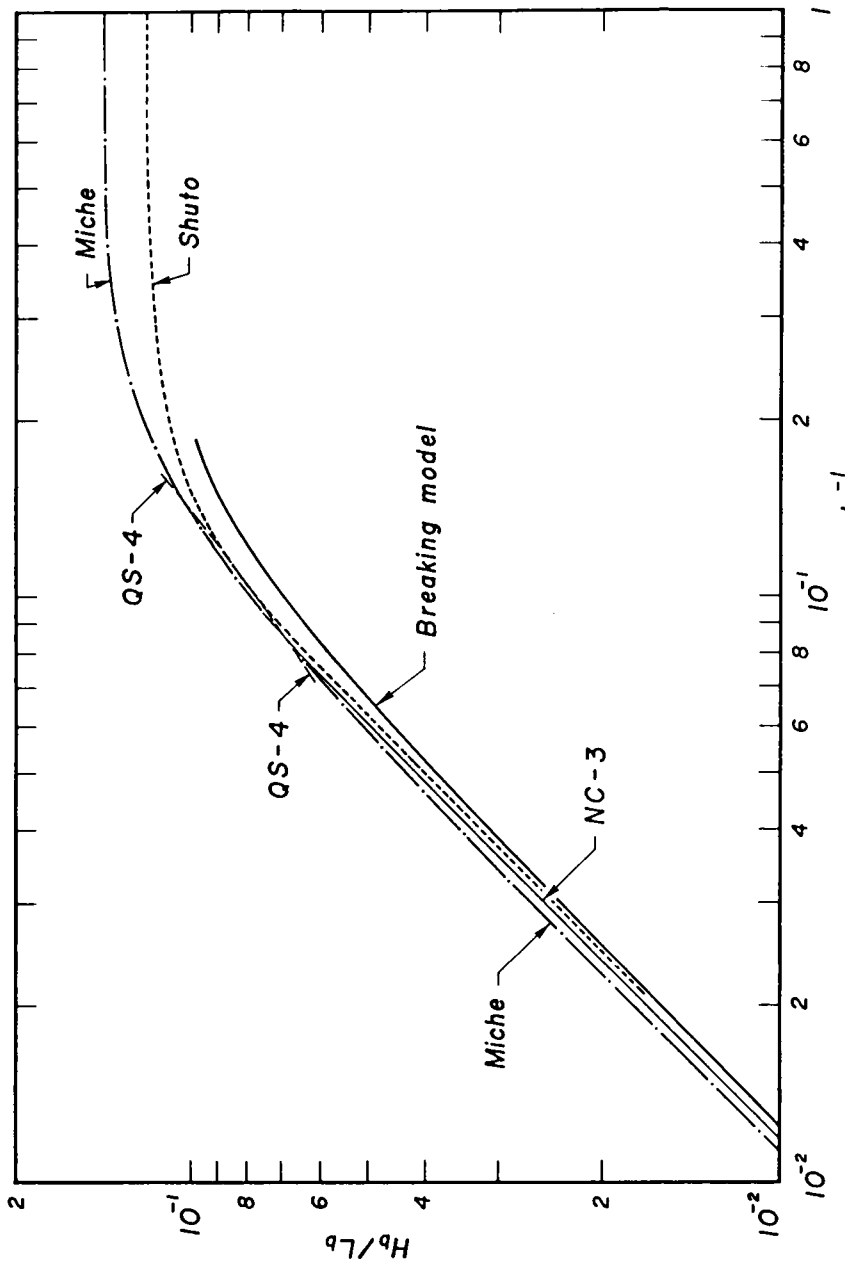

Fig. 2.16 Comparison of various breaking inceptions.

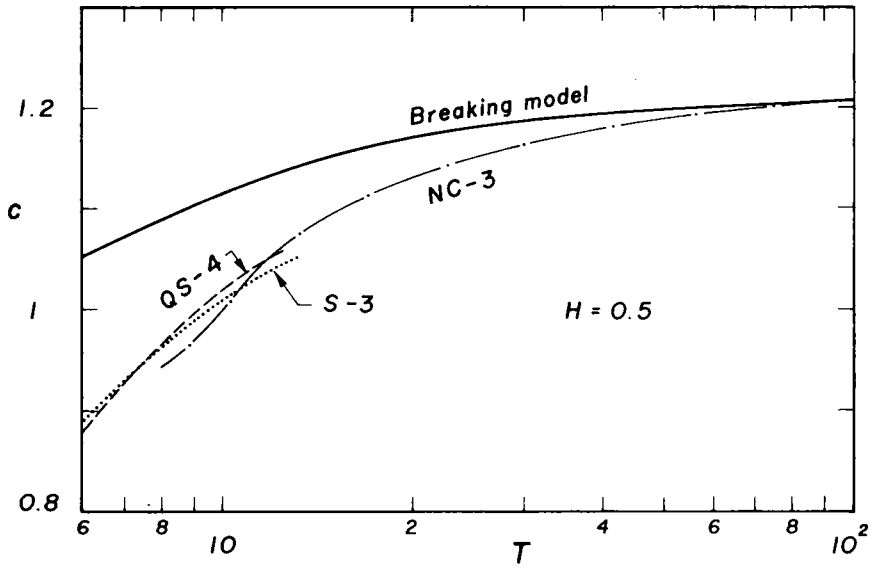

(1) H = 0.5

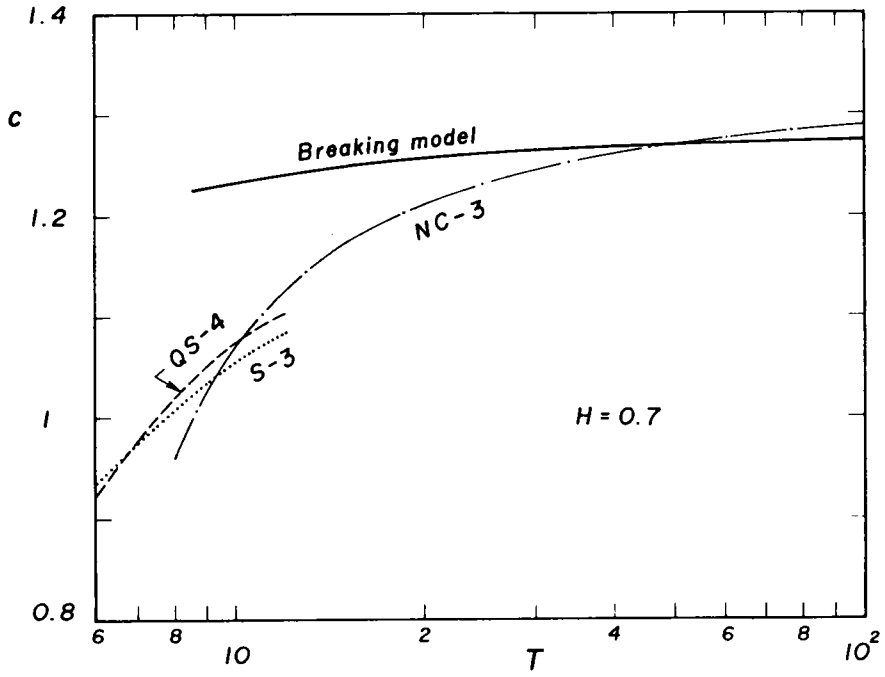

(2) H = 0.7

Fig. 2.17 Changes in wave velocity for small wave heights.

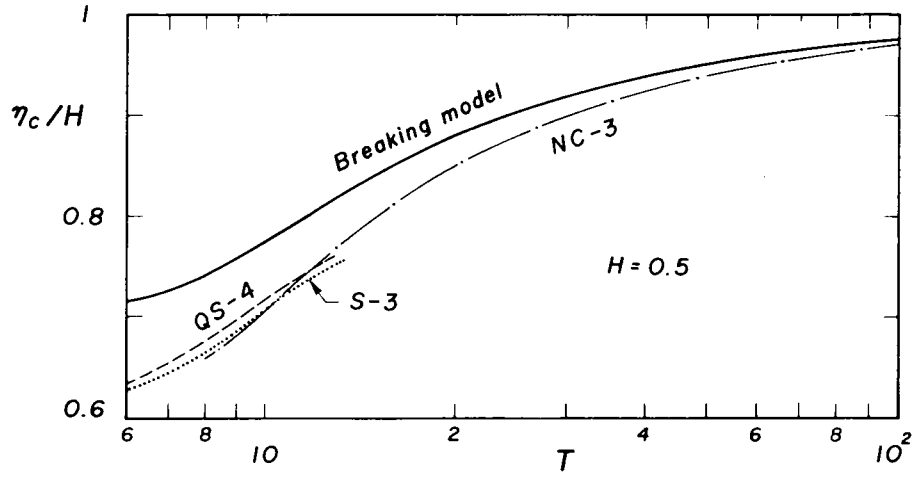

(1) H = 0.5

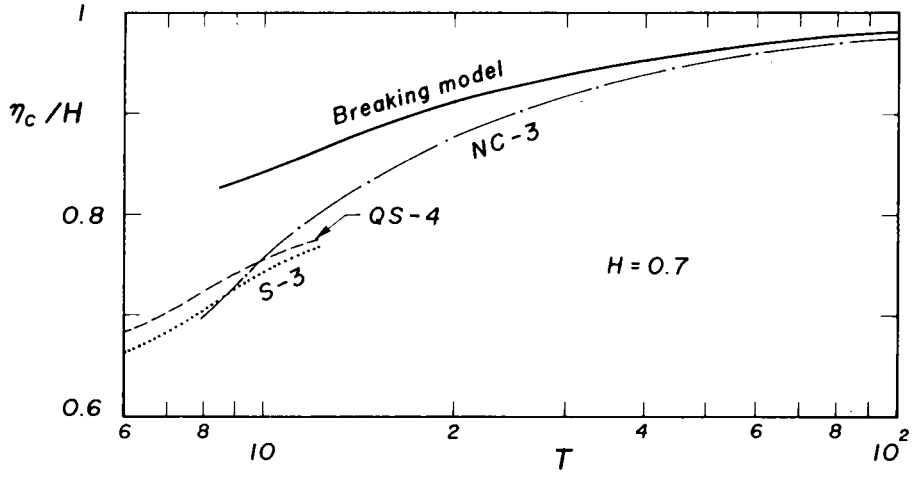

(2) H = 0.7

Fig. 2.18 Changes in crest height for small wave heights.

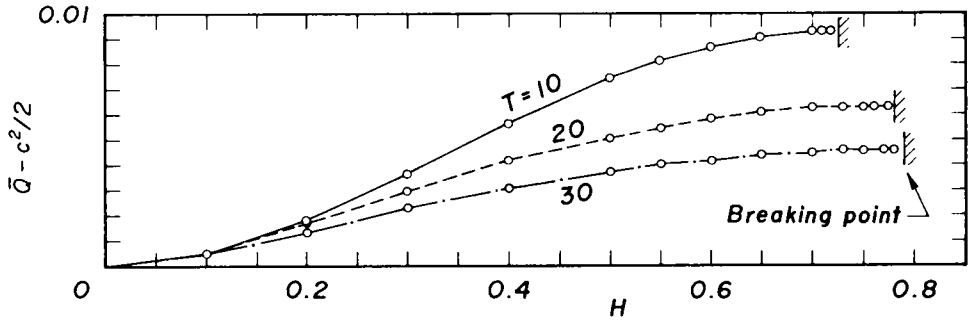

Fig. 2.19 Gross error function for the dynamical boundary condition based on the stream function theory.

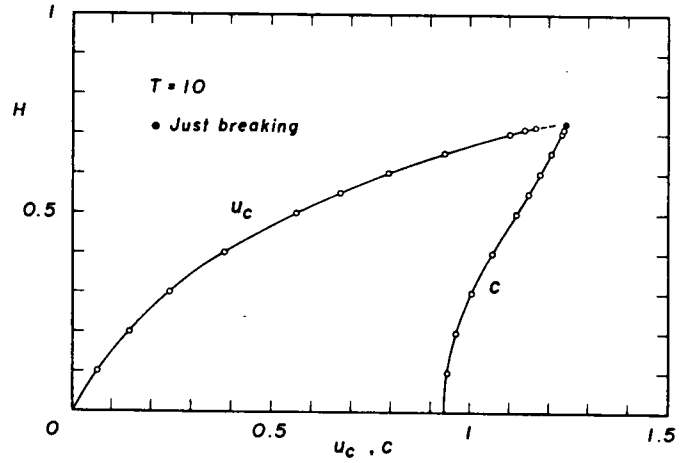

(1) T = 10

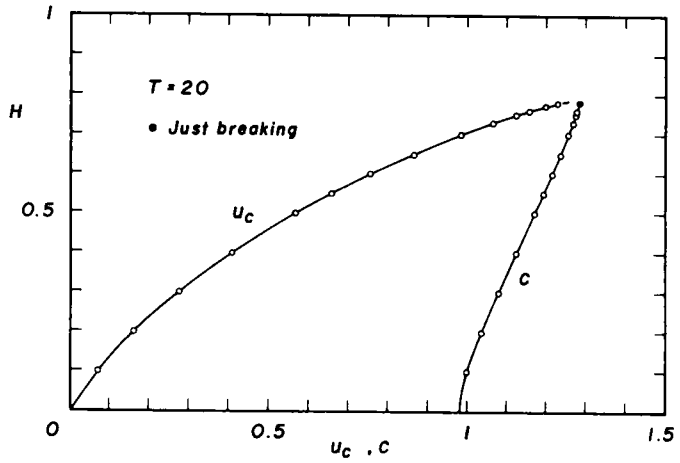

(2) T = 20

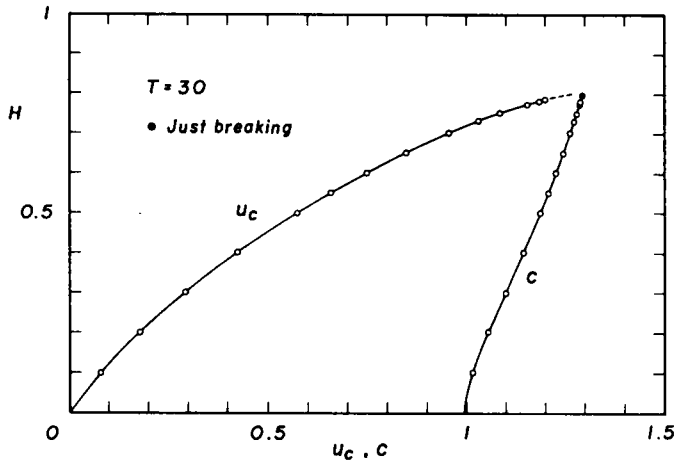

(3) T = 30

Fig. 2.20 Changes in horizontal component of water particle velocities at wave crests based on the stream function theory.

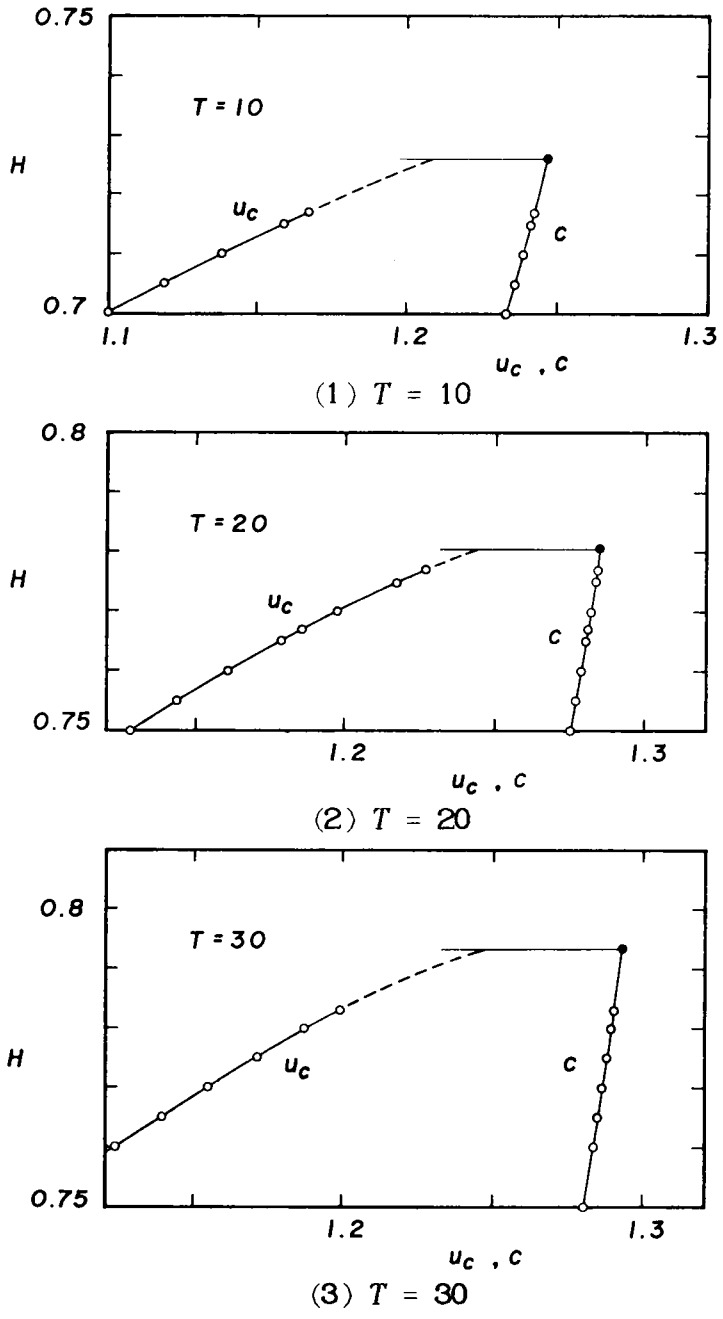

Fig. 2.21 Small portions of the changes in horizontal component of water particle velocities at wave crests based on the stream function theory.

2.3 Small Scale Wave Breaking by Wind

- Incipient Breaking -

(1) Vorticity Equations

In this section small scale wave breaking by wind, termed the "incipient breaking" by Banner and Phillips[7], is discussed in detail and some questions are raised.

Take a local coordinate $(\mathbf{s}^*, n^*) \equiv (s_1^*, s_2^*, n^*)$ such that the $\mathbf{s}^*$-axis is parallel to a wave surface η^* with the coordinate origin on it and n^*-axis, normally upward as shown in **Fig. 2.22**, and consider the behaviour of a thin sheet of vorticity $\mathbf{w}^*$ parallel to the wave surface. In this wind-drift layer, the tangential velocity $\mathbf{u}^* \equiv (u_1^*, u_2^*)$ varies rapidly with depth and approaches the tangential velocity $\mathbf{U}^*$ of the lower fluid which can be assumed to be irrotational. Non-dimensional variables are used as follows:

$$\left.\begin{aligned} &(\mathbf{X},Z) = (\mathbf{X}^*,Z^*)/h, \quad (\mathbf{s},n) = (\mathbf{s}^*,n^*)/h, \quad t = t^*\sqrt{g/h}, \quad \eta = \eta^*/h, \\ &(\mathbf{u},w) = (\mathbf{u}^*,w^*)/\sqrt{gh}, \quad \mathbf{U} = \mathbf{U}^*/\sqrt{gh}, \quad \mathbf{c} = \mathbf{c}^*/\sqrt{gh}, \\ &p = p^*/\rho gh, \quad \tau = \tau^*/\rho gh, \quad \mathbf{w} = \mathbf{w}^*\sqrt{h/g}, \quad R = h\sqrt{gh}/\nu, \end{aligned}\right\} \tag{2.94}$$

where the asterisk indicates a dimensional variable, and h is the mean depth of water, t^* the time, g the acceleration of gravity, w^* the velocity of n^*-component, $\mathbf{c}^*$ the wave velocity, p^* the pressure, τ^* the shear stress, ρ the density of water, R the Reynolds number, and ν the kinetic viscosity of water.

The vorticity[36] can be approximated by

$$\mathbf{w} \fallingdotseq (-\partial u_2/\partial n, \ \partial u_1/\partial n, \ 0). \tag{2.95}$$

With the aid of the equation of continuity, the vorticity transport equation, then, becomes

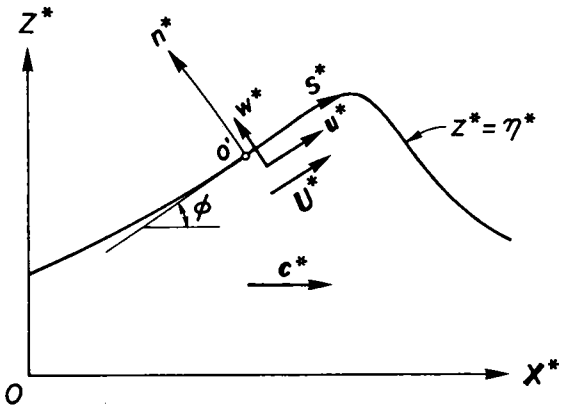

Fig. 2.22 Orthogonal curvilinear coordinate system.

$$\frac{\partial}{\partial t}\frac{\partial u_j}{\partial n}+\frac{\partial}{\partial s_j}\left\{u_i\frac{\partial u_i}{\partial n}\right\}+\frac{\partial}{\partial n}\left\{w\frac{\partial u_j}{\partial n}\right\}\fallingdotseq\frac{1}{R}\frac{\partial^3 u_j}{\partial n^3}, \tag{2.96}$$

in the notation of Cartesian tensors. By integrating Eq. (2.96) in the wind-drift layer with respect to n from $-\delta$ to 0, and by using the conditions that the normal velocity w vanishes at the wave surface and that the vorticity $\partial u_j/\partial n \fallingdotseq 0$ $(j = 1,2)$ below the layer, the second and third terms become

$$\left.\begin{aligned}\int_{-\delta}^{0}\frac{\partial}{\partial s_j}\left\{u_i\frac{\partial u_i}{\partial n}\right\}dn&=\frac{1}{2}\frac{\partial}{\partial s_j}\{u_i(0)^2-u_i(-\delta)^2\}\equiv\frac{1}{2}\frac{\partial}{\partial s_j}\Delta u_i^2,\\ \int_{-\delta}^{0}\frac{\partial}{\partial n}\left\{w\frac{\partial u_j}{\partial n}\right\}dn&=w(0)\frac{\partial u_j(0)}{\partial n}-w(-\delta)\frac{\partial u_j(-\delta)}{\partial n}\fallingdotseq 0,\end{aligned}\right\} \tag{2.97}$$

in which δ is the drift layer thickness and Δ denotes the difference across it. Therefore, Eq. (2.96) becomes

$$\frac{\partial}{\partial t}\Delta u_j+\frac{1}{2}\frac{\partial}{\partial s_j}\Delta u_i^2\fallingdotseq\frac{1}{R}\Delta\frac{\partial^2 u_j}{\partial n^2}. \tag{2.98}$$

This equation is expressed generally in the vector form

$$\frac{\partial}{\partial t}\Delta\mathbf{u}+\frac{1}{2}\nabla_s\Delta|\mathbf{u}|^2\fallingdotseq\frac{1}{R}\Delta\frac{\partial^2\mathbf{u}}{\partial n^2}, \tag{2.99}$$

where $\nabla_s\equiv(\partial/\partial s_1,\partial/\partial s_2)$.

Now, define a local drift $\mathbf{q}$ as the difference of velocities between $n = 0$ and $n = -\delta$ in the vortical wind-drift layer as

$$\mathbf{q} = \Delta \mathbf{u}. \tag{2.100}$$

Since at the wave surface $\mathbf{u} = \mathbf{U} + \mathbf{q}$, while below the layer $\mathbf{u} = \mathbf{U}$,

$$\partial \mathbf{q}/\partial t + \nabla_s \{\mathbf{U}\cdot\mathbf{q} + (1/2)q^2\} \fallingdotseq \Delta(\partial\tau/\partial n), \tag{2.101}$$

where $\tau = (1/R)(\partial u/\partial n)$ is the tangential component of viscous stresses. Eq. (2.101) consists of the same directional component of $\mathbf{U}$ with $\mathbf{q}$. The variations in component of $\mathbf{U}$ normal to $\mathbf{q}$ stretch the vortex lines, but the drift layer thickness decreases, then the relative drift $\mathbf{q}$ may be unaffected. Phillips and Banner[8] have evaluated the right hand side of Eq. (2.101) as the order of $d\tau/\delta$ on the consideration that when waves exist, τ varies with the shear stress of wind, but the distortions of the layer are sufficiently rapid such that the viscous diffusion of vorticity in a wave period can be neglected. Therefore, if the assumption

$$d\tau/\delta \ll \mathbf{q} \tag{2.102}$$

holds, Eq. (2.101) is approximated by

$$\partial \mathbf{q}/\partial t + \nabla_s \{\mathbf{U}\cdot\mathbf{q} + (1/2)q^2\} \fallingdotseq 0. \tag{2.103}$$

This equation specifies the distribution of surface drift $\mathbf{q}$ in terms of the underlying velocity field $\mathbf{U}$.

(2) Surface Drift at Just Breaking

In a single wave train with a wave velocity c, the motion is steady in the frame of reference moving with the wave, so that Eq. (2.103) integrates to give

$$Uq + (1/2)q^2 = (u_0 - c_s)q_0 + (1/2)q_0^2, \tag{2.104}$$

where the subscript s denotes a component parallel to a stream line, and q_0 and u_0 are, respectively, the surface drift and tangential component of orbital velocities at the mean water level. Therefore, the surface drift is

given by

$$q = -U - \sqrt{U^2 - 2(c_s - u_0)q_0 + q_0^2}, \tag{2.105}$$

in which the sign is chosen negative since $q = q_0$ when $U = u_0 - c_s$. At arbitrary phases of the wave $U = u - c_s$, then Eq. (2.105) reduces to

$$q = c_s - u - \sqrt{(c_s - u)^2 - 2(c_s - u_0)q_0 + q_0^2}. \tag{2.106}$$

If the Rankine-Stokes breaking condition[1] is assumed, $q_c + U_c = q_c + u_c - c = 0$ at the wave crest, so that Eq. (2.106) gives

$$(c - u_c)^2 = q_0 \{2(c_s - u_0) - q_0\} . \tag{2.107}$$

Therefore, Eq. (2.106) together with Eq. (2.107) can determine surface drift at just breaking.

On the other hand, corresponding breaking wave heights are evaluated from the equation of momentum. The variations of pressure in the thin vortical surface drift layer usually have little influence on the propagation speed of a wave. Furthermore, the response time of the vortical layer under influence of the variations in shear stress on the wave surface is considered great compared with the wave period. Namely, when a vortical layer is formed in a scale of time larger than the time in which a water particle travels from a wave crest to a trough, the effects of viscosity on the already vortical fluid generated in a wave period can be neglected. Under these conditions, the equation of momentum for the steady state becomes

$$\mathbf{W} \times \mathbf{V} + \nabla \{ (1/2) V^2 + z + p \} = (1/R) \nabla^2 \mathbf{V} \fallingdotseq 0 \tag{2.108}$$

in the $(\xi, Z) \equiv (X - ct, Z)$ coordinate, where $\nabla \equiv (\partial/\partial\xi, \partial/\partial Z)$. Both the velocity vector $\mathbf{V}$ and vorticity vector $\mathbf{W}$ are on the wave surface, then the product $\mathbf{W} \times \mathbf{V}$ is normal to the wave surface. Furthermore, if the variations of pressure along the wave surface can be neglected compared with those of velocity field, the tangential component of Eq. (2.108) is

$$\partial \{ (1/2) V^2 + \eta \} / \partial s \fallingdotseq 0, \tag{2.109}$$

so that

$$(1/2)\,V^2 + \eta = \text{const.} \tag{2.110}$$

along the wave surface. This means that the velocity V takes on the minimum value when the water surface displacement η is maximum, then separation occurs first at the wave crest. Since $V = q_0 + u_0 - c_s$ at $\eta = 0$ and $V = q_c + u_c - c = 0$ at $\eta = \eta_{max}$, Eq. (2.110) reduces to

$$2\,\eta_{max} = (c_s - u_0 - q_0)^2. \tag{2.111}$$

For the lower fluid, assumed to be approximately irrotational, the stream line is given by

$$\tan\phi = w_w/(u_w - c), \tag{2.112}$$

where u_w and w_w are orbital velocities and ϕ is the slope of the stream line at the origin o'. Then, it holds that

$$c_s - u = \sqrt{(c - u_w)^2 + w_w^2}. \tag{2.113}$$

Thus, Eqs. (2.106), (2.107), and (2,111) become

$$q/c = \lambda - \sqrt{\lambda^2 - 2\,\lambda_0\,(q_0/c) + (q_0/c)^2}, \tag{2.114}$$

$$\{1 - (u_c/c)\}^2 = (q_0/c)\,\{2\,\lambda_0 - (q_0/c)\}, \tag{2.115}$$

$$(2/c^2)\,\eta_{max} = \{\lambda_0 - (q_0/c)\}^2, \tag{2.116}$$

where

$$\lambda = \sqrt{\{1 - (u_w/c)\}^2 + (w_w/c)^2}, \tag{2.117}$$

and λ_0 is a value of λ at $\eta = 0$. These equations are also expressed in terms of q_c as

$$q/c = \lambda - \sqrt{\lambda^2 - (q_c/c)^2}, \tag{2.118}$$

$$q_0/c = \lambda_0 - \sqrt{\lambda_0^2 - (q_c/c)^2}, \tag{2.119}$$

$$(2/c^2)\,\eta_{max} = \lambda_0^2 - (q_c/c)^2. \tag{2.120}$$

Now, some remarks on the paramter λ are given. For irrotational motion,

$$\lambda_0 = 1 \tag{2.121}$$

holds exactly[37], while the dynamical boundary condition at an irrotational wave surface is

$$(c - u_w)^2 + w_w^2 + 2\eta = c^2 + \text{const.} \tag{2.122}$$

Thus, at $\eta = 0$

$$\lambda_0^2 \equiv \{1 - (u_{w0}/c)\}^2 + (w_{w0}/c)^2 = 1 + \text{const.}/c^2. \tag{2.123}$$

In the Quasi-Stokes[12] and cnoidal[13] wave theories, the constant is taken to be uniquely zero, while in the Stokes wave theory[32] it is expressed as a power series of the small parameter approximately satisfying Eq. (2.121). Equating Eq. (2.122) at $\eta = 0$ and $\eta = \eta_{max}$ gives Eq. (2.120). Therefore, the analysis above for the breaking wave height corresponds to small scale wave breaking, in which the dynamical boundary condition without wind effects is approximately applicable. When $\lambda_0 = 1$, the results correspond to those of Banner and Phillips and others.

(3) Discussion

Figs. 2.23 and **2.24** show the breaking conditions in terms of the surface drift q_0 given by Eqs. (2.115) and (2.116), that is, the maximum water particle velocity at the wave crest and the maximum wave elevation above the mean water level that can be attained without breaking, respectively. When surface drift vanishes, these figures give the Rankine-Stokes breaking condition with no wind; but, as q_0/c increases, the maximum unbroken crest height and water particle velocity at the wave crest both diminish rapidly. Similarly, **Fig. 2.25** gives the maximum wave elevation η_{max} as a function of surface drift at the wave crest q_c. The relation of surface drift q_c to q_0 is shown in **Fig. 2.26**, indicating that for small q_0/c surface drift chiefly occurs near the wave crest and predominates.

Fig. 2.27 shows distributions of surface drift at just breaking with respect to the phase of waves for three finite amplitude waves obtained

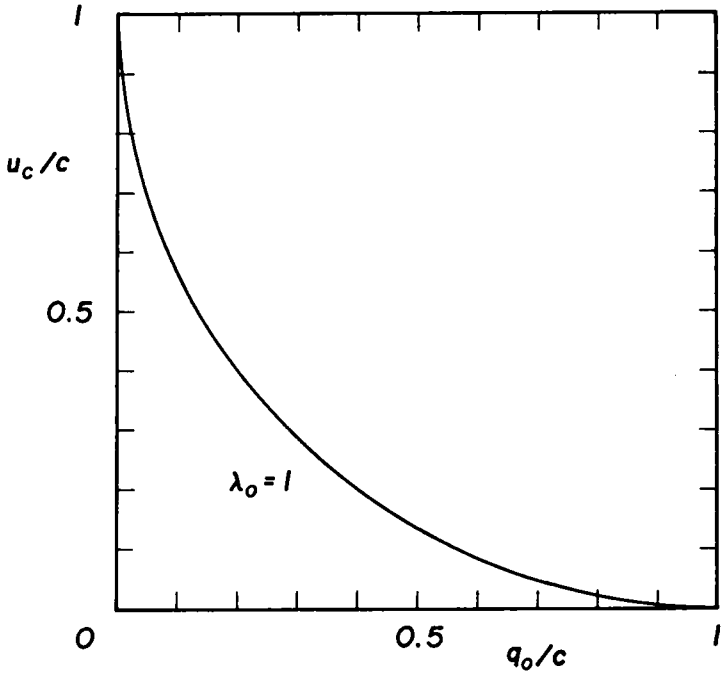

Fig. 2.23 Relation between the maximum water particle velocity at the wave crest and surface drift at the mean water level.

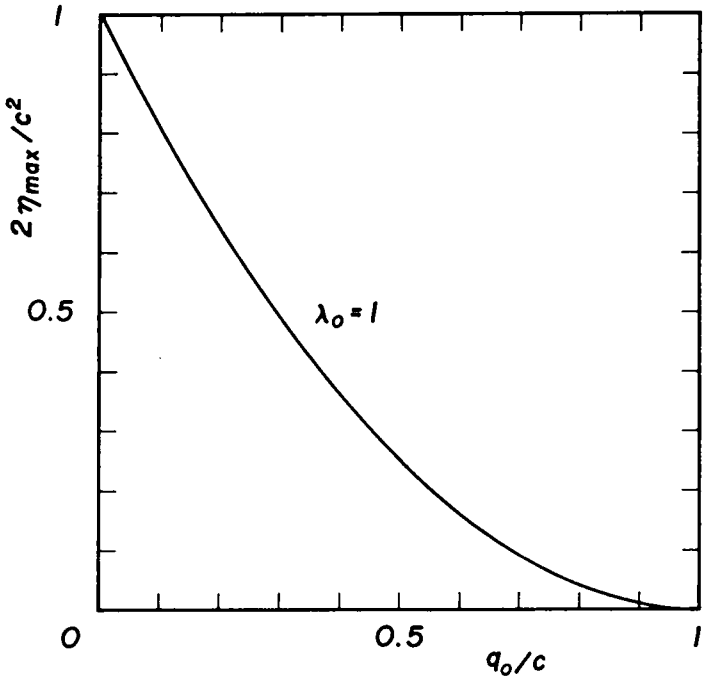

Fig. 2.24 Relation between the maximum wave elevation without breaking and surface drift at the mean water level.

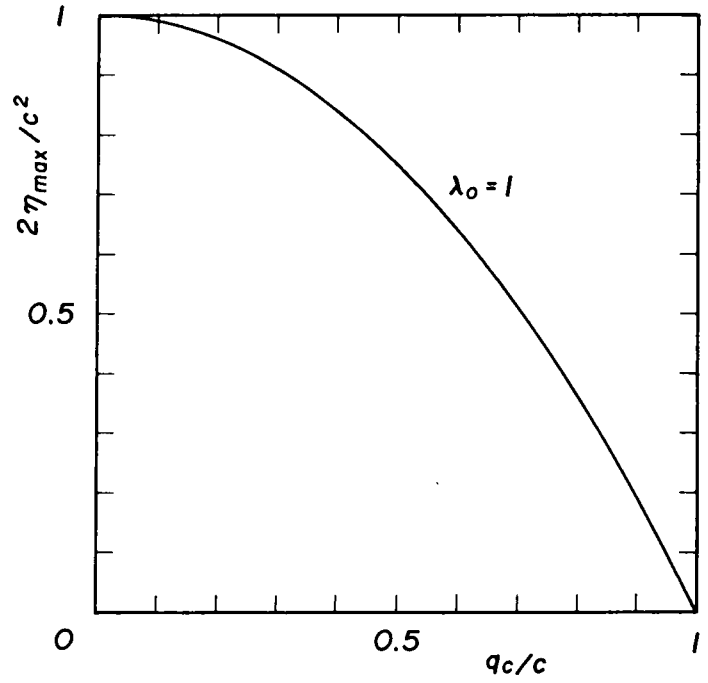

Fig. 2.25 Relation between the maximum wave elevation without breaking and surface drift at the wave crest.

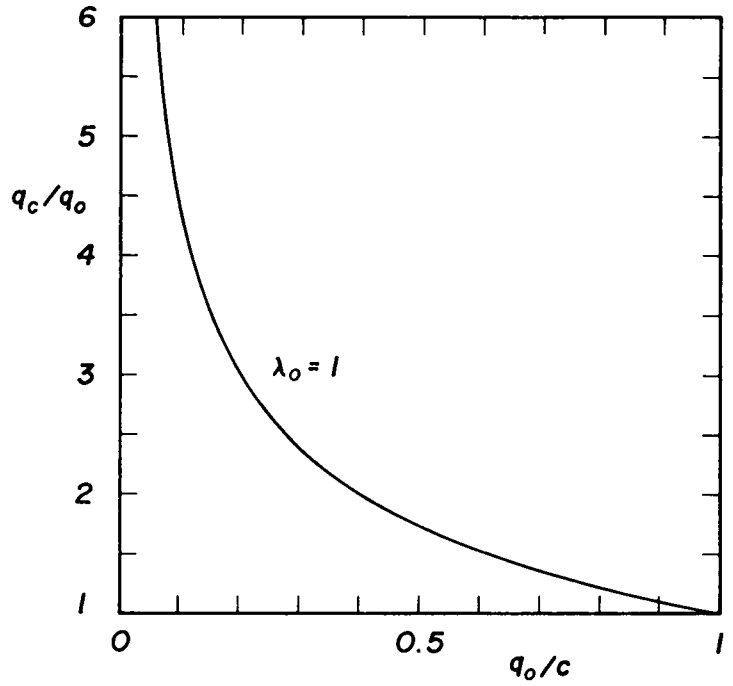

Fig. 2.26 Relation of surface drift at the wave crest to that at the mean water level.

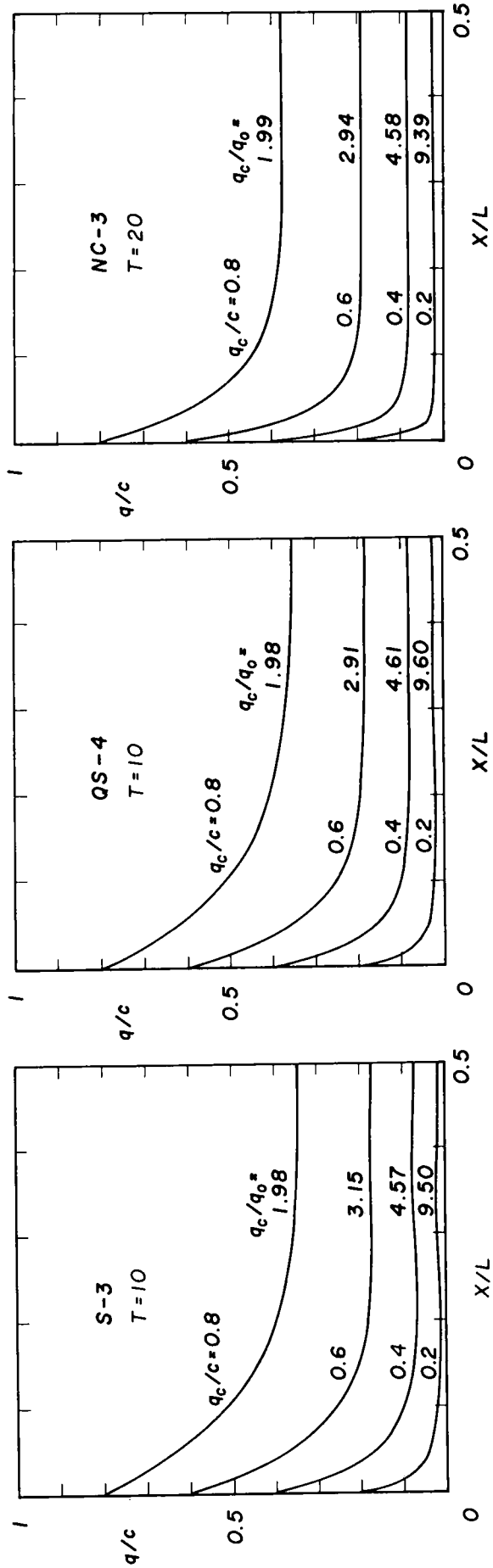

(1) Stokes waves (2) Quasi-Stokes waves (3) Cnoidal waves

Fig. 2.27 Distributions of surface drift at just breaking with respect to the phase of waves.

Table 2.2 Physical properties of breaking waves of permanent type in the presence of surface drift.

Theories	T	q_c/c	q_o/c	q_c/q_o	H_b	c	λ_o
S-3	10	0.2	0.0211	9.50	0.653	1.044	0.960
		0.4	0.0875	4.57	0.549	1.020	0.958
		0.6	0.191	3.15	0.422	0.992	0.975
		0.8	0.404	1.98	0.255	0.959	0.995
QS-4	10	0.2	0.0208	9.60	0.686	1.070	0.970
		0.4	0.0869	4.61	0.566	1.037	0.964
		0.6	0.0206	2.91	0.427	1.000	0.977
		0.8	0.404	1.98	0.255	0.960	0.995
NC-3	20	0.2	0.0213	9.39	0.731	1.222	0.950
		0.4	0.0873	4.58	0.605	1.172	0.960
		0.6	0.0204	2.94	0.446	1.111	0.983
		0.8	0.401	1.99	0.248	1.039	0.998

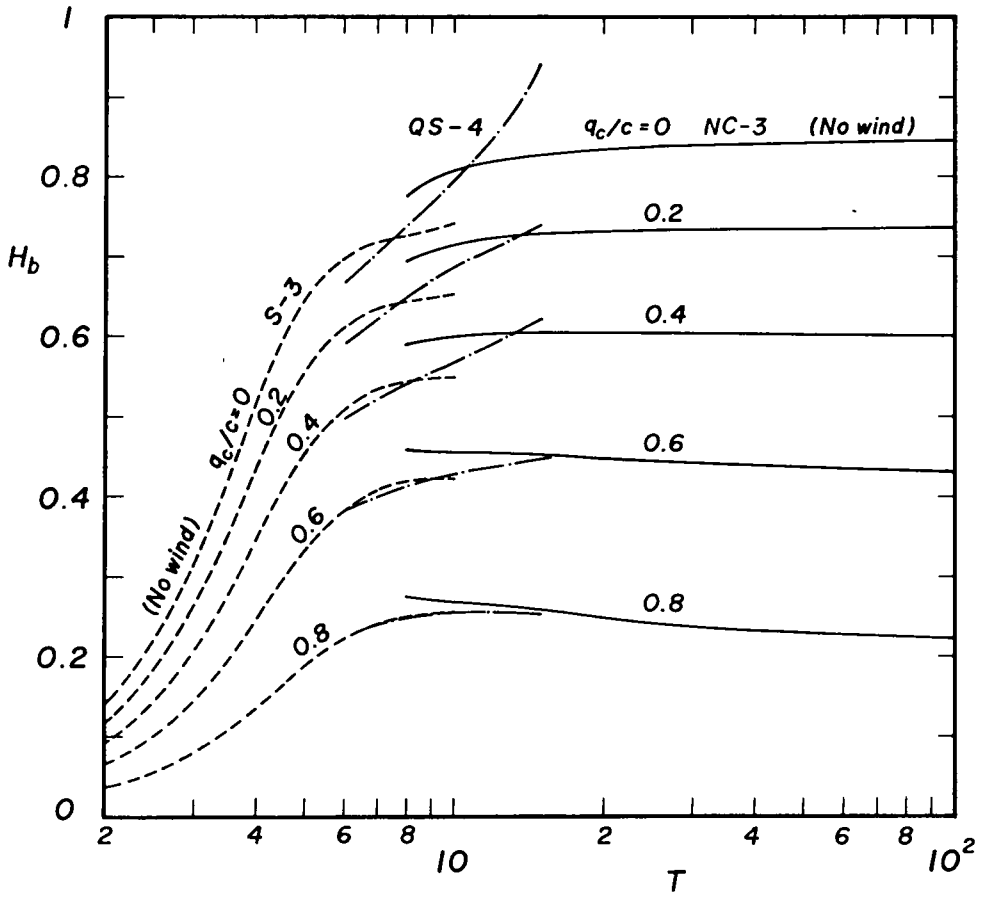

Fig. 2.28 Breaking inception for progressive waves of permanent type in the presence of surface drift.

from the Stokes, Quasi-Stoke, and cnoidal wave theories. **Table 2.2** gives corresponding physical properties. **Fig. 2.27** and **Table 2.2** indicate that when surface drift q_c/c is small, q_c/q_0 is reasonably great, therefore surface drift predominates near the wave crest. However, as q_c/c increases, great surface drift occurs throughout the phase of waves and the breaking wave height becomes small. Furthermore, note that positive surface drift always occurs, even in the wave trough.

The breaking inception for progressive waves of permanent type in the presence of surface drift is shown in **Fig. 2.28**, where breaking inception with no wind has also been added. Wave profiles at just breaking affected by surface drift are theoretically symmetric, but wave profiles for great surface drift would become asymmetric, so that the criterion of this figure does exist for suitable surface drift q_c/c. This model also offers no information about the wind stresses in connection with surface drift, about which further investigation is required.

2.4 Wave Breaking in the Presence of Surface Drift

(1) Intrinsic Equations[10)]

To investigate the normal distribution of surface drift in the wind-drift layer along the surface of a single wave train, consider a stream line o's and its orthogonal trajectory o'n as shown in **Fig. 2.29**, the motion being two-dimensional and steady in the $(\xi,Z) \equiv (X-ct,Z)$ frame of reference moving with the wave. Let ds and dn be elements of the arcs of o's and o'n, and let κ_s and κ_n be the corresponding curvatures at the origin o'. We need the intrinsic equations at o'

Temporarily introduce a rectangular coordinate (x,z), taking x- and z-axes at o' to be tangent and normal to the stream line, and let the tangent

at s make the angle θ with the x-axis. Thus,

$$\left.\begin{aligned} &\kappa_s = \partial\theta/\partial s, \quad \kappa_n = \partial\theta/\partial n, \quad \text{for } \theta \to 0, \\ &\partial x/\partial s = \cos\theta, \quad \partial z/\partial s = \sin\theta, \\ &\partial x/\partial n = -\sin\theta, \quad \partial z/\partial n = \cos\theta. \end{aligned}\right\} \tag{2.124}$$

Therefore, differentiating and putting $\theta = 0$,

$$\partial^2 x/\partial s^2 = 0, \ \partial^2 z/\partial s^2 = \kappa_s, \ \partial^2 x/\partial n^2 = -\kappa_n, \ \partial^2 z/\partial n^2 = 0. \tag{2.125}$$

If f is any function of x and z, derivatives of f at $\theta = 0$ are

$$\left.\begin{aligned} &\partial f/\partial x = \partial f/\partial s, \quad \partial f/\partial z = \partial f/\partial n, \\ &\partial^2 f/\partial x^2 = \partial^2 f/\partial s^2 - \kappa_s(\partial f/\partial n), \\ &\partial^2 f/\partial z^2 = \partial^2 f/\partial n^2 + \kappa_n(\partial f/\partial s). \end{aligned}\right\} \tag{2.126}$$

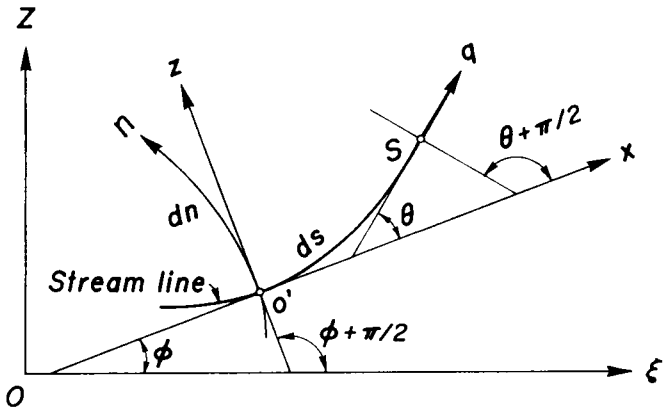

Fig. 2.29 Orthogonal curvilinear coordinate system.

With the aid of these relations, the convection and viscous terms in the Navier-Stokes equations of motion in the (x,z) plane become, respectively,

$$\left.\begin{aligned} &\left\{u\frac{\partial}{\partial x} + w\frac{\partial}{\partial z}\right\}(q\,e^{i\theta}) = q\frac{\partial q}{\partial s} + i\cdot\kappa_s q^2 \qquad \text{and} \\ &\left\{\frac{\partial^2}{\partial x^2} + \frac{\partial^2}{\partial z^2}\right\}(q\,e^{i\theta}) = \left[\frac{\partial^2 q}{\partial s^2} + \frac{\partial^2 q}{\partial n^2} - \kappa_s\frac{\partial q}{\partial n} + \kappa_n\frac{\partial q}{\partial s} - q\,(\kappa_s^2 + \kappa_n^2)\right] \\ &\qquad + i\cdot\left[2\,\kappa_s\frac{\partial q}{\partial s} + 2\,\kappa_n\frac{\partial q}{\partial n} + q\left\{\frac{\partial \kappa_s}{\partial s} + \frac{\partial \kappa_n}{\partial n}\right\}\right], \end{aligned}\right\} \tag{2.127}$$

at $\theta = 0$, where $\upsilon = u + i \cdot w = q\, e^{i\theta}$ and $q = \sqrt{u^2 + w^2}$. The real and imaginary parts are the required components. Similarly, the other terms can be expressed in the (s,n) coordinate. Therefore, intrinsic equations of motion at the origin of the orthogonal curvilinear coordinate (s,n) are expressed by

$$\left.\begin{aligned} \frac{\partial p}{\partial s} + q\frac{\partial q}{\partial s} + \frac{\partial \Omega}{\partial s} &= \frac{1}{R}\left[\frac{\partial^2 q}{\partial s^2} + \frac{\partial^2 q}{\partial n^2} - \kappa_s \frac{\partial q}{\partial n} + \kappa_n \frac{\partial q}{\partial s} - q\,(\kappa_s{}^2 + \kappa_n{}^2)\right], \\ \frac{\partial p}{\partial n} + \kappa_s\, q^2 + \frac{\partial \Omega}{\partial n} &= \frac{1}{R}\left[2\,\kappa_s \frac{\partial q}{\partial s} + 2\,\kappa_n \frac{\partial q}{\partial n} + q\left\{\frac{\partial \kappa_s}{\partial s} + \frac{\partial \kappa_n}{\partial n}\right\}\right], \end{aligned}\right\} \quad (2.128)$$

where Ω is the potential of the external force. In addition, the equation of continuity is

$$\partial q/\partial s + \kappa_n q = 0. \quad (2.129)$$

The vorticity is also given by

$$\omega = -\,\partial q/\partial n + \kappa_s q. \quad (2.130)$$

Eq. (2.128) can be written in terms of the vorticity as

$$\left.\begin{aligned} \frac{\partial}{\partial s}\{p + (1/2)q^2 + \Omega\} &= \frac{1}{R}\left[-\frac{\partial \omega}{\partial n} + q\left\{\frac{\partial \kappa_s}{\partial n} - \frac{\partial \kappa_n}{\partial s}\right\} - q(\kappa_s{}^2 + \kappa_n{}^2)\right], \\ \frac{\partial}{\partial n}\{p + (1/2)q^2 + \Omega\} &= -q\,\omega + \frac{1}{R}\left[-2\,\kappa_n\,\omega + q\left\{\frac{\partial \kappa_s}{\partial s} + \frac{\partial \kappa_n}{\partial n}\right\}\right], \end{aligned}\right\} \quad (2.131)$$

with the aid of Eqs. (2.129) and (2.130). Therefore, if the curvatures, vorticity, and their derivatives are small compared with the Reynolds number, Bernoulli's theorem holds as a first approximation. However, if the vortical surface drift layer is formed, viscous terms have important roles.

Similarly, the shear stress and pressure in the wind-drift layer are evaluated as

$$\tau = (1/R)(\partial q/\partial n + k_s q), \quad (2.132)$$

$$p_n = p - (2/R)\, k_n q. \quad (2.133)$$

Since the form of equations above is independent of the position of the coordinate origin, they are valid for all points on the stream line.

a. Boundary layer approximations

Making the approximation of the boundary layer theory, Eq.(2.128) reduces to

$$\left.\begin{aligned} &\frac{\partial p}{\partial s} + q\frac{\partial q}{\partial s} + \frac{\partial \Omega}{\partial s} \fallingdotseq \frac{1}{R}\frac{\partial^2 q}{\partial n^2}, \\ &\frac{\partial p}{\partial n} + \kappa_s q^2 + \frac{\partial \Omega}{\partial n} \fallingdotseq 0, \end{aligned}\right\} \tag{2.134}$$

provided that the curvatures are not large. Eliminating p and Ω from these equations gives

$$\frac{\partial}{\partial n}\left\{q\frac{\partial q}{\partial s}\right\} = \frac{1}{R}\frac{\partial^3 q}{\partial n^3}. \tag{2.135}$$

Banner and Phillips' results can be obtained by neglecting the viscous term in this equation. With the help of the equation of continuity, Eq. (2.135) becomes

$$\frac{\partial}{\partial n}\left\{\frac{1}{R}\frac{\partial^2 q}{\partial n^2} + \kappa_n q^2\right\} = 0. \tag{2.136}$$

This equation is also written in terms of the vorticity as

$$\frac{\partial}{\partial s}(q\,\omega) = \frac{1}{R}\frac{\partial^2 \omega}{\partial n^2}, \tag{2.137}$$

which expresses the balance between the convection of vorticity and the diffusion by viscosity.

b. Boundary conditions

Since the water particle velocity in the lower fluid distributes vertically, boundary conditions require smooth contact with this velocity distribution at the lower edge of the surface drift layer, i.e.

$$\left.\begin{aligned} &q \equiv -\lambda = -\sqrt{(u_w - c)^2 + w_w^2}, \\ &\partial q/\partial n = \partial u_w/\partial Z \\ &\qquad - \{\partial u_w/\partial \xi - \lambda\,\kappa_s(\partial \eta/\partial \xi)\}\,(\partial \eta/\partial \xi), \end{aligned}\right\} \quad \text{at } n = -\delta. \tag{2.138}$$

(2) Normal Distribution of Surface Drift

Transformations

$$q = -\lambda(s)\cdot f(n) \quad \text{and} \quad Re = \lambda \cdot R \tag{2.139}$$

turn Eqs. (2.136) and (2.138), respectively, into

$$\frac{\partial}{\partial n}\{(1/Re)(d^2f/dn^2) - \kappa_n f^2\} = 0, \tag{2.140}$$

and

$$f = 1 \quad \text{and} \quad df/dn = -(1/\lambda)(\partial q/\partial n) \quad \text{at } n = -\delta. \tag{2.141}$$

Eq. (2.140) together with boundary conditions (2.141) specify the normal distribution of surface drift in terms of the underlying velocity.

First, when $\kappa_n \neq 0$, Eq. (2.140) integrates to

$$(1/Re)(d^2f/dn^2) - \kappa_n f^2 = \tilde{A}(s), \tag{2.142}$$

where $\tilde{A}(s)$ is independent of n and, therefore, an unknown function of s to be determined from the conditions of wind stresses exerting on the wave surace. Since the surface drift layer can be considered thin enough compared with the water depth, the curvature κ_n may be assumed to be nearly constant across the layer, so that Eq. (2.142) integrates twice to give

$$(df/dn)^2 = F(f), \tag{2.143}$$

where $F(f)$ is the cubic polynomial

$$F(f) = (f-1)\{(2/3)\kappa_n Re(f^2 + f + 1) + 2Re\,\tilde{A}\} + \tilde{B}^2, \tag{2.144}$$

with $\tilde{B} = df/dn$ at $n = -\delta$.

The equation $F(f) = 0$ has real coefficients, thus there are three roots a, b, and c. One at least, say a, is real and other two are either real or conjugate complex. The relations between these roots can be determined as follows:

(a) When $\kappa_n > 0$, $\quad F(f) = (2/3)\kappa_n Re(f-a)(f-b)(f-c).$ (2.145)

In case of only one real root, b and c are conjugate complex and, then, $(f-b)(f-c) > 0$ for real f. Thus, a is a lower bound of f, and $a < 1$

because $F(1) > 0$. In the case of three real roots, number them such that $a > b > c$. Since $a + b + c = 0$, c becomes negative. When $b < 1$, the inequality $b < a < 1$ holds from the condition that $F(1) > 0$, so that a is a lower bound of f. Similarly, b is an upper bound of f when $b > 1$.

(b) When $\kappa_n < 0$, since $F(1) > 0$, there is at least one real root, say a, in $f > 1$. Thus,

$$F(f) = -(2/3)\,\kappa_n\, Re(a - f)(f - b)(f - c). \tag{2.146}$$

In case of only one real root, a is an upper bound of f. When b and c are real, $a > 1 > b > c$ provided that $c < 0$, thus a also becomes an upper bound of f.

Fig. 2.30 illustrates the possible five-types of $F(f)$, and corresponding solutions are given by following equations expressed in terms of the Jacobian elliptic functions:

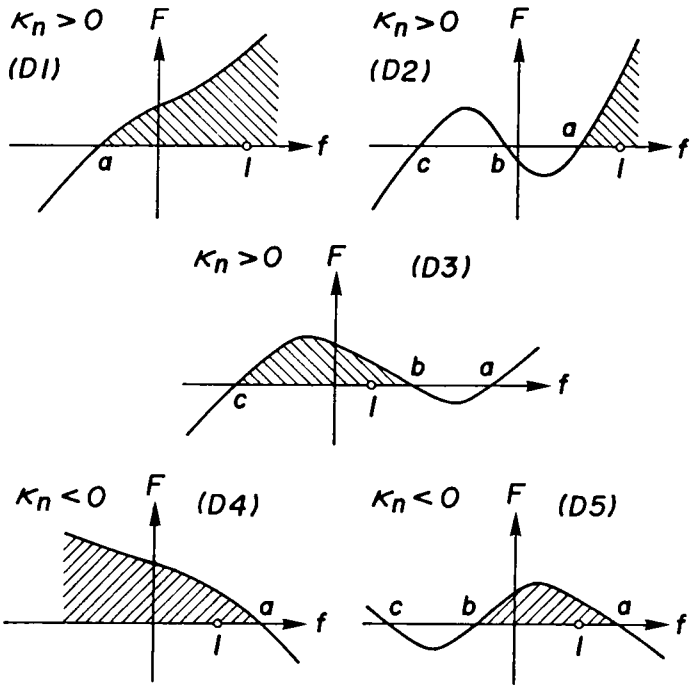

Fig. 2.30 Schematic diagrams of the cubic function $F(f)$.

(D 1) When $\kappa_n > 0$, $a < 1$, and b and c are conjugate complex:

$$f = a + A(1-\mathrm{cn}v)/(1+\mathrm{cn}v) \quad \text{for} \quad df(-\delta)/dn < 0, \tag{2.147.1}$$

$$f = a + A(1+\mathrm{cn}v)/(1-\mathrm{cn}v) \quad \text{for} \quad df(-\delta)/dn > 0, \tag{2.147.2}$$

$$\left.\begin{aligned} v &= \sqrt{(2/3)\,\kappa_n\, Re\, A}\cdot (n+\delta) + v_1, \\ k^2 &= (2A - 3a)/(4A), \quad A^2 = (9/4)\,a^2 - (1/4)\,(b-\bar{b})^2. \end{aligned}\right\} \tag{2.147.3}$$

(D 2) When $\kappa_n > 0$ and $1 > a > b > c$:

$$f = b + (a-b)/\mathrm{cn}^2 v \quad \text{for} \quad df(-\delta)/dn < 0, \tag{2.148.1}$$

$$f = -(a+b) + (2a+b)/\mathrm{sn}^2 v \quad \text{for} \quad df(-\delta)/dn > 0, \tag{2.148.2}$$

$$\left.\begin{aligned} v &= \sqrt{(1/6)\,\kappa_n\, Re\,(2a+b)}\cdot (n+\delta) + v_1, \\ k^2 &= (a+2b)/(2a+b). \end{aligned}\right\} \tag{2.148.3}$$

(D 3) When $\kappa_n > 0$ and $a > b > 1 > c$:

$$\left.\begin{aligned} f &= (a+2b)\,\mathrm{sn}^2 v - (a+b), \\ v &= \sqrt{(1/6)\,\kappa_n\, Re\,(2a+b)}\cdot (n+\delta) + v_1, \\ k^2 &= (a+2b)/(2a+b). \end{aligned}\right\} \tag{2.149}$$

(D 4) When $\kappa_n < 0$, $a > 1$, and b and c are conjugate complex:

$$f = a - A(1+\mathrm{cn}v)/(1-\mathrm{cn}v) \quad \text{for} \quad df(-\delta)/dn < 0, \tag{2.150.1}$$

$$f = a - A(1-\mathrm{cn}v)/(1+\mathrm{cn}v) \quad \text{for} \quad df(-\delta)/dn > 0, \tag{2.150.2}$$

$$\left.\begin{aligned} v &= \sqrt{-(2/3)\,\kappa_n\, Re\, A}\cdot (n+\delta) + v_1, \\ k^2 &= (2A + 3a)/(4A), \quad A^2 = (9/4)\,a^2 - (1/4)(b-\bar{b})^2. \end{aligned}\right\} \tag{2.150.3}$$

(D 5) When $\kappa_n < 0$ and $a > 1 > b > c$:

$$\left.\begin{aligned} f &= b + (a-b)\,\mathrm{cn}^2 v, \\ v &= \sqrt{-(1/6)\,\kappa_n\, Re\,(2a+b)}\cdot (n+\delta) + v_1, \\ k^2 &= (a-b)/(2a+b). \end{aligned}\right\} \tag{2.151}$$

In Eqs. (2.147) to (2.151), v_1 is a value of v for $f = 1$, the over-bar denotes a complex conjugate, and also sn and cn are the Jacobian elliptic functions of the first and second kinds with the modulus k, respectively.

Secondly, when $\kappa_n = 0$, $\partial q/\partial s = 0$ from the equation of continuity, thus surface drift takes on locally either the maximum or minimum value. A sixth-type of surface drift is, therefore, admittable:

(D 6) When $\kappa_n = 0$, Eq. (2.140) becomes $d^3f/d^3n = 0$ and integrates to

$$f = (1/2)\, Re\, \tilde{A}(n + \delta)^2 + \tilde{B}\,(n + \delta) + 1, \tag{2.152}$$

with the aid of boundary conditions and because this equation must coincide with the limiting form of Eq. (2.143) when $\kappa_n \to 0$.

Now, the analysis needs to be completed by deciding the unknown function $\tilde{A}(s)$ and the drift layer thickness δ. The first of the basic equation (2.134) is transformed into

$$\partial p/\partial s + \partial \Omega/\partial s = -\lambda^2 \{ (1/Re)(d^2f/d^2n) - \kappa_n f^2 \}, \tag{2.153}$$

then $\tilde{A}$ is identical to the gradient of pressure exerting on the wave surface, i.e.

$$\tilde{A}(s) = -(1/\lambda^2)(\partial p/\partial s) \qquad \text{at } n = 0. \tag{2.154}$$

The pressure can, as usual, be assumed as

$$p_s = C_s(\rho_a/\rho)(W_a - c)^2 \cdot (\partial \eta/\partial \xi) \equiv \sigma_p \cdot (\partial \eta/\partial \xi), \tag{2.155}$$

where $W_a \equiv W_a^*/\sqrt{gh}$ is the wind speed, C_s the sheltering coefficient, and $p_s \equiv p_s^*/\rho gh$ and ρ_a are the pressure and density of air, respectively. Therefore, the gradient of pressure at the origin of the (s,n) coordinate becomes

$$\partial p/\partial s = -\sigma_p \kappa_s \{1 + (\partial \eta/\partial \xi)^2\}. \tag{2.156}$$

From Eqs. (2.154) and (2.156), $\tilde{A}$ is given by

$$\tilde{A}(s) = \kappa_s(\sigma_p/\lambda^2)\{1 + (\partial \eta/\partial \xi)^2\} \qquad \text{at } n = 0. \tag{2.157}$$

On the other hand, the equation of continuity (2.129) may be applicable at the lower edge of the drift layer; then,

$$\partial(q_\delta - q)/\partial s + \kappa_n(q_\delta - q) = 0, \quad q_\delta \equiv -\lambda, \tag{2.158}$$

provided that the curvature k_n is nearly constant across the layer, where q_δ is surface drift at $n = -\delta$.

By the definition for the displacement thickness δ_1

$$q_\delta \cdot \delta_1 = \int_{-\delta}^{0} (q_\delta - q)\, dn, \tag{2.159}$$

Eq. (2.158) takes the form

$$\partial (q_\delta \cdot \delta_1)/\partial s + \kappa_n (q_\delta \cdot \delta_1) = 0 \tag{2.160}$$

and integrates exactly to

$$\delta_1/\delta_{1c} = (\lambda_c/\lambda)/\sqrt{1 + (\partial \eta/\partial \xi)^2}, \tag{2.161}$$

where the condition that $q_\delta \cdot \delta_1 = q_{\delta c} \cdot \delta_{1c}$ at the wave crest has been used.

(3) Breaking Conditions

Physical properties of wave breaking can be determined as follows: At the wave crest $\kappa_n = 0$, therefore the normal distribution of surface drift is given by Eq. (2.152). If $f = f_0$ at $n = 0$, the drift layer thickness at the wave crest δ_c is the greater root of the equation

$$(1/2)\, Re\, \tilde{A}\, \delta_c^2 + \tilde{B}\, \delta_c + (1 - f_0) = 0, \tag{2.162}$$

i.e.

$$\delta_c = 2(1 - f_0)/\{\sqrt{\tilde{B}^2 - 2\, Re\, \tilde{A}(1 - f_0)} - \tilde{B}\}, \tag{2.163}$$

because the direction of surface drift at the wave crest should be the same as the wave propagation, i.e. $df(-\delta)/dn < 0$, and because $\tilde{A}$ is negative at the wave crest as seen in Eq. (2.157). The displacement thickness δ_{1c} is, thus, given by

$$\delta_{1c} = (1/3)(1 - f_0)\delta_c - (1/6)\tilde{B}\, \delta_c^2. \tag{2.164}$$

The Rankine-Stokes breaking condition, i.e. $f_0 = 0$, gives

$$\delta_c = 2/\{\sqrt{\tilde{B}^2 - 2\, Re\, \tilde{A}} - \tilde{B}\}, \tag{2.165}$$

$$\delta_{1c} = (1/3)\, \delta_c - (1/6)\tilde{B}\, \delta_c^2. \tag{2.166}$$

Furthermore, since the shear stress on the wave surface is given by

$$\tau = -(\lambda^2/Re)(\,df/dn + k_s f\,), \tag{2.167}$$

the shear stress at just breaking becomes

$$\tau_c = (\lambda^2/Re)\sqrt{\tilde{B}^2 - 2Re\,\tilde{A}}. \tag{2.168}$$

Therefore, δ_c, δ_{1c}, and τ_c are all proportional to $Re^{-1/2}$ as is usual in the boundary layer theory.

When the pressure exerting on a wave surface is given, $\tilde{A}$ is evaluated based on Eq. (2.157). Thicknesses at the wave crest δ_c and δ_{1c} can be determined by either Eqs. (2.163) and (2.164) or Eqs. (2.165) and (2.166), respectively. Furthermore, δ_1 at arbitrary phases of the wave is evaluated by Eq. (2.161), so that δ is determined so as to satisfy the definition for the displacement thickness

$$\left.\begin{aligned} \delta_1 &= (d\upsilon/dn)^{-1}\cdot\int_{-\delta}^{0}(1-f)\,d\upsilon \qquad \text{for} \quad \partial f(-\delta)/\partial n < 0, \\ \delta_1 &= (d\upsilon/dn)^{-1}\cdot\int_{-\delta}^{0}(f-1)\,d\upsilon \qquad \text{for} \quad \partial f(-\delta)/\partial n > 0. \end{aligned}\right\} \tag{2.169}$$

Finally, the normal distribution of surface drift in the wind-drift layer is found from the corresponding solutions (D 1) to (D 6), and the distribution of shear stress with respect to the phase of waves, from Eq. (2.167).

(4) Discussion

In the analysis above, there are four parameters; wave period T, surface drift at a wave crest q_c/c, Reynolds number R, and pressure σ_p. To combine the Reynolds number R with the wave period T, the wave Reynolds number $R_w = \sigma/(\nu k^2)$, where σ is the frequency and k the wave number, is introduced. Thus, the relation of Reynolds numbers R and R_w to the wave period T becomes

$$R/R_w = 2\pi/(c^2 T) \tag{2.170}$$

in dimensionless form. For surface drift at just breaking q_c/c, Eq. (2.170) varies with the wave period as shown in **Fig. 2.31**, while the Reynolds number takes on values within from 10^5 to 10^8 for water at a temperature of 20°C as the water depth varies from 10 cm to 20 m. Therefore, it is sufficient for the wave Reynolds number to be within from 10^5 to 10^8 to cover the overall range of the Reynolds number; consequently, the Reynolds number for a greater wave period corresponds to a shallower water depth.

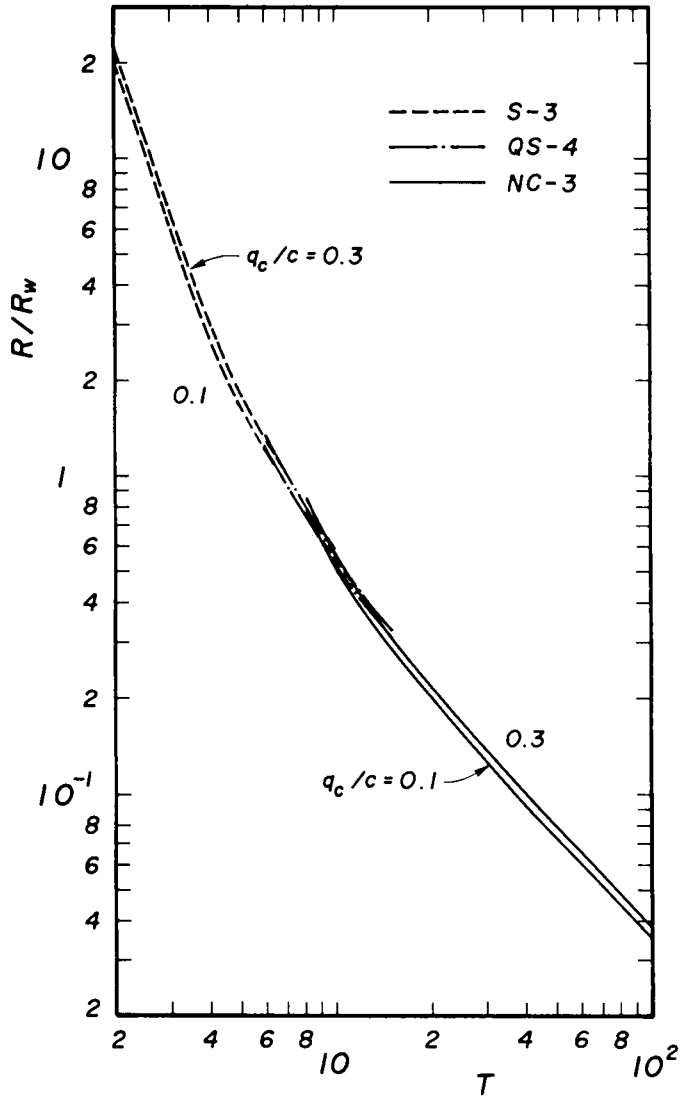

Fig. 2.31 Relation between the Reynolds number and wave Reynolds number.

Fig. 2.32 shows the distributions of displacement thickness δ_1, gradient of pressure $\tilde{A}$, shear stress τ, and substantial surface drift $1-f$ with respect to the phase of waves based on the Stokes(**S-3**), Quasi-Stokes(**QS-4**), and cnoidal wave theories(**NC-3**). The surface drift and shear stress are values at the wave surface, $n = 0$, and all values are normalized by values at the wave crests. Corresponding wave profiles have also been shown in the figure.

Both the displacement thickness and gradient of pressure are indistinguishable from the other changes for various pressure $\bar{\sigma}_p = \sigma_p/c^2$. The displacement thickness takes on a maximum value at the wave crest and from Eq. (2.157) the gradient of pressure is clearly negative there, so that the pressure is manifested as suction near the wave crest. On the contrary, the shear stress and surface drift are sensitively affected both by the changes in pressure and by underlying velocity fields.

As to the velocity fields given by the Stokes wave theory, as shown in **Figs. 2.32**(1) and (2), where slight secondary waves are present, for small values of pressure, the shear stress and surface drift are positive in the leeward side of the wave crest and negative in the windward side. As the pressure inceases, the influence of underlying velocity fields appears to be effective; that is, both the shear stress and surface drift become positive near the secondary wave crests and negative in these wave troughs. This circumstance is predominant in **Fig. 2.32**(3), where secondary waves in the primary wave trough are apparent. Positive regions of the shear stress and surface drift vary evidently corresponding to the primary and secondary wave crests. Accordingly, the shear stress and surface drift distribute in much the same way as if the leeward side of the wave crest were sheltered. There exist positions where the shear stress is greater than that at the wave crest, $|\tau/\tau_c| > 1$, but water particles are not spilled forward because surface drift there is less than unity, $|1 - f| < 1$.

For the velocity field given by the Quasi-Stokes wave theory without apparent secondary waves, the distributions of shear stress and surface drift may show a little difference from that for Stokes waves, but basic characteristics are the same; the shear stress and surface drift vary as if there were sheltered regions in the leeward slopes of the wave crests.

Of the Stokes, Quasi-Stokes, and cnoidal wave theories, the velocity field based on the cnoidal wave theory gives representative stress distributions because this theory offers no possibility for the presence of secondary waves in the wave trough. Both the shear stress and surface drift are slightly negative in the trough region and take on negative minima in the windward and leeward sides of the wave crest.

These characteristics of wind stresses fundamentally coincide with those determined by Benjamin[38], who calculated the stress distributions of air flow over a wavy boundary. In his analysis, the pressure distribution has a substantial component in phase with the wave slope, the same as for the present model, and the similar stress distributions for a solid hump with **Fig. 2.32.(7)** are given.

However, it is notable that for small pressure the reversal of the shear stress and also of the surface drift occurs just at the leeward side of the primary wave crest. When the pressure increases, this reversal diminishes gradually. To investigate this feature, the ratios of shear stress at the wave crest to pressure are given in **Table 2.3.** It can be seen that the shear stress for small pressure is stronger than that for great pressure. Therefore, when the effect of the shear stress at the wave crest is much greater in comparison with that of the pressure, a reversal of the shear stress and surface drift occurs at the leeward side as described above, and the region may turn into a spilling one.

Generally, the shear stress and surface drift change sign and become negative in the leeward side of the wave crest, indicating a tendency

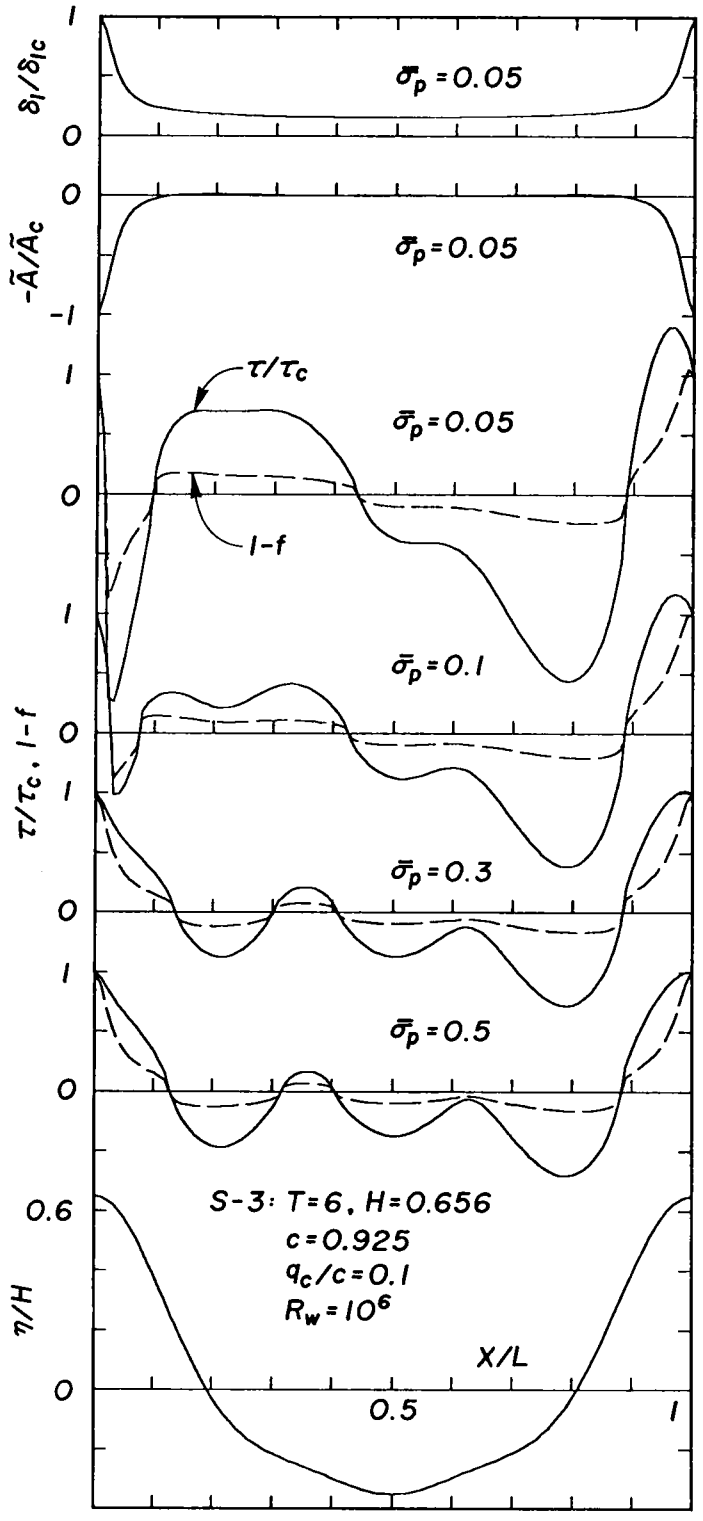

(1) Stokes wave : T = 6, q_c/c = 0.1

Fig. 2.32 Distributions of displacement thickness, gradient of pressure, shear stress, and surface drift with respect to the phase of waves.

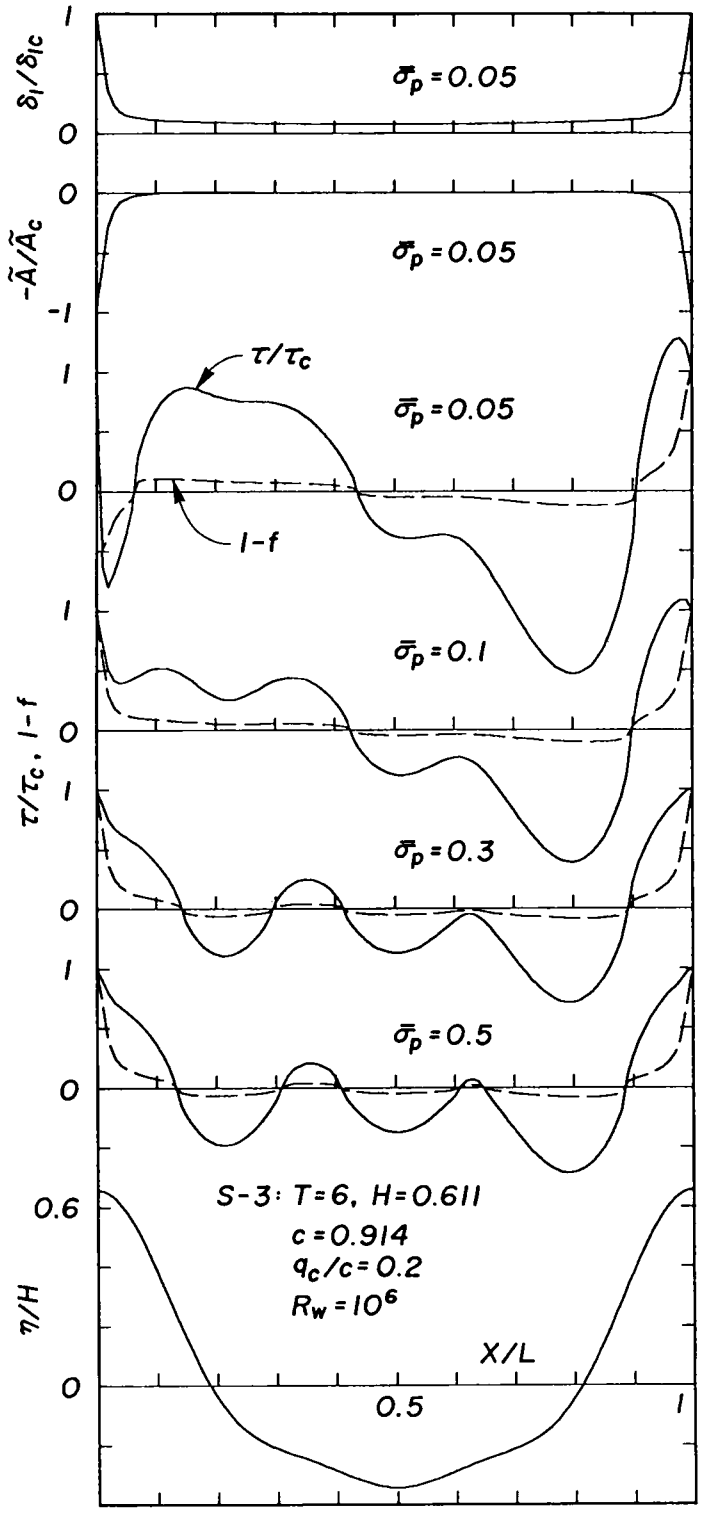

(2) Stokes wave : T = 6, q_c/c = 0.2

Fig. 2.32 Continued.

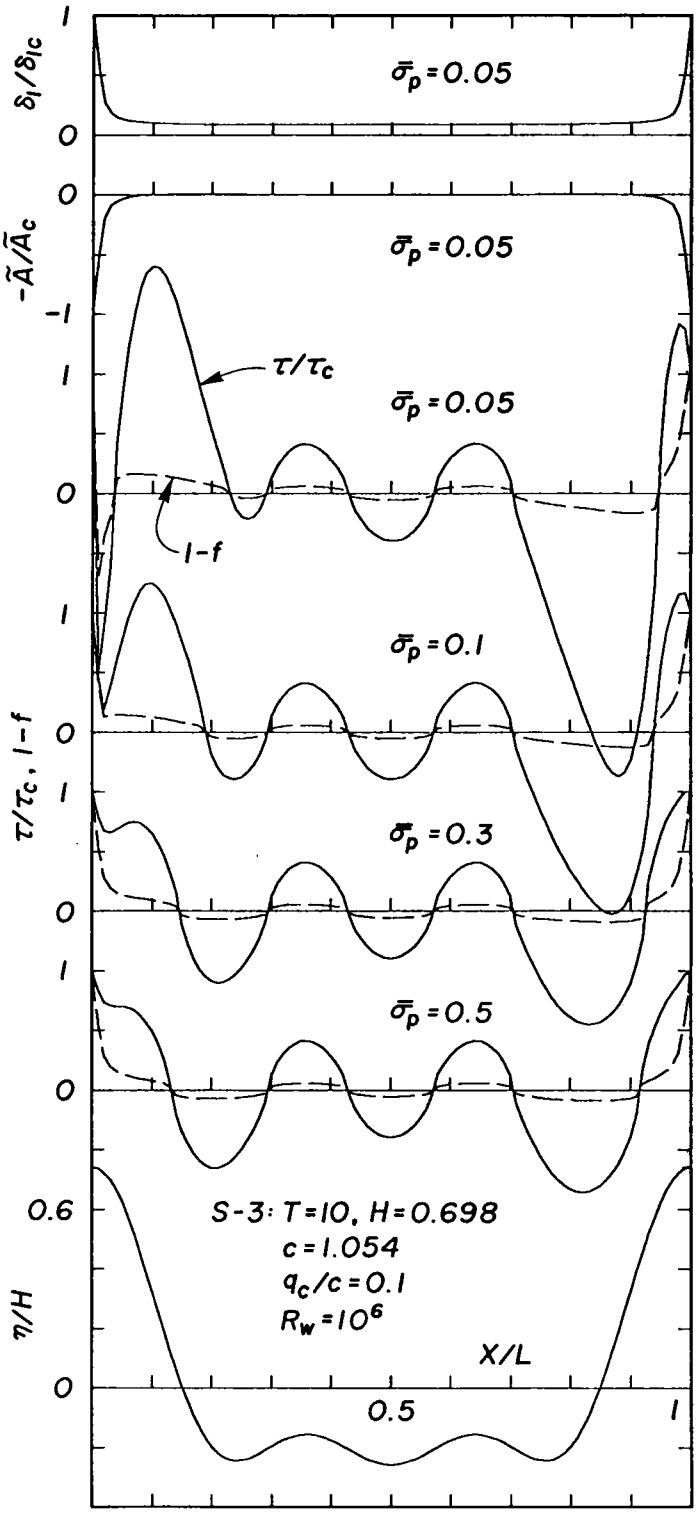

(3) Stokes wave : T = 10, q_c/c = 0.1

Fig. 2.32 Continued.

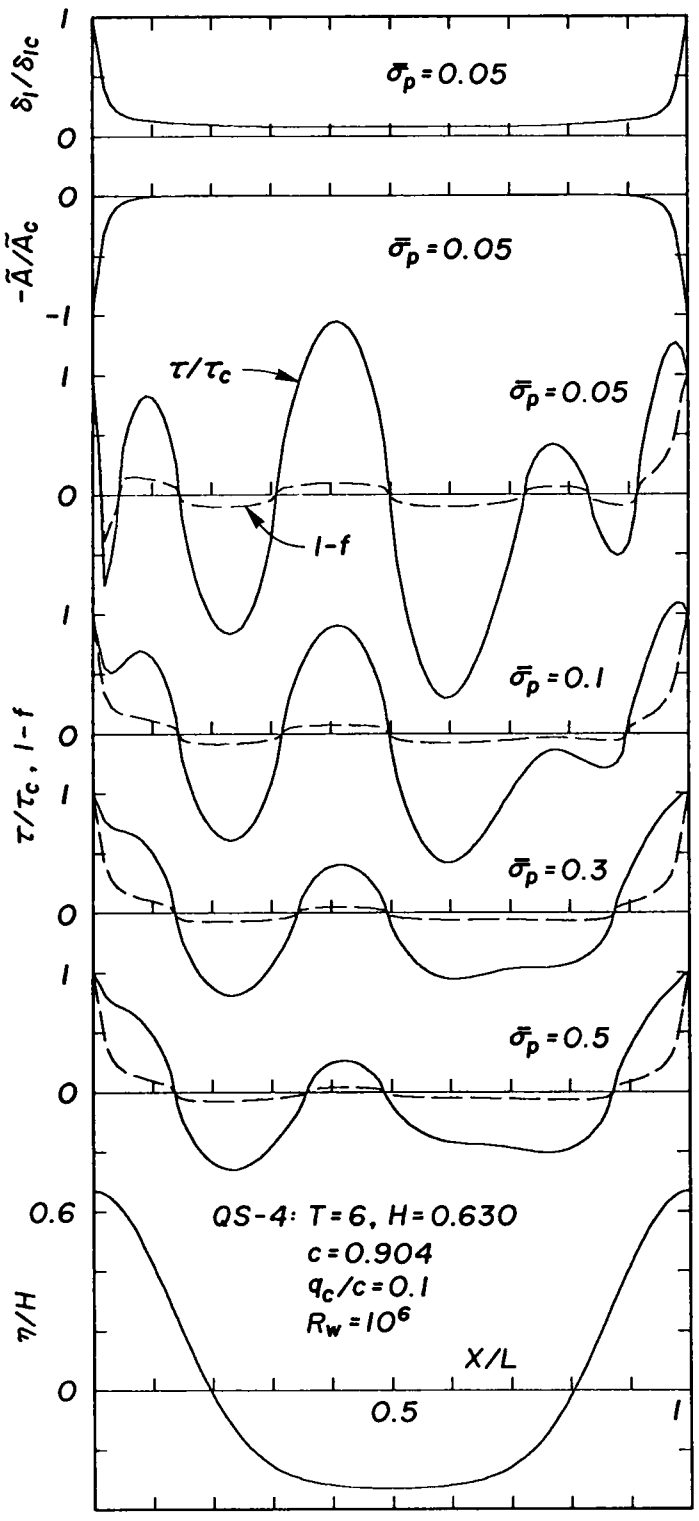

(4) Quasi-Stokes wave : T = 6, q_c/c = 0.1

Fig. 2.32 Continued.

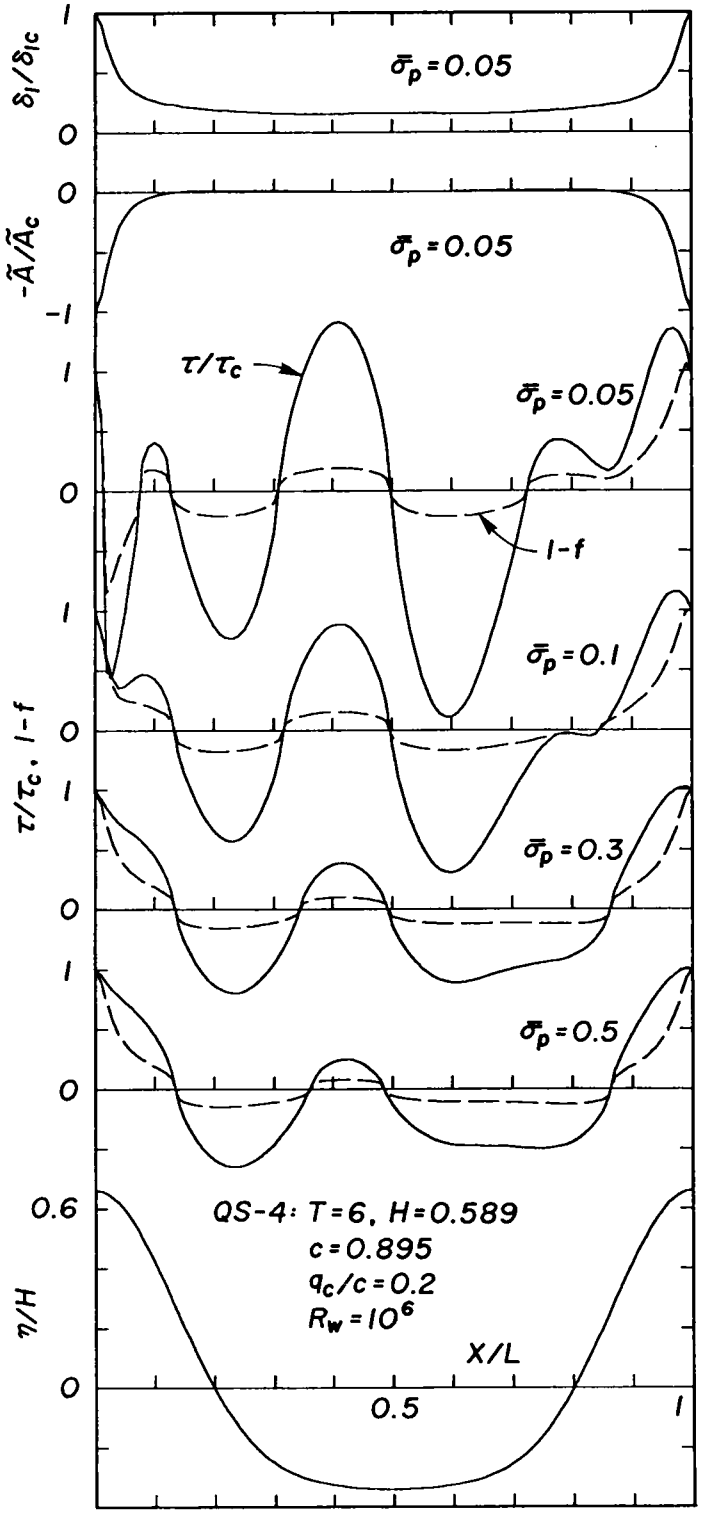

(5) Quasi-Stokes wave : $T = 6$, $q_c/c = 0.2$

Fig. 2.32 Continued.

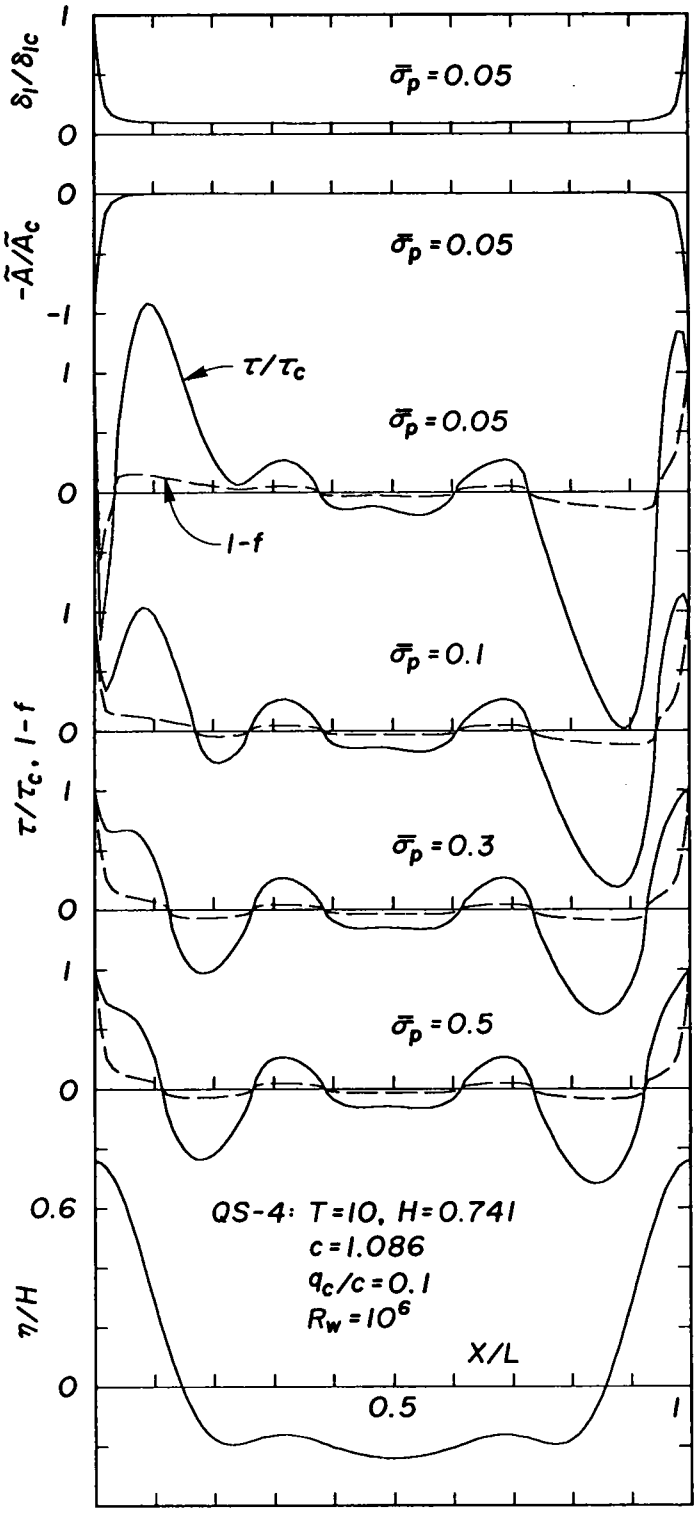

(6) Quasi-Stokes wave : T = 10, q_c/c = 0.1

Fig. 2.32 Continued.

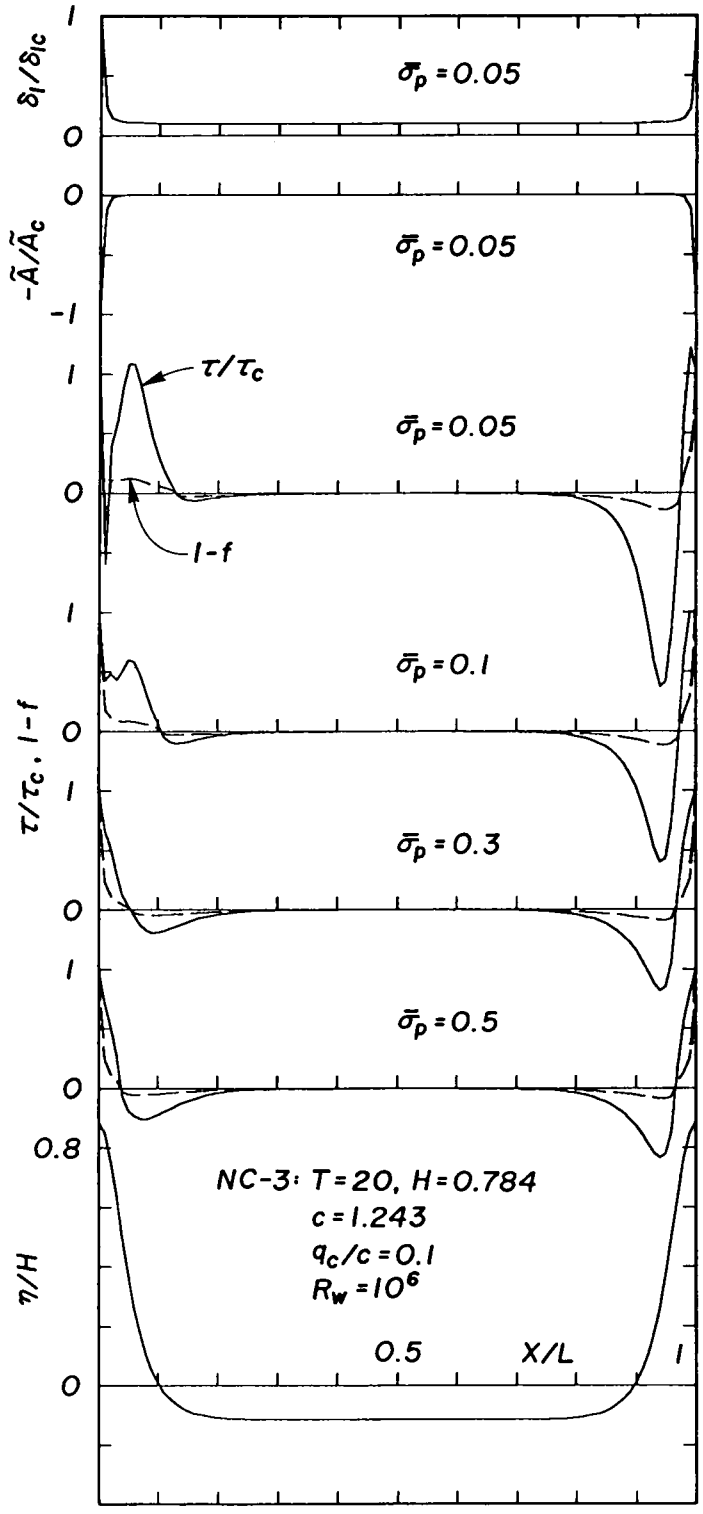

(7) Cnoidal wave : T = 20, q_c/c = 0.1

Fig. 2.32 Continued.

Table 2.3 Ratios of shear stress to pressure at the crests of just breaking waves.

Theories	R_w	T	q_c/c	$\bar{\sigma}_p$	$\tau_c/\bar{\sigma}_p$
S-3	10^6	6	0.1	0.05	1.89×10^{-3}
				0.1	1.33
				0.3	0.77
				0.5	0.59
	10^6	6	0.2	0.05	2.47
				0.1	1.74
				0.3	1.03
				0.5	0.90
	10^6	10	0.1	0.05	2.33
				0.1	1.64
				0.3	0.95
				0.5	0.73
QS-4	10^6	6	0.1	0.05	1.69
				0.1	1.19
				0.3	0.69
				0.5	0.53
	10^6	6	0.2	0.05	2.22
				0.1	1.56
				0.3	0.90
				0.5	0.70
	10^6	10	0.1	0.05	2.77
				0.1	1.95
				0.3	1.21
				0.5	0.87
NC-3	10^6	20	0.1	0.05	5.87
				0.1	4.13
				0.3	2.37
				0.5	1.83

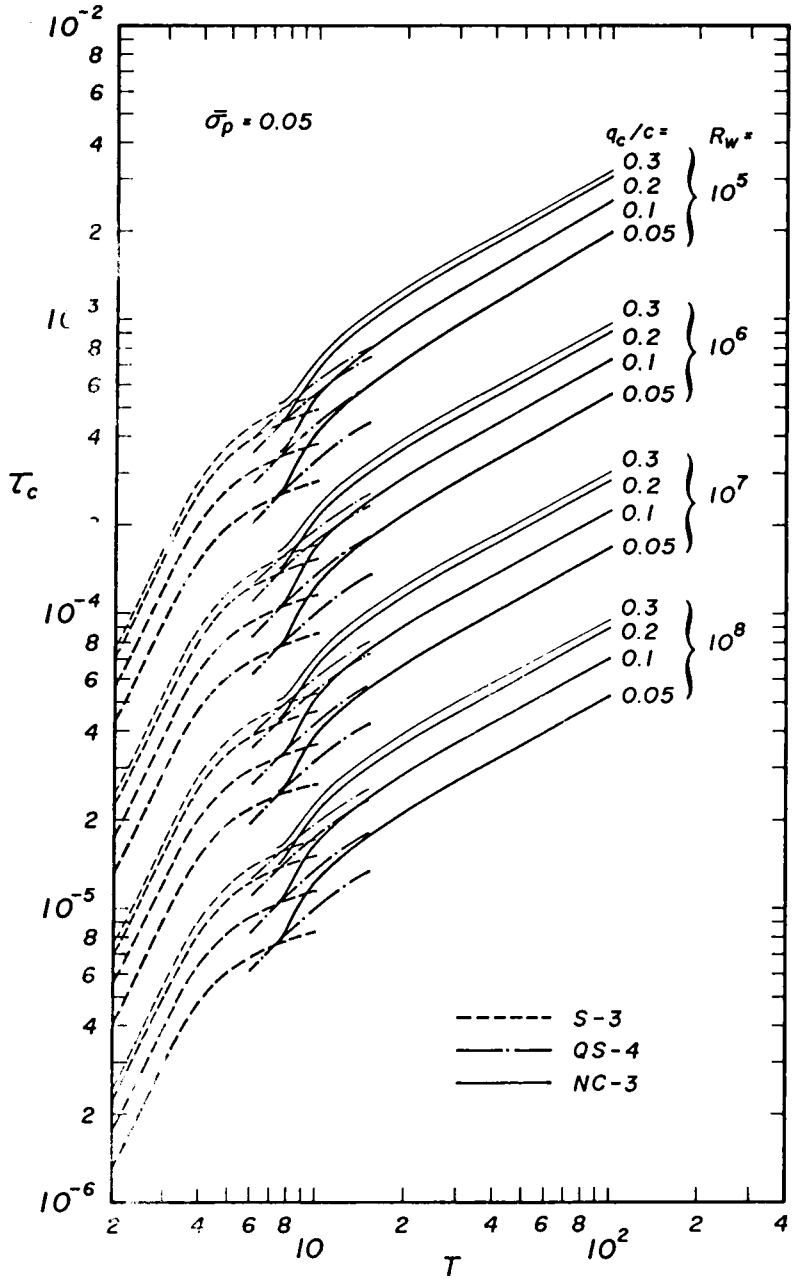

(1) $\bar{\sigma}_p$ = 0.05

Fig. 2.33 Changes in shear stress at the crests of just breaking waves.

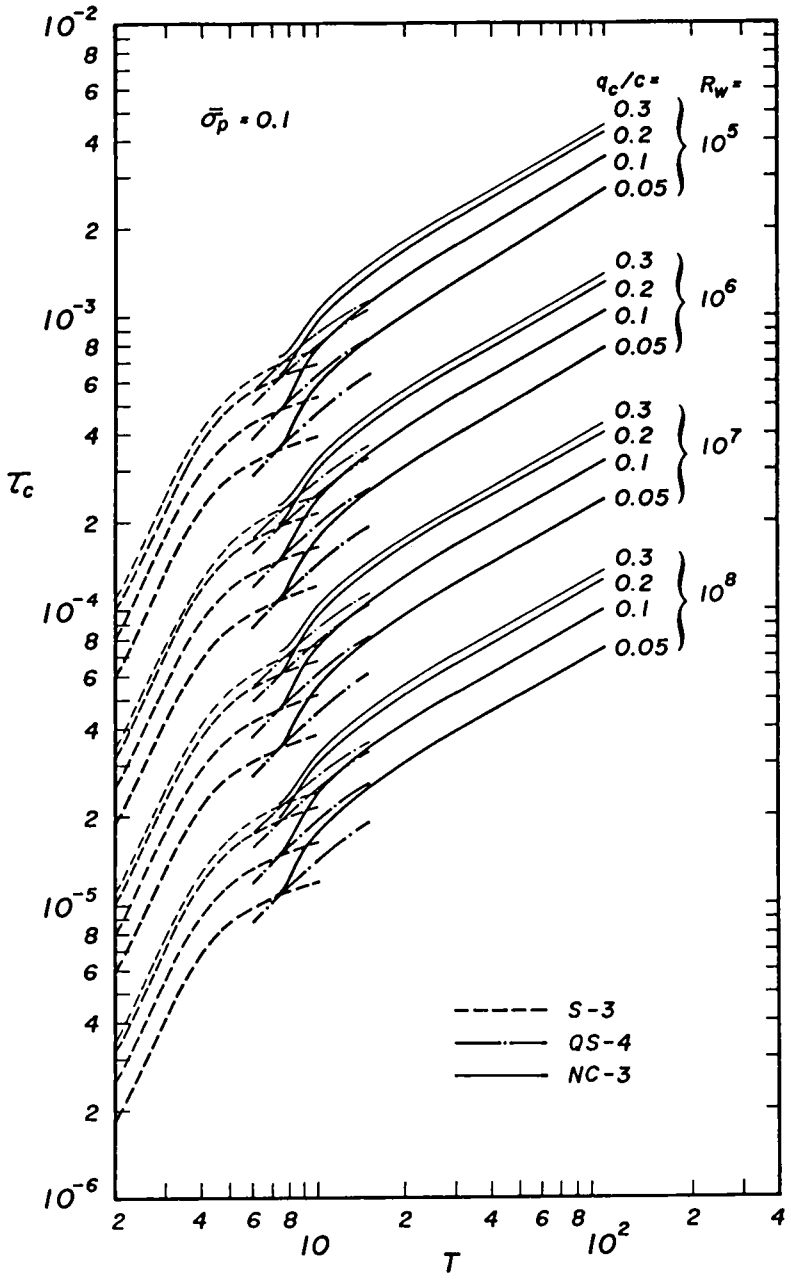

(2) $\bar{\sigma}_p$ = 0.1

Fig. 2.33 Continued.

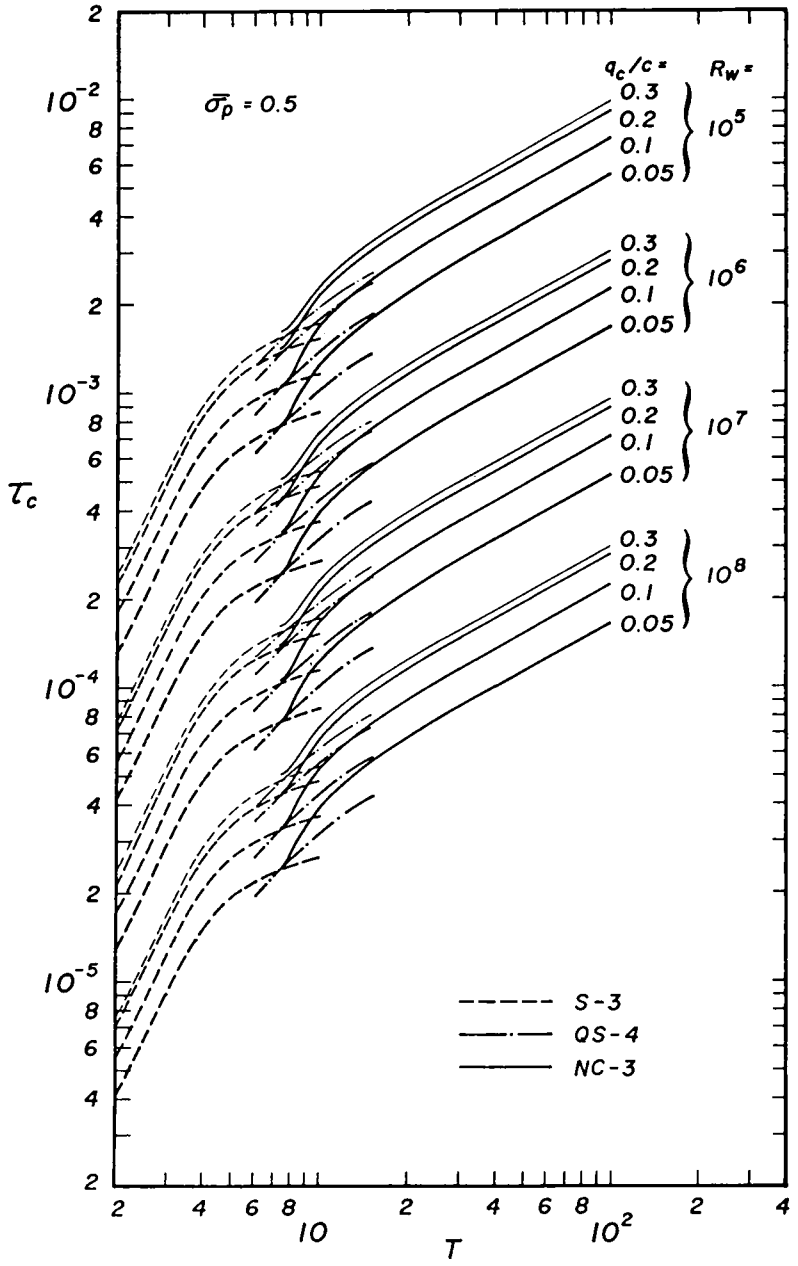

(3) $\bar{\sigma}_p$ = 0.5

Fig. 2.33 Continued.

towards a reversal of the surface drift. This feature has the same general character as if the air flow were separated on the downstream side, thus causing a sheltered region in the usually understood sense.

Fig. 2.33 shows the changes in shear stress at the crests of just breaking waves τ_c for various $\bar{\sigma}_p$, q_c/c, and R_w. The shear stress increases monotonically with respect to the wave period because the required surface drift q_c is greater than that for smaller wave periods. It is clear from

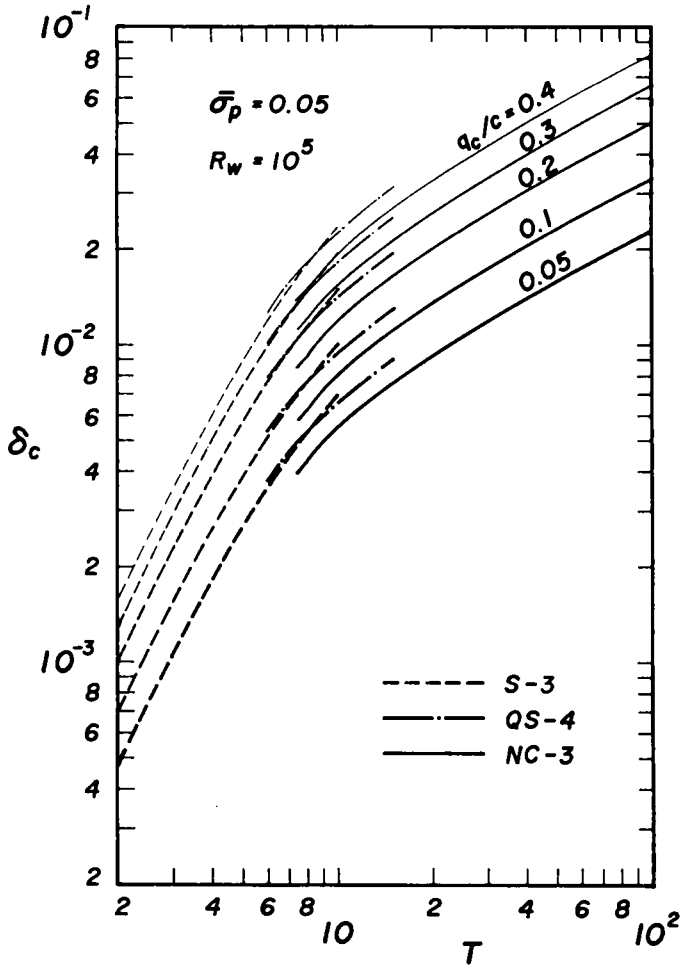

(1) $\bar{\sigma}_p$ = 0.05

Fig. 2.34 Changes in drift layer thickness at the crests of just breaking waves.

Eq. (2.168) that the shear stress varies in proportion to $R_w^{-1/2}$ and the term in the order of R_w^{-1} has little effect on the stress distribution, so these curves are nearly identical. Judging from the fact that the drag coefficient is of the order of 10^{-3}, the values for the shear stress in the figure are physically reasonable ones.

Changes in drift layer thickness at the crests of just breaking waves δ_c are shown in Fig. 2.34. This thickness is also proportinal to $R_w^{-1/2}$,

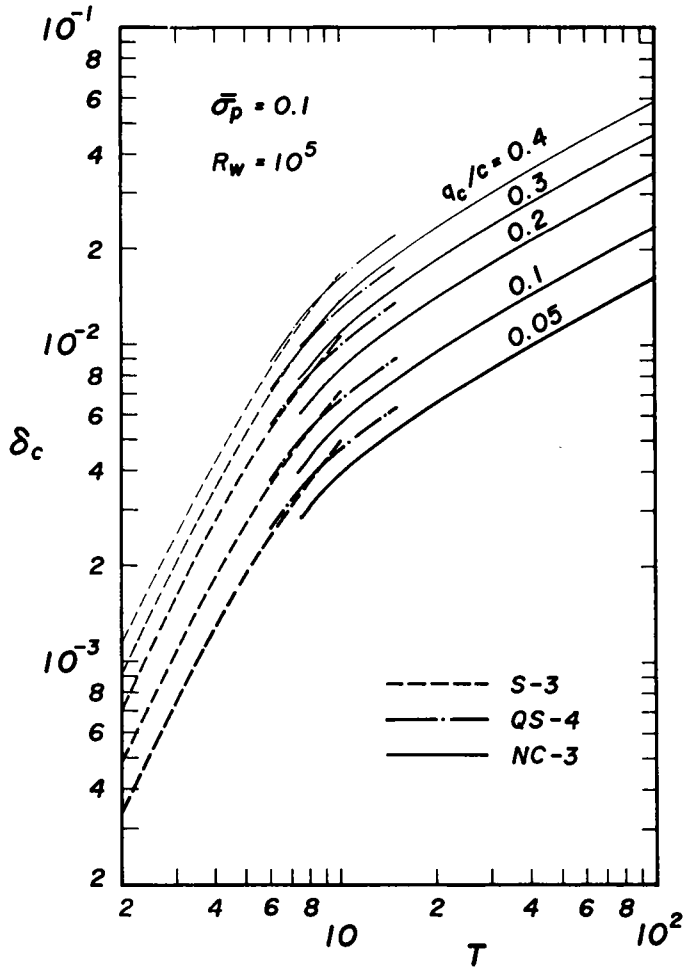

(2) $\bar{\sigma}_p = 0.1$

Fig. 2.34 Continued.

thus only the curves for $R_w = 10^5$ are presented. For a given q_c/c, the greater the wave period and the smaller the pressure, the thicker the drift layer. The displacement thickness is about one-third of the drift layer thickness, as given by Eq. (2.166).

Finally, let it be noted that the applicability of the distribution model for surface drift is dependent upon the evaluation of the pressure exerting on waves.

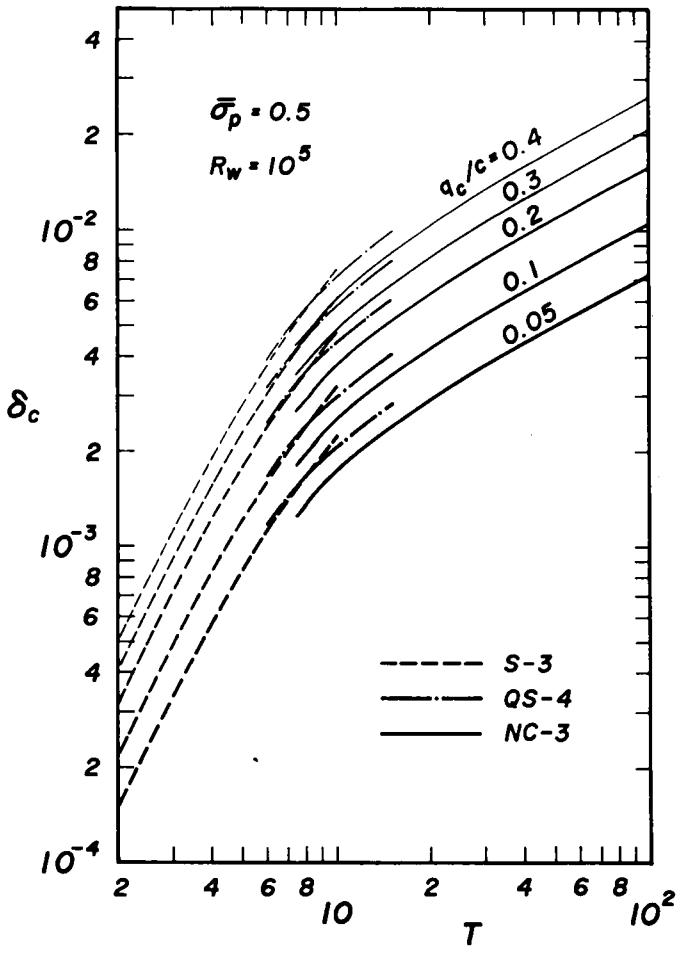

(3) $\bar{\sigma}_p = 0.5$

Fig. 2.34 Continued.

2.5 Conclusion

This chapter has dealt with two types of breaking conditions. The first is wave breaking of irrotational motion without wind effects and the second is that in the presence of wind-induced surface drift.

First, a breaking model for progressive waves of permanent type has been presented, which is capable of showing both non-breaking waves with rounded crests and breaking waves whose crests are angled rather than rounded. The derivation of the model and chief resultant properties are summarized below:

The wave equation, expressed by only the water surface displacement, can be derived from the usual basic equations for irrotational motion, based on the reductive perturbation method. The dynamical system here is for the potential field, thus the system can also be transformed into the Hamiltonian system through the variational principle. The Hamiltonian is found to be an approximate solution of the basic equations and is, in essence, a cubic function consisting of three parameters. There is, in addition, a singular point in the solution which corresponds to the wave crest at just breaking and, therefore, has an important role for wave breaking; the usual perturbation procedure, on the contrary, loses this singularity because of the quasi-linearization of the governing equations, then the solution has no possibility of being a breaking model. Since the Hamiltonian is regarded as a Taylor approximation of the solution near the stationary point for the variational principle and, therefore, contains topologically significant properties, the Hamiltonian should be converted into a form of the elliptic umbilic-type suitable for a breaking model, based on the catastrophe theory.

When waves break, wave crests cease to be rounded, becoming crested, and the so-called Rankine-Stokes breaking condition may hold. The maximum

wave height and wave velocity generated by the model agree well with those found by Byatt-Smith, Fenton, and others. The breaking wave heights for periodic waves are slightly smaller than those based on the Stokes, Quasi-Stokes, and cnoidal wave theories, but the breaking inception is in accordance with that found by Miche, Shuto, and those based on the Quasi-Stokes and cnoidal wave theories. However, the breaking angle of the solitary wave is about 100.4°, which is less than Stokes' angle of 120°, thus the wave profiles given by the breaking model are generally slimmer than those in other theoretical discussions and the wave velocities for small wave periods are greater.

Secondly, wind stresses exerting on waves produce additional velocity near the wave surface, that is, surface drift. To investigate the wind stresses at just breaking, shear stress and pressure, the normal distribution of surface drift has been formulated based on intrinsic equations, in the orthogonal curvilinear coordinate system along the stream line, derived from the Navier-Stokes equations of motion with boundary layer approximations. Following characteristics of wave breaking in the presence of surface drift have been found.

The shear stress and drift layer thickness, which are proportional to the inverse of the square root of the Reynolds number as is usual in the boundary layer theory, increase monotonically with the decrease in water depth. The displacement thickness at the wave crest is about one-third of the drift layer thickness. The shear stress and surface drift distribute with respect to the phase of waves as if the leeward side of the wave crest were sheltered. When the shear stress is reasonably great in comparison with the pressure, there occurs the reversal of the shear stress and surface drift just at the leeward side of the wave crest and they may become negative there. The pressure acts like suction near the wave crest. Thus, a spilling region may be formed, where the water tumbles forward.

References

1) Stokes,G.G.: On the theory of oscillatory waves, Trans. Camb. Phil. Soc., Vol.8, 1847, pp.441-455.
2) Stokes,G.G.: Supplement to a paper on the theory of oscillatory waves. Mathematical and Physical Papers, Vol.1, Camb. Univ. Press, 1880, pp.314-326.
3) Michell,A.G.M.: The highest waves in water, Phil. Mag., Ser.5, Vol.36, 1893, pp.430-437.
4) Luke,J.C.: A variational principle for a fluid with a free surface, Jour. Fluid Mech., Vol.27, 1967, pp.395-397.
5) Korteweg,D.J. and G.deVries: On the change of form of long waves advancing in a rectangular channel, and on a new type of long stationary waves, Phil. Mag., Ser.39, 1895, pp.422-443.
6) Thom,R.: Structural Stability and Morphogenesis, (Trans. by Fowler,D.H. and C.H.Waddington), Benjamin, Massachusetts, 1975, 348p.
7) Banner,M.L. and O.M.Phillips: On the incipient breaking of small scale waves, Jour. Fluid Mech., Vol.65, 1974, pp.647-656.
8) Phillips,O.M. and M.L.Banner: Wave breaking in the presence of wind drift and swell, Jour. Fluid Mech., Vol.66, 1974, pp.625-640.
9) Banner,M.L. and W.K.Melville: On the separation of air flow over water waves, Jour. Fluid Mech., Vol.77, 1976, pp.825-842.
10) Milne-Thomson,L.M.: Theoretical Hydrodynamics, 5th Ed., Macmillan, London, 1968, 743p.
11) Le Mehèuté: Mass transport in cnoidal waves, Jour. Geophys. Res., Vol.73, 1968, pp.5973-5979.
12) Tsuchiya,Y. and T.Yasuda: Quasi-Stokes wave theory by the reductive perturbation method, Proc. 25th Japanese Conf. on Coastal Engrg., JSCE, 1978, pp.6-9(in Japanese).
13) Tsuchiya,Y. and T.Yasuda: A study on the new cnoidal wave theory, Proc. 21th Japanese Conf. on Coastal Engrg., JSCE, 1974, pp.65-71(in Japanese).
14) Gardner.C.S. and G.K.Morikawa: Courant Inst. Math. Soc., Rep. NYO-9082, 1960.
15) Whitham,G.B.: Variational methods and applications to water waves, Proc. Roy. Soc. Lond., A.299, 1967, pp.6-25.
16) Poston,T. and I.N.Stewart: Taylor Expansions and Catastrophes, Pitman, 1976, 168p.
17) Grant,M.A.: The singularity at the crest of a finite amplitude progressive Stokes waves, Jour. Fluid Mech., Vol.59, 1973, pp.257-262.
18) Seliger.R.: A note on breaking waves, Proc. Roy. Soc. Lond., A.303, 1968, pp.493-496.
19) Whitham,G.B.: Linear and Nonlinear Waves, Pure Appl. Math., Wiley - Interscience, 1974, 636p.
20) McCowan,J.: On the highest waves of permanent type, Phil. Mag., Ser.5, Vol.38, 1894, pp.351-358.
21) Yamada,H.: On the highest solitary wave, Rep. Res. Inst. Appl. Mech., Kyushu Univ., Vol.5, 1957, pp.53-67.
22) Lenau,C.W.: The solitary waves of maximum amplitude, Jour. Fluid Mech., Vol.26, 1966, pp.309-320.
23) Byatt-Smith,J.G.S.: An exact integral equation for steady surface waves, Proc. Roy. Soc. Lond., A.315, 1970, pp.405-418.
24) Strelkoff,T.: An exact numerical solution of the solitary wave, Proc. 2nd Int. Conf. on Num. Methods Fluid Dyn., Springer, 1971.
25) Fenton,J.D.: A ninth-order solution for the solitary wave, Jour. Fluid Mech., Vol.53, 1972, pp.257-271.
26) Longuet-Higgins,M.S.: On the mass, momentum, energy and circulation of a solitary wave, Proc. Roy. Soc. Lond., A.337, 1974, pp.1-13.

27) Longuet-Higgins,M.S. and J.D.Fenton: On the mass, momentum, energy and circulation of a solitary wave. II, Proc. Roy. Soc. Lond., A.340, 1974, pp.471-493.
28) Schwartz,L.W.: Computer extension and analytic continuation of Stokes' expansion for gravity waves, Jour. Fluid Mech., Vol.62, 1974, pp.553-578.
29) Cokelet,E.D.: Steep gravity waves in water of arbitrary uniform depth, Proc. Roy. Soc. Lond., A.286, 1977, pp.183-230.
30) Williams,J.M.: Limiting gravity waves in water of finite depth, Phil. Trans. Roy. Soc. Lond., A.302, 1981, pp.139-188.
31) Grimshaw,R.: The solitary wave in water of variable depth. Part 2, Jour. Fluid Mech., Vol.46, 1971, pp.611-622.
32) Skjelbreia,L.: Gravity waves, Stokes' third order approximation, Tables of functions, Council on Wave Reseach, The Engineering Foundation, ASCE, 1959, 337p.
33) Shuto,N.: On finite amplitude waves - Breaking inception of progressive waves based on the higher power series solution, Rep. Public Works Res. Inst., Vol.111, 1961, pp.1-9(in Japanese).
34) Miche,M.: Mouvements ondulatoires de la Mer en profondeur constante ou décroissante, Annales des Ponts et Chaussées, 1944.
35) Dean,R.G.: Stream function representation of nonlinear ocean waves, Jour. Geophys. Res., 1965, pp.4561-4572.
36) Longuet-Higgins,M.S.: Mass transport in the boundary layer at a free oscillating surface, Jour. Fluid Mech., Vol.8, 1960, pp.293-306.
37) Lamb,H.: Hydrodynamics, Cambridge Univ. Press, 6th Ed., London, 1953, 738p.
38) Benjamin,T.B.: Shearing flow over a wavy boundary, Jour. Fluid Mech., Vol.6, 1959, pp.161-205.

CHAPTER 3

EXPERIMENTS ON INTERNAL BREAKING CONDITIONS FOR PROGRESSIVE WAVES OF PERMANENT TYPE

3.1 Introduction

Observing waves from a beach, one sees waves pushing sand as they advance, and then the sand is thrown ahead simultaneously with breaking. After breaking, the waves flow up on the beach. What happens as a wave breaks?

Various breaking conditions have been proposed, for example, the so-called Rankine-Stokes breaking condition[1] with a cuspidal crest angle of 120° and the breaker index[2]. The former deals with local conditions relating to the breaking phenomena, and the latter is usually obtained by experiments to determine breaking conditions, so that it may well be impossible to describe the whole history of a beaking wave; there may exist breaking conditions subject not only to the local breaking conditions but also to the internal breaking conditions. However, if some of the internal properties of a wave can be evaluated, it may be possible to discuss the internal characteristics of the wave train.

There are some physical quantities, such as potential and kinetic energies, mass flux, energy flux, and radiation stresses, which are properties of the wave train that have been completely defined, and several relations between these integral properties[3),4),5)] have been explained.

In this chapter, experimental investigations on wave breaking are presented, and fundamental phenomena occurring in breaking waves are discussed to propose an internal breaking condition based on the instabil-

ity of waves. Section 3.2 describes an experiment on wave breaking, where the breaking waves are generated in such a wav that the mass flux accompanied by progressive waves is not restrained by the endwalls of the wave tank. Characteristics of the shoaling waves, such as changes in wave profile, in wave height, and in wave length, are shown in comparison with theoretical estimations. Section 3.3 discusses some of the usual breaking conditions. The mass transport induced by breaking waves is investigated in Section 3.4, where the behaviour of water particles is observed by simulations using tracers, and the resultant motion of water particles near the breaking point is found to be very active.

Section 3.5 sets out the formulation of an internal breaking mechanism and discusses the mechanism in comparison with experimental results. Partition laws of wave energies are derived based on the conservation law of energy flux(energy flux method). The radiation stress and wave set-down are also investigated. The radiation stress, defined as the excess momentum flux of waves, gradually increases with the decrease in water depth and leads to a depression of the mean water level in front of the breaking point, that is, the wave set-down. This phenomenon may strongly affect on wave breaking. Nevertheless, only a formula for the wave set-down[6] derived from the Stokes wave theory has been proposed. Therefore, it is neccesary to develop a formula for the wave set-down applicable in shallower regions. Formulae are derived based on the balance of the momentum flux of waves with use of shallow water wave theories. The ever-changing potential energy, which is the only single property directly measurable by experiments, can be estimated. Changes in the potential and kinetic energies of shoaling waves are discussed in reference to the imbalance of the partition rate of these two energies to investigate phenomena which may occur in just-breaking waves. By the comparison of experimental and theoretical results, the essential point of difference is considered with the conclu-

sion that there possibly exists an internal breaking condition, as mentioned before.

In Section 3.6 the preceding characters related to the internal breaking conditions are summarized.

3.2 Experiments on Wave Breaking

(1) Experimental Apparatus and Procedures

a. Wave tank

If physical properties in breaking waves abruptly change, it may be impossible to measure breaking properties, such as water particle velocities near the wave surface and wave profiles. Furthermore, it is also well-known that a wave of breaker-type, which can be discussed based on the shallow water wave theory, is a so-called spilling breaker forming on water of gradually varying depth. It is, therefore, convenient in an experiment that the gradient of a slope be as mild as possible. In the present work it was set at 1/150.

The wave tank is a double-deck type as illustrated in **Fig. 3.1**, belonging to the Ujigawa Hydraulic Laboratory, Disaster Prevention Research Institute, Kyoto University. The slope is located in the middle portion of the wave tank. Water depths at the front and rear sides of the slope are fixed, the latter having been determined so that waves should break at the end of the slope. The mass flux accompanied by waves returns to the wave generator-side through a circulating duct between the upper and lower decks. By using this apparatus, the mass transport of waves is not constrained by the endwalls of the wave tank; furthermore, the breaking properties, such as breaking points, wave heights, and wave profiles, remain steady. This wave tank can, then, be used to properly carry out the purpose

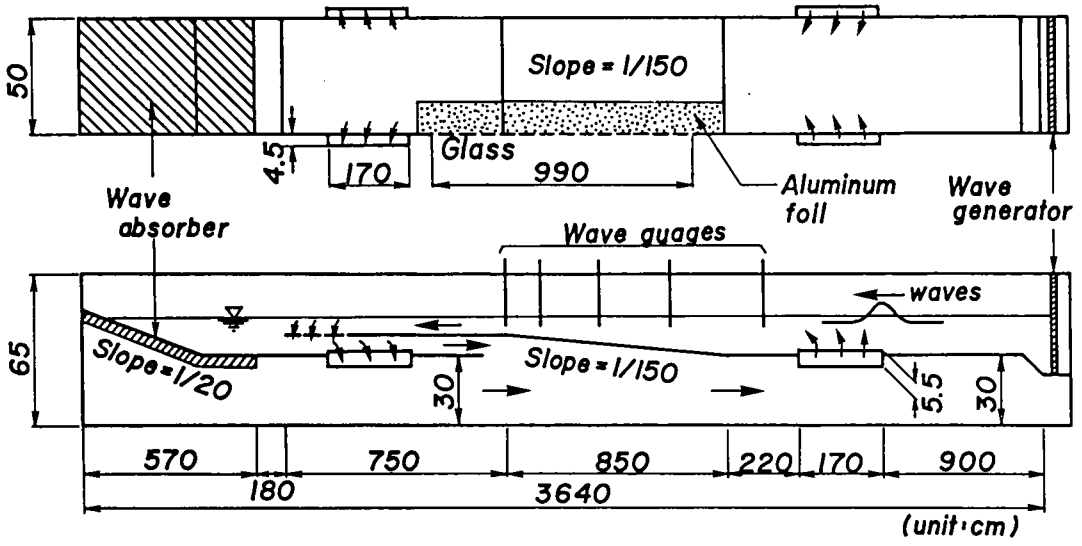

Fig. 3.1 Wave tank of double-deck type.

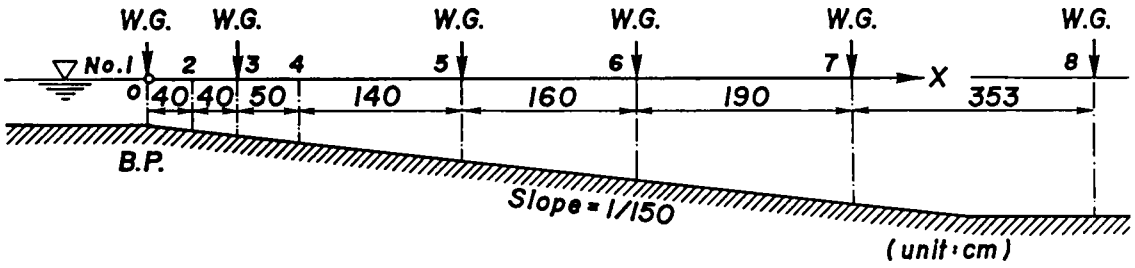

Fig. 3.2 Measuring points.

of the present study.

There is a glass observatinal window on one side of the wave tank with 2 cm high and 4 cm long meshes. These meshes were used as the base line for measurements of the water surface displacements on photographs.

b. Measurements of breaking properties

i) Steadiness of wave properties

Wave gauges were set up at six locations in the wave tank as shown in Fig. 3.2, and wave records were continuously taken from the beginning of

wave generation. Steadiness was confirmed from the wave records by checking that wave heights were uniform at measured points and that harmonic changes in wave height did not appear at the breaking point. Changes in wave height within 2 mm at the breaking point, however, were considered allowable. Measurements were taken one hour after wave generation began in all runs.

ii) **Wave profiles in time and in space**

Wave profiles in time were measured by wave gauges set up in the wave tank as illustrated in **Fig. 3.2**, and wave profiles in space were measured by the photographical method as illustrated in **Fig. 3.3**. A motor-driven carriage is set up about 3 m away from the observation window, parallel to the axis of the wave tank. This carriage moves at a constant speed, nearly equal to the measured mean wave velocity. Photographs of wave profiles over the slope are taken with a 35 mm camera(3 frames per second) through the glass. This procedure was carried out three times during each run. The negatives were magnified to life-size projected on a screen and the water surface displacements were measured at 1 cm intervals near the wave crests and 2 cm intervals near the wave troughs.

A simple device was used to make these photographs sharper, as shown in Fig. 3.3. A 10 cm strip of aluminum foil is pasted to the bottom of the

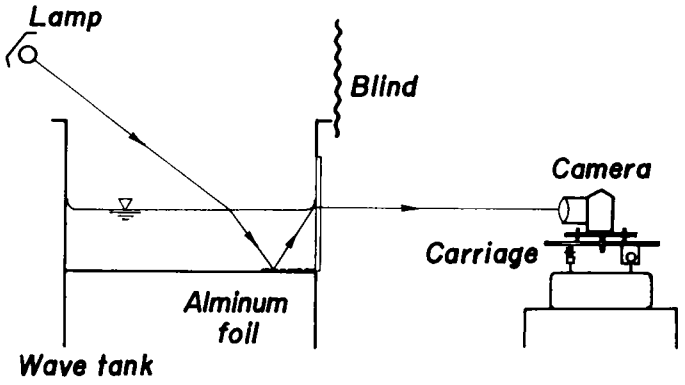

Fig. 3.3 Photographical method for wave profiles in space.

wave tank to reflect the light from above. This reflected light is again scattered by the meniscus on the glass and caught by the camera on the carriage.

iii) Wave length

A wave length was defined as the distance between two adjacent wave crests of wave profiles in space.

iv) Wave set-down

Depression of the mean water level, that is, wave set-down defined as the difference between the still and mean water levels, was measured from wave profiles in space.

v) Water particle velocity

The tracer method using neutrally buoyancy particles was adopted for measurements of trajectories of water particles under the still water level. The neutrally buoyancy particles used were made of white polystyrene(1.72 mm in mean diameter and 1.093 in specific weight), which were heated to be a specific weight of very close to 1, and those suitable for remaining neutrally in water for a long time were selected. The photographical method used is illustrated in **Fig. 3.4(1)**. Neutrally buoyancy particles are added to the water through a syringe at measuring points, taking scrupulous care not to disturb the water. Particles in the light(3-4 cm in width) from an ellispotlight are caught in the middle portion of the lense of the 35 mm camera, possibly decreasing aberration. The particles are photographed together with a scale(10 cm in total length with intervals of 2 cm), the top of the scale being set up at the still water level to determine the base line for the vertical coordinate.

Behaviour of water particles on the wave surface were measured photo-

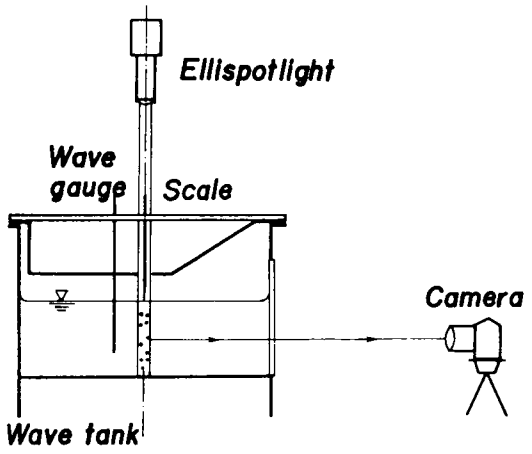

(1) Neutrally buoyancy particles under the still water level

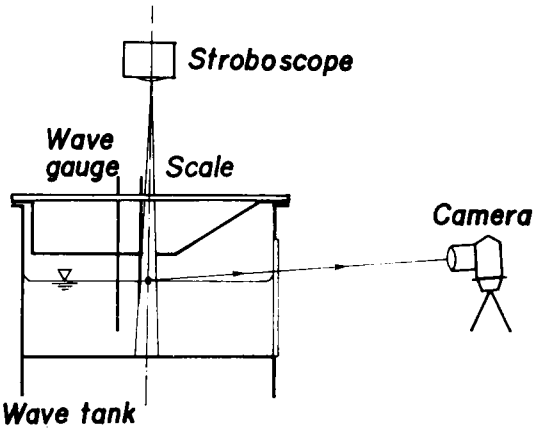

(2) Floats on the wave surface

Fig. 3.4 Photographical method for water particle velocities.

Table 3.1 Experimental conditions at the breaking point.

Run	T(sec)	h_b(cm)	$T\sqrt{g/h_b}$	H_b/h_b
1	1.00	5.12	13.8	0.734
2	1.40	5.06	19.5	0.734
3	0.79	4.97	11.2	0.684

graphically with a stroboscope as illustrated in **Fig. 3.4(2)** using floats of styro-foam(about 3 mm in diameter) as the tracer. And, for both measurements, a wave gauge was set up at the same place to measure wave profiles in time.

Negatives were magnified to about double and projected on a screen, and the mass transport velocity was defined as the ratio of horizontal distance to wave period, in which the distance was that from one vertical tangent for a trajectory to the next. In measuring the distance, trajectories of neutrally buoyancy particles were selected such that they moved nearly horizontally over several wave periods and were within ± 5 cm from the each measuring point.

The experimental conditions at the breaking point are given in **Table 3.1**, where T is the wave period, H the wave height, h the water depth, and g the acceleration of gravity. The subscript b denotes quantities at the breaking point.

(2) Wave Properties over a Mild Slope

In this section, properties of breaking waves, such as changes in wave profiles in time and in space, in wave length, and in wave height due to the wave shoaling, are shown in comparison with theoretically evaluated ones. Theories adopted are the Stokes wave theory of third order approximation (**S-3**)[7] based on the Stokes first definition for the wave velocity, the Quasi-Stokes wave theory(**QS-4**)[8], and the cnoidal wave theory(**NC-3**)[9], the last two being derived by the reductive perturbation method.

a. Wave profiles in time

Fig. 3.5 shows comparisons of the experimental wave profiles in time with theoretical ones, where x is the distance from the breaking point, and

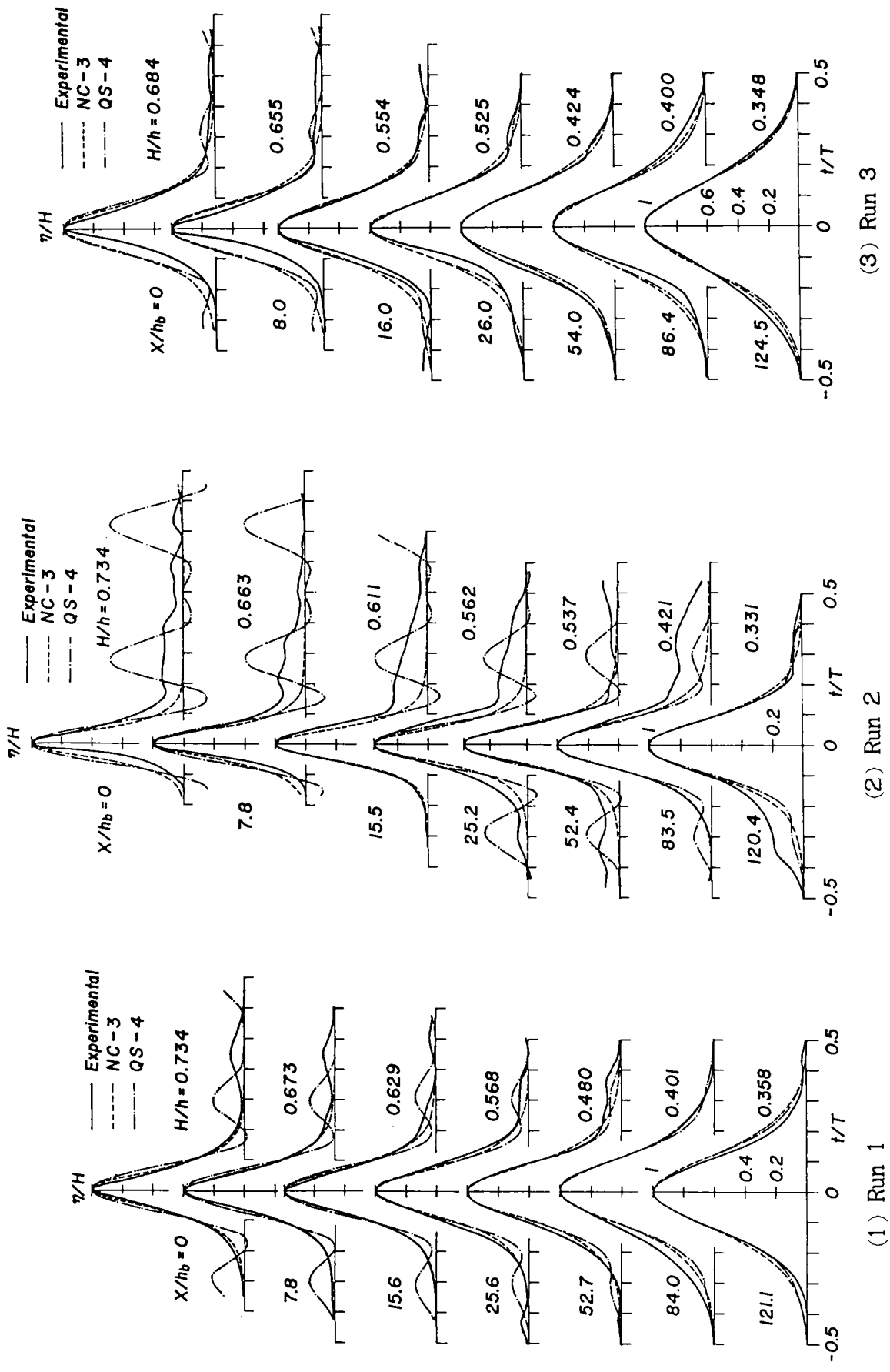

Fig. 3.5 Comparison of experimental wave profiles in time with theoretical ones.

η the water surface displacement. In the figure, experimental and theoretical wave crests are arranged in phase to draw attention to characteristics of the changes in wave profile. Thus, the coordinate origin is taken at the end point of the slope for the convenience of comparison of experimental and theoretical results.

In Run 1, wave profiles near the wave crest are roughly symmetric at all measured points and become steep near the breaking point. A weak secondary wave is seen at x/h_b = 52.7 in the phase of the main wave trough and it grows with shoaling. In Run 2, a secondary wave has already occurred in the offshore region x/h_b = 120.4. This wave is outrun by the main wave approaching the breaking point. This phenomenon is chiefly due to the nonlinearity of waves in the shoaling process as also seen in Run 1. Representative asymmetry of wave profiles near the breaking point is seen in Run 3, where the occurrence of the secondary wave is not as conspicuous compared with the others, and the development of the shoaling wave into the breaking wave is clearly shown. Reasonable agreement of wave profiles in the offshore region is presented, but the theories cannot simulate the steep wave profiles near the breaking points.

b. Wave profiles in space

Secondary waves apparently occurred in Run 2, which cannot be simulated theoretically as mentioned above. Thus, wave profiles in space except for those in Run 2 are now discussed. Physical quantities of the first wave for Runs 1 and 3 over the slope are given in **Table 3.2**, where L is the wave length and the subscript o denotes quantities of corresponding deep water waves. An example of wave profiles in space is presented in **Photo. 3.1**, and **Fig. 3.6** shows representative wave profiles in space measured with these photographs for Runs 1 and 3, where x' is the distance when the coordinate origin is taken in phase with the wave crest. The curves are theoretical

Table 3.2 Physical quantities of incident waves in space.

Run	$T\sqrt{g/h}$	H/h	h/L_0	H_0/L_0	Adopted theories
1-1	10.3	0.313	0.0589	0.0182	
1-2	10.3	0.300	0.0596	0.0181	QS-4
1-3	10.3	0.323	0.0594	0.0189	
3-1	8.15	0.295	0.0938	0.0293	
3-2	8.08	0.312	0.0954	0.0315	S-3
3-3	8.26	0.293	0.0914	0.0283	

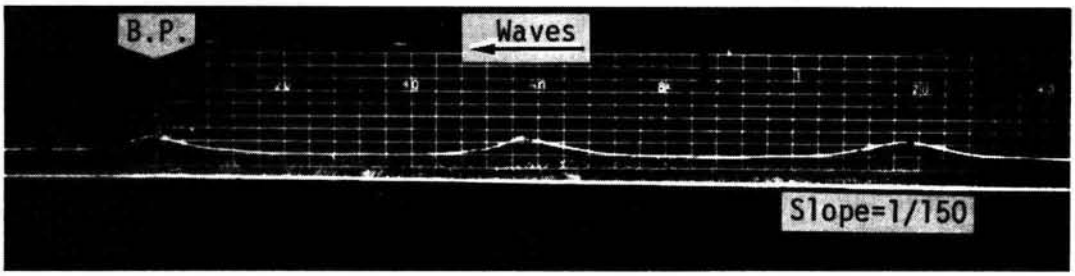

Photo. 3.1 Example of wave profiles in space (Run 3).

ones based on the energy flux method.

Wave profiles near the wave crests in Run 1 are roughly symmetric in the deeper region and conserve this symmetry even in the shallower region, but the symmetry of wave profiles is slightly marred at the breaking point. Run 3 shows typical wave profiles which are symmetric in the offshore region but become asymmetric due to the wave shoaling. In both these runs, the theoretical wave profiles are in accordance with experimental ones in the offshore region. However, it is remarkable that the asymmetric waves near the breaking point cannot be simulated theoretically even on the sufficiently mild slope of 1/150.

In the previous studies on wave breaking, wave profiles in time have frequently been adopted as the experimental wave profiles. but wave profiles in time and in space may differ. Therefore, it is important for the

clarification of the breaking phenomenon that these two wave profiles be compared. **Fig. 3.7** shows examples of wave profiles in time and in space for Runs 1 and 3, where the measured points x/h_b are nearly equal. Two values of x/h_b and H/h are given in the figure. Values in parentheses are those corresponding to wave profiles in space. In these runs, the asymmetry of wave profiles in space is more remarkable than those in time. It is, however, necessary to investigate this relation more in detail.

c. Changes in wave length

Changes in wave length over the slope are shown in **Fig. 3.8.** The heavy line in each figure is the experimental curve, and the lighter solid and broken lines are theoretical ones based on the energy flux method. These broken and solid lines show, respectively, wave lengths evaluated by the adoption of the wave height of the first wave in space over the slope and by that of the wave height in time at the measuring point 5. There are differences in the theoretical curves because of the discrepancy in these incident wave heights.

Experimental wave lengths in Runs 1 and 3 agree well with theoretical ones in the deeper region, and the former becomes slightly shorter than the latter with the decrease in water depth. The measurement errors in wave length are within about 5 %. In Run 2, there exist differences between these results; the reason is basically due to the occurrence of secondary waves as shown out in **Fig 3.5.**

Fig. 3.9 shows the changes in wave length for the particular waves given in **Table 3.2.** In both Runs 1 and 3, measured wave lengths are shorter than theoretical ones near the breaking point, but the experimental tendency of the changes in wave length due to the decrease in water depth is very similar to the theoretical tendency.

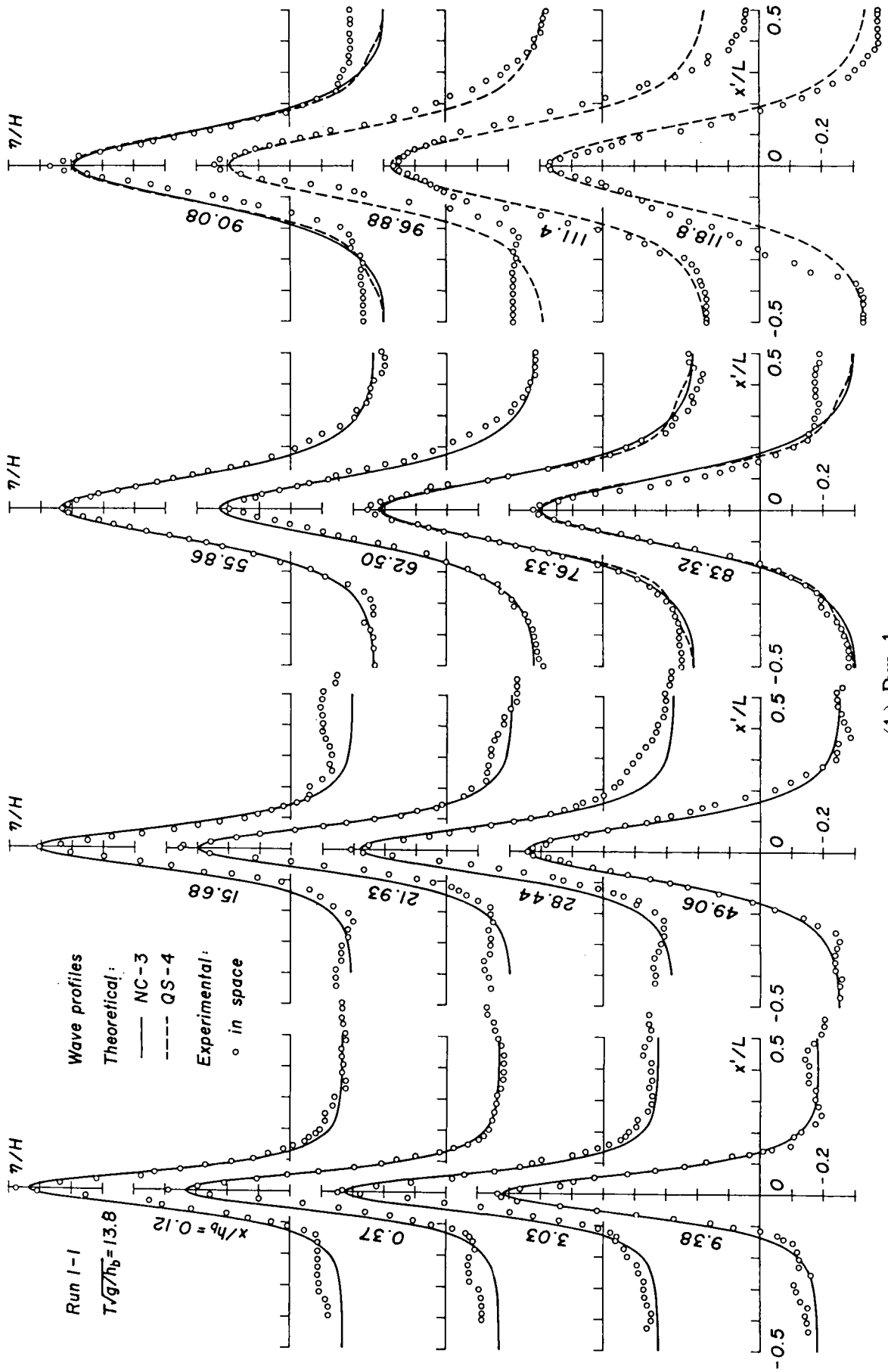

(1) Run 1

Fig. 3.6 Comparison of experimental wave profiles in space with theoretical ones.

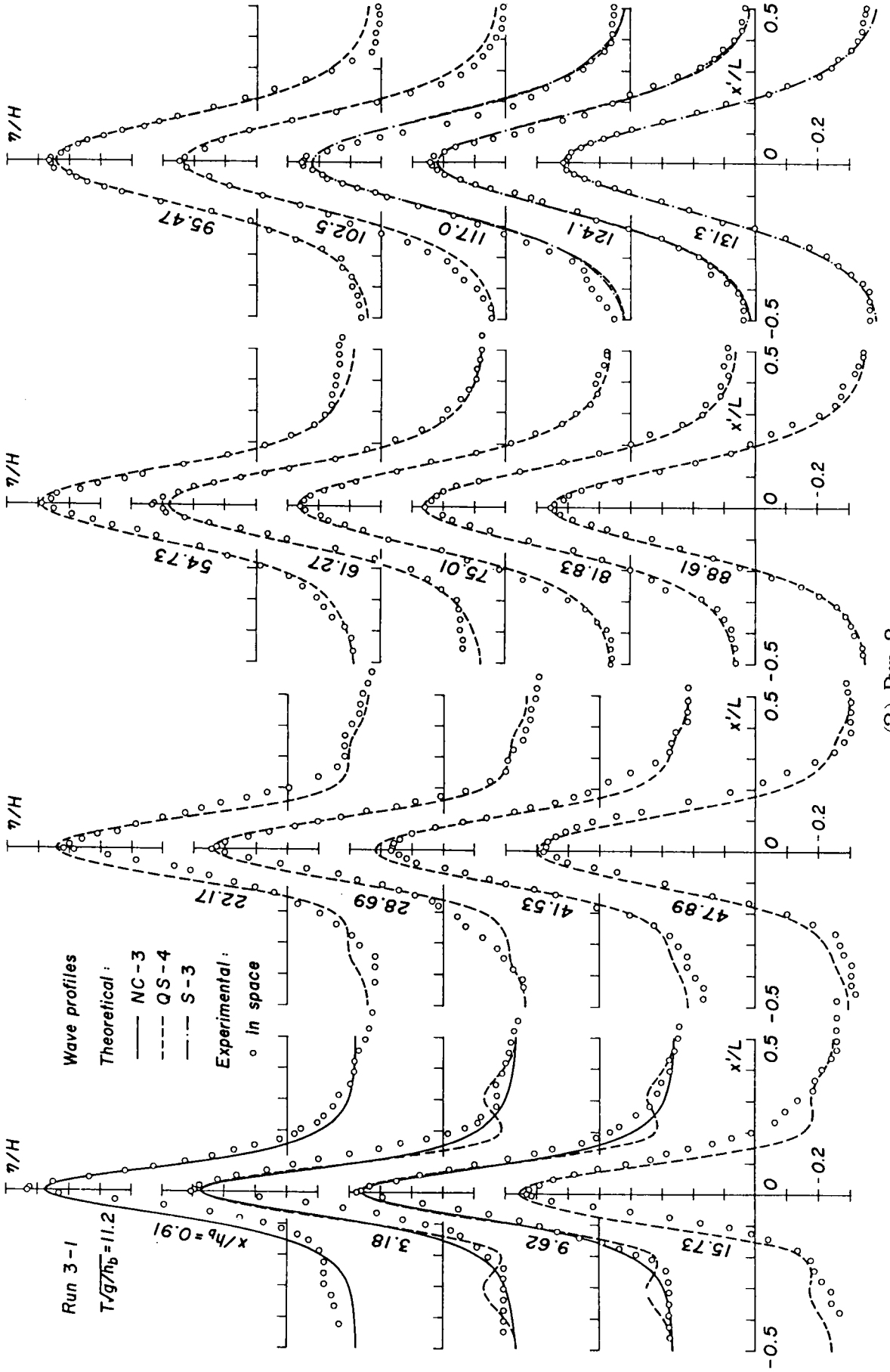

(2) Run 3

Fig. 3.6 Continued.

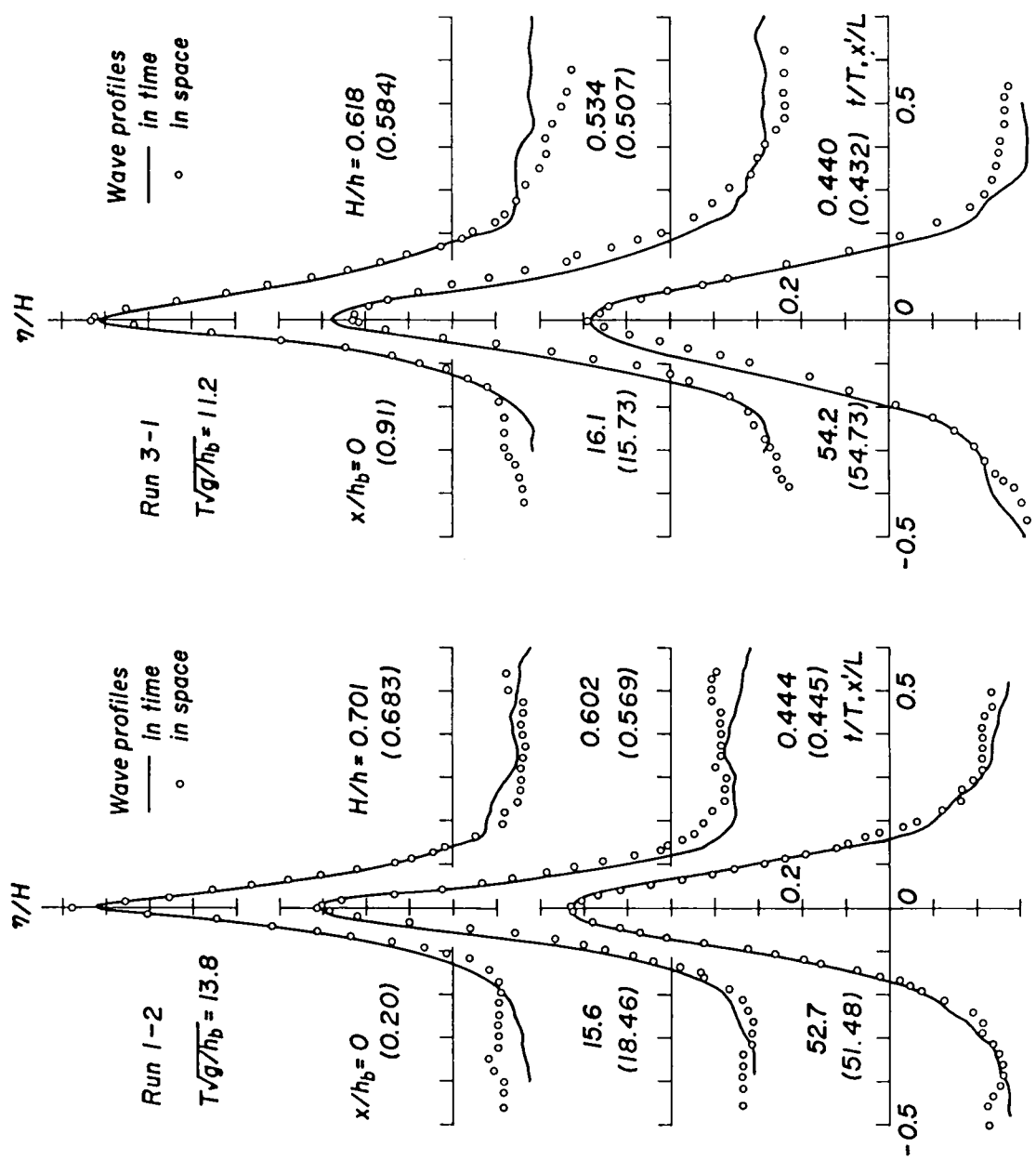

(1) Run 1 (2) Run 3

Fig. 3.7 Comparison of wave profiles in space and in time.

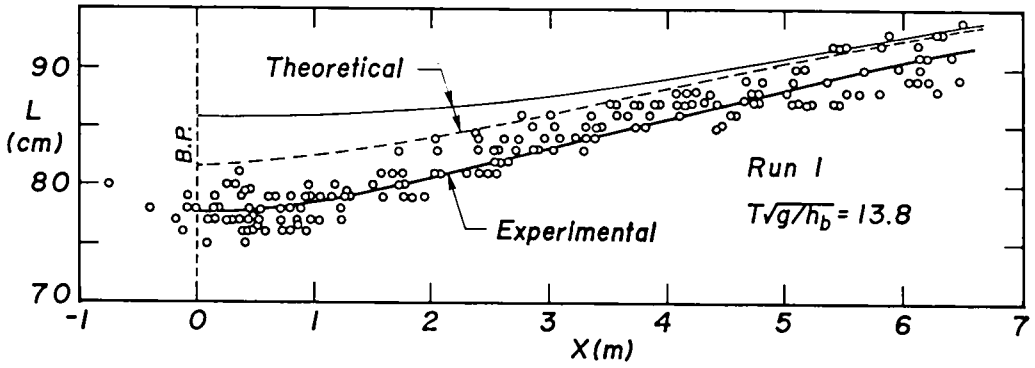

(1) Run 1

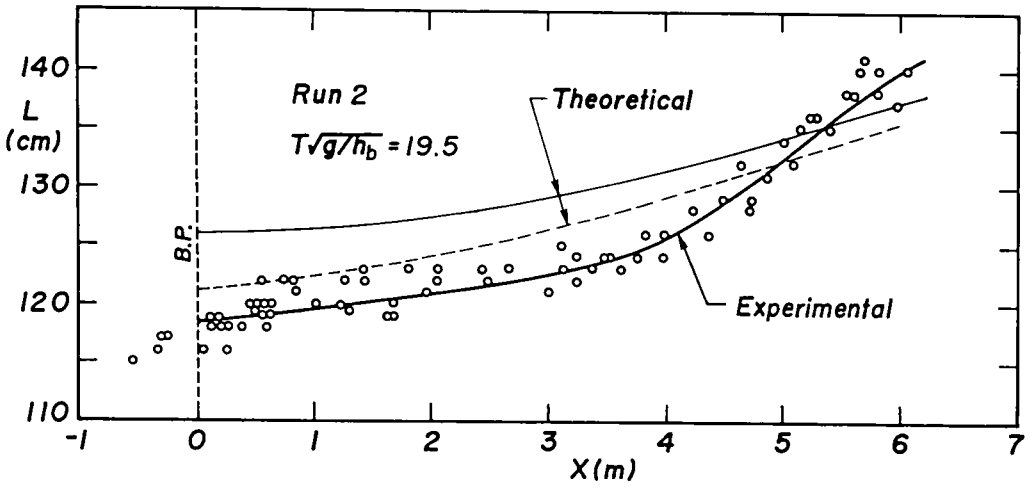

(2) Run 2

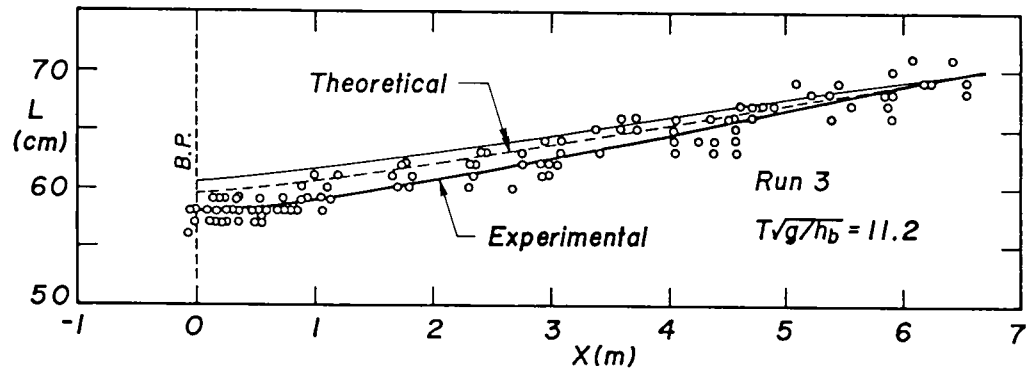

(3) Run 3

Fig. 3.8 Changes in wave length of shoaling waves.

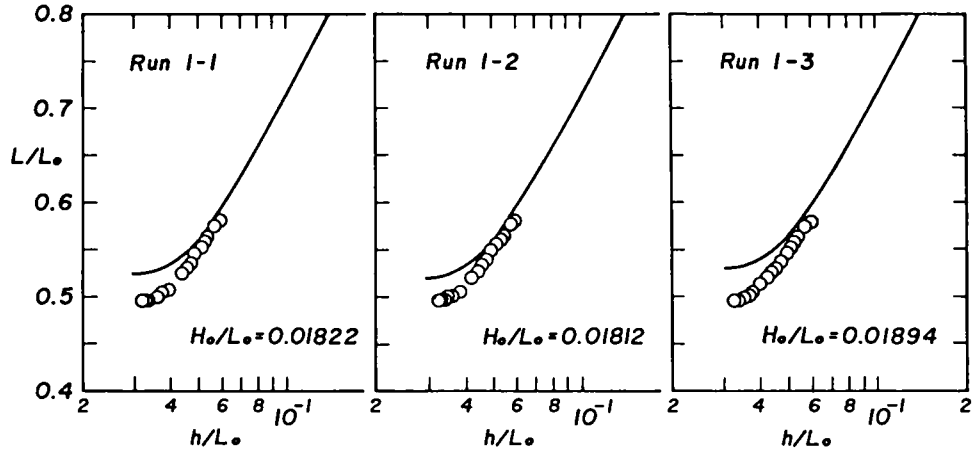

(1) Run 1

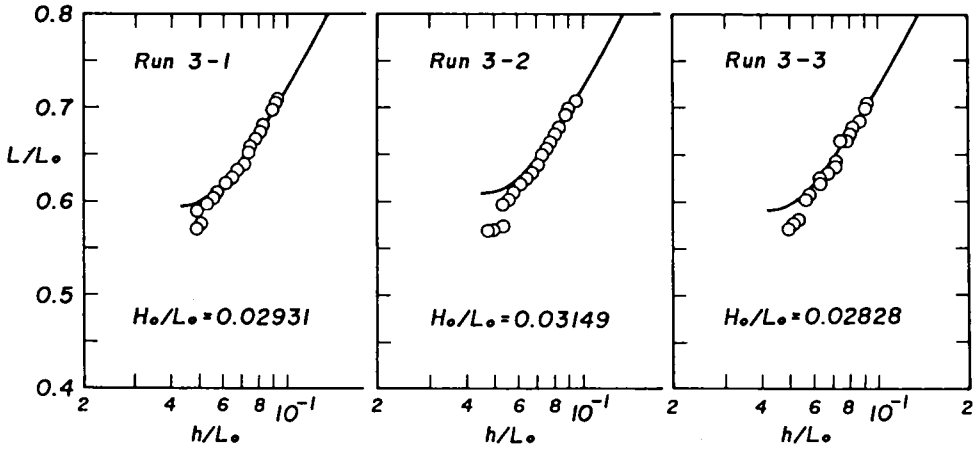

(2) Run 3

Fig. 3.9 Changes in wave length of particular waves given in Table 3.2.

d. Changes in wave height

Fig. 3.10 shows the changes in wave height over the slope, which were obtained from wave profiles in time at each measuring point. The curves in the figure are theoretical ones based on the energy flux method using wave heights at point 5 as incident waves. In all runs, wave heights in the offshore region are slightly depressed because of bottom friction, thus experimental wave heights are smaller than theoretically estimated ones, but these results agree fairly well over the whole range of h/L_0.

Changes in wave height for the particular waves in space, given in

Table 3.2, are also shown in **Fig. 3.11** together with theoretical curves drawn by solid lines, where solid circles denote wave heights obtained from wave profiles in time, the broken lines show the corresponding theoretical curves, and the steepness of deep water waves is given in parentheses. Apart from some slight irregularity in wave height, experimental wave heights coincide with theoretical ones in the offshore region in both Runs 1 and 3, the former being slightly smaller than the latter near the breaking point. This is nearly the same tendency as in the changes in wave length. The chief cause of this irregularity of wave height in space may be due to the photographical measurement error for wave profiles. Seen from an observational point, as waves approach the breaking point, wave crests become steep and the dynamical condition near the wave crests on the glass window is similar to that of wave fronts propagating over a dry-bed. Therefore, these phenomena occasionally occur near the breaking point, where pictures taken very close to the wave crests lack clarity.

e. Changes in steepness

Fig. 3.12 shows the relation between the wave height and wave length for the waves given in **Table 3.2**. As shown above in **Figs. 3.9** and **3.11**, experimental wave lengths and wave heights are both slightly smaller than theoretical ones near the breaking point. Nevertheless, these experimental values of steepness agree very closely with the theoretical ones over almost the whole range of wave length. Theoretical breaking depths are shallower than the experimental ones as seen in **Fig. 3.12**. However, by the adoption of the representation h/H versus L/h, the influence of discrepancies in breaking depth does not apparently arise, and this is the reason the experimental and theoretical characteristics of the changes in steepness due to the varying depth coincide.

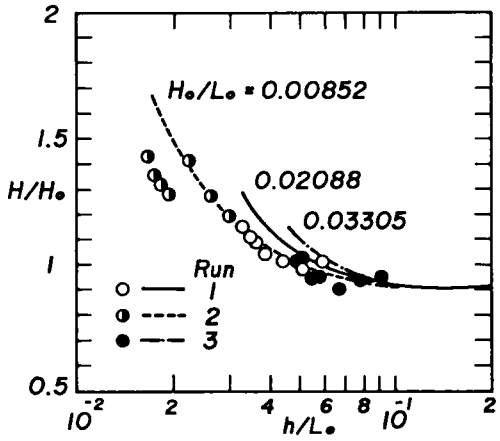

Fig. 3.10 Changes in wave height of shoaling waves, obtained from wave profiles in time.

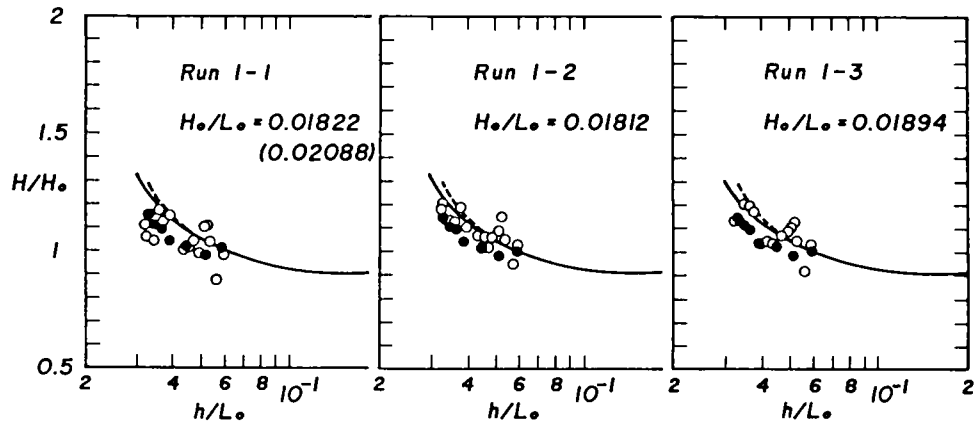

(1) Run 1

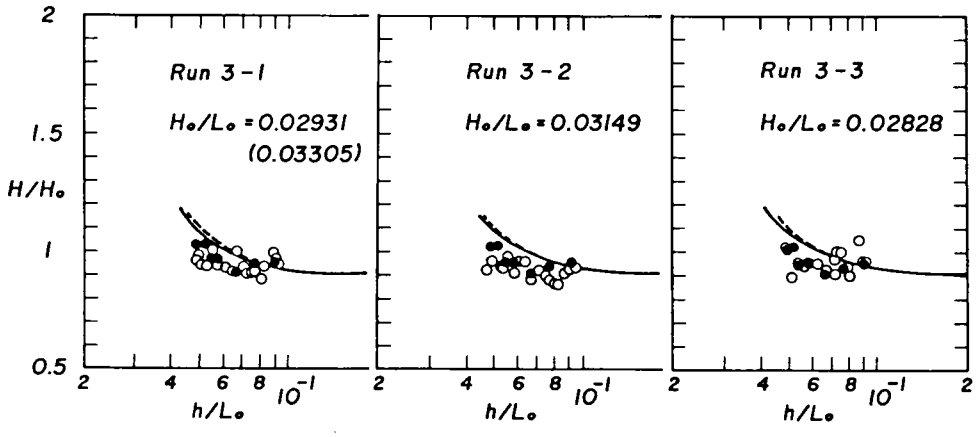

(2) Run 3

Fig. 3.11 Changes in wave height of shoaling waves, obtained from wave profiles in space.

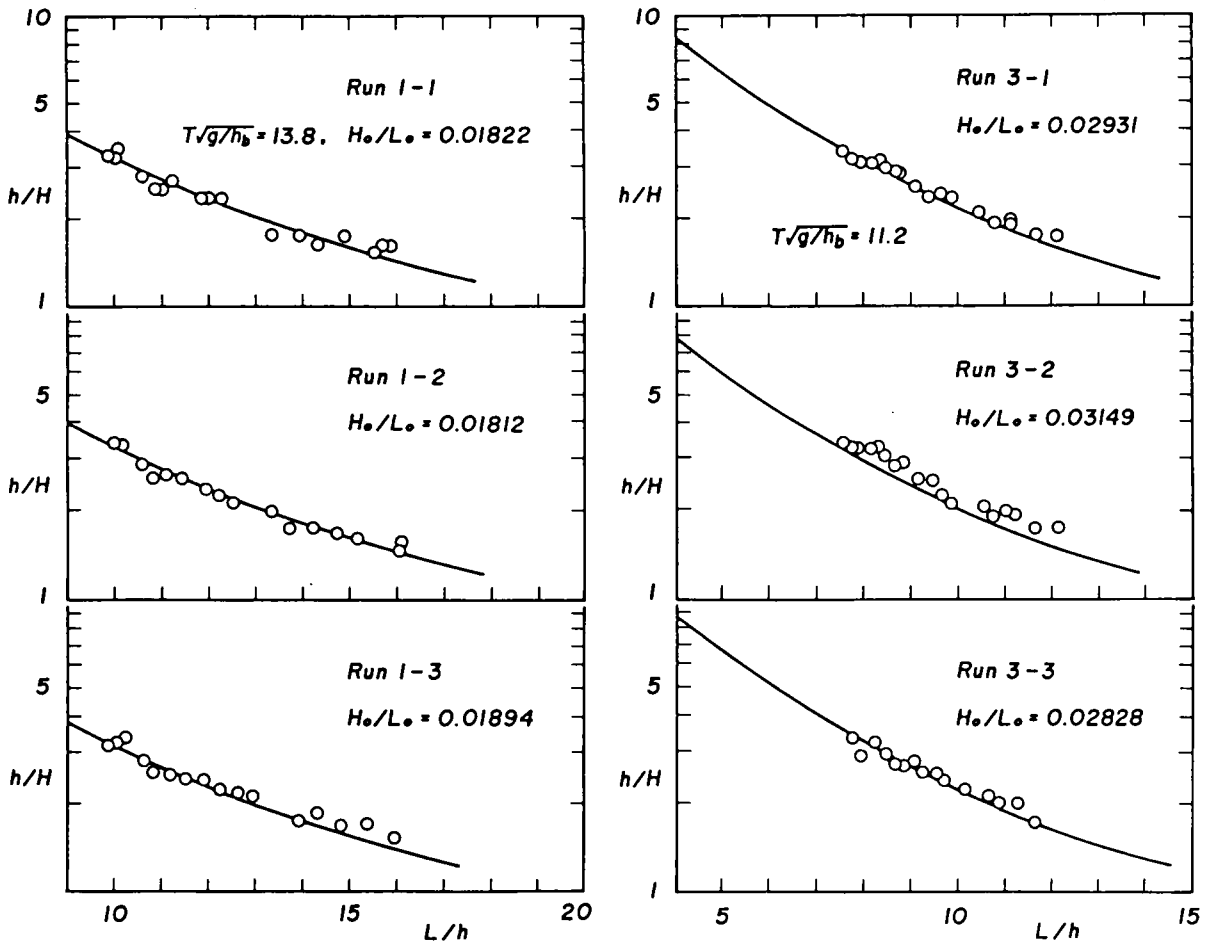

(1) Run 1 (2) Run 3

Fig. 3.12 Changes in steepness of shoaling waves.

3.3 Some Usual Breaking Conditions

(1) Rankine-Stokes Breaking Condition

Photo. 3.2 shows the representative behaviour of the floats on the wave surface. The maximum horizontal component of the water particle velocities on the wave surface u_{max} was derermined from the maximum gradient of the travel-time curve of the float, obtained from these photographs. Fig. 3.13

shows the comparison of these water particle velocities with wave velocities defined as the ratio of wave length to wave period. The ratio u_{max}/c often takes on greater values than unity near the breaking point, but the discrepancies are about 10 %, which may be considered the maximum acceptable error for experimental measurements. Therefore, it can be concluded that the ratio u_{max}/c becomes equal to unity at the breaking point, that is, the Rankine-Stokes breaking condition is satisfied.

(2) **Breaking Wave Height**

Fig. 3.14 shows the comparison of experimental breaking wave heights with the breaking inception calculated with use of the Rankine-Stokes breaking condition and with the breaker index. The breaking wave height for the solitary wave evaluated by the breaking model (see Chapter 2) is also plotted in the figure. Experimental breaking wave heights have values about 10 % smaller than theoretically evaluated values. Moreover, experimental results have 4 % smaller values than those of the breaker index. However, considering the accuracy of the breaker index, both of these experimental and theoretical values may well agree.

(3) **Breaking Angle**

This type of breaking wave was for a so-called spilling breaker, and the angles of wave crest at just breaking were within from 90° to 93°, determined from photographs as shown in **Photo. 3.3.** The breaking model (see Chapter 2, **Fig. 2.15**) indicates that breaking angles for the present experimental waves are of about 102° to 104°, while, according to Schwartz[10], waves with breaking angles of about 90° predominate in deep water. These experimental breaking angles may, therefore, be reasonable.

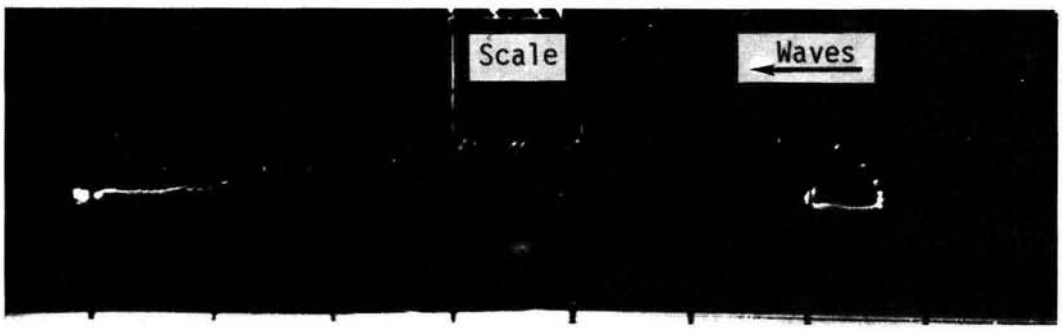

(1) x/h_b = 0 : Breaking point

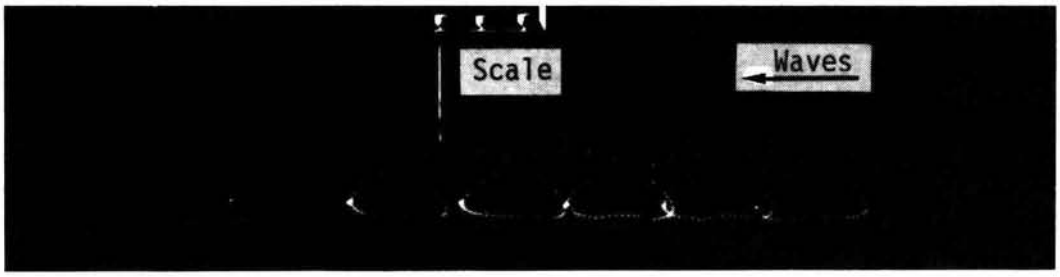

(2) x/h_b = 7.8

Photo. 3.2 Behaviour of floats on the wave surface (Run 2).

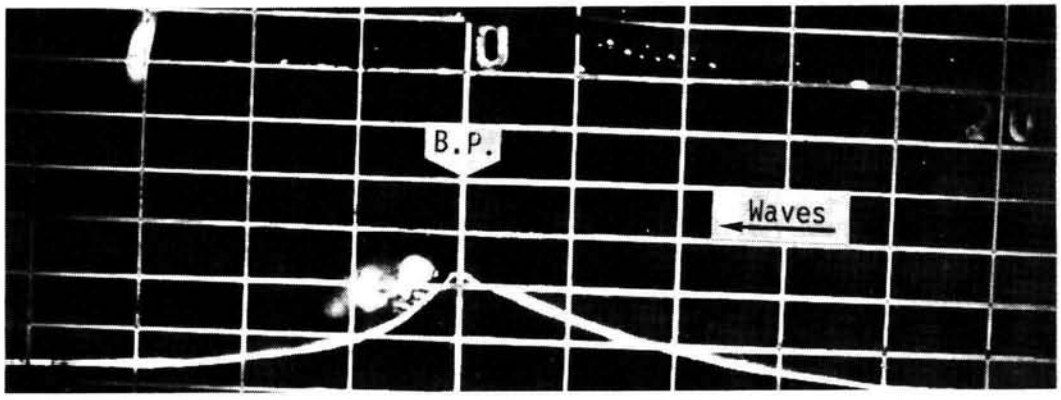

Photo. 3.3 Wave profile at just breaking (Run 2).

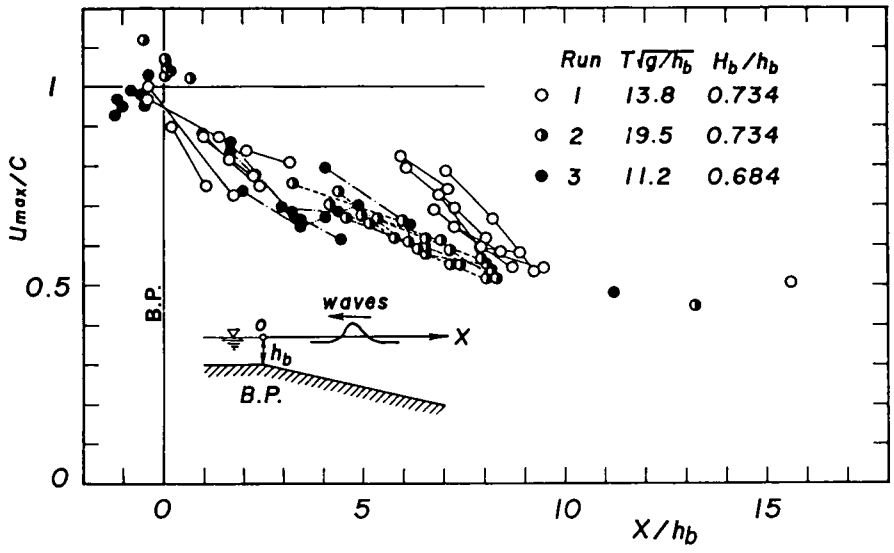

Fig. 3.13 Changes in maximum horizontal component of water particle velocities.

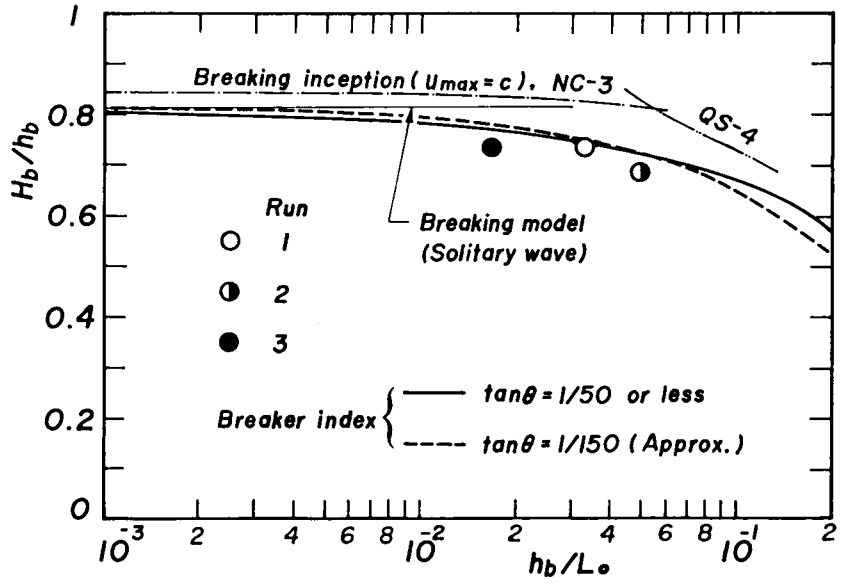

Fig. 3.14 Comparison of breaking wave heights with theoretical ones and the breaker index.

3.4 Mass Transport Induced by Breaking Waves

Photo. 3.4 shows the trajectories of neutrally buoyancy particles under the still water level. It is notable that the shallower the water depth, the more active the motion of water particles. The horizontal component of water particle velocities on the wave surface also amounts to several times the vertical one, as seen in **Photo. 3.2.**

The vertical distributions of mass transport velocity U_m for Runs 1, 2, and 3, obtained from these photographs, are shown in **Figs. 3.15, 3.16,** and **3.17,** respectively, where the vertical coordinate z is measured upward from the mean water level.

Theoretically evaluated values by the Stokes, Quasi-Stokes, and cnoidal wave theories are indicated by chain, broken, and solid lines, respectively. Furthermore, in the pairs of curves, the heavy line shows the vertical distribution estimated based on the shoaling of the first wave over the slope, and the light line, estimated using the measured wave heights from wave profiles in time at each measuring point. The dotted lines at the breaking point $x/h_b = 0$ were evaluated with the Rankine-Stokes breaking condition, and the bouble chain lines, with the breaker index.

In Run 1, in the region apart from measuring point 5, $x/h > 52.7$, experimental mass transport velocities distribute nearly uniformly throughout the whole water depth and give slightly smaller values than theoretical ones in the upper zone of the water. In the shallower region, from points 1 to 3, experimental and theoretical values roughly coincide near the bottom, but near the still water level the former approaches 5 times the latter.

The deviations of the experimental values in Run 2 are of the same order as in Run 1, as shown in **Fig. 3.16,** and the experimental values are greater than the theoretical ones for almost the whole region. The chief reason stems from the nonlinearity of shoaling waves and from the resulting

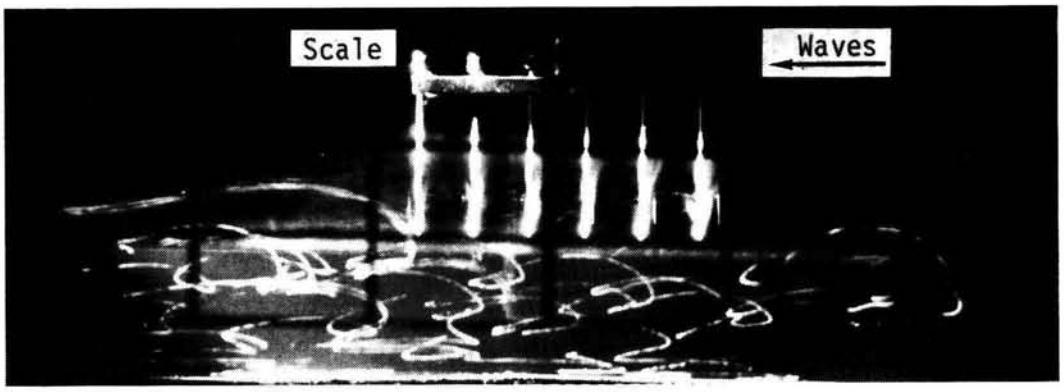

(1) x/h_b = 0 : Breaking point

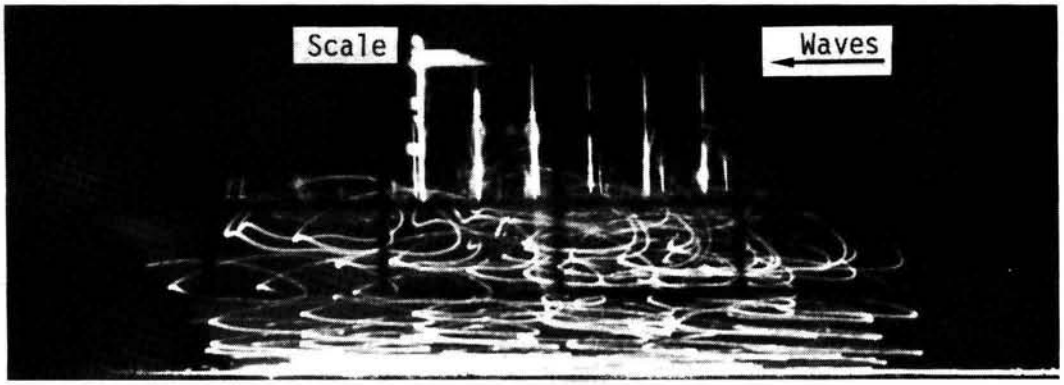

(2) x/h_b = 8.0

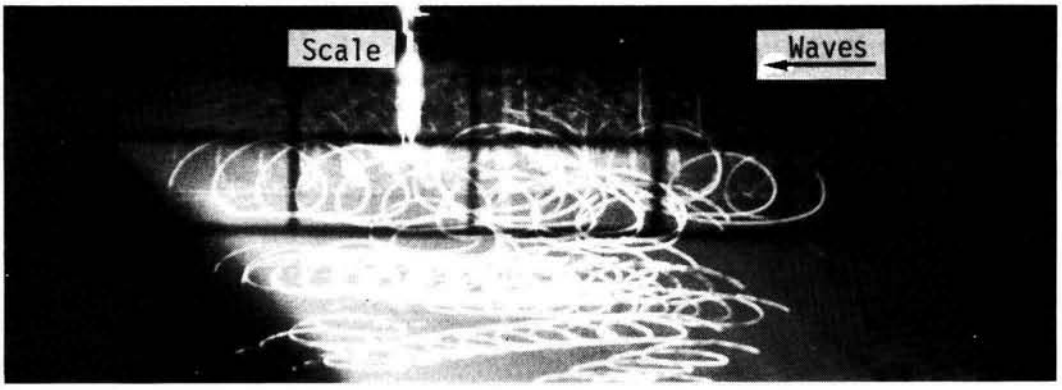

(3) x/h_b = 124.5

Photo. 3.4 Trajectories of neutrally buoyancy particles under the still water level (Run 3).

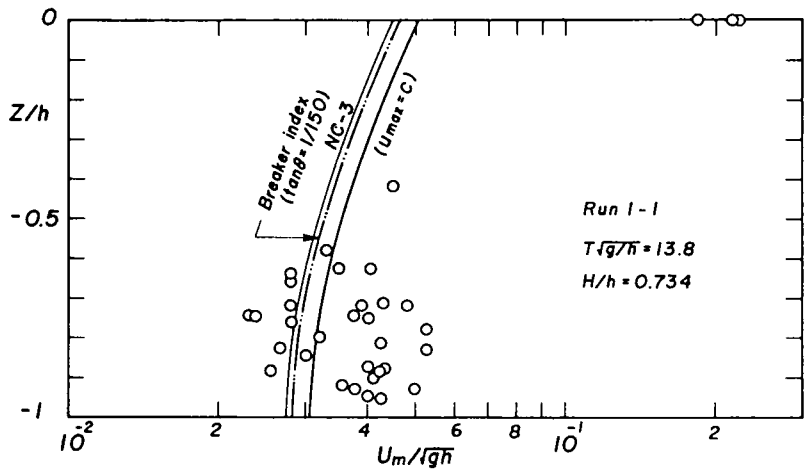

(1) $x/h_b = 0$

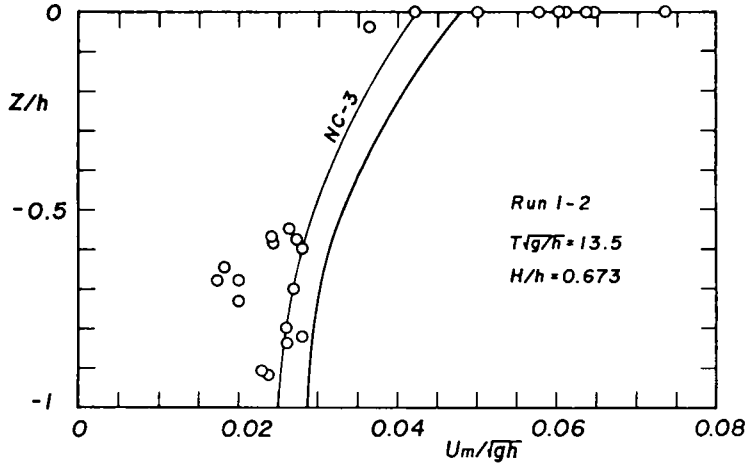

(2) $x/h_b = 7.8$

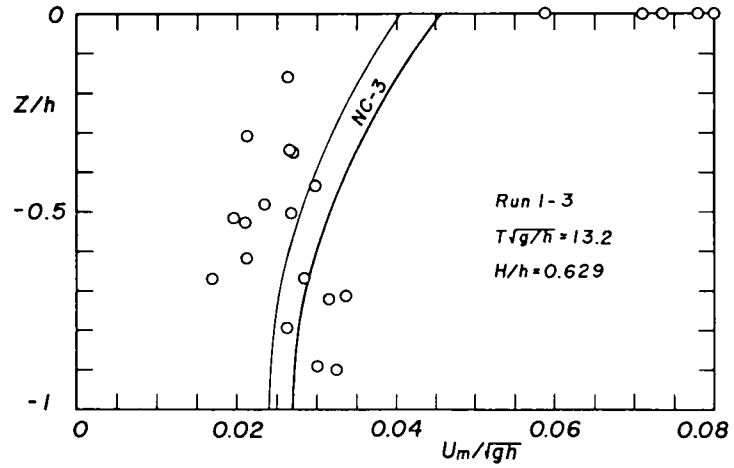

(3) $x/h_b = 15.6$

Fig. 3.15 Vertical distribution of mass transport velocity (Run 1).

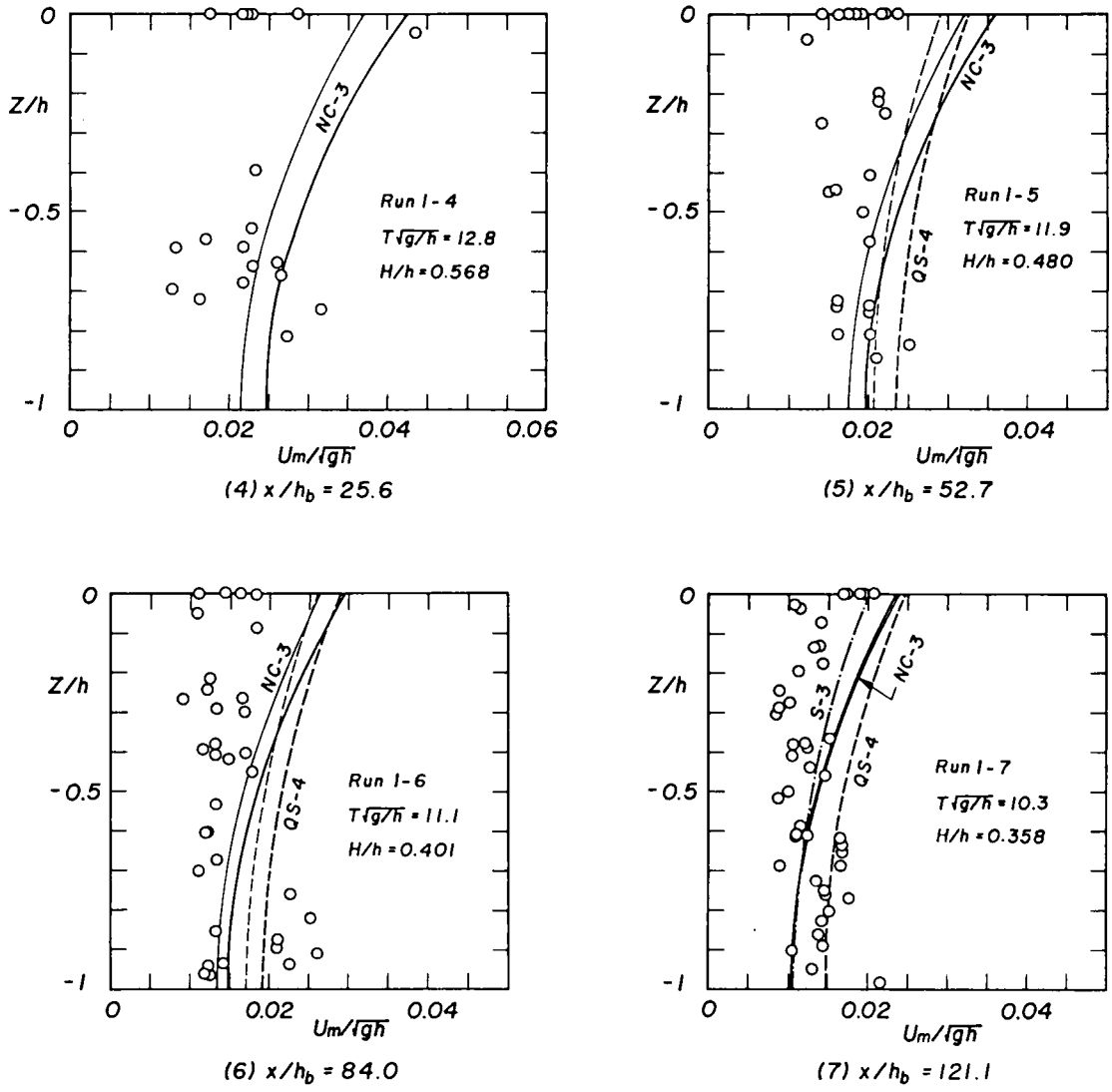

Fig. 3.15 Continued.

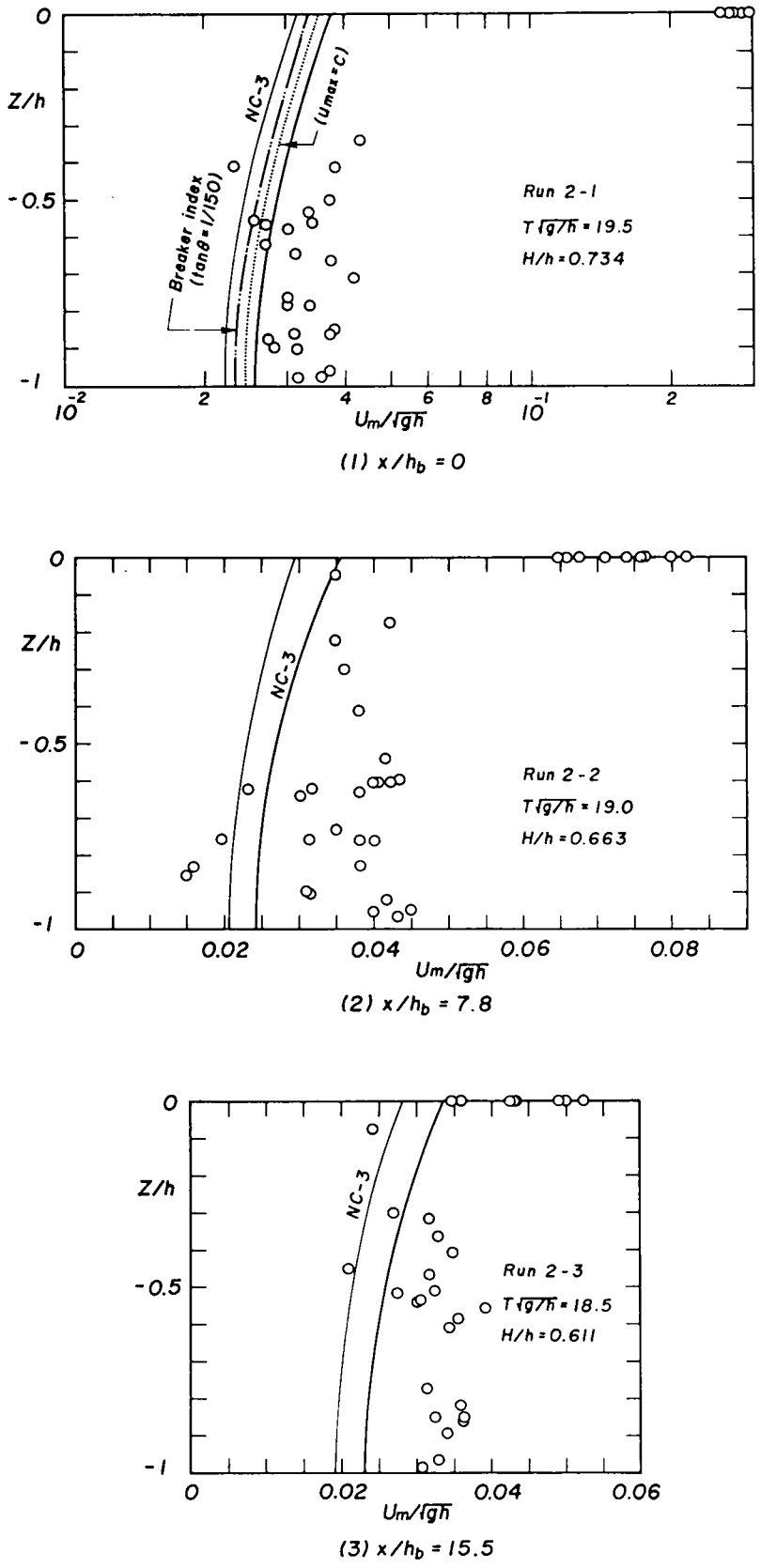

Fig. 3.16 Vertical distribution of mass transport velocity (Run 2).

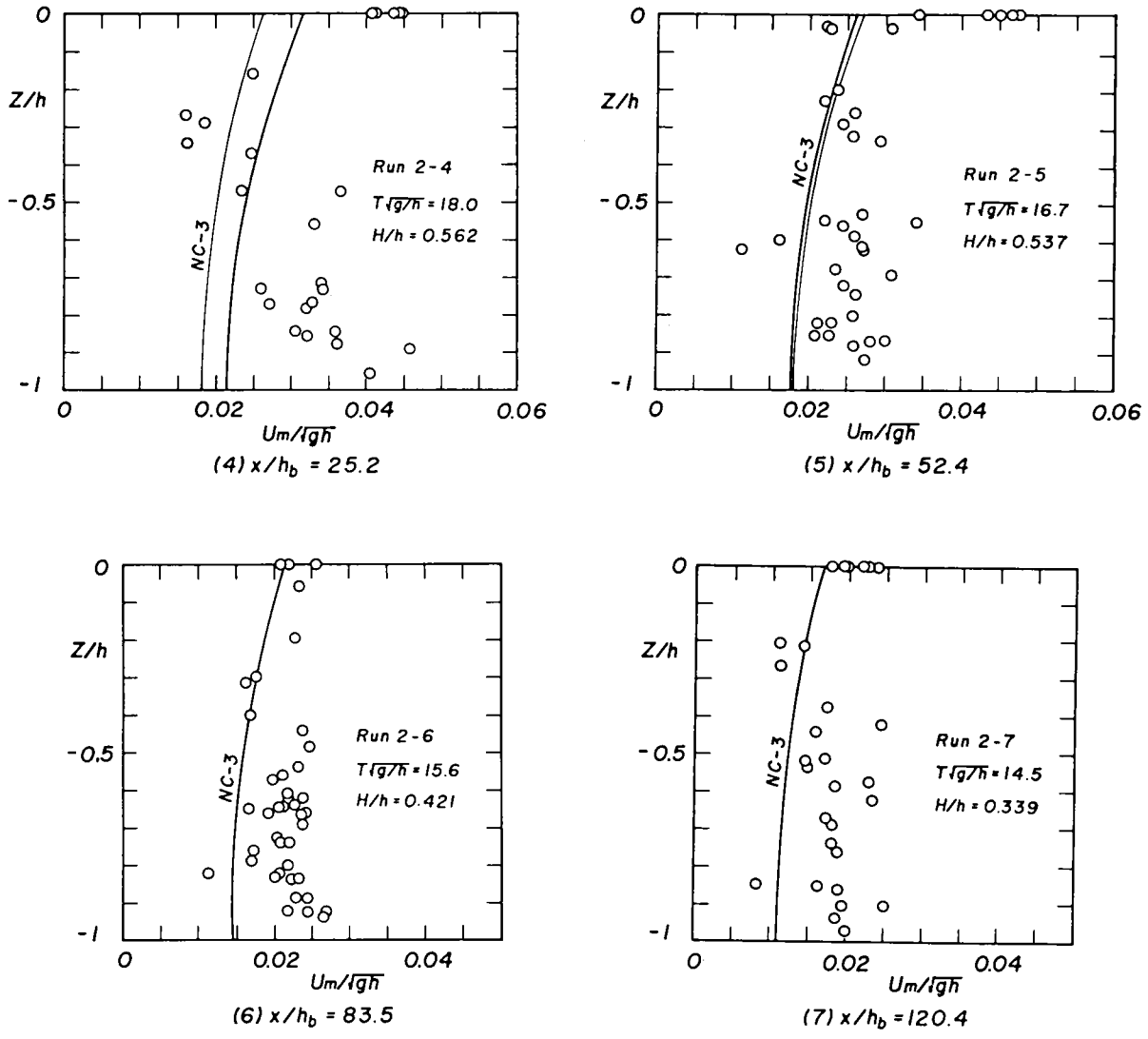

Fig. 3.16 Continued.

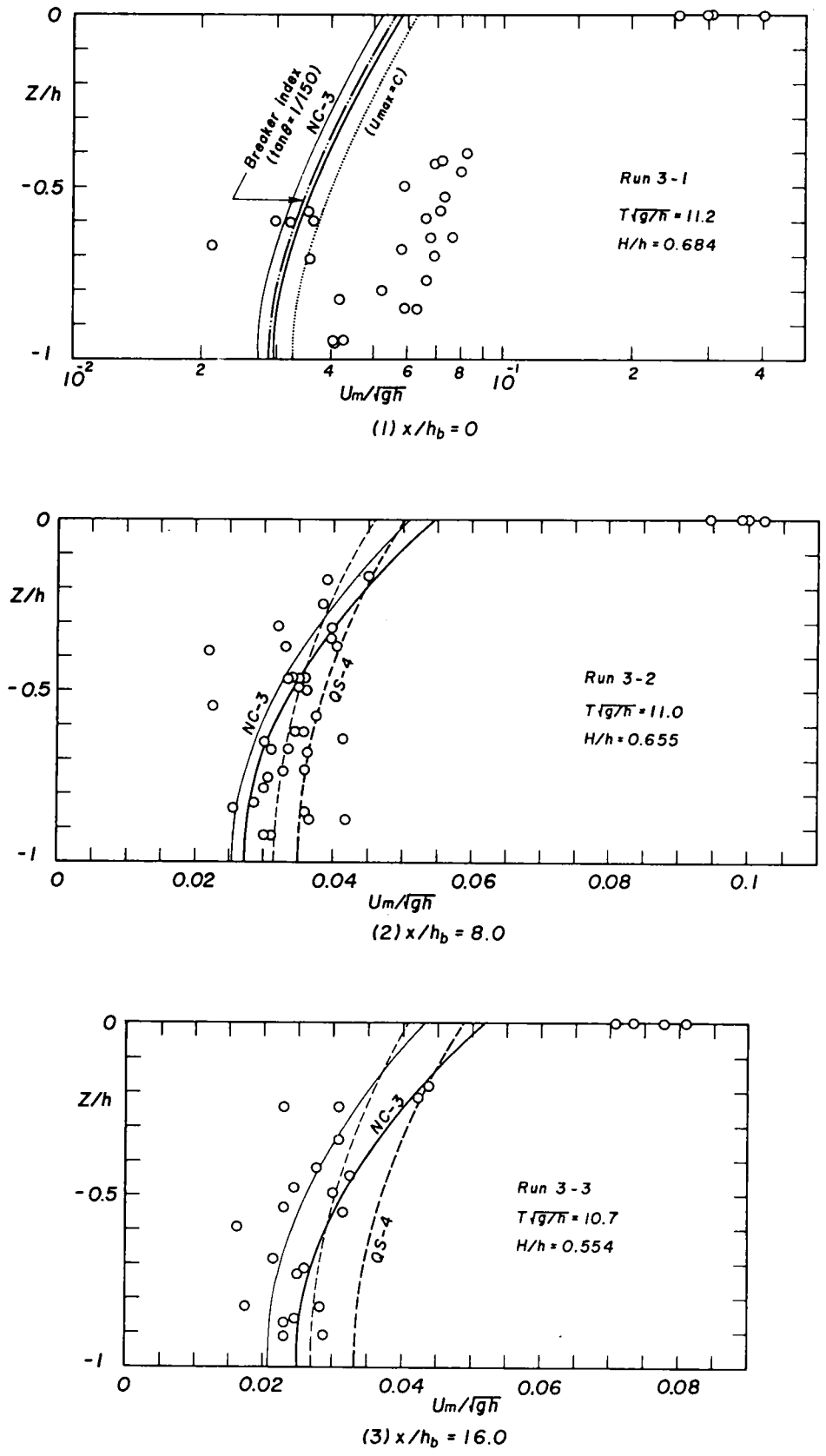

Fig. 3.17 Vertical distribution of mass transport velocity (Run 3).

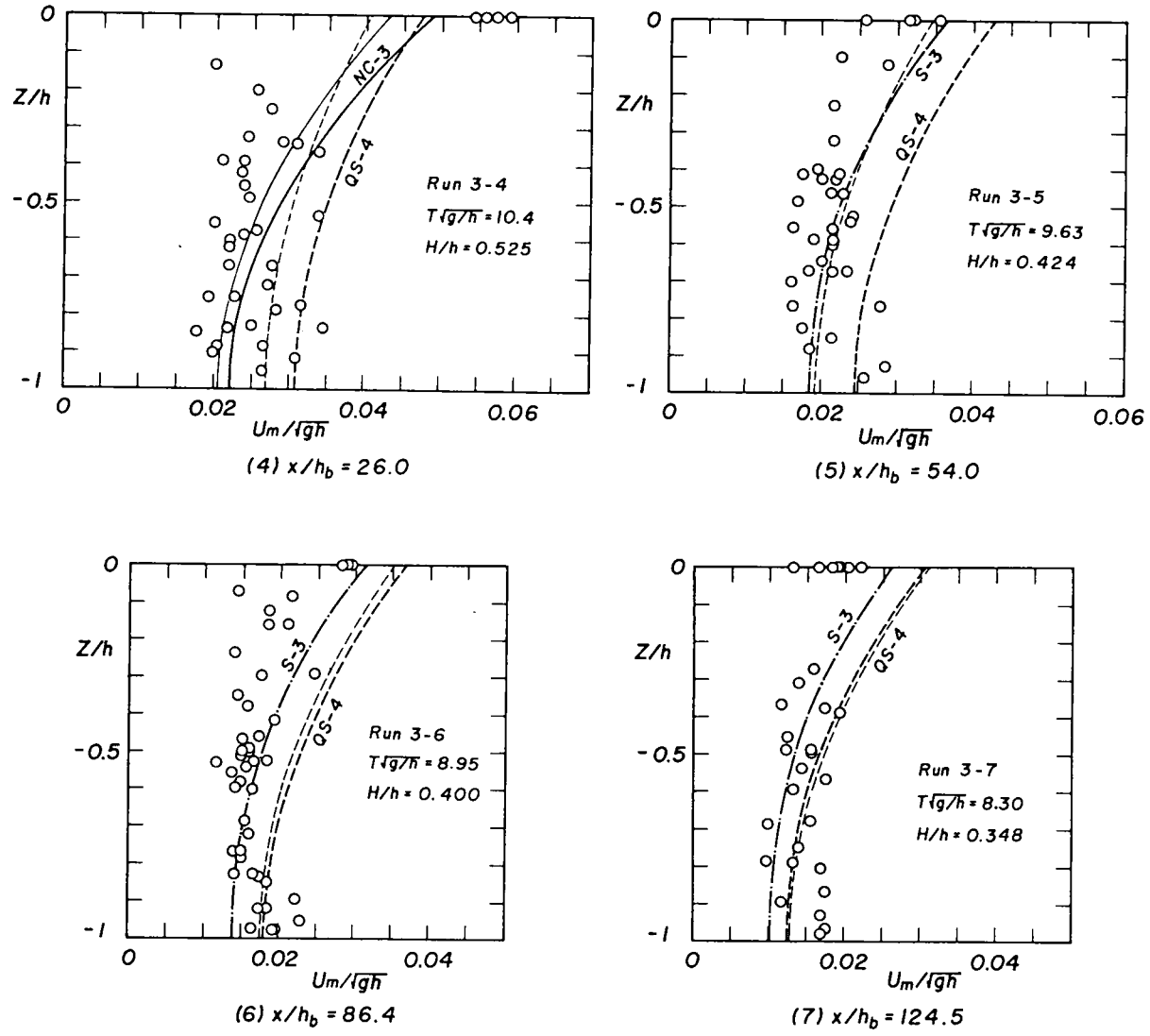

Fig. 3.17 Continued.

occurrence of secondary waves, as mentioned before. Mass transport velocities at the breaking point take on values of about 7 times theoretical ones near the still water level.

In Run 3, which is the case of the weakest nonlinearity of waves here, the results in the offshore region are similar to those of Run 1, and the deviations are smaller than in Runs 1 and 2. From points 2 to 7, $8.0 < x/h_b < 124.5$, experimental and theoretical results agree well except for in the upper zone of the water. At the breaking point $x/h_b = 0$, experimental values amount to several times theoretically evaluated ones.

All runs show that the shallower the water depth, the greater the deviation. This fact is due to the activity of water particles near the breaking point as seen in **Photos. 3.2, and 3.4.** It is also notable that there exists mass transport in the direction of wave propagation and it extends over the whole depth for the shoaling waves on a slope as well as for waves on a uniform depth of water[11].

Fig. 3.18 shows the changes in mass flux with respect to the dimensionless wave period $T\sqrt{g/h}$, where the mass flux was evaluated from the vertical distributions of mass transport velocity shown in **Figs. 3.15, 3.16, and 3.17.** The theoretical curves represent the total mass flux Q and the Stokes drift Q_2 induced by the nonlinear interaction between the water surface displacement and water particle velocity. The difference $Q - Q_2$ is the mass flux caused by the existence of the mean water particle velocity in the Eulerian coordinates for the Quasi-Stokes[8] and cnoidal waves[9]. The mass flux at just breaking, the upper bound of Q, is also drawn into the figure with use of the Rankine-Stokes breaking condition and the breaker index.

It is theoretically natural that evaluated values for Q based on the Quasi-Stokes wave theory smoothly coincide with cnoidal theory's because these two wave theories are derived standing upon the same physical assumption, non-periodicity of water particle velocities, and they are closely in

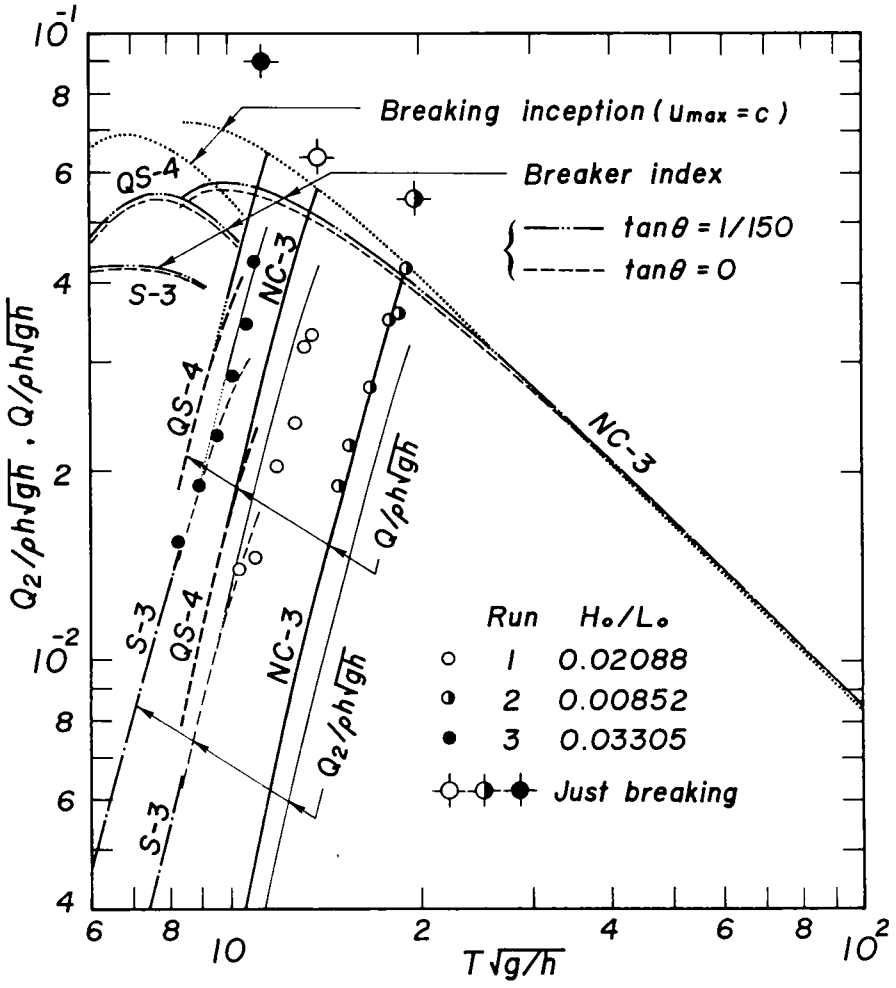

Fig. 3.18 Changes in mass flux.

accodance near-by their bounds of validity. The experimental mass flux in Runs 1 and 3 agree well with the Stokes drift Q_2. The results in Run 2, on the contrary, are similar to values of total mass flux Q because mass transport velocities take on greater values than theoretical ones due to the occurrence of secondary waves. The mass flux can be theoretically estimated in the deeper region. However, in the shallower region where the nonlinearity of waves becomes strong, the theoretical estimation of the mass flux gives values about 30 % smaller than experimental ones as seen in Fig. 3.18.

Generally, the theoretical estimation of the mass flux is not always possible near the breaking point, but one can obtain approximate values. Theoretical results indicate that the mass flux at just breaking takes on a maximum value near the point $T\sqrt{g/h} \fallingdotseq 10$.

3.5 Internal Breaking Conditions

(1) Partition Laws of Wave Energies for Progressive Waves

Consider two-dimensional surface waves propagating on water of gradually varying depth h with constant density ρ, under the influence of gravity g. Assume that the fluid is inviscid and incompressible and the motion is irrotational. Let the potential and kinetic energies, and group velocity be denoted by E_p, E_k, and c_g, respectively.

If the energy flux of the progressive waves is conserved, the energy conservation law $(E_p + E_k)c_g = \text{const.}$ leads to

$$E_k/E_{ki} = c_{gi}/c_g + (E_{pi}/E_{ki})(c_{gi}/c_g - E_p/E_{pi}), \tag{3.1}$$

where the subscript i denotes quantities of offshore waves (incident waves). The partition rate of wave energies, defined as the ratio of kinetic to potential energies, becomes

$$E_k/E_p = (c_{gi}/c_g)(E_{pi}/E_p)(E_{ki}/E_{pi} + 1) - 1. \tag{3.2}$$

Now consider the waves in the region where the condition

$$kh \gg 1 \tag{3.3}$$

is satisfied, where k is the wave number. In this region, the partition rate in the incident waves can be evaluated as

$$E_{ki}/E_{pi} \fallingdotseq 1. \tag{3.4}$$

Therefore, Eqs. (3.1) and (3.2) reduce to

$$E_k/E_{ki} = 2(c_{gi}/c_g) - E_p/E_{pi}, \tag{3.5}$$

$$E_k/E_p = 2(c_{gi}/c_g)(E_{pi}/E_p) - 1. \tag{3.6}$$

These equations govern the partition laws of wave energies until the waves break.

Fig. 3.19 shows an example of the partition rates of wave energies. The changes in physical properties, such as wave length, wave height, and group velocity, are also shown. The coordinate origin is, in the figure, taken at a point on the shoreline with the x-axis horizontally offshoreward, and θ is the slope of a beach. The breaking conditions adopted are the Rankine-Stokes breaking condition and the breaker index.

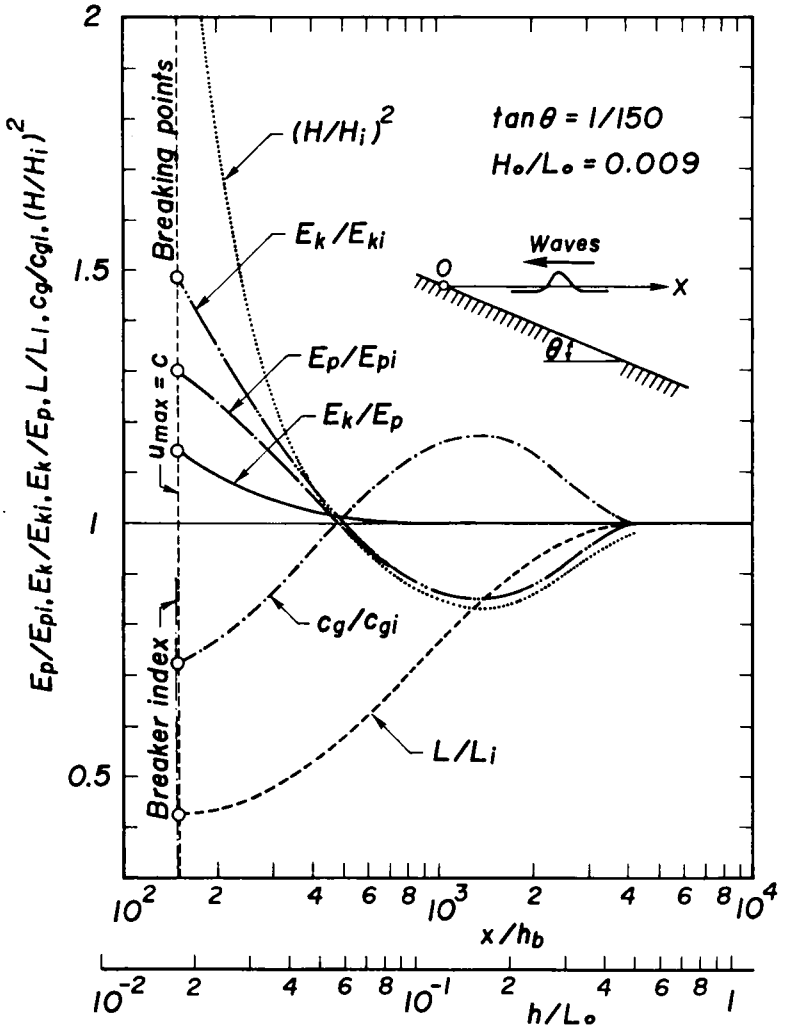

Fig. 3.19 Changes in physical quantities of a shoaling wave.

This figure shows that the wave length and group velocity decrease in shallow regions $x/h_b < 10^3$ as the wave propagates over the beach, but the other quantities, on the contrary, increase monotonically until the wave breaks. The example of $E_k/E_p \fallingdotseq 1.14$ at the breaking point leads to the fact that the kinetic energy is slightly greater than the potential one.

To verify these theoretical internal characteristics, the physical quantities in Eqs. (3.5) and (3.6) should be investigated experimentally. However, the changes in potential energy E_p/E_{pi} can only be determined directly in these quantities because when the shoaling wave profiles in space are measured experimentally, the potential energy can be estimated by the definition

$$E_p = (\rho g/L)\int_0^L (1/2)\eta^2 \, dx. \tag{3.7}$$

As the wave energy flux is conserved, if the changes in group velocity c_g/c_{gi} is evaluated properly, it is possible to determine the partition rate of wave energies E_k/E_p near the breaking point based on Eq. (3.6). Consequently, through discussion of the partition of wave energies of shoaling waves, one might find an internal breaking condition.

(2) Wave Set-Down

One of the most important wave-driven effects occurs when waves encounter a sloping beach. The waves shorten, steepen, and eventually break. In the steady state, the shoreward flux of momentum must be independent of x, which is taken perpendicular to the shore. It is well-known that the resulting change in radiation stress produces a change in the mean water level, that is, wave set-down.

Let the horizontal and vertical components of water particle velocities, the pressure, and the time be u, w, p, and t, respectively. The

radiation stress[12] is defined by

$$S = (1/T)\int_0^T\int_0^{h+\eta}(p+\rho u^2)\,dzdt - (1/2)\rho g h^2 - (1/\rho h)\left\{(1/T)\int_0^T\int_0^{h+\eta}\rho u\,dzdt\right\}^2, \tag{3.8}$$

where z is the vertical coordinate measured upward from the sea bottom. For Stokes waves, Eq. (3.8) leads to

$$S/\rho g h^2 = \frac{1}{2}\left\{\frac{a}{h}\right\}^2\left\{1+\lambda^2\frac{8\,ch^4-8\,ch^2+9}{8\,sh^4}\right\} \times\left[\frac{1}{2}+\frac{kh}{sh\,ch}+\lambda^2\left\{\frac{kh}{sh\,ch}\cdot\frac{-20\,ch^8+36\,ch^6-12\,ch^4+5\,ch^2-9}{16\,sh^8} + \frac{20\,ch^6-28\,ch^4+35\,ch^2-18}{32\,sh^6}-\frac{1}{2\,sh^2}\frac{sh\,ch}{kh}\right\}\right], \tag{3.9}$$

where a and λ are parameters concerned with wave properties, and the notation, for brevity, is made such that $sh = \sinh kh$ and $ch = \cosh kh$.

Longuet-Higgins and Stewart[6] have integrated the equation of horizontal momentum balance to yield the formula for the wave set-down Δh as

$$\Delta h/d = -\frac{1}{4}\left\{\frac{a}{d}\right\}^2\frac{2kd}{\sinh 2kd}, \tag{3.10}$$

where d is the local depth of water. In Eq. (3.10), the lowest order term of the radiation stress of Eq. (3.9) is adopted and the local depth d is assumed to be nearly equal to the mean water depth h. This formula has the validity only in the region where the Stokes wave theory is applied. Thus, similar formulae for the wave set-down must be developed in shallow regions where proper wave theories, for example, the cnoidal wave theory, are applicable.

Based on Eq. (3.8), the radiation stresses for Quasi-Stokes and cnoidal waves are expressed[13], respectively, as

$$S/\rho g h^2 = (\lambda_0^2/16)\left[\,3-(2/3)(kh)^2+(14/45)(kh)^4-(57/1890)(kh)^6 + (3/64)\lambda_0^2\left\{\,3(kh)^{-4}+10(kh)^{-2}\,\right\}\right], \tag{3.11}$$

$$S/\rho g h^2 = (1/2)(\lambda^2/k^4)\{ -(E/K)\{3(E/K)+2k^2-4\}\}+k^2-1\}$$
$$+(1/10)(\lambda^3/k^6)\{100(E/K)^2\{(E/K)+k^2-2\}+2(E/K)(11k^4-61k^2+61)$$
$$-11(k^4-3k^2+2)\}$$
$$+(1/168)(\lambda^4/k^8)\{-3(E/K)^3\{1113(E/K)+1496k^2-2968\}$$
$$-2(E/K)^2(861k^4-4200k^2+4200)$$
$$-28(E/K)(7k^6-72k^4+174k^2-116)$$
$$+(k^2-1)(98k^4-413k^2+413)\}, \qquad (3.12)$$

where k in Eq. (3.12) is the modulus of the Jacobian elliptic functions, and K and E are the complete elliptic integrals of the first and second kinds, respectively. λ_0 and λ are also the parameters which are functions of wave properties.

Since these two expressions for the radiation stress are too complicated to lead formulae for the wave set-down as by the direct integral method used by Longuet-Higgins and Stewart[6], following other simple arguments by them[14], let us investigate the general relation for the vertical momentum flux and propose a formula for the wave set-down.

Consider the vertical momentum balance in a section of water bounded by the wave surface $z = h + \eta$, a horizontal plane $z = z_0$, and two vertical planes $x = x_0$ and $x = x_0 + dx$ as illustrated in **Fig. 3.20.** The mean flux of vertical momentum(per unit cross-section) across the horizontal plane is

$$\overline{p+\rho w^2} - \frac{\partial}{\partial x}\overline{\int_{z_0}^{h+\eta} \rho uw \, dz}$$

in terms of the pressure and Reynolds stresses, in which the over-bar denotes the time average. This average flux of momentum must balance the total weight of the section of water, so that the relation for the vertical momentum flux can be obtained

$$\overline{p+\rho w^2} - \frac{\partial}{\partial x}\overline{\int_{z_0}^{h+\eta} \rho uw \, dz} = \overline{p_0+\rho g(h+\eta-z_0)}, \qquad p_0 = \rho g(h-z_0). \qquad (3.13)$$

On the other hand, the time average in the Bernoulli equation gives

$$\rho\overline{\frac{\partial\phi}{\partial t}}+\overline{p}+(1/2)\rho\overline{(u^2+w^2)}+\rho g\overline{(z_0-h)}=\overline{f(t)}=\text{const.}, \tag{3.14}$$

where ϕ is the velocity potential, $f(t)$ a certain function of time. From Eqs. (3.13) and (3.14),

$$\rho g(h-d)=-(1/2)\rho\overline{(u^2-w^2)}-\rho\overline{\frac{\partial\phi}{\partial t}}-\frac{\partial}{\partial x}\overline{\int_d^{h+\eta}\rho uw\,dz}+C \tag{3.15}$$

at the still water level $z_0=d$, where C is a constant. This equation expresses the time average of the vertical momentum flux at the still water level, thus likely giving the wave set-down at any point of x.

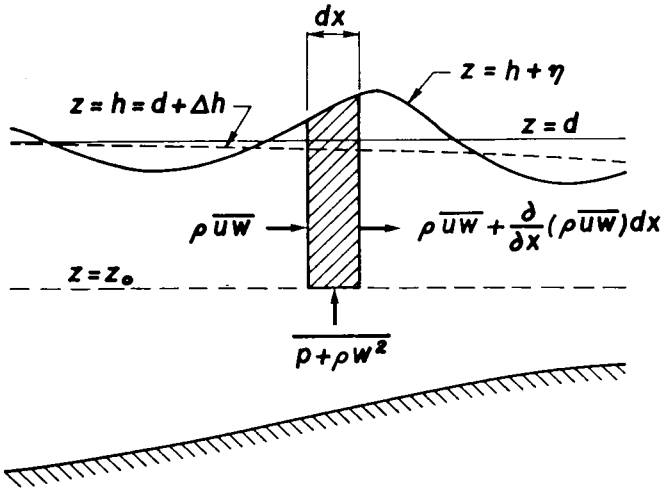

Fig. 3.20 Vertical momentum balance in a shoaling wave.

The terms contained in Eq. (3.15) can be evaluated as follows; the velocity potential for Stokes waves is determined such that the relation $C=\rho\overline{\partial\phi/\partial t}$ must be held[7),12)], while in the Quasi-Stokes and cnoidal wave theories[13)], the horizontal water particle velocity is given by

$$u=\frac{\partial\phi}{\partial x}=\overline{u}+\sum(\text{periodic terms}),\qquad \overline{u}=(1/T)\int_0^T u\,dt\neq 0, \tag{3.16}$$

thus, the velocity potential becomes

$$\phi=\overline{u}x+\int\sum(\text{periodic terms})\,dx, \tag{3.17}$$

in which the secular term is determined to have vanished. Therefore, the time averaged term $\overline{\partial \phi / \partial t}$ vanishes in these two wave theories. The constant C is also null in the basic equations.

In evaluating the third term of Eq. (3.15), the slope is assumed to be sufficiently gentle such that the reflection of waves is of negligible importance in the calculation of shoaling waves. So the order of approximation of the derivative with respect to x may lead to

$$\frac{\partial}{\partial x}\overline{\int_d^{h+\eta} \rho u w \, dz} \fallingdotseq \frac{\partial}{\partial x}\overline{\int_h^{h+\eta} \rho u w \, dz}. \tag{3.18}$$

This is higher than the highest order of the theories adopted, so that this term is also negligible; consequently, the wave set-down $\Delta h = h - d$ can be evaluated by

$$g \Delta h \fallingdotseq -(1/2)\overline{(u^2 - w^2)} \tag{3.19}$$

under the condition that $z = d \fallingdotseq h$.

Substituting the known expressions of the water particle velocities for the Stokes, Quasi-Stokes, and cnoidal waves in Eq. (3.19), required expressions are written for the Stokes wave theory as

$$\Delta h/h = -\frac{1}{4}\left\{\frac{a}{h}\right\}^2 \frac{kh}{sh\, ch}\left\{1+\lambda^2 \frac{8\, ch^4 - 8\, ch^2 + 9}{8\, sh^4}\right\}$$

$$\times\left\{1+\lambda^2 \frac{-20\, ch^6 + 16\, ch^4 + 4\, ch^2 + 9}{16\, sh^6}\right\}, \tag{3.20}$$

for the Quasi-Stokes wave theory

$$\Delta h/h = -(\lambda_0^2/16)\{\, 1-(2/3)(kh)^2+(14/45)(kh)^4-(461/3870)(kh)^6$$

$$+(3/64)\lambda_0^2\{\, 3(kh)^{-4}-7(kh)^{-2}\,\}\,\}, \tag{3.21}$$

and for the cnoidal one,

$$\Delta h/h = -(1/6)(\lambda^2/k^4)\{\, -(E/K)\{3(E/K)+2k^2-4\}+k^2-1\,\}$$

$$-(1/30)(\lambda^3/k^6)\{\, 75(E/K)^2\{\,((E/K)+k^2-2)\}$$

$$+(E/K)(14k^4-89k^2+89)-7(k^4-3k^2+2)\,\}$$

$$-(1/2100)(\lambda^4/k^8)\{\, -175(E/K)^3\{129(E/K)+188k^2-352\}$$

$$-2(E/K)^2(6307\,k^4-30982\,k^2+29582)$$
$$-4(E/K)(247\,k^6-3524\,k^4+8740\,k^2-5710)$$
$$+(k^2-1)(494k^4-2701k^2+2701)\,]\,. \qquad (3.22)$$

Eq. (3.10) coincides with Eq. (3.20) in the lowest order of approximations, assuming that the local depth d nearly equals the mean depth of water h. By comparison of Eqs. (3.11) and (3.12) with Eqs. (3.21) and (3.22), respectively, it is noted that the wave set-down is about one-third of the radiation stress in the shallower region. The resulting changes in radiation stress and in wave set-down, expressed respectively by Eqs. (3.9) to (3.12) and Eqs. (3.20) to (3.22), will be discussed in the next section, comparing them with experimental results.

(3) Occurrence of Wave Breaking Subject to the Imbalance in the Partition Rate of Wave Energies

Because the potential energy must be evaluated from wave profiles in space without strong secondary waves, wave profiles for only Runs 1 and 3 could be used here. Wave lengths were evaluated from experimental curves with an error of about 5 % as shown in **Fig. 3.8.**

To estimate the left-hand sides of Eqs. (3.5) and (3.6), which govern the partition rate of wave energies, measurements of the changes in group velocity are required. Since it is impossible to measure the changes directly, the following approximations are adopted.

Fig. 3.21 shows the theoretical results of the changes in potential and kinetic energies, in radiation stress, in group velocity, in wave length, and in wave height. Experimental curves for wave lengths are also shown in the figure. These experimental and theoreticl results of wave length coincide over the whole range of the distance x/h_b within an error of 5 %. Assuming that the wave period does not change with the varying depth, the

changes in wave length L/L_i equal those in wave velocity c/c_i. Therefore, the changes in group velocity c_g/c_{gi} near the breaking point may be approximated by the changes in wave length L/L_i, i.e.

$$c_g/c_{gi} \fallingdotseq L/L_i = c/c_i . \tag{3.23}$$

On the other hand, according to the theoretical results, the partition rates of incident waves E_{ki}/E_{pi} for Runs 1 and 3 are equal to 1.027 and 1.029, respectively. This means that the assumption (3.4) is sufficiently satisfied by the experimental incident waves. Eqs. (3.5) and (3.6) can, then, be approximated by

$$E_k/E_{ki} = 2(c_i/c) - E_p/E_{pi} , \tag{3.24}$$

$$E_k/E_p = 2(c_i/c)(E_{pi}/E_p)-1 , \tag{3.25}$$

respectively.

Fig. 3.21 shows that the wave length L/L_i and group velocity c_g/c_{gi} both decrease with wave shoaling, while the energies E_p/E_{pi}, E_k/E_{ki}, and E_k/E_p and wave height $(H/H_i)^2$ all increase until the wave breaks. Among them, it is well worth remarking that the radiation stress S/S_i takes on a maximum value at certain points of h/L_0 and its change differs from the monotonical changes in the other physical quantities. The non-dimensional radiation stress $S/\rho g h^2$ increases toward the breaking point as shown in **Fig. 3.22**; however, the increasing rates are depressed after a certain point of h/L_0 (marked by a symbol;→). This is the reason the radiation stress S/S_i takes on a maximum value.

The experimental results of the changes in wave energies E_p/E_{pi} and E_k/E_{ki} are plotted in **Fig. 3.23**, in which the open and solid circles indicate the potential and kinetic energies, respectively. The experimental values of kinetic energy in this figure were calculated from Eq. (3.24) using the experimental values of wave length and potential energy.

Certain amount of fluctuations arise in Run 3 within $80 < x/h_b < 90$ because of weak meandering of waves. It is, however, remarkable that the

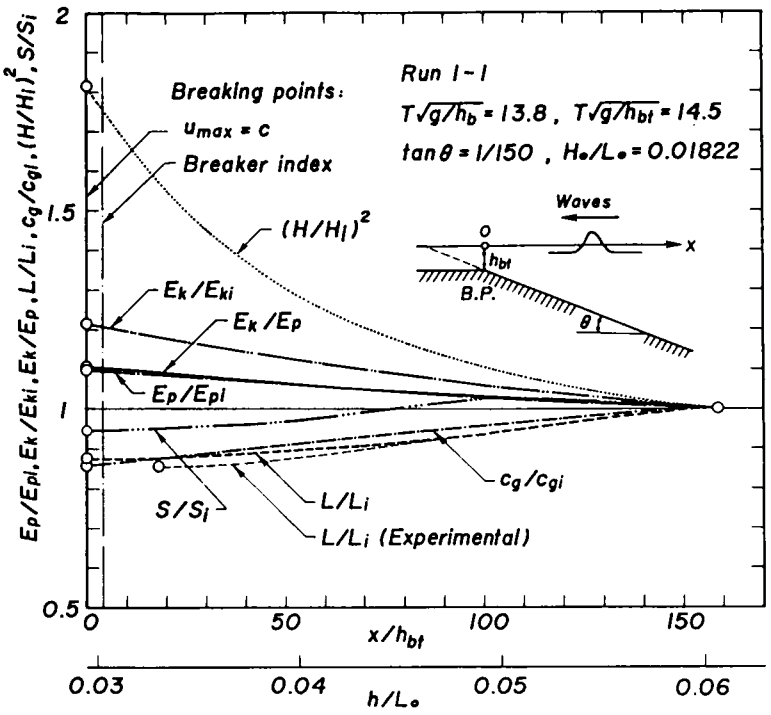

(1) Run 1

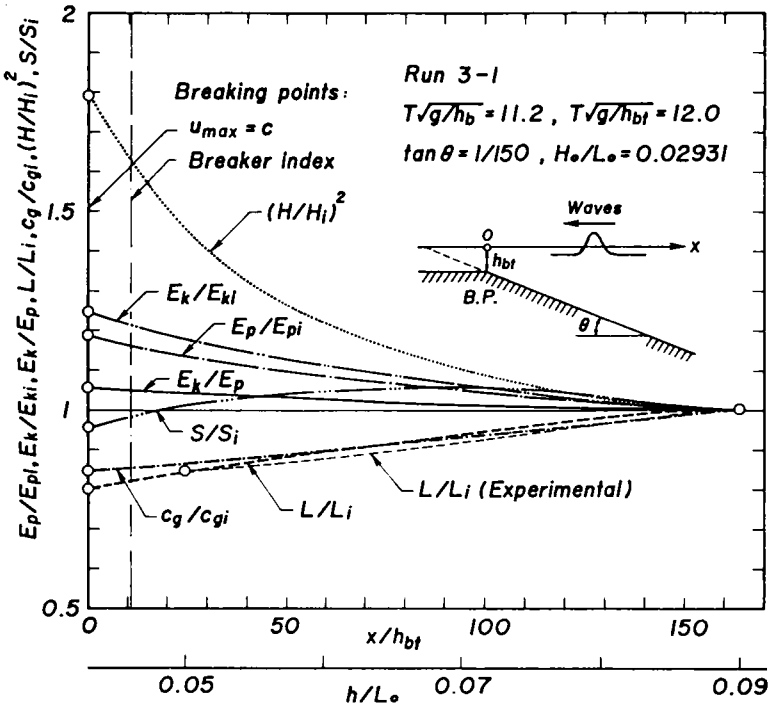

(2) Run 3

Fig. 3.21 Changes in physical quantities of the shoaling wave.

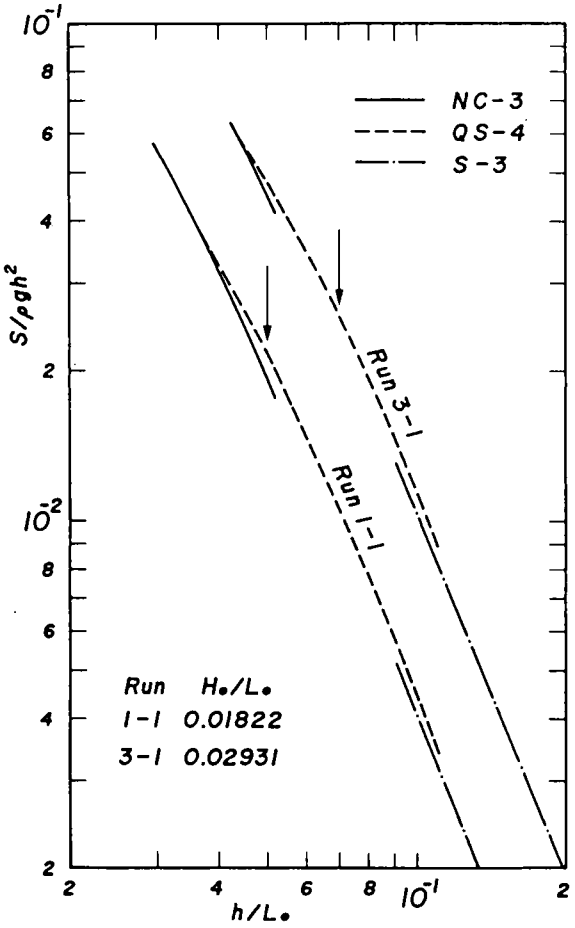

Fig. 3.22 Changes in radiation stress.

potential energies gradually increase in the offshore region $x/h_b > 100$, as does the theoretical estimation, decreasing slightly to 50-60 of x/h_b, after which they begin to decrease sharply. Let us define the points where the potential energy turns from a increase to a decrease and then when it begins to decrease sharply as the turning and initiating points, respectively. For Run 1, the breaking depth h_b and wave length L_b equal about 5.12 cm and 78 cm, respectively, so that the turning and initiating points of the potential energy, x_t/L_b and x_i/L_b, nearly equal 6.6 and 3.6, respectively. In Run 3, the potential energy begins to decrease sharply before the breaking point as in Run 1. These points x_t/L_b and x_i/L_b are about 8.6 and 3.6, respectively.

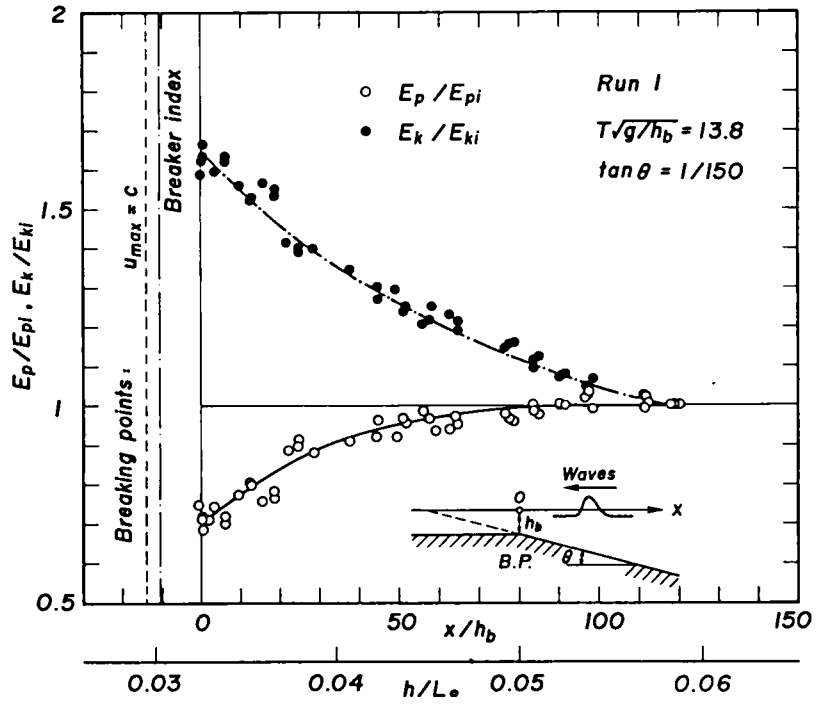

(1) Run 1

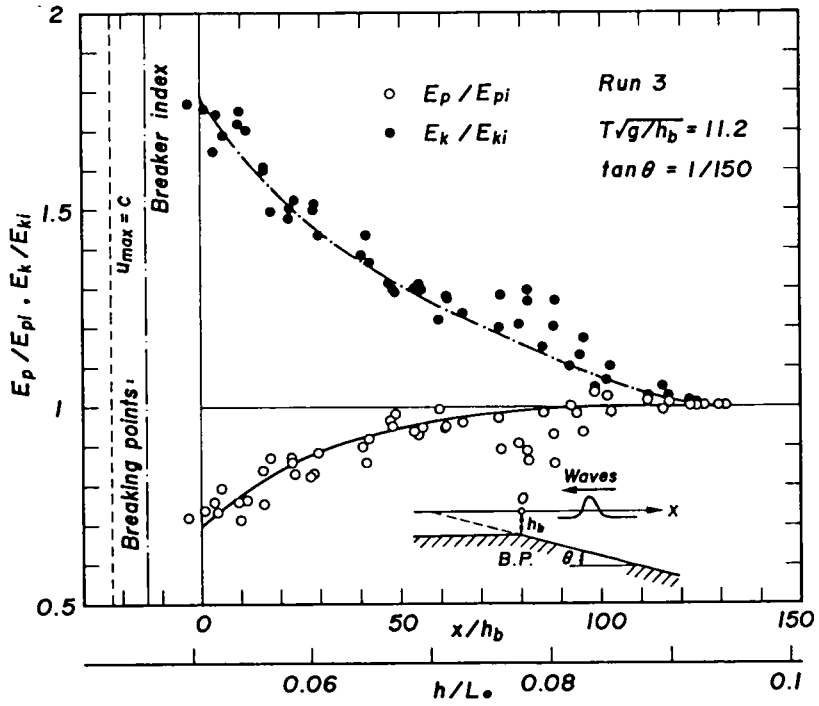

(2) Run 3

Fig. 3.23 Changes in potential and kinetic energies.

To justify the changes in wave properties based on the assumption (3.23), we need to discuss the changes in group velocity with the aid of the stream function theory[15]. According to the stream function theory in the frame of reference moving with a wave, the water surface displacement of the wave is given as

$$\eta = (1/c)\Big[\varphi_0 - \sum_{n=4,6,\cdots}^{N-1} \sinh(n-2)\pi\frac{h+\eta}{L} \times\Big\{X_n\cos(n-2)\pi\frac{x_1}{L} + X_{n+1}\sin(n-2)\pi\frac{x_1}{L}\Big\}\Big], \qquad (3.26)$$

where $x_1 = x-ct$, N is an odd number, φ_0 is the stream function at the wave surface, and X_j are coefficients of the Fourier series. The values of φ_0, L, and X_j are, originally, determined by the measurements of the wave profile and wave period. However, there exists a problem in adopting the theory to estimate wave properties over a slope; because the value of stream function is a constant only in the frame of reference moving with the wave, measured water surface displacements in time are able to satisfy the role of those in space only when the wave propagates on water of uniform depth. For the waves on a slope, on the contrary, water surface displacements in space must be used in Eq. (3.26). Therefore, at this stage we deal with the stream function theory in a slightly unusual manner; the parameters in the stream function representation are determined so as to strictly satisfy the kinematic boundary condition within an error of about 10^{-4} to 10^{-5}, using measured values of wave period and wave length. The gross error for the dynamical boundary condition is evaluated by the standard deviation

$$\left.\begin{aligned} &\sigma_2 = \sqrt{E_2}, \quad E_2 = (1/I)\sum_{i=1}^{I}(\bar{Q}-Q_i)^2, \\ &\bar{Q} = (1/I)\sum_{i=1}^{I}Q_i, \quad Q_i = \eta_{mi} + (1/2)\{(u_i - c)^2 + w_i^2\}, \end{aligned}\right\} \qquad (3.27)$$

where Q_i are Bernoulli's constants at the wave surface, and the subscript i is a phase index for a sequence consisting of I values. The resultant error for the dynamical boundary condition is in the range of 10^{-3} to 10^{-4}.

Fig. 3.24 shows the change in group velocity over the slope of 1/150, where the group velocity is defined by the ratio of energy flux to total energy. The solid lines in the figure are experimental curves for wave velocity c/c_i. Since the kinetic energy is extremely sensitive to the asymmetry of wave profiles, estimated values of group velocity c_g/c_{gi} show certain amount of fluctuations in the offshore region, which resembles that of the wave profiles in **Fig. 3.6.**

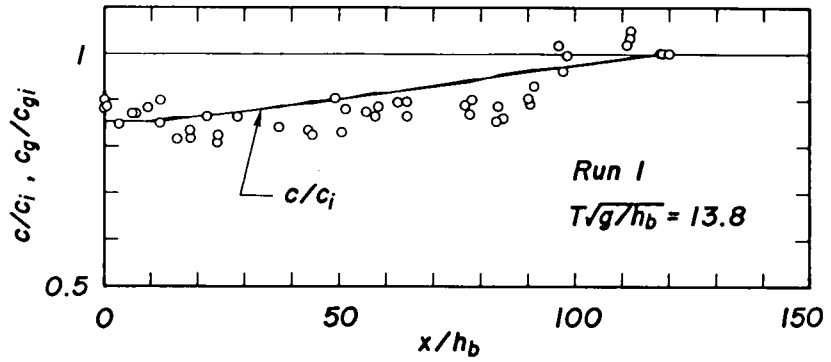

(1) Run 1

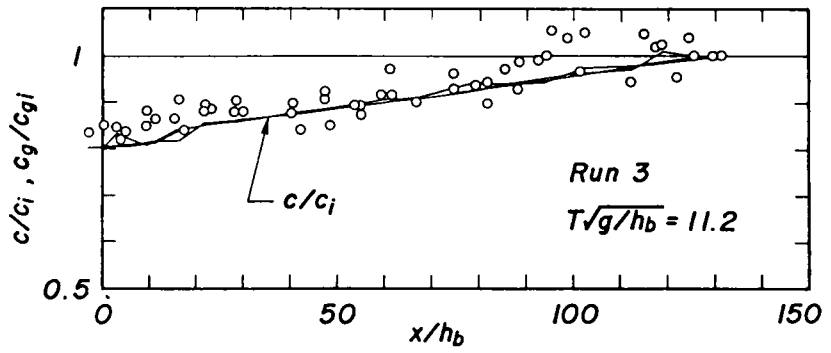

(2) Run 3

Fig. 3.24 Comparison of group velocities based on the stream function theory with experimental wave velocities.

The changes in kinetic energy $(E_k/E_{ki})_s$ are shown in **Fig. 3.25**, evaluated by Eq. (3.5). In the figure, the subscript s denotes values based on the stream function theory, and the chain lines are the experimental curves of E_k/E_{ki} based on Eq. (3.5) already shown in **Fig. 3.23**. $(E_k/E_{ki})_s$ takes on values less than unity in the offshore region, but both $(E_k/E_{ki})_s$ and E_k/E_{ki} reasonably coincide with experimental errors of wave velocities c/c_i in regard to group velocities c_g/c_{gi}.

Figs. 3.24 and **3.25** demonstrate that the assumption (3.23) is well satisfied by shallow water waves over the slope of 1/150. The estimated changes in potential energy E_p/E_{pi}, of course, agree with those shown in **Fig. 3.23**, satisfying the kinematic boundary condition.

Comparison of **Fig 3.21** with **Fig. 3.23** shows a remarkable difference between the experimental and theoretical results, an abrupt decrease in potential energy before the wave breaks. Moreover, it is notable that the point of abrupt decrease is nearly equal to the point where the radiation stress takes on a maximum value. The experimental tendency for the kinetic energy to increase as the wave approaches the breaking point is the same as the theoretical tendency. However, the increasing rates of kinetic energy in the experiments are several times the theoretical ones because of the abrupt decrease in potential energy.

Next, let us investigate the wave set-down caused by changes in radiation stress which has a strong effect on wave breaking. **Fig. 3.26** shows experimental results for wave set-down, in which the curves are the theoretically estimated ones for the wave set-down and radiation stress. Experimental and theoretical wave set-down are roughly the same in the deeper region, but the former is greater over the whole range of distance and is about three times the latter near the breaking point, that is, the values are more or less the same as for the radiation stress. The true wave set-down is sensitively affected by how the mass flux of the wave balances

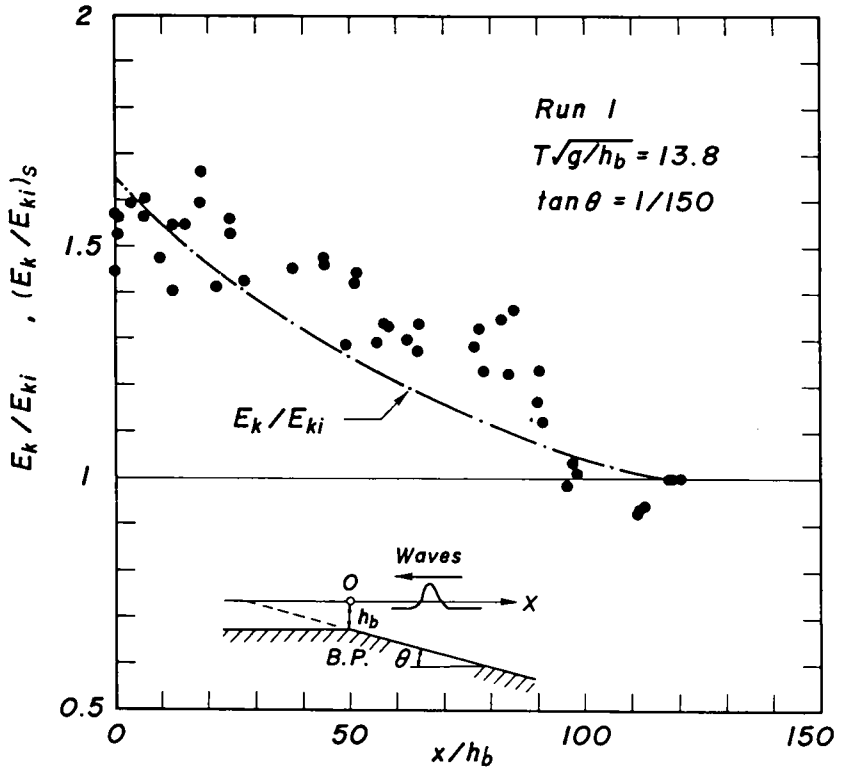

(1) Run 1

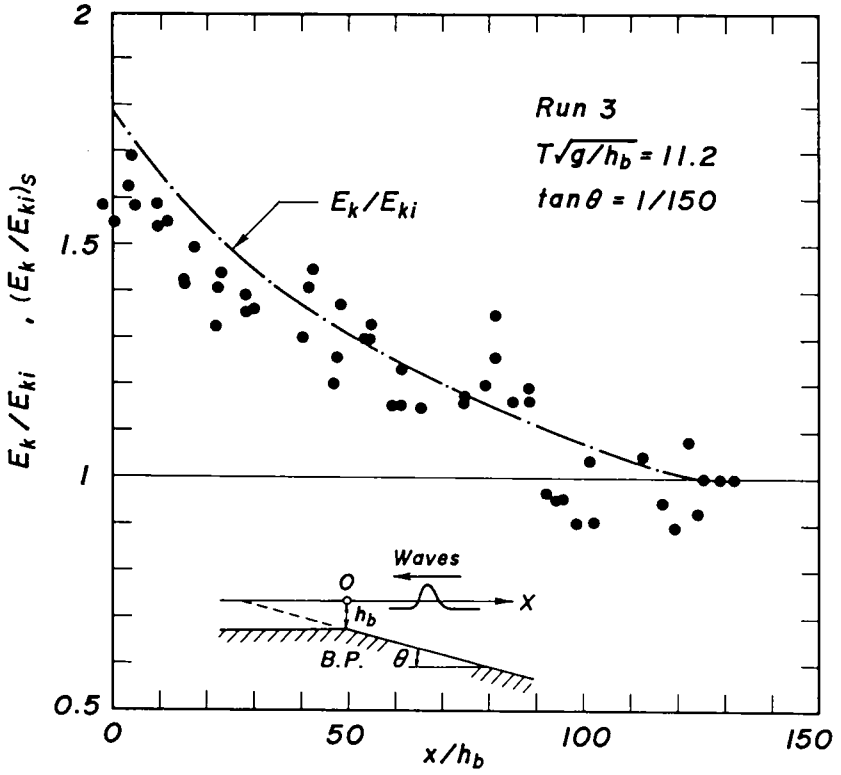

(2) Run 3

Fig. 3.25 Comparison of kinetic energies based both on the present theory and on the stream function theory.

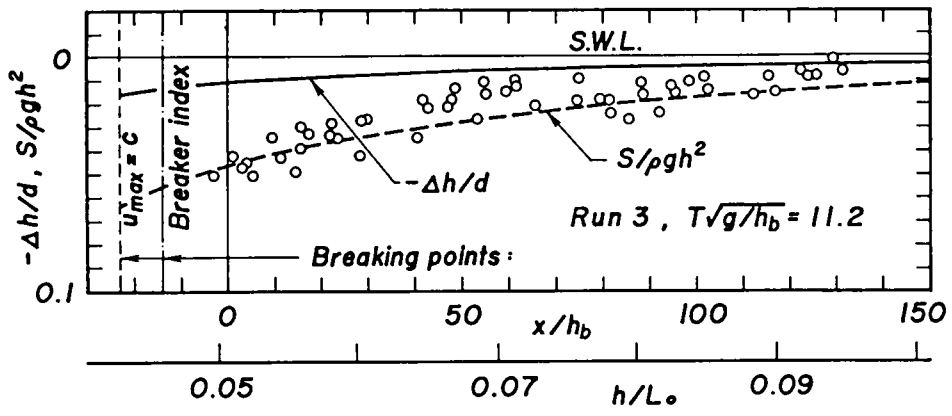

(1) Run 1

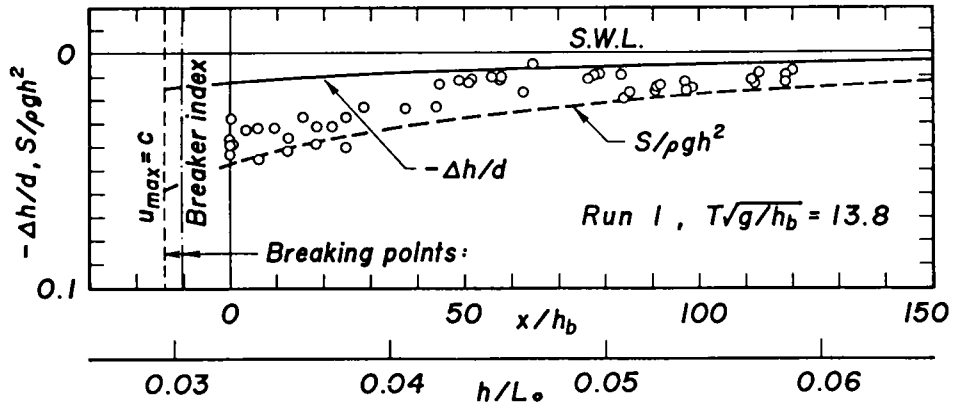

(2) Run 3

Fig. 3.26 Changes in wave set-down.

the discharge resupplied through the circulating duct in the wave tank. Therefore, the chief cause of the discrepancy in wave set-down may come from the fact that the mass flux is slightly greater than the resupplied discharge. This resembles the tendency of experimental wave lengths to be shorter and that the breaking points are, consequently, more seaward than the theoretical ones.

Investigating the experimental results of wave set-down in detail, it is to be noted that the wave set-down begins to change sharply near the initiating points of 50-60 for x_i/L_b, the same as for the potential energy and radiation stress.

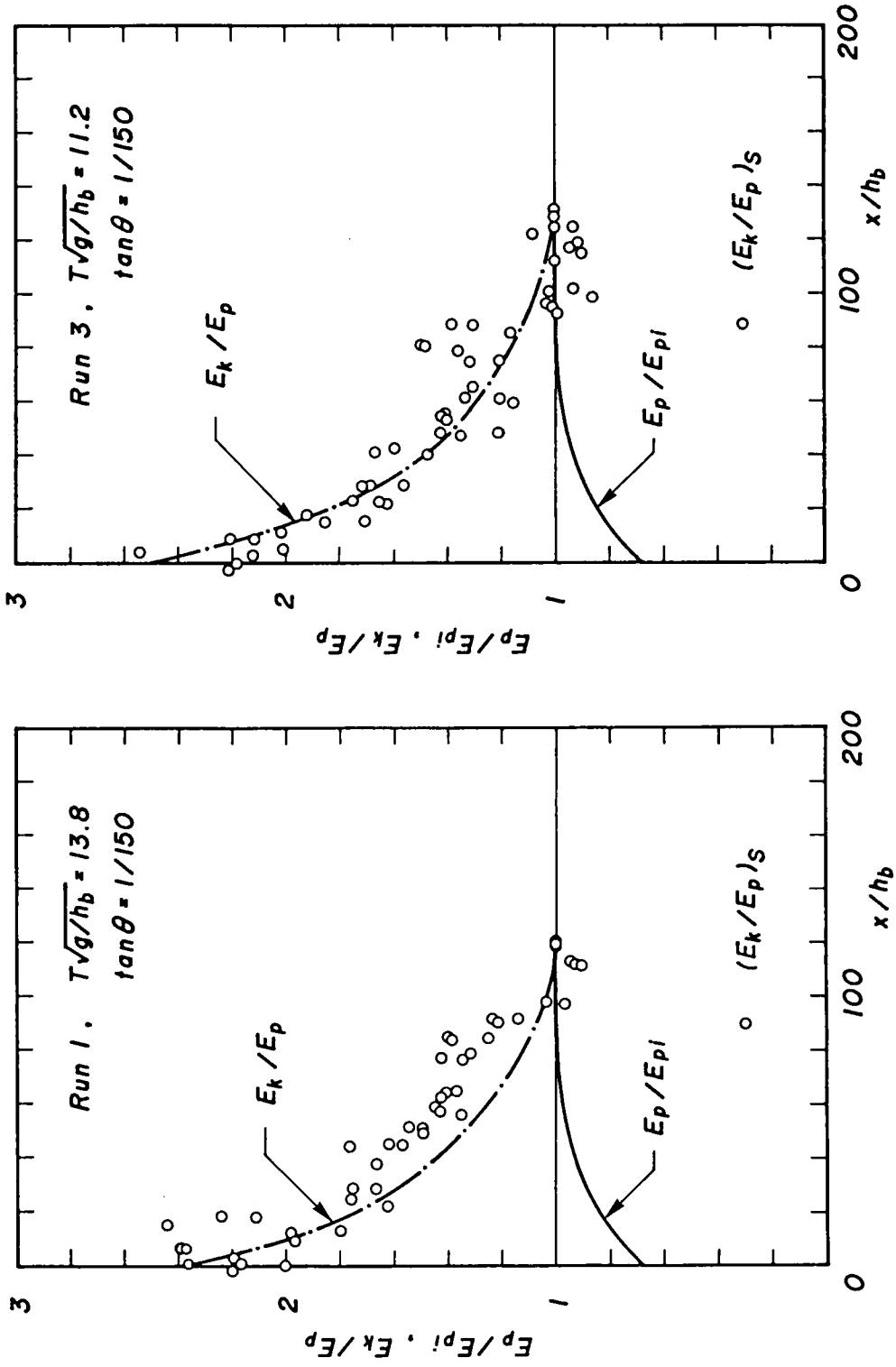

(2) Run 3

(1) Run 1

Fig. 3.27 Partition rates of wave energies.

Now, **Fig. 3.27** shows the partition rates of wave energies, which is defined as the ratio of kinetic to potential energies E_k/E_p and evaluated from the experimental curves shown in **Fig. 3.23.** Corresponding values of $(E_k/E_p)_s$ based on the stream function theory and on Eq. (3.6) are also plotted in the figure. Both values of E_k/E_p and $(E_k/E_p)_s$ agree fairly well as in **Fig. 3.25.** The ratios E_k/E_p approximately equal 2.4 at the breaking points. These results conclusively show that the kinetic energy is predominant when the wave breaks.

From the discussion above, it is concluded that the radiation stress S/S_i approaches a maximum value, while the potential energy E_p/E_{pi} decreases near the breaking point, resulting in the break in the energy balance of the wave, and that this phenomena has significant effects upon wave breaking. In addition, the imbalance in the partition rate of wave energies is confirmed as a premonitory phenomenon of wave breaking.

3.6 Conclusion

Breaking waves of spilling-type were generated on a mild slope of 1/150, the mass transport accompanied by the wave propagation not being restrained by the end walls of the wave tank. Characteristics relevant to wave breaking, such as the water particle velocity, mass transport, mass flux, radiation stress, wave set-down, and partition rate of wave energies, were investigated experimentally and compared with the theoretical estimation based on the law of the conservation of energy flux. The significant results are as follows:

From the behaviour of water particles, there exists the mass transport in the direction of wave propagation, and it extends over the whole water depth for waves on a slope as well as for progressive waves on water of uniform depth. As the water depth decreases, such as in the region near the

breaking point, water particle velocities in the upper zone of the water become much greater than those near the bottom.

The changes in dimensionless total mass flux and in so-called Stokes' drift with respect to the dimensionless wave period are similar to the theoretical estimation. It can be expected from the theory that the mass flux can be roughly estimated and that at just breaking it reaches to its maximum value, when the dimensionless wave period nearly equals 10.

As to the breaking conditions, the Rankine-Stokes breaking condition may be satisfied by spilling-type breakers, that is, the maximum horizontal component of water particle velocities becomes equal to the wave velocity at the crest of breaking waves. Breaking wave heights can be also simulated by the energy flux method or the breaker index.

The changes in wave energies, however, cannot be sufficiently explained based on the theoretical method. This indicates that wave breaking is subject not only to local hydrodynamical conditions, such as the Rankine-Stokes breaking condition and the occurrence of a cusp on the wave crest at just breaking, but also to internal breaking conditions which relate to whole properties of waves. From the experimental investigation of the changes in potential energy and in partition rate of wave energies due to the wave shoaling, the premonitory phenomenon occuring in the breaking waves can be described.

When waves propagate and approach the breaking points, the potential energy in waves abruptly begins to decrease in front of the breaking points, at which point the radiation stress takes on a maximum value. On the contrary, the kinetic energy abruptly increases because of the decrease in potential energy and predominantes. These phenomena have significant effects upon wave breaking. As a result, the partition rate of wave energies becomes imbalanced and waves fall into an unstable state as a whole, leading to the breaking.

References

1) Stokes,G.G.: On the theory of oscillatory waves, Trans. Camb. Phil. Soc., Vol.8, 1847, pp.441-455.
2) Goda,Y.: A synthesis of breaker index, Proc. JSCE, Vol.180, 1970, pp.39-49(in Japanese).
3) Longuet-Higgins,M.S.: Integral properties of periodic gravity waves of finite amplitude, Proc. Roy. Soc. Lond., A.342, 1975, pp.157-174.
4) Cokelet,E.D.: Steep gravity waves in water of arbitrary uniform depth, Proc. Roy. Soc. Lond., A.286, 1977, pp.183-230.
5) Williams,J.M.: Limiting gravity waves in water of finite depth, Phil. Trans. Roy. Soc. Lond., A.302, 1981, pp.139-188.
6) Longuet-Higgins,M.S. and R.W.Stewart: Radiation stress and mass transport in gravity waves, with application to "surf-beat", Jour. Fluid Mech., Vol.13, 1962, pp.481-504.
7) Skjelbreia,L.: Gravity waves, Stokes' third order approximation, Tables of functions, Council on Wave Reseach, The Engineering Foundation, ASCE, 1959, 337p.
8) Tsuchiya,Y. and T.Yasuda: Quasi-Stokes wave theory by the reductive perturbation method, Proc. 25th Japanese Conf. on Coastal Engrg., JSCE, 1978, pp.6-9(in Papanese).
9) Tsuchiya,Y. and T.Yasuda: A study on the new cnoidal wave theory, Proc. 21th Japanese Conf. on Coastal Engrg., JSCE, 1974, pp.65-71(in Japanese).
10) Schwartz,L.W.: Computer extension and analytic continuation of Stokes' expansion for gravity waves, Jour. Fluid Mech., Vol.62, 1974, pp.553-578.
11) Tsuchiya,Y., T.Okamura, T.Yasuda, and T.Yamashita: Mass transport in water waves of permanent type, Proc. 26th Japanese Conf. on Coastal Engrg., JSCE, 1979, pp.36-40(in Japanese).
12) Whitham,G.B.: Mass, momentum, and energy flux in water waves, Jour. Fluid Mech., Vol.12, 1962, pp.135-147.
13) Yasuda,T.: Studies on finite amplitude wave theories in shallow water, with validity of applications, Doctoral Dissertation, Kyoto Univ., 1978, 145p(in Japanese).
14) Longuet-Higgins,M.S. and R.W.Stewart: Radiation stresses in water waves; a physical discussion, with applications, Deep-Sea Res., Vol.11, 1964, pp.529-562.
15) Dean,R.G.: Stream function representation of nonlinear ocean waves, Jour. Geophys. Res. 1965, pp.4561-4572.

CHAPTER 4

DYNAMICS OF THE WIND-FORCED WAVES

4.1 Introduction

Wind above a certain threshold speed gives rise to ripples on a water surface. These ripples are chiefly governed by the surface tension and friction at the air-sea interface. Furthermore, as the wind speed surpasses the minimum speed necessary to create the ripples, the forces at the air-sea interface may become a function of the ripples created. At a higher wind speed with sufficient duration, oscillatory gravity waves arise and the direct pressure on the wave surface and effects of suction in the leeward eddies are added to the friction force. At the same time a vortical layer is formed at the air-sea interface as well as at the sea bottom. The friction caused by the ripples seems, however, to remain the most prominent component of the resultant forces on the wave surface.

This chapter investigates the steady oscillatory gravity waves generated by strong wind, termed "wind-forced waves", which occur in an equilibrium state of the internal and external forces, such as shear stress and pressure exerting on the wave surface, friction at the sea bottom, and viscous damping in water. Moreover, at a particular wind speed, energy transfer from wind to waves excedes the energy dissipation by bottom friction and by the viscoos damping in water, and this exess energy spills from wave crests often as "white caps" or "white horses". In this limiting situation, the successive formation of spilling regions ahead of wave crests becomes visible. This breaking phenomenon is also termed "breaking wave trains", a special type of wind-forced wave.

In Section 4.2 the formulation for the wind-forced waves is set out. For shallow water waves, the Korteweg-deVries equation[1] is the natual stating place, but it contains no energy dissipation or wind stress. The governing equations, which include terms for these external forces, can be derived for waves in a variable water depth from the Navier-Stokes equations of motion based on a perturbation procedure similar to that used by Keller[2]. Though they have the bottom friction and wind stress terms, they correspond fundamentally to the Boussinesq equations[3] for waves in a uniform water depth. These terms added are non-homogeneous terms and act like external forcing terms for wave motion by wind. Wind stresses surely distribute with respect to the phase of waves. The pressure is, therefore, assumed to vary in phase with the wave slope and the shear stress, in phase with the wave elevation. The effect of bottom friction is treated as an empirical friction law like Chézy's law.

In Section 4.3 formulas for wind-forced waves on water of uniform depth are developed and mathematical expressions for hydraulic quantities together with the existence condition for the waves are given. For steady waves, the governing equations reduce to one similar to the Korteweg-deVries-Burgers equation[4] having forcing terms by wind and an empirical dissipation term at the sea bottom. The periodic solution for this non-homogeneous partial differential equation is investigated with the use of the method of averaging and results in the solution for cnoidal waves, accompaning wind-induced currents. Next, the stability of the cnoidal wave solution in a phase plane is analyzed based on the usual stability theory for ordinary linear differential equations, and the most stable wave motion is defined by introducing a physical motion. The phase shift in the wave which renders the wave profile asymmetric is, then, determined from the phase equation which arose from the averaging procedure. Finally, the relations between wave properties and external forces necessary for non-

trivial wave motion to exist are determined, which leads the existence condition for wind-forced waves.

In Section 4.4 wind stresses exerting on wind-forced waves are presented in relation both to the friction at the sea bottom and to the Reynolds number. The shear stress at just breaking is evaluated using the results in Chapter 2.

In Section 4.5 the quantitative character of wind-forced waves is discussed. Wind-forced waves can be formulated as a one parameter family of a shear stress parameter; if the parameter, whose region is determined from the existence condition for wind-forced waves, is given together with the Reynolds number and the friction at the sea bottom, hydraulic quantities and wind stresses can be expressed as functions of the wave period for required wave heights. It is found that wind stresses, such as pressure and shear stress, have local maxima at certain wave periods, which relates to the distribution of wind stresses assumed. This may have strong effects on wave breaking. It is, furthermore, noted here that the shear stress acts like a positive external force. The wave profile and the horizontal component of water particle velocities averaged over the water depth become asymmetric if the bottom friction is reasonably great, and, for small water particle velocities, the velocity field in a frame of reference moving with the wave can be regarded as subcritical near the wave crest and supercritical near the wave trough, as in roll waves.

In Section 4.6 the analysis of wind-forced waves is verified by comparison with experimental and field data. First, to determine properties of the breaking wave trains, hydraulic experiments are carried out with a recirculating wind wave tank which can reproduce wind-generated waves accompaning wind-induced currents. It is found that wave periods and wave heights of breaking wave trains are nearly the same as for the peak frequencies of wind-wave power spectra and for significant wave heights,

respectively. The wind-induced currents have an important role in the mass transport of wave trains; because of the strong currents, the wave field may be regarded as a unidirectional flow, and there exists a critical depth in the frame of reference moving with the wave trains, occuring near the the mean water depth.

Secondly, field measurements from an observational pier give data for actual wind-forced waves. From the spectral analysis, significant wave periods are found to be smaller than those obtained from spectral peaks; this differs from the experimental results and may be attributed to the nonlinear wave interaction due to wave shoaling, such as soliton separation. The two different types of wind-forced waves corresponding to the significant wave periods and to the wave periods obtained from spectral peaks are discussed in comparison with the theoretical estimations.

According to the experiments and field observations, hydraulic quantities, such as wave velocity, mass transport velocity, average velocity, and wind-induced current, are in the theoretically estimated region, that is, the gross features of the wind-forced waves can be simulated satisfactorily by the present model. However, the actual and experimental wave profiles are more asymmetric and steep than the theoretically estimated ones, indicating the significant effect of bottom friction.

In Section 4.7 the preceding characters of wind-forced waves are summarized.

4.2 Governing Equations of Motion

When wind of sufficient duration and speed blows over a sea surface, a vortical layer is formed at an air-sea interface and a similar vortical layer is formed at the sea bottom due to the friction. Consider the two-dimensional motion of water between these two vortical layers which can be

defined as the regions in the flow where the water particle velocity varies rapidly with depth. These regions may be regarded as extermely thin compared with the water depth. Suppose that a wave propagates with a velocity c^* under a wind speed W_a^*. Take the origin of the coordinate (x^*, z^*) at the mean depth of water, the positive x^*-axis being in the direction of wave propagation and z^*-axis, vertically upwards, then the wave surface is defined by $z^* = \eta^*$ and the sea bottom, $z^* = -h^*(x^*)$ as shown in **Fig. 4.1**. Let u^*, w^*, t^*, p^*, and τ^* be the horizontal and vertical components of water particle velocities, time, pressure, and shear stress, respectively.

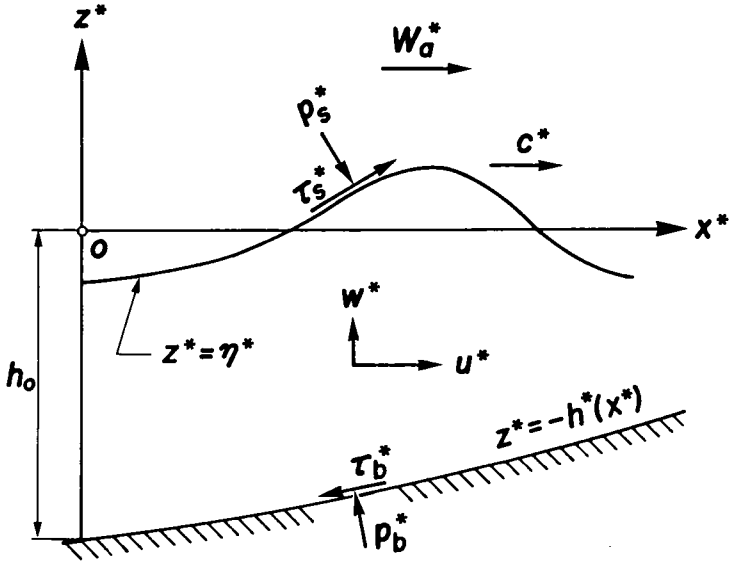

Fig. 4.1 Coordinate system.

Non-dimensional variables are, then, defined as

$$\left.\begin{aligned}
&(x,z) = (x^*,z^*)/h_0, \quad t = t^*\sqrt{g/h_0}, \quad \eta = \eta^*/h_0, \quad h = h^*/h_0, \\
&(u,w) = (u^*,w^*)/\sqrt{gh_0}, \quad c = c^*/\sqrt{gh_0}, \quad W_a = W_a^*/\sqrt{gh_0}, \\
&(p_s,p_b) = (p_s^*,p_b^*)/\rho g h_0, \quad (\tau_s,\tau_b) = (\tau_s^*,\tau_b^*)/\rho g h_0, \quad R = h_0\sqrt{gh_0}/\nu,
\end{aligned}\right\} \quad (4.1)$$

where the asterisk denotes a dimensional variable, and h_0 is a length representative of the water depth at the origin, g the acceleration of

gravity, ρ the density of water, R the Reynolds number, and ν the kinetic viscosity of water. The subscripts s and b denote quantities at the wave surface and sea bottom, respectively.

The equation of continuity and the Navier-Stokes equations of motion are, respectively, described as

$$\partial u/\partial x+\partial w/\partial z = 0, \tag{4.2}$$

$$\left.\begin{aligned} \partial u/\partial t+u(\partial u/\partial x)+w(\partial u/\partial z) &= -\partial p/\partial x+(1/R)\nabla^2 u, \\ \partial w/\partial t+u(\partial w/\partial x)+w(\partial w/\partial z) &= -1-\partial p/\partial z+(1/R)\nabla^2 w, \end{aligned}\right\} \tag{4.3}$$

where ∇^2 is the Laplacian. The kinematic boundary conditions at the air-sea interface and sea bottom are

$$\left.\begin{aligned} \partial\eta/\partial t+u(\partial\eta/\partial x)-w = 0 \qquad & \text{at } z = \eta-\delta_s \fallingdotseq \eta, \\ u(dh/dx)+w = 0 \qquad & \text{at } z = -h+\delta_b \fallingdotseq -h, \end{aligned}\right\} \tag{4.4}$$

where δ is the boundary layer thickness assuming that $\delta_s \ll 1$, and $\delta_b \ll 1$. In addition, the continuity conditions for stresses at the two interfaces are given by

$$p_s = p - 2\frac{\partial w/\partial z-(\partial u/\partial z+\partial w/\partial x)(\partial\eta/\partial x)+(\partial u/\partial x)(\partial\eta/\partial x)^2}{R\{1+(\partial\eta/\partial x)^2\}} \qquad \text{at } z = \eta-\delta_s \fallingdotseq \eta, \tag{4.5.1}$$

$$\tau_s = \frac{(\partial u/\partial z+\partial w/\partial x)\{1-(\partial\eta/\partial x)^2\}-2(\partial u/\partial x-\partial w/\partial z)(\partial\eta/\partial x)}{R\{1+(\partial\eta/\partial x)^2\}} \qquad \text{at } z = \eta-\delta_s \fallingdotseq \eta, \tag{4.5.2}$$

$$p_b = p - 2\frac{\partial w/\partial z+(\partial u/\partial z+\partial w/\partial x)(dh/dx)+(\partial u/\partial x)(dh/dx)^2}{R\{1+(dh/dx)^2\}} \qquad \text{at } z = -h+\delta_b \fallingdotseq -h, \tag{4.6.1}$$

$$\tau_b = \frac{(\partial u/\partial z+\partial w/\partial x)\{1-(dh/dx)^2\}+2(\partial u/\partial x-\partial w/\partial z)(dh/dx)}{R\{1+(dh/dx)^2\}} \qquad \text{at } z = -h+\delta_b \fallingdotseq -h. \tag{4.6.2}$$

There are two important parameters associated with shallow water waves. One is the ratio of amplitude to depth, and the other is the ratio of depth to length representative of the horizontal scale. These parameters will be defined by ε and σ, respectively. For all long wave theories $\sigma \ll 1$, and

for finite amplitude wave theory $\varepsilon = O(1)$, while ε and σ^2 are of the same order for waves governed by the Boussinesq or the Korteweg-deVries equation. Here, appropriately choosing the horizontal length scale, the wave motion with the Ursell number[5] $Ur \fallingdotseq 1$, i.e. $\varepsilon \fallingdotseq \sigma^2$, will be discussed. The physical quantities can, then, be expanded in the forms

$$\left.\begin{aligned} u &= \varepsilon u_1 + \varepsilon^2 u_2 + \ldots, \\ w &= \sigma(\varepsilon w_1 + \varepsilon^2 w_2 + \ldots), \\ \eta &= \varepsilon \eta_1 + \varepsilon^2 \eta_2 + \ldots, \\ p &= -z + \varepsilon p_1 + \varepsilon^2 p_2 + \ldots, \\ \tau &= \sigma\varepsilon(\varepsilon\tau_1 + \varepsilon^2\tau_2 + \ldots). \end{aligned}\right\} \tag{4.7}$$

Furthermore, independent variables x and t are scaled such that

$$(x_1, t_1) = \sigma(x, t). \tag{4.8}$$

In the following analysis, assume further that

$$\nu_1 \equiv 1/(\sigma R) = O(1), \tag{4.9}$$

and that all variables and their derivatives with respect to x_1 and t_1 are of the order of unity. Since Eq. (4.5) must be held just below $z \fallingdotseq \eta$, it is impossible to approximate these boundary conditions by a power series around $z = 0$ as in previous finite amplitude wave theories for irrotational wave motion. Though this limitation is, on the contrary, not necessary for the kinematic boundary condition at $z \fallingdotseq \eta$, the first of Eq. (4.4), the expansion procedure using a power series will not be adopted in order to unify the treatment of all boundary conditions.

Before developing the analysis, with the aid of the average velocity defined by

$$\bar{u} = \frac{1}{h+\eta}\int_{-h}^{\eta} u \, dz, \tag{4.10}$$

the usual equations of continuity and momentum become

$$\frac{\partial \eta}{\partial t} + \frac{\partial}{\partial x}\{\bar{u}(h+\eta)\} = 0, \tag{4.11}$$

$$\left.\begin{aligned}
&\frac{\partial \bar{u}}{\partial t}+\bar{u}\frac{\partial \bar{u}}{\partial x}+\frac{1}{h+\eta}\frac{\partial}{\partial x}\int_{-h}^{\eta}(u-\bar{u})^2 dz = \frac{1}{(h+\eta)}\int_{-h}^{\eta}\left\{-\frac{\partial p}{\partial x}+\frac{1}{R}\frac{\partial \omega}{\partial z}\right\}dz,\\
&\omega = \frac{\partial u}{\partial z}-\frac{\partial w}{\partial x},
\end{aligned}\right\} \qquad (4.12)$$

by integrating Eq. (4.2) and the first of Eq. (4.3) with respect to z, where ω is the vorticity. Here, it is clearly important that the pressure and visous terms be evaluated properly. Chester[6], for instance, has evaluated the pressure term, assuming that the dispersion effect is small and that it can be accounted for by a two-dimensional linear theory with dissipation neglected, which led to Boussinesq's dispersion term.

Based on the scheme of approximations above, Eq. (4.2) to Eq. (4.6) give the first order equations of approximations

$$\left.\begin{aligned}
&\partial u_1/\partial x_1+\partial w_1/\partial z = 0,\\
&\partial u_1/\partial t_1+\partial p_1/\partial x_1-\nu_1(\partial^2 u_1/\partial z^2) = 0,\\
&\partial p_1/\partial z = 0,\\
&\partial \eta_1/\partial t_1-w_1 = 0 \qquad \text{at } z \fallingdotseq \varepsilon\eta_1,\\
&u_1(dh/dx_1)+w_1 = 0 \qquad \text{at } z \fallingdotseq -h,\\
&p_1-p_{s1} = 0 \qquad \text{at } z \fallingdotseq \varepsilon\eta_1,\\
&\nu_1(\partial u_1/\partial z) = 0 \qquad \text{at } z \fallingdotseq \varepsilon\eta_1,\\
&p_1-p_{b1} = 0 \qquad \text{at } z \fallingdotseq -h,\\
&\nu_1(\partial u_1/\partial z) = 0 \qquad \text{at } z \fallingdotseq -h.
\end{aligned}\right\} \qquad (4.13)$$

At both $z \fallingdotseq \varepsilon\eta_1$ and $z \fallingdotseq -h$, $\partial u_1/\partial z = 0$, and since the forth of Eq. (4.13) indicates that the motion is for small amplitude waves, the possible velocity u_1 is independent of z, i.e.

$$u_1 = u_1(x_1, t_1) = \bar{u}_1. \qquad (4.14)$$

The third of Eq. (4.13) gives

$$p_1 = \eta_1+p_{s1}(x_1, t_1), \qquad (4.15)$$

which combined with the boundary condition $-z+\varepsilon(p_1-p_{s1}) = 0$ at $z \fallingdotseq \varepsilon\eta_1$. The equation of continuity can be obtained by integrating the first of Eq.

(4.13) with respect to z from $-h$ to $\varepsilon\eta_1$ and by leaving the higher order terms of ε, such as $\varepsilon\eta_1(\partial\bar{u}_1/\partial x_1)$, to the next order approximation.

$$\partial\eta_1/\partial t_1+\partial(\bar{u}_1 h)/\partial x_1 = 0. \tag{4.16}$$

The second of Eq.(4.13) gives the equation of momentum

$$\partial\bar{u}_1/\partial t_1+\partial\eta_1/\partial x_1 = -\partial p_{s1}/\partial x_1. \tag{4.17}$$

These are equations for linearized long waves due to the wind pressure exerting on the wave surface. The vertical velocity w_1 can be found by integrating the first of Eq. (4.13) with respect to z and by applying the boundary condition at $z = -h$,

$$w_1 = -\partial(\bar{u}_1 h)/\partial x_1 - z(\partial\bar{u}_1/\partial x_1). \tag{4.18}$$

The pressure at the sea bottom is also given by

$$p_{b1} = \eta_1 + p_{s1}(x_1, t_1). \tag{4.19}$$

Using the results of the first order approximation above, the second order equations are followed by

$$\left.\begin{aligned}
&\partial u_2/\partial x_1+\partial w_2/\partial z = 0,\\
&\partial u_2/\partial t_1+u_1(\partial u_1/\partial x_1)+\partial p_2/\partial x_1-\nu_1(\partial^2 u_1/\partial x_1{}^2+\partial^2 u_2/\partial z^2) = 0,\\
&\partial w_1/\partial t_1+\partial p_2/\partial z = 0,\\
&\partial\eta_2/\partial t_1+ u_1(\partial\eta_1/\partial x_1)-w_2 = 0 \qquad \text{at } z \fallingdotseq \varepsilon\eta_1+\varepsilon^2\eta_2,\\
&u_2(dh/dx_1)+w_2 = 0 \qquad \text{at } z \fallingdotseq -h,\\
&p_2 - p_{s2} - 2\nu_1(\partial w_1/\partial z) = 0 \qquad \text{at } z \fallingdotseq \varepsilon\eta_1+\varepsilon^2\eta_2,\\
&\tau_{s1} - \nu_1(\partial u_2/\partial z+\partial w_1/\partial x_1) = 0 \qquad \text{at } z \fallingdotseq \varepsilon\eta_1+\varepsilon^2\eta_2,\\
&p_2 - p_{b2} - 2\nu_1(\partial w_1/\partial z) = 0 \qquad \text{at } z \fallingdotseq -h,\\
&\tau_{b1} - \nu_1\{\partial u_2/\partial z+\partial w_1/\partial x_1+2(\partial u_1/\partial x_1-\partial w_1/\partial z)(dh/dx_1)\} = 0\\
&\qquad\qquad \text{at } z \fallingdotseq -h.
\end{aligned}\right\} \tag{4.20}$$

The third of Eq. (4.20) integrates to

$$p_2 = \eta_2 + p_{s2} + z\frac{\partial^2}{\partial t_1\partial x_1}(\bar{u}_1 h)+\frac{z^2}{2}\frac{\partial^2\bar{u}_1}{\partial t_1\partial x_1} - 2\nu_1\frac{\partial\bar{u}_1}{\partial x_1}, \tag{4.21}$$

where the boundary condition at $z = \varepsilon\eta_1+\varepsilon^2\eta_2$ has been used. The equation of continuity becomes

$$\frac{\partial \eta_2}{\partial t_1} + \bar{u}_1 \frac{\partial \eta_1}{\partial x_1} + \frac{\partial}{\partial x_1}(\bar{u}_2 h) = 0, \tag{4.22}$$

by integrating the first of Eq. (4.20) with respect to z. The equation of momentum in terms of the average velocity $\bar{u}_2$ can be obtained from the second of Eq. (4.20) by integrating with respect to z and by substituting for p_2,

$$\frac{\partial \bar{u}_2}{\partial t_1} + \bar{u}_1 \frac{\partial \bar{u}_1}{\partial x_1} + \frac{\partial \eta_2}{\partial x_1} = -\frac{\partial p_{s2}}{\partial x_1} + \frac{\tau_{s1} - \tau_{b1}}{h} + 4\nu_1 \left\{ \frac{\partial^2 \bar{u}_1}{\partial x_1^2} + \frac{1}{h}\frac{dh}{dx_1}\frac{\partial \bar{u}_1}{\partial x_1} \right\}$$

$$+ \frac{h}{2}\frac{\partial^3}{\partial t_1 \partial x_1^2}(\bar{u}_1 h) - \frac{h^2}{6}\frac{\partial^3 \bar{u}_1}{\partial t_1 \partial x_1^2}, \tag{4.23}$$

where the boundary conditions at $z = \varepsilon\eta_1 + \varepsilon^2\eta_2$ and $z = -h$, the seventh and ninth of Eq. (4.20), have been used to express the viscous terms by τ_{s1} and τ_{b1}. From the eighth of Eq. (4.20), the pressure at the sea bottom becomes

$$p_{b2} = \eta_2 + p_{s2} - h\frac{\partial^2}{\partial t_1 \partial x_1}(\bar{u}_1 h) + \frac{h^2}{2}\frac{\partial^2 \bar{u}_1}{\partial t_1 \partial x_1}. \tag{4.24}$$

Accordingly, in terms of $\bar{u}$, the equations of continuity and momentum become

$$\frac{\partial \eta}{\partial t} + \frac{\partial}{\partial x}\{\bar{u}(h+\eta)\} = O(\varepsilon^3), \tag{4.25}$$

$$\frac{\partial \bar{u}}{\partial t} + \bar{u}\frac{\partial \bar{u}}{\partial x} + \frac{\partial \eta}{\partial x} = -\frac{\partial p_s}{\partial x} + \frac{\tau_s - \tau_b}{h+\eta} + \frac{4}{R}\left\{ \frac{\partial^2 \bar{u}}{\partial x^2} + \frac{1}{h}\frac{dh}{dx}\frac{\partial \bar{u}}{\partial x} \right\}$$

$$+ \frac{h}{2}\frac{\partial^3}{\partial t \partial x^2}(\bar{u} h) - \frac{h^2}{6}\frac{\partial^3 \bar{u}}{\partial t \partial x^2} + O(\varepsilon^3), \tag{4.26}$$

which are formed by adding ε times Eqs. (4.22) and (4.23) to Eqs. (4.16) and (4.17) respectively and by changing back to the variables x and t. Similarly, the vertical velocity and pressure are, respectively, given by

$$w = -\frac{\partial}{\partial x}(\bar{u} h) - z\frac{\partial \bar{u}}{\partial x} + O(\varepsilon^{5/2}), \tag{4.27}$$

$$p = -z + \eta + p_s + z\frac{\partial^2}{\partial t \partial x}(\bar{u}h) + \frac{z^2}{2}\frac{\partial^2 \bar{u}}{\partial t \partial x} - \frac{2}{R}\frac{\partial \bar{u}}{\partial x} + O(\varepsilon^3). \tag{4.28}$$

The third term in the general equation (4.12) is of the order of ε^4, thus this term can be neglected. In Eq. (4.26) the second order effect of the variations in water depth remains chiefly in the fourth and fifth terms of the right-hand side. They are the same as those for long waves, obtained by Peregrine[7] on the assumption of irrotationality of wave motion. This assumption is not adopted in the present analysis, but the same terms have been derived from the fact that the horizontal velocity of the first order approximation is independent of z. The depth effect also occurs in the viscous term, and, furthermore, Eq.(4.26) contains the significant terms due to the damping by viscosity of water, the external forces caused by wind, and the friction at the sea bottom.

4.3 Wind-Forced Waves on Water of Uniform Depth

(1) Basic Equations

For waves on water of the uniform depth, $h = 1$, the equations of continuity and momentum respectively reduce to

$$\frac{\partial \eta}{\partial t} + \frac{\partial}{\partial x}\{\bar{u}(1+\eta)\} = 0, \tag{4.29}$$

$$\frac{\partial \bar{u}}{\partial t} + \bar{u}\frac{\partial \bar{u}}{\partial x} + \frac{\partial \eta}{\partial x} - \frac{1}{3}\frac{\partial^3 \bar{u}}{\partial t \partial x^2} = -\frac{\partial p_s}{\partial x} + \frac{\tau_s - \tau_b}{1+\eta} + \frac{4}{R}\frac{\partial^2 \bar{u}}{\partial x^2}. \tag{4.30}$$

These equations with damping and external forces are just variants of the Boussinesq equations. The external forces can be assumed as follows: the pressure and shear stress may vary along the wave surface and be asymmetric in the front and rear sides of the wave crest, so the surface displacement η and its slope $\partial\eta/\partial x$, at least, effect on their variations. However, the

slope effect is, as usual, chiefly concerned with the pressure, then the effect of wave elevation may predominate in generation of the shear stress. In addition, these effects can be assumed to be linear in the lowest order approximation. The pressure can, then, be expressed by the form

$$p_s = C_s\,(\rho_a/\rho)(W_a - c)^2 \cdot (\partial\eta/\partial x) \equiv \sigma_p \cdot (\partial\eta/\partial x), \text{ say,} \tag{4.31}$$

which varies with respect to the wave slope, and the shear stress can take the form of the variation with respect to the wave elevation

$$\tau_s = C_d(\rho_a/\rho)(W_a - u_s)^2(1 + \delta_1\eta) \fallingdotseq C_d(\rho_a/\rho)\,W_a^2(1 + \delta_1\eta), \tag{4.32}$$

where ρ_a is the density of the air, C_s and C_d are the seltering and drag coefficients, respectively, and u_s is the water particle velocity at the wave surface, then $W_a \gg u_s$. δ_1 is a coefficient to be discussed later. Eq. (4.32) is similar to the assumption which was used by Stewart[8] and Longuet-Higgins[9] to discussed variable surface stresses on small amplitude waves. From analogy to storm surges[10], it follows that

$$\begin{aligned}\tau_s - \tau_b &= (1 + m_b)\,C_d(\rho_a/\rho)\,W_a^2 \cdot (1 + \delta_1\eta) - s\,\bar{u}^2 \\ &\equiv \sigma_\tau \cdot (1 + \delta_1\eta) - s\bar{u}^2, \text{ say,}\end{aligned} \tag{4.33}$$

where the dissipation at the sea bottom is assumed to be given by Chézy's law, s is the coefficient of bottom friction, and m_b the coefficient of the effect of bottom friction on the shear stress. If Eqs. (4.31) and (4.33) are substituted into Eq. (4.30), the basic equation of momentum reduces to

$$\frac{\partial\bar{u}}{\partial t} + \bar{u}\frac{\partial\bar{u}}{\partial x} + \frac{\partial\eta}{\partial x} - \frac{1}{3}\frac{\partial^3\bar{u}}{\partial t\,\partial x^2} = -\sigma_p\frac{\partial^2\eta}{\partial x^2} + \frac{4}{R}\frac{\partial^2\bar{u}}{\partial x^2} + \sigma_\tau\frac{1 + \delta_1\eta}{1 + \eta} - s\frac{\bar{u}^2}{1 + \eta}. \tag{4.34}$$

A steady state solution can be found by looking for a solution in which $\bar{u}$ and η are functions of the single variable

$$\xi = x - ct. \tag{4.35}$$

The equation of continuity, thus, integrates to

$$(1 + \eta)(c - \bar{u}) = \text{const.} = Q, \text{ say,} \tag{4.36}$$

where Q is called the progressive discharge[11]. Therefore, eliminating η in Eq. (4.34) with the aid of Eq. (4.36) gives

$$\frac{1}{3}\frac{d^3U}{d\xi^3} + \left[\left\{1 + 2\frac{\bar{Q}}{c^2}\right\}U - \left\{1 - \frac{\bar{Q}}{c^2}\right\}\right]\frac{dU}{d\xi}$$

$$= \left\{\frac{4}{\bar{R}} - \bar{\sigma}_p\bar{Q}\right\}\frac{d^2U}{d\xi^2} + \frac{\bar{\sigma}_\tau}{\bar{Q}}\left\{(1-\delta_1) + \delta_1\bar{Q} - (1-\delta_1)U\right\} - \frac{S}{\bar{Q}}U^2, \qquad (4.37)$$

in which

$$U = \bar{u}/c, \quad \bar{Q} = Q/c, \quad \bar{\sigma}_\tau = \sigma_\tau/c^2, \quad \bar{\sigma}_p = \sigma_p/c^2, \quad \bar{R} = Rc, \qquad (4.38)$$

and terms of the order of U^3 are neglected.

The quadratic equation in the right-hand side of Eq. (4.37),

$$U^2 + (\bar{\sigma}_\tau/S)(1-\delta_1)U - (\bar{\sigma}_\tau/S)(\delta_1\bar{Q} + 1 - \delta_1) = 0, \qquad (4.39)$$

will have real roots for real coefficients, and they are uniform flow solutions of the equation itself. Thus, let these real roots be $-U_1$ and U_2. The transformation

$$\mathfrak{U} = \left\{1 + 2\frac{\bar{Q}}{c^2}\right\}U - \left\{1 - \frac{\bar{Q}}{c^2}\right\} \qquad (4.40)$$

leads Eq. (4.37) to

$$\left.\begin{aligned} &\frac{1}{3}\frac{d^3\mathfrak{U}}{d\xi^3} + \mathfrak{U}\frac{d\mathfrak{U}}{d\xi} = \mu G(\mathfrak{U}), \\ &\mu G(\mathfrak{U}) = \varepsilon_1\frac{d^2\mathfrak{U}}{d\xi^2} + \varepsilon_2(\mathfrak{U}_1 + \mathfrak{U})(\mathfrak{U}_2 - \mathfrak{U}), \end{aligned}\right\} \qquad (4.41)$$

with

$$\left.\begin{aligned} &\varepsilon_1 = \frac{4}{\bar{R}} - \bar{\sigma}_p\bar{Q}, \quad \varepsilon_2 = \left\{\frac{S}{\bar{Q}}\right\}\Big/\left\{1 + 2\frac{\bar{Q}}{c^2}\right\}, \\ &\mathfrak{U}_1 = \left\{1 + 2\frac{\bar{Q}}{c^2}\right\}U_1 + \left\{1 - \frac{\bar{Q}}{c^2}\right\}, \\ &\mathfrak{U}_2 = \left\{1 + 2\frac{\bar{Q}}{c^2}\right\}U_2 - \left\{1 - \frac{\bar{Q}}{c^2}\right\}. \end{aligned}\right\} \qquad (4.42)$$

This equation with an empirical dissipation term is the generalization of the Korteweg-deVries-Burgers equation($\varepsilon_2 = 0$) for steady state wave motion and specifies the distribution of average velocity generated by wind.

Johnson[4] used the Korteweg-deVries-Burgers equation in the analysis for the undular bore, while Byatt-Smith[12] dealt with a similar equation for the case of $\varepsilon_1 = 0$ to see if the steady undular bore is possible.

(2) Method of Averaging

When $\varepsilon_1 = \varepsilon_2 = 0$, Eq. (4.41) can be integrated twice to give

$$(1/3)(d\mathfrak{U}/d\xi)^2 = -(1/3)\mathfrak{U}^3 + A\,\mathfrak{U} + B, \tag{4.43}$$

where A and B are integral constants. This equation can be integrated again in terms of the Jacobian elliptic function of the second kind, leading to the cnoidal wave solution;

$$\mathfrak{U} = \beta + (\alpha - \beta)\,\mathrm{cn}^2 v, \qquad v = \frac{1}{2}\sqrt{2\alpha + \beta}\,(\xi + \xi_0), \qquad k^2 = \frac{\alpha - \beta}{2\alpha + \beta}, \tag{4.44}$$

where α and β are the largest two roots of the equation $-\mathfrak{U}^3 + 3A\mathfrak{U} + 3B = 0$, k is the modulus of the elliptic functions, and the integral constant ξ_0, the phase.

The cnoidal wave expressed by Eq. (4.44) is periodic with respect to ξ and has the wave length

$$L = 4K/\sqrt{2\alpha + \beta}, \tag{4.45}$$

where K is the complete elliptic integral of the first kind. The wave length, of course, depends on (α,β) or (A,B). Therefore, the cnoidal wave train for Eq. (4.41) can be written in the form $\mathfrak{U} = \mathfrak{F}(\xi + \xi_0, A, B)$, where μ is assumed to be a small parameter as in the theory of nonlinear oscillations, and A, B (or α, β), and ξ_0 are slowly varying functions of ξ to be determined.

The dependence of A, B, and ξ_0 on ξ is derived as follows[12]:

Setting

$$\xi + \xi_0 = \chi(\xi) \tag{4.46}$$

and assuming that A and B are functions of ξ give

$$\frac{d\mathfrak{U}}{d\xi} = \frac{\partial \mathfrak{F}}{\partial \chi} + \frac{\partial \mathfrak{F}}{\partial \chi}\frac{d\xi_0}{d\xi} + \frac{\partial \mathfrak{F}}{\partial A}\frac{dA}{d\xi} + \frac{\partial \mathfrak{F}}{\partial B}\frac{dB}{d\xi} = \frac{\partial \mathfrak{F}}{\partial \chi}, \tag{4.47}$$

on the condition that

$$\frac{\partial \mathfrak{F}}{\partial \chi}\frac{d\xi_0}{d\xi} + \frac{\partial \mathfrak{F}}{\partial A}\frac{dA}{d\xi} + \frac{\partial \mathfrak{F}}{\partial B}\frac{dB}{d\xi} = 0. \tag{4.48}$$

The derivative of Eq. (4.47) again becomes

$$\frac{d^2\mathfrak{U}}{d\xi^2} = \frac{\partial^2 \mathfrak{F}}{\partial \chi^2} + \frac{\partial^2 \mathfrak{F}}{\partial \chi^2}\frac{d\xi_0}{d\xi} + \frac{\partial^2 \mathfrak{F}}{\partial \chi \partial A}\frac{dA}{d\xi} + \frac{\partial^2 \mathfrak{F}}{\partial \chi \partial B}\frac{dB}{d\xi}. \tag{4.49}$$

Furthermore, the derivatives of

$$(1/3)(d\mathfrak{F}/d\chi)^2 = -(1/3)\,\mathfrak{F}^3 + A\,\mathfrak{F} + B \tag{4.50}$$

with respect to χ, A, and B respectively become

$$\left.\begin{aligned} \frac{2}{3}\frac{\partial \mathfrak{F}}{\partial \chi}\frac{\partial^2 \mathfrak{F}}{\partial \chi^2} &= -\mathfrak{F}^2\frac{\partial \mathfrak{F}}{\partial \chi} + A\frac{\partial \mathfrak{F}}{\partial \chi}, \\ \frac{2}{3}\frac{\partial \mathfrak{F}}{\partial \chi}\frac{\partial^2 \mathfrak{F}}{\partial \chi \partial A} &= -\mathfrak{F}^2\frac{\partial \mathfrak{F}}{\partial A} + A\frac{\partial \mathfrak{F}}{\partial A} + \mathfrak{F}, \\ \frac{2}{3}\frac{\partial \mathfrak{F}}{\partial \chi}\frac{\partial^2 \mathfrak{F}}{\partial \chi \partial B} &= -\mathfrak{F}^2\frac{\partial \mathfrak{F}}{\partial B} + A\frac{\partial \mathfrak{F}}{\partial B} + 1. \end{aligned}\right\} \tag{4.51}$$

Multiplying these equations by $d\xi_0/d\xi$, $dA/d\xi$, and $dB/d\xi$, respectively, and adding both sides gives

$$\frac{2}{3}\left\{\frac{\partial^2 \mathfrak{F}}{\partial \chi^2}\frac{d\xi_0}{d\xi} + \frac{\partial^2 \mathfrak{F}}{\partial \chi \partial A}\frac{dA}{d\xi} + \frac{\partial^2 \mathfrak{F}}{\partial \chi \partial B}\frac{dB}{d\xi}\right\}\frac{\partial \mathfrak{F}}{\partial \chi} = \mathfrak{F}\frac{dA}{d\xi} + \frac{dB}{d\xi}, \tag{4.52}$$

because of Eq. (4.48). If the condition

$$\mathfrak{F}\frac{dA}{d\xi} + \frac{dB}{d\xi} = 0 \tag{5.53}$$

is imposed, Eq. (4.49) becomes

$$d^2\mathfrak{U}/d\xi^2 = d^2\mathfrak{F}/d\chi^2, \tag{4.54}$$

with the aid of Eq. (4.52), and thus,

$$\frac{d^3\mathfrak{U}}{d\xi^3} = \frac{\partial^3\mathfrak{F}}{\partial\chi^3} + \frac{\partial^3\mathfrak{F}}{\partial\chi^3}\frac{d\xi_0}{d\xi} + \frac{\partial^3\mathfrak{F}}{\partial\chi^2\partial A}\frac{dA}{d\xi} + \frac{\partial^3\mathfrak{F}}{\partial\chi^2\partial B}\frac{dB}{d\xi}. \tag{4.55}$$

Similarly, taking the derivatives of Eq. (4.51) with respect to χ and multiplying by $d\xi_0/d\xi$, $dA/d\xi$, and $dB/d\xi$, and adding yields

$$\frac{\partial^3\mathfrak{F}}{\partial\chi^3}\frac{d\xi_0}{d\xi} + \frac{\partial^3\mathfrak{F}}{\partial\chi^2\partial A}\frac{dA}{d\xi} + \frac{\partial^3\mathfrak{F}}{\partial\chi^2\partial B}\frac{dB}{d\xi} = \frac{3}{2}\frac{dA}{d\xi}, \tag{4.56}$$

with the help of Eqs. (4.48), (4.52), and (4.53). Substituting Eq. (4.56) into Eq. (4.55) leads to

$$\frac{d^3\mathfrak{U}}{d\xi^3} = \frac{\partial^3\mathfrak{F}}{\partial\chi^3} + \frac{3}{2}\frac{dA}{d\xi}. \tag{4.57}$$

From Eqs. (4.41), (4.47), and (4.57), it follows that

$$\frac{1}{3}\frac{\partial^3\mathfrak{F}}{\partial\chi^3} + \frac{1}{2}\frac{dA}{d\xi} + \mathfrak{F}\frac{\partial\mathfrak{F}}{\partial\chi} = \mu G(\mathfrak{F}), \tag{4.58}$$

which reduces to

$$dA/d\xi = 2\mu G(\mathfrak{F}), \tag{4.59}$$

because of Eq. (4.50). Therefore, Eqs. (4.53) and (4.48) respectively give

$$dB/d\xi = -2\mu\mathfrak{F}G(\mathfrak{F}), \tag{4.60}$$

$$\frac{d\xi_0}{d\xi} = 2\mu G(\mathfrak{F})\frac{\mathfrak{F}(\partial\mathfrak{F}/\partial B) - \partial\mathfrak{F}/\partial A}{\partial\mathfrak{F}/\partial\chi} \equiv 2\mu\mathfrak{K}, \text{ say.} \tag{4.61}$$

Consequently, the dependence of A, B, and ξ_0 on ξ is governed by Eqs. (4.59), (4.60), and (4.61), respectively. Since χ is the function of A and B through α and β, if the change of variables from χ to Φ, defined by

$$\chi = \xi + \xi_0 = L(A,B)\cdot\Phi, \tag{4.62}$$

is introduced to exclude the dependence, this makes $\mathfrak{F}$, expressed in terms of A, B, and Φ, periodic in Φ with a unit wave length. A, B, and ξ_0 being functions of ξ, it follows that

$$L\frac{d\Phi}{d\xi} = 1 + 2\mu\mathfrak{R}, \tag{4.63}$$

with

$$\mathfrak{R} = \mathfrak{K} - \left\{\frac{\partial L}{\partial A} - \mathfrak{F}\frac{\partial L}{\partial B}\right\} G(\mathfrak{F}) \cdot \Phi, \tag{4.64}$$

where Eqs. (4.59), (4.60), and (4.61) have been used. The change of variables also transforms Eqs. (4.59) and (4.60) into

$$\frac{\partial A}{\partial \Phi} = 2\mu L \frac{G(\mathfrak{F})}{1 + 2\mu \mathfrak{R}}, \tag{4.65}$$

$$\frac{\partial B}{\partial \Phi} = -2\mu L \frac{\mathfrak{F}\, G(\mathfrak{F})}{1 + 2\mu \mathfrak{R}}. \tag{4.66}$$

It will be proven that $\mathfrak{R}$, expressed in terms of A, B, and Φ, is periodic in Φ with a unit wave length. The derivatives of both sides of

$$\mathfrak{F}\{\chi + L(A,B), A, B\} = \mathfrak{F}(\chi, A, B) \tag{4.67}$$

with respect to A and B are

$$\left.\begin{aligned} \frac{\partial L}{\partial A}\frac{\partial}{\partial \chi}\mathfrak{F}(\chi + L, A, B) + \frac{\partial}{\partial A}\mathfrak{F}(\chi + L, A, B) &= \frac{\partial}{\partial A}\mathfrak{F}(\chi, A, B), \\ \frac{\partial L}{\partial B}\frac{\partial}{\partial \chi}\mathfrak{F}(\chi + L, A, B) + \frac{\partial}{\partial B}\mathfrak{F}(\chi + L, A, B) &= \frac{\partial}{\partial B}\mathfrak{F}(\chi, A, B). \end{aligned}\right\} \tag{4.68}$$

These equations lead to

$$\mathfrak{K}(\chi + L, A, B) = \mathfrak{K}(\chi, A, B) + \left\{\frac{\partial L}{\partial A} - \mathfrak{F}(\chi, A, B)\frac{\partial L}{\partial B}\right\} G(\mathfrak{F}), \tag{4.69}$$

because

$$\frac{\partial}{\partial \chi}\mathfrak{F}(\chi + L, A, B) = \frac{\partial}{\partial \chi}\mathfrak{F}(\chi, A, B). \tag{4.70}$$

Eq. (4.69) indicates that $\mathfrak{K}$ is non-periodic, and this equation can be transformed into

$$\begin{aligned} &\mathfrak{K}(\chi, A, B) - \left\{\frac{\partial L}{\partial A} - \mathfrak{F}(\chi, A, B)\frac{\partial L}{\partial B}\right\} G(\mathfrak{F}) \cdot \Phi \\ &= \mathfrak{K}(\chi + L, A, B) - \left\{\frac{\partial L}{\partial A} - \mathfrak{F}(\chi + L, A, B)\frac{\partial L}{\partial B}\right\} G(\mathfrak{F}) \cdot (\Phi + 1), \end{aligned} \tag{4.71}$$

and, furthermore, from Eq. (4.64), this turns into the required form

$$\mathfrak{R}(\Phi + 1, A, B) = \mathfrak{R}(\Phi, A, B). \qquad \text{Q.E.D.} \tag{4.72}$$

Accordingly, the right-hand sides of Eqs. (4.63), (4.65), and (4.66) are functions of A, B, and Φ, and periodic in Φ with a unit wave length. The basic, ordinary differential equations (4.65) and (4.66) can describe A and B as functions of Φ, while the integral of Eq. (4.63) gives the phase shift ξ_0. Furthermore, these equations can be linearized provided that $|\mu\mathcal{R}| \ll 1$. Therefore, the cnoidal wave train can be, finally, expressed as

$$\mathcal{U} = \mathcal{F}\{\xi + \xi_0(\xi),\ A(\xi),\ B(\xi)\}\ . \tag{4.73}$$

The bounded solutions for the periodic system of the ordinary differential equations (4.65) and (4.66) are required. For this purpose, the method of averaging is available on the assumption that μ is a small parameter. Before doing this, however, for insight it is advantageous to analyze the structure of the cnoidal wave solution, satisfying Eq. (4.50).

(3) Structure of the Cnoidal Wave Solution

The structure of the solution for Eq. (4.50) in the $(\mathcal{F}, d\mathcal{F}/d\chi)$ phase plane is fundamentally the same as that described briefly in Chapter 2, but here it will be presented in detail. Equilibrium points satisfy the equation

$$(2/3)d^2\mathcal{F}/d\chi^2 = -\mathcal{F}^2 + A = 0. \tag{4.74}$$

Thus, if $A < 0$, there are no equilibrium points, while if $A > 0$, there are two, given by $\mathcal{F} = \pm\sqrt{A}$. The separatorix, which splits the phase plane into stable and unstable regions, is expressed as

$$(d\mathcal{F}/d\chi)^2 = (\mathcal{F} + \sqrt{A})^2(2\sqrt{A} - \mathcal{F}) - 2A^{3/2} + 3B. \tag{4.75}$$

The function $(d\mathcal{F}/d\chi)^2$ has local maximum and minimum values

$$(d\mathcal{F}/d\chi)^2 = \pm 2A^{3/2} + 3B \qquad \text{at } \mathcal{F} = \pm\sqrt{A}. \tag{4.76}$$

Therefore, the point $(\sqrt{A}, 0)$ is a center and the other $(-\sqrt{A}, 0)$ is a saddle point in the $(\mathcal{F}, d\mathcal{F}/d\chi)$ phase plane as shown in Fig. 4.2. They are

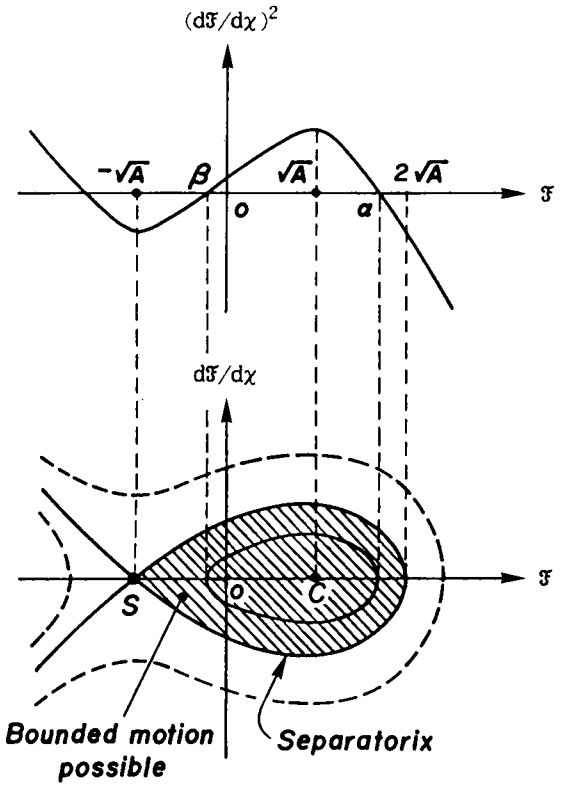

Fig. 4.2 Relation of integral curves to roots of the cubic function.

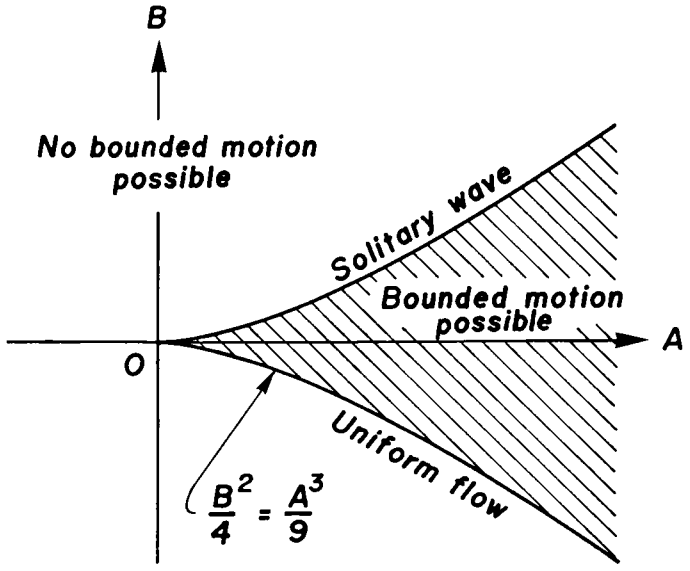

Fig. 4.3 The (A,B) phase plane.

indicated by the symbols c and s, respectively. The region where the cnoidal wave solution exists is that enclosed by the separatorix. There is, then, a condition

$$B^2 < (4/9)\, A^3, \tag{4.77}$$

which restricts the region where the bounded motion is possible in the (A,B) phase plane as shown in **Fig. 4.3.** The bounded solution, clearly from Eq. (4.76), varies from the solitary wave on the upper branch of Eq. (4.77) to the uniform flow on the lower branch.

(4) Stability Analysis

The averaged equations for Eqs. (4.65) and (4.66) are

$$\left.\begin{aligned} \frac{dA}{d\Phi} &= g_1(A,B) \equiv 2\int_0^{L(A,B)} \mu\, G(\mathfrak{F})\, d\chi \\ &= 2L\,\varepsilon_2 \{ \mathfrak{U}_1\mathfrak{U}_2 + (\mathfrak{U}_2 - \mathfrak{U}_1)\tilde{l}\alpha - \tilde{m}\,\alpha^2 \}, \\ \frac{dB}{d\Phi} &= g_2(A,B) \equiv -2\int_0^{L(A,B)} \mu\, \mathfrak{F}\, G(\mathfrak{F})\, d\chi \\ &= -2L\,\varepsilon_2\,\alpha \{ \mathfrak{U}_1\mathfrak{U}_2\tilde{l} + (\mathfrak{U}_2 - \mathfrak{U}_1)\tilde{m}\,\alpha - \{ (\varepsilon_1/\varepsilon_2)\tilde{n}_1 + \tilde{n}_2 \}\alpha^2 \}, \end{aligned}\right\} \tag{4.78}$$

where

$$\left.\begin{aligned} \tilde{l} &= \frac{3(E/K) - 2 + k^2}{1 + k^2}, \qquad \tilde{m} = \frac{1 - k^2 + k^4}{(1 + k^2)^2}, \\ \tilde{n}_1 &= \frac{(9/5)}{(1 + k^2)^3} \{ 2(1 - k^2 + k^4)(E/K) - (1 - k^2)(2 - k^2) \}, \\ \tilde{n}_2 &= (2/3)\tilde{n}_1 + \tilde{m}\,\tilde{l}, \end{aligned}\right\} \tag{4.79}$$

and E is the complete elliptic integral of the second kind. The equilibrium points in the (A,B) phase plane are given by $dA/d\Phi = dB/d\Phi = 0$, that is,

$$\left.\begin{aligned} &\mathfrak{U}_1\mathfrak{U}_2 + (\mathfrak{U}_2 - \mathfrak{U}_1)\tilde{l}\alpha - \tilde{m}\,\alpha^2 = 0, \\ &\mathfrak{U}_1\mathfrak{U}_2\tilde{l} + (\mathfrak{U}_2 - \mathfrak{U}_1)\tilde{m}\,\alpha - \{ (\varepsilon_1/\varepsilon_2)\tilde{n}_1 + \tilde{n}_2 \}\alpha^2 = 0. \end{aligned}\right\} \tag{4.80}$$

The two quadratic equations of Eq. (4.80) have equal roots when the modulus

k satisfies the equation

$$\frac{\mathfrak{U}_1\mathfrak{U}_2}{(\mathfrak{U}_2-\mathfrak{U}_1)^2}=\frac{1}{(\varepsilon_1/\varepsilon_2+2/3)^2}\frac{\tilde{m}-\tilde{l}^2}{\tilde{n}_1}\left\{\tilde{m}\frac{\tilde{m}-\tilde{l}^2}{\tilde{n}_1}-(\varepsilon_1/\varepsilon_2+2/3)\tilde{l}\right\}, \tag{4.81}$$

in which

$$\tilde{m}-\tilde{l}^2=\frac{3}{(1+k^2)^2}\{-3(E/K)^2+2(2-k^2)(E/K)-(1-k^2)\}\ . \tag{4.82}$$

The equal roots are

$$\left.\begin{aligned}\alpha_1&=\frac{\mathfrak{U}_2-\mathfrak{U}_1}{\varepsilon_1/\varepsilon_2+2/3}\frac{\tilde{m}-\tilde{l}^2}{\tilde{n}_1},\\ \alpha_2&=-\frac{\mathfrak{U}_2-\mathfrak{U}_1}{\varepsilon_1/\varepsilon_2+2/3}\left\{\frac{\tilde{m}-\tilde{l}^2}{\tilde{n}_1}-(\varepsilon_1/\varepsilon_2+2/3)\frac{\tilde{l}}{\tilde{m}}\right\}.\end{aligned}\right\} \tag{4.83}$$

The equilibrium point of the averaged equation (4.78) is, then, either α_1 or α_2.

$$\left.\begin{aligned}&\text{When } k^2\to 0,\quad \alpha_1=(1/3)(\mathfrak{U}_2-\mathfrak{U}_1)/(\varepsilon_1/\varepsilon_2+2/3),\\ &\qquad\qquad\ \alpha_2=(\mathfrak{U}_2-\mathfrak{U}_1)(\varepsilon_1/\varepsilon_2+1/3)/(\varepsilon_1/\varepsilon_2+2/3),\\ &\text{when } k^2\to 1,\quad \alpha_1=(10/3)(\mathfrak{U}_2-\mathfrak{U}_1)/(\varepsilon_1/\varepsilon_2+2/3),\\ &\qquad\qquad\ \alpha_2=-2(\mathfrak{U}_2-\mathfrak{U}_1)(\varepsilon_1/\varepsilon_2+7/3)/(\varepsilon_1/\varepsilon_2+2/3),\end{aligned}\right\} \tag{4.84}$$

so that α_2 changes sign independently of $(\mathfrak{U}_2-\mathfrak{U}_1)/(\varepsilon_1/\varepsilon_2+2/3)$. Considering that physically α must be positive because it corresponds to the wave crest, α_2 is unsuitable for an equilibrium point. Therefore, the equilibrium point must be given by α_1, and for the positive α_1 it should be held that

$$(\mathfrak{U}_2-\mathfrak{U}_1)/(\varepsilon_1/\varepsilon_2+2/3)>0. \tag{4.85}$$

To study the character of this equilibrium point, it is convenient to work with A and B in terms of α and β, which relate to

$$3A=\alpha^2+\alpha\beta+\beta^2,\qquad 3B=-\alpha\beta(\alpha+\beta). \tag{4.86}$$

Then, the equilibrium point in the (A,B) phase plane is given by

$$\left.\begin{aligned}A/\alpha^2&=(1-k^2+k^4)/(1+k^2)^2,\\ B/\alpha^3&=-(1/3)(1-2k^2)(2-k^2)/(1+k^2)^2,\end{aligned}\right\} \tag{4.87}$$

where $\alpha \equiv \alpha_1$ and the subscript 1 of α, for brevity, will be omitted hereafter.

Eq. (4.81) gives the relation of external forces $\varepsilon_1/\varepsilon_2$ and $\mathfrak{U}_1/\mathfrak{U}_2$ to the mudulus k. The right-hand side of Eq. (4.81) increases monotonically with respect to k^2 as shown in **Fig. 4.4** and takes on definite values for $k^2 \to 1$, so that

$$\left.\begin{aligned} -M_1 < \frac{\mathfrak{U}_1\mathfrak{U}_2}{(\mathfrak{U}_2 - \mathfrak{U}_1)^2} < M_2, \\ M_1 = \frac{1}{3}\frac{\varepsilon_1/\varepsilon_2 + 1/3}{(\varepsilon_1/\varepsilon_2 + 2/3)^2}, \qquad M_2 = \frac{5}{3}\frac{\varepsilon_1/\varepsilon_2 + 7/3}{(\varepsilon_1/\varepsilon_2 + 2/3)^2}. \end{aligned}\right\} \tag{4.88}$$

Therefore, the external force $\mathfrak{U}_1/\mathfrak{U}_2$ varies in the range

$$\frac{1}{M_1}\{ M_1 - 1/2 + \sqrt{1/4 - M_1} \} < \frac{\mathfrak{U}_1}{\mathfrak{U}_2} < \frac{1}{M_2}\{ M_2 + 1/2 - \sqrt{1/4 + M_2} \}, \tag{4.89}$$

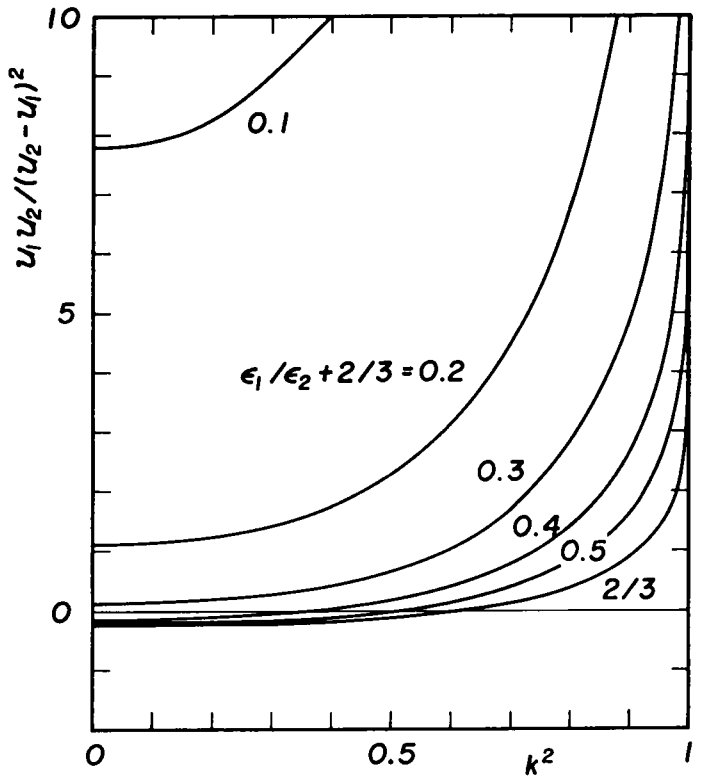

Fig. 4.4 Variations in function $\mathfrak{U}_1\mathfrak{U}_2/(\mathfrak{U}_2 - \mathfrak{U}_1)^2$ with respect to the modulus.

provided that $\mathcal{U}_2 > \mathcal{U}_1$, while when $\mathcal{U}_1 > \mathcal{U}_2$, the ratio $\mathcal{U}_1/\mathcal{U}_2$ in this equation can be replaced by $\mathcal{U}_2/\mathcal{U}_1$.

If the coefficient matrix for the ordinary differential equation (4.78)

$$S_t = \begin{bmatrix} \partial g_1/\partial A & \partial g_1/\partial B \\ \partial g_2/\partial A & \partial g_2/\partial B \end{bmatrix} \tag{4.90}$$

is invertible, a periodic solution for Eq. (4.78) is known to exist provided that μ is small enough. The trace, Tr, and determinant, Det, of this matrix, are

$$\mathrm{Tr}/(2L\,\varepsilon_2) = (3/2)(\varepsilon_1/\varepsilon_2), \tag{4.91}$$

$$\begin{aligned} \mathrm{Det}/(2L\,\varepsilon_2)^2 = & -\frac{(1+k^2)^5}{18\,k^3(1-k^2)}\frac{\tilde{n}_1}{\tilde{m}-\tilde{l}^2}\left\{\frac{\varepsilon_1}{\varepsilon_2}+\frac{2}{3}\right\} \\ & \times\left[\left\{(\varepsilon_1/\varepsilon_2+2/3)\frac{\tilde{n}_1}{\tilde{m}-\tilde{l}^2}(\tilde{m}-3\,\tilde{l}^2)+4\,\tilde{m}\,\tilde{l}\right\}\frac{\partial\tilde{l}}{\partial k}\right. \\ & +\left\{(\varepsilon_1/\varepsilon_2+2/3)\frac{\tilde{n}_1}{\tilde{m}-\tilde{l}^2}\tilde{l}-(3\,\tilde{m}-\tilde{l}^2)\right\}\frac{\partial\tilde{m}}{\partial k} \\ & \left.-\left\{(\varepsilon_1/\varepsilon_2+2/3)\tilde{l}-2\,\tilde{m}\frac{\tilde{m}-\tilde{l}^2}{\tilde{n}_1}\right\}\frac{\partial\tilde{n}_1}{\partial k}\right]. \end{aligned} \tag{4.92}$$

The condition that equilibrium points must always be stable can be described such that the real part of the eigen values is negative, i.e.

$$\mathrm{Re}(\lambda) < 0. \tag{4.93}$$

Fig. 4.5 shows variations in determinant, Eq. (4.92); for $\varepsilon_1/\varepsilon_2 + 2/3 < 0$, there are always positive and negative eigen values, so the corresponding equilibrium points are unstable. If there are real eigen values, the inequality (4.93) requires that Det > 0 and Tr < 0. For complex conjugate roots, the inequality also requires that Tr < 0. The existence condition for stable equilibrium points is, therefore, given by

$$0 < \varepsilon_1/\varepsilon_2 + 2/3 < 2/3, \tag{4.94}$$

because ε_2 is physically positive as seen in Eq. (4.42). The locations of the stable equilibrium points in the (A,B) phase plane are shown in Fig.

4.6 for several values of $\varepsilon_1/\varepsilon_2$.

Fig. 4.7 shows the changes in real part of the eigen value $\mathrm{Re}(\lambda)$ for stable equilibrium points with respect to the modulus k. The discriminant of the characteristic equation for Eq. (4.90), D, is positive on the decreasing solid curves, negative on the level broken lines, and at the intersections of these curves, $D = 0$. Thus, these stable equilibrium points correspond to the stable node, spiral, and node, respectively. The wave motion at the equilibrium points for $D \leqq 0$ is more stable than at those for $D > 0$ because, for given values of ε_2 and L, the former takes on greater values of $|\mathrm{Re}(\lambda)|$ than the latter. However, the stability of wave motion for k^2 greater than k^2_{ms}, satisfying $D = 0$, is considered the same degree of stability judging from the linear stability analysis; therefore, most stable wave motion cannot be determined uniquely from this linear analysis.

Now, the following physical motion can be introduced to define the most stable wave motion. If the surrounding conditions of waves, such as water depth, do not change, it may be considered natural that short period waves

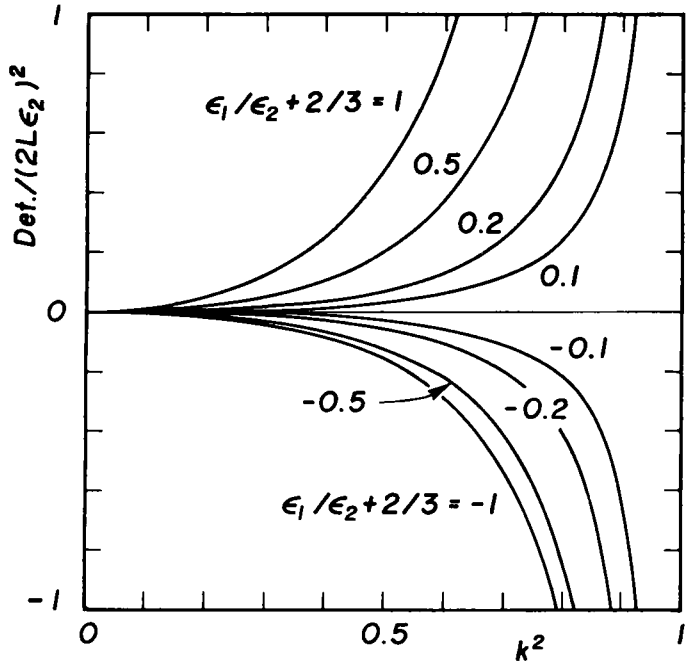

Fig. 4.5 Variations in determinant with respect to the modulus.

can be more easily generated by wind than long period waves because the energy density of the former is greater than that of the latter. Therefore, at this stage, for a given external force $\varepsilon_1/\varepsilon_2$, the wave for the minimum modulus k_{ms}, satisfying $D = 0$, is defined to be the most stable wave among stable waves for the moduli k, satisfing $D \leqq 0$.

Fig. 4.8 shows the relation between the external force $\varepsilon_1/\varepsilon_2$ and modulus k for the most stable wave motion. In the figure, the broken line indicates the approximations:

$$\left.\begin{aligned} &\text{when } k^2 \to 0, \quad \varepsilon_1/\varepsilon_2 = -k^2\{1 - (7/16)k^2\}, \\ &\text{when } k^2 \to 1, \quad \varepsilon_1/\varepsilon_2 + 2/3 = (5/12)(1-k^2)^2(E/K)^{-3}\{1 - (3/2)(E/K) \\ &\qquad\qquad + (3/2)(1-k^2)\{1 - (4/3)(E/K)\}(E/K)^{-1}\} \end{aligned}\right\} \quad (4.95)$$

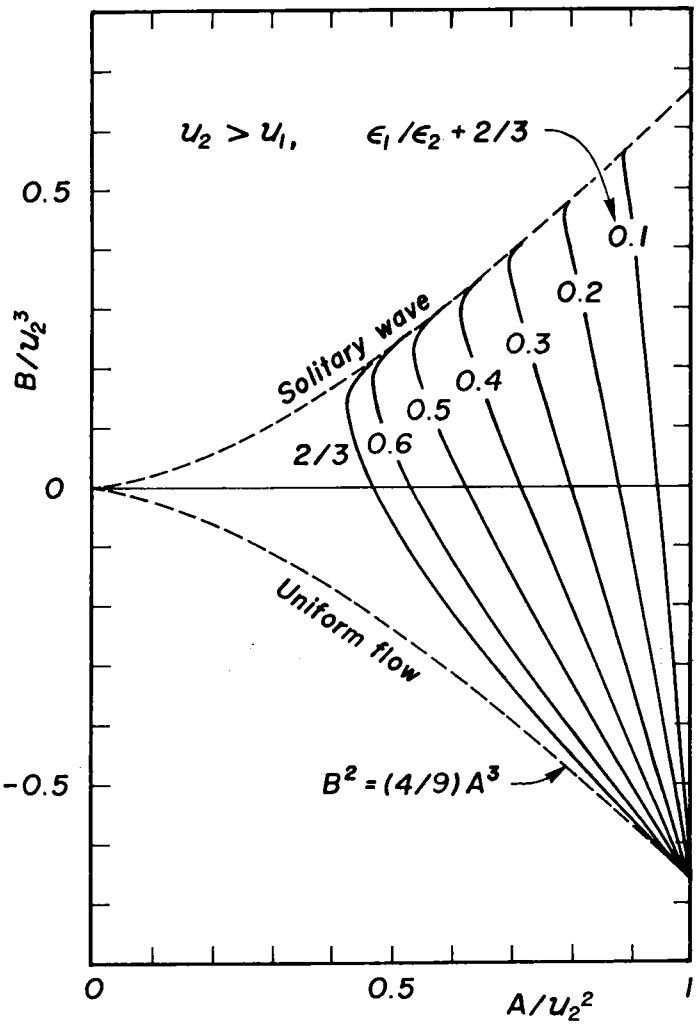

Fig. 4.6 Stable equilibrium points in the (A,B) phase plane for various external forces $\varepsilon_1/\varepsilon_2$.

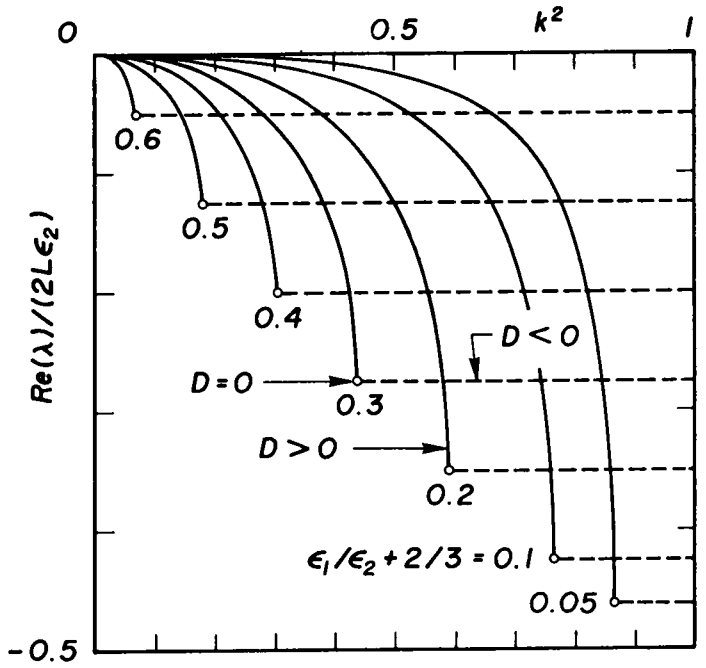

Fig. 4.7 Changes in real part of eigen values $\mathfrak{Re}(\lambda)$ with respect to the modulus.

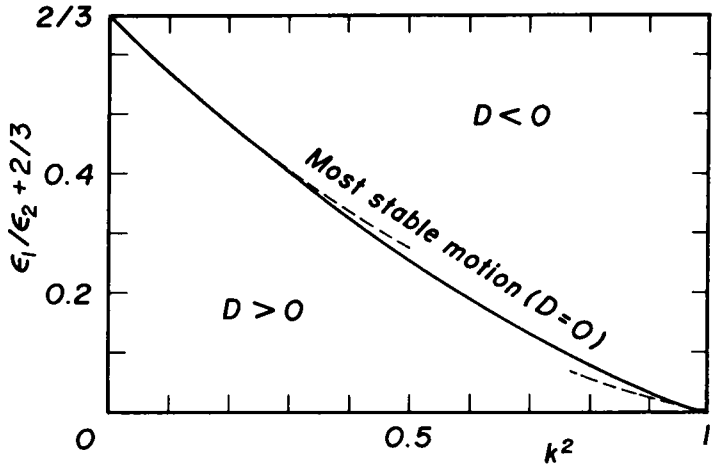

Fig. 4.8 Variations in external force $\varepsilon_1/\varepsilon_2$ for the most stable wave motion with respect to the modulus.

(5) **Phase Equation**

The phase shift must be determined from the differential equation (4.63). Under the condition that $|\mu \mathcal{R}| \ll 1$, the phase equation can be linearized as

$$\left.\begin{aligned} &\frac{d\xi}{L} = \frac{1}{2K}\{1 - 2\mu\,\mathcal{R}(\upsilon)\}\,d\upsilon, \\ &2\mu\,\mathcal{R} = -\varepsilon_2\left\{\frac{\varepsilon_1}{\varepsilon_2}+\frac{2}{3}\right\}\left\{\frac{3\alpha}{1+k^2}\right\}^{-1/2}\frac{1}{(1-k^2)^2} \\ &\qquad\times\{\ \tilde{C}_0 + \tilde{C}_2\,\mathrm{cn}^2\upsilon + \tilde{C}_4\,\mathrm{cn}^4\upsilon\ \} \\ &\qquad\times\{\ 2(1-k^2+k^4)\,\mathrm{sn}\upsilon\,\mathrm{cn}\upsilon\,\mathrm{dn}\upsilon \\ &\qquad\quad + \{(1-k^2)(1-2k^2) - 2(1-k^2+k^4)\,\mathrm{cn}^2\upsilon\}\,Z(\upsilon)\ \}\,. \end{aligned}\right\} \tag{4.96}$$

with

$$\left.\begin{aligned} \tilde{C}_0 &= 2(1+k^2)\frac{\tilde{n}_1}{\tilde{m}-\tilde{l}^2}I_2 - 3(1-k^2), \\ \tilde{C}_2 &= -2(1+k^2)\frac{\tilde{n}_1}{\tilde{m}-\tilde{l}^2} + 6(1-2k^2), \\ \tilde{C}_4 &= 9k^2, \\ I_2 &= (1/k^2)(E/K - 1 + k^2), \end{aligned}\right\} \tag{4.97}$$

where sn and dn are the Jacobian elliptic functions of the first and third kinds, respectively, and $Z(\upsilon)$ is the Jacobian Zeta function defined by

$$Z(\upsilon) = E(\upsilon) - (E/K)\upsilon, \tag{4.98}$$

in terms of the incomplete elliptic integral of the second kind, $E(\upsilon)$.

If Eq. (4.96) is integrated such that the phase shift $\xi_0 = 0$ at a wave trough, after some algebraic calculations with the aid of Eq. (4.80), it follows that

$$\begin{aligned} \frac{\xi}{L} = \frac{\upsilon}{2K} - \frac{1}{2K}\varepsilon_2\left\{\frac{\varepsilon_1}{\varepsilon_2}+\frac{2}{3}\right\}\left\{\frac{3\alpha}{1+k^2}\right\}^{-1/2}\frac{1}{(1-k^2)^2} \\ \times\{\ \tilde{\gamma}_1\,\mathrm{cn}^2\upsilon + \tilde{\gamma}_2\,\mathrm{cn}^4\upsilon + \tilde{\gamma}_3\,\mathrm{cn}^6\upsilon \\ + \tilde{\delta}_1\,\mathrm{sn}\upsilon\,\mathrm{cn}\upsilon\,\mathrm{dn}\upsilon\cdot Z(\upsilon) \\ + \tilde{\delta}_2\,\mathrm{sn}\upsilon\,\mathrm{cn}^3\upsilon\,\mathrm{dn}\upsilon\cdot Z(\upsilon) + \tilde{\delta}_3 Z^2(\upsilon)\ \}\,, \end{aligned} \tag{4.99}$$

with

$$\left.\begin{aligned}
\tilde{\gamma}_1 &= (1-k^2+k^4)\{\tilde{C}_0-(1/3)I_2\tilde{C}_2\}\\
&\quad+(1/30)(1-2k^2)(8-3k^2+3k^4)I_2(\tilde{C}_4/k^2),\\
\tilde{\gamma}_2 &= (2/3)(1-k^2+k^4)\tilde{C}_2\\
&\quad-(1/60)\{6(1-k^2+k^4)(E/K)+(2-7k^2-3k^4)\}(\tilde{C}_4/k^2),\\
\tilde{\gamma}_3 &= (2/5)(1-k^2+k^4)\tilde{C}_4,\\
\tilde{\delta}_1 &= (2/3)(1-k^2+k^4)(\tilde{C}_2/k^2)\\
&\quad-(1/15)(1-2k^2)(8-3k^2+3k^4)(\tilde{C}_4/k^4),\\
\tilde{\delta}_2 &= (2/5)(1-k^2+k^4)(\tilde{C}_4/k^2),\\
\tilde{\delta}_3 &= (27/5)\{(1-k^2)/(1+k^2)\}^2/(\tilde{m}-\tilde{l}^2).
\end{aligned}\right\} \quad (4.100)$$

When $k^2 \to 0$, $\qquad \xi/L \fallingdotseq \upsilon/(2K)+O(k^2)$, $\qquad (4.101)$

then the phase shift $\xi_0/L = O(k^2) \to 0$, while when $k^2 \to 1$, the phase shift can be evaluated as

$$\xi_0/L = O\{\varepsilon_2(\varepsilon_1/\varepsilon_2+2/3)\alpha^{-1/2}K^{-2}(1-k^2)^{-2}\} = O(\varepsilon_2 K\alpha^{-1/2}), \quad (4.102)$$

with the aid of Eq. (4.95). Therefore, the averaging procedure above is allowable under the condition that $|\varepsilon_2 K\alpha^{-1/2}| \ll 1$.

Since the phase shift ξ_0/L is assumed to be a slowly varying function within a unit wave length, Eq. (4.99) gives the explicit expression for the phase shift

$$\begin{aligned}
\frac{\xi_0}{L} &= \frac{1}{2K}\varepsilon_2\left\{\frac{\varepsilon_1}{\varepsilon_2}+\frac{2}{3}\right\}\left\{\frac{3\alpha}{1+k^2}\right\}^{-1/2}\frac{1}{(1-k^2)^2}\\
&\quad\times\{\tilde{\gamma}_1\,\mathrm{cn}^2\upsilon_1+\tilde{\gamma}_2\,\mathrm{cn}^4\upsilon_1+\tilde{\gamma}_3\,\mathrm{cn}^6\upsilon_1\\
&\qquad+\tilde{\delta}_1\,\mathrm{sn}\upsilon_1\,\mathrm{cn}\upsilon_1\,\mathrm{dn}\upsilon_1\cdot Z(\upsilon_1)\\
&\qquad+\tilde{\delta}_2\,\mathrm{sn}\upsilon_1\,\mathrm{cn}^3\upsilon_1\,\mathrm{dn}\upsilon_1\cdot Z(\upsilon_1)+\tilde{\delta}_3 Z^2(\upsilon_1)\}+O(\varepsilon_2^2),
\end{aligned} \quad (4.103)$$

with $\upsilon_1 \equiv 2K(\xi/L)$.

(6) Hydraulic Quantities

To obtain clear expressions for hydraulic quantities of wind-forced

waves, the transformations

$$X_1 = \{1 + 2(\bar{Q}/c^2)\}/\mathfrak{U}_2, \qquad X_2 = \{1 - (\bar{Q}/c^2)\}/\mathfrak{U}_2 \tag{4.104}$$

can be adopted, and then, from Eq. (4.42)

$$X_1 = \frac{1 + \mathfrak{U}_1/\mathfrak{U}_2}{U_1 + U_2}, \qquad X_2 = \frac{U_2(\mathfrak{U}_1/\mathfrak{U}_2) - U_1}{U_1 + U_2}. \tag{4.105}$$

The chief hydraulic quantities are, then, given as follows:

a. Wave profile

$$\eta = \frac{X_1\bar{Q}}{X_1 - X_2 - \alpha/\mathfrak{U}_2 + (\alpha - \beta)/\mathfrak{U}_2 \cdot \mathrm{sn}^2 v} - 1. \tag{4.106}$$

The wave height is, then, given by

$$H = \frac{X_1\bar{Q}}{(X_1 - X_2 - \alpha/\mathfrak{U}_2)(X_1 - X_2 - \beta/\mathfrak{U}_2)} \frac{\alpha - \beta}{\mathfrak{U}_2}. \tag{4.107}$$

These solutions are bounded only if

$$0 < \alpha/\mathfrak{U}_2 < X_1 - X_2. \tag{4.108}$$

b. Average velocity

$$U = \frac{X_2}{X_1} + \frac{1}{X_1}\left\{\frac{\beta}{\mathfrak{U}_2} + \frac{\alpha - \beta}{\mathfrak{U}_2}\mathrm{cn}^2 v\right\}. \tag{4.109}$$

The velocity at the wave crest $U_c = (X_2 + \alpha/\mathfrak{U}_2)/X_1$, so it always holds that $X_2/X_1 < U_c < 1$ from Eq. (4.108), and the inequality

$$0 < \bar{Q}/c^2 < 1 \tag{4.110}$$

is obtained for $U_c > 0$.

c. Vertical velocity

$$W = (1 + z)\frac{2}{X_1}\frac{\alpha - \beta}{\mathfrak{U}_2}\frac{\mathrm{d}v}{\mathrm{d}\xi}\mathrm{sn}v\,\mathrm{cn}v\,\mathrm{dn}v. \tag{4.111}$$

d. Wave velocity

$$\overline{Q}/c^2 = (X_1 - X_2)/(X_1 + 2X_2). \tag{4.112}$$

e. Progressive discharge

The integral mean of the water surface displacement over a unit wave length reduces to

$$\begin{aligned}(1/L)\int_0^L \eta(\chi)\,d\chi &= (1/L)\int_0^L \eta(\xi+\xi_0)(1+d\xi_0/d\xi)\,d\xi \\ &= (1/L)\int_0^L \eta(\xi+\xi_0)(d\xi_0/d\xi)\,d\xi \\ &= (1/L)\int_0^L \eta(\xi)\{d\xi_0(\xi)/d\xi\}\,d\xi + O(\varepsilon_2^2),\end{aligned} \tag{4.113}$$

considering that

$$\left.\begin{aligned}&\mathrm{sn}^2\upsilon = \mathrm{sn}^2\{(2K/L)(\xi+\xi_0)\} \\ &\quad = \mathrm{sn}^2\upsilon_1 + 4K(\xi_0/L)\,\mathrm{sn}\upsilon_1\,\mathrm{cn}\upsilon_1\,\mathrm{dn}\upsilon_1 + O\{(\xi_0/L)^2\}, \\ &\xi_0/L = O(\varepsilon_2), \qquad d\xi_0/d\xi = O(\varepsilon_2).\end{aligned}\right\} \tag{4.114}$$

Since $d\xi_0/d\xi$ is an odd function of ξ and $\eta(\xi)$ is an even one, the integral in the right-hand side of Eq. (4.113) vanishes, so the conservative condition of mass can be evaluated as

$$(1/L)\int_0^L \eta\,d\chi = O(\varepsilon_2^2). \tag{4.115}$$

This condition is nearly the same as for symmetric waves without phase shift.

Inserting Eq. (4.106) into Eq. (4.115) gives the progressive discharge. Noting that the integral

$$(1/K)\int_0^K \frac{d\upsilon}{1-\gamma^2\mathrm{sn}^2\upsilon}, \qquad 0 < -\gamma^2 \equiv \frac{\alpha-\beta}{X_1-X_2-\alpha} < \infty \tag{4.116}$$

must be performed for two separate cases of the modulus k,

$$0 < -\gamma^2 < k \qquad \text{and} \qquad k < -\gamma^2 < \infty, \tag{4.117}$$

the progressive discharge is given by the following equations:

i) for $0 < \dfrac{\alpha}{\mathfrak{U}_2} < \dfrac{1+k^2}{1+3k+k^2}(X_1 - X_2)$

$$\frac{1}{\overline{Q}} = \frac{X_1}{X_1 - X_2 - \beta/\mathfrak{U}_2}\left[\frac{X_1 - X_2 - \beta/\mathfrak{U}_2}{X_1 - X_2 + (\alpha+\beta)/\mathfrak{U}_2} + \frac{\pi}{2K}\Lambda_0(\varphi_1, k)\frac{\sin\varphi_1}{\sin\varphi_2}\right], \quad (4.118.1)$$

ii) for $\dfrac{\alpha}{\mathfrak{U}_2} = \dfrac{1+k^2}{1+3k+k^2}(X_1 - X_2)$

$$\overline{Q} = \frac{6}{1+k+\pi/(2K)}\frac{k(1+k)}{1+3k+k^2}\frac{X_1 - X_2}{X_1}, \quad (4.118.2)$$

iii) for $\dfrac{1+k^2}{1+3k+k^2}(X_1 - X_2) < \dfrac{\alpha}{\mathfrak{U}_2} < (X_1 - X_2)$

$$\frac{1}{\overline{Q}} = \frac{X_1}{X_1 - X_2 - \beta/\mathfrak{U}_2}\left[1 + \frac{\pi}{2K}\{1 - \Lambda_0(\varphi_2, k)\}\frac{\sin\varphi_1}{\sin\varphi_2}\right], \quad (4.118.3)$$

with $$\sin^2\varphi_1 = \frac{(2\alpha+\beta)/\mathfrak{U}_2}{X_1 - X_2 + (\alpha+\beta)/\mathfrak{U}_2}, \qquad \sin^2\varphi_2 = \frac{X_1 - X_2 - \alpha/\mathfrak{U}_2}{X_1 - X_2 - \beta/\mathfrak{U}_2}, \quad (4.118.4)$$

where Λ_0 is Heuman's Lambda function defined by

$$\frac{\pi}{2K}\Lambda_0(\varphi, k) = (E/K - 1)F(\varphi, k') + E(\varphi, k'), \qquad k' = \sqrt{1-k^2}, \quad (4.119)$$

and $F(\varphi,k)$ is the incomplete elliptic integral of the first kind.

f. Mass transport velocity

The mass transport velocity in the Eulerian coordinates, defined by the mean velocity over a unit wave length, can be approximated as

$$U_m \equiv (1/L)\int_0^L U(\xi + \xi_0)\, d\xi \fallingdotseq (1/L)\int_0^L U\, d\chi = X_2/X_1 + (\tilde{\imath}/X_1)(\alpha/\mathfrak{U}_2), \quad (4.120)$$

where $\tilde{\imath}$ is given in Eq. (4.79).

g. Wind-induced current

The average velocity U contains the velocity added by wind, the wind-induced current, as

$$U_w = X_2/X_1. \quad (4.121)$$

(7) Existence Condition

For the cnoidal wave solution mentioned in previous sections, the quadratic equation (4.39) should have real roots, and some physical conditions for external forces must be satisfied.

First, suppose that the modulus can take on values over the whole range of $0 < k^2 < 1$, then it follows that

$$\left.\begin{array}{lll} \text{when } k^2 \to 0, & \varepsilon_1/\varepsilon_2 \to -0, & \\ & \mathfrak{U}_1/\mathfrak{U}_2 \fallingdotseq -1-3(\varepsilon_1/\varepsilon_2), & \\ & \alpha/\mathfrak{U}_2 \fallingdotseq 1+(9/4)(\varepsilon_1/\varepsilon_2)^2, & \\ \text{when } k^2 \to 1, & \varepsilon_1/\varepsilon_2+2/3 \to +0, & \\ & \mathfrak{U}_1/\mathfrak{U}_2 \fallingdotseq 1-(3/5)(\varepsilon_1/\varepsilon_2+2/3), & \\ & \alpha/\mathfrak{U}_2 \fallingdotseq 2-(6/5)(\varepsilon_1/\varepsilon_2+2/3). & \end{array}\right\} \quad (4.122)$$

The stability conditions (4.85) and (4.94) give $\mathfrak{U}_2 > \mathfrak{U}_1$, so

$$U_2 - U_1 > 2(X_2/X_1) = 2\frac{U_2(\mathfrak{U}_1/\mathfrak{U}_2) - U_1}{1+\mathfrak{U}_1/\mathfrak{U}_2}. \quad (4.123)$$

Since $|\mathfrak{U}_1/\mathfrak{U}_2| < 1$, Eq. (4.123) gives the condition for the stable wave motion,

$$U_1 + U_2 > 0. \quad (4.124)$$

Furthermore, the inequality (4.110) for the positive velocity at the wave crest implies that

$$0 < X_2/X_1 < 1 \quad (4.125)$$

from Eq. (4.112), thus

$$U_2 - U_1 > 0. \quad (4.126)$$

Eq. (4.125) indicates that the wind-induced current is always positive and less than unity. Since the relation between the roots and coefficients of Eq. (4.39) is

$$U_2 - U_1 = (\overline{\sigma_\tau}/S)(\delta_1 - 1), \quad (4.127)$$

the condition for the coefficient δ_1 becomes

$$\delta_1 > 1, \tag{4.128}$$

which means from Eq. (4.34) that the shear stress always acts like a positive external force. Generally, $0 < U_2 < 1$, so the inequality

$$(\bar{\sigma}_\tau/s)\delta_1 \bar{Q} < 1 \tag{4.129}$$

is necessary for real roots of Eq. (4.39) to exist. Under these conditions, Eq. (4.39) has real roots if

$$\left.\begin{aligned} &(\bar{\sigma}_\tau/s)\,\delta_1 \bar{Q} > 1 - (1/4)(2-S)^2, \\ &S \equiv (\bar{\sigma}_\tau/s)(\delta_1 - 1), \\ &0 < S < 2, \end{aligned}\right\} \tag{4.130}$$

in which the range of S is determined from Eq. (4.124).

Moreover, the condition (4.108) for the bounded solution becomes

$$\frac{\alpha}{\mathfrak{U}_2} < \frac{1 + U_1 + (1 - U_2)(\mathfrak{U}_1/\mathfrak{U}_2)}{U_1 + U_2}. \tag{4.131}$$

When $k^2 \to 0$, it takes the form

$$1 < \frac{\alpha}{\mathfrak{U}_2} < 1 - 3\frac{1 - U_2}{U_1 + U_2}\frac{\varepsilon_1}{\varepsilon_2}, \tag{4.132}$$

and this is always satisfied because of the first of Eq. (4.122), while when $k^2 \to 1$, Eq. (4.131) also becomes

$$\frac{\alpha}{\mathfrak{U}_2} < \frac{2 + U_1 - U_2}{U_1 + U_2} - \frac{3}{5}\frac{1 - U_2}{U_1 + U_2}\left\{\frac{\varepsilon_1}{\varepsilon_2} + \frac{2}{3}\right\}. \tag{4.133}$$

Therefore, the condition for $\alpha/\mathfrak{U}_2 < 2$ is

$$U_1 < -3U_2 + 2. \tag{4.134}$$

This inequality can be expressed as

$$(\bar{\sigma}_\tau/s)\,\delta_1 \bar{Q} < 1 - (3/16)(2-S)^2, \tag{4.135}$$

in terms of S and $\bar{Q}$ as in Eq. (4.130).

The existence condition necessary for the bounded motion, given by Eqs. (4,129), (4.130), and (4.135), is shown in **Fig. 4.9** by shaded areas. By the adoption of a new parameter m, the general expression for this portion becomes

$$\left.\begin{aligned} &(\bar{\sigma}_\tau/s)\,\delta_1\,\bar{Q} = 1 - m(2-S)^2, \\ &3/16 < m < 1/4, \\ &0 < S < 2. \end{aligned}\right\} \tag{4.136}$$

In terms of S and m, the two roots U_1, U_2 and the relation between the coefficient δ_1 and progressive discharge $\bar{Q}$ are, respectively, given by

$$U_{1,2} = \mp\,(1/2)\,\{\,1 \pm \sqrt{1-4m}\,\}\,S + \sqrt{1-4m}\,, \tag{4.137}$$

$$\frac{\delta_1}{\delta_1 - 1}\,\bar{Q} = m(4-S) + \frac{1-4m}{S}. \tag{4.138}$$

In Eq. (4.137), the upper and lower signs correspond to U_1 and U_2, respectively. **Figs. 4.10** and **4.11** show the region of U_1, U_2, and $\bar{Q}$, where the bounded motion is possible.

The conditions above have been derived on the assumption that the modulus can vary within the whole range of $0 < k^2 < 1$ independently of external forces. On the contrary, since $X_1 > 0$, it should be held that $X_2 > 0$ as seen in Eq. (4.125). Therefore, from Eqs. (4.105) and (4.124),

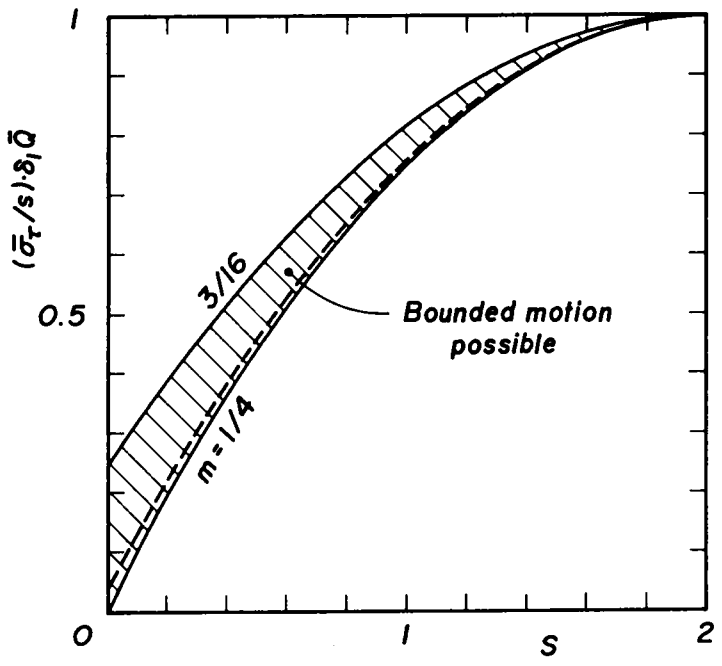

Fig. 4.9 The range where the bounded motion is possible.

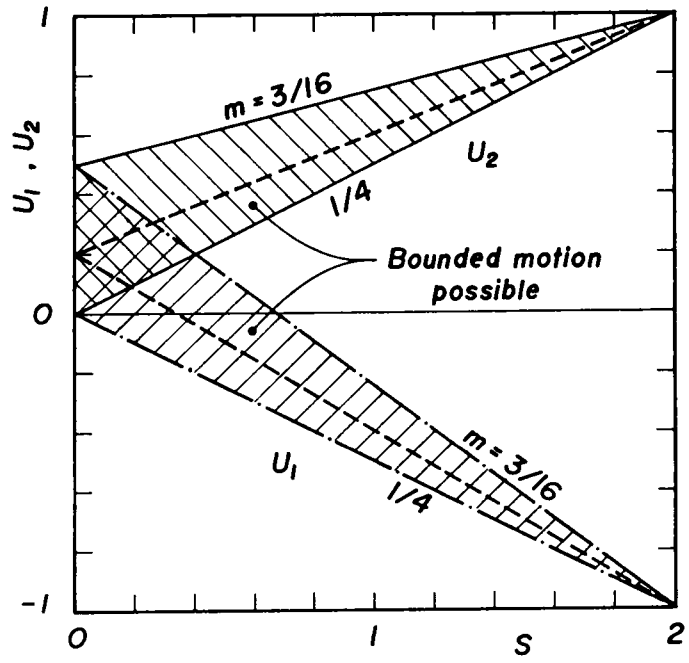

Fig. 4.10 Relation of roots U_1 and U_2 to the external force S.

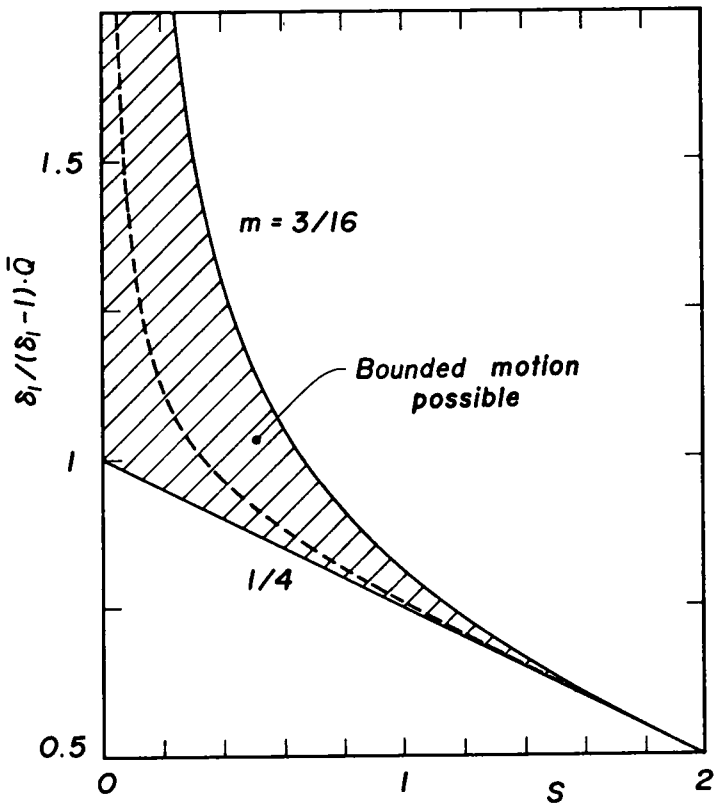

Fig. 4.11 Relation of the progressive discharge $\bar{Q}$ to the external force S.

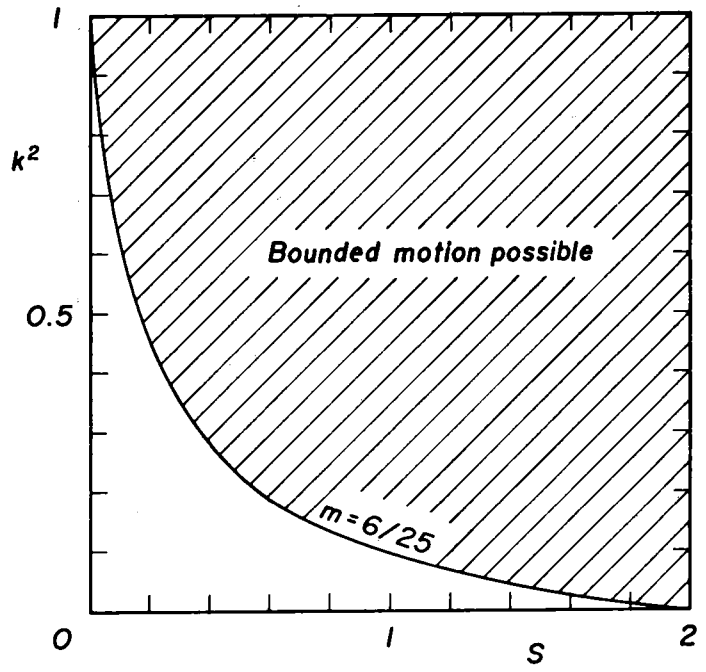

(1) Modulus k

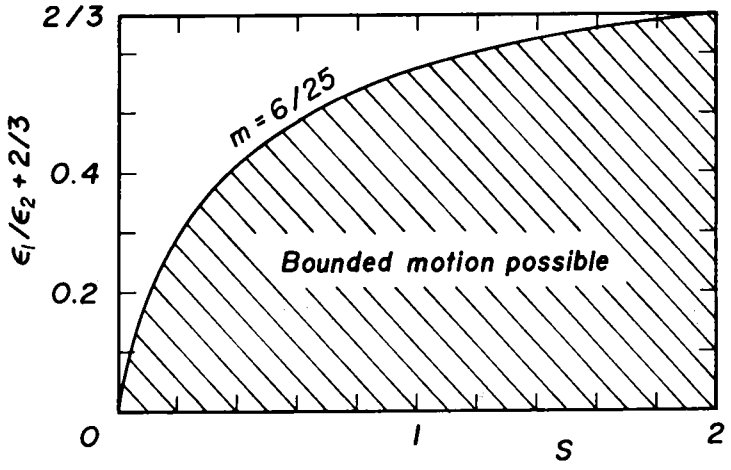

(2) External force $\varepsilon_1/\varepsilon_2$

Fig. 4.12 The ranges of the modulus k and external force $\varepsilon_1/\varepsilon_2$ for the bounded motion.

the additional condition is given by

$$\mathfrak{U}_1/\mathfrak{U}_2 > U_1/U_2, \tag{4.139}$$

which, of course, relates to external forces. If k_0^2 and $(\varepsilon_1/\varepsilon_2)_0$ are roots of $\mathfrak{U}_1/\mathfrak{U}_2 = U_1/U_2$, Eq. (4.139) is held for

$$k_0^2 < k^2 < 1, \qquad 0 < \varepsilon_1/\varepsilon_2 < (\varepsilon_1/\varepsilon_2)_0. \tag{4.140}$$

Fig. 4.12 shows an example of the relation of Eq. (4.140) for $m = 6/25$, indicating that when $S \to 0$, long period waves chiefly occur.

(8) Limiting States

The external force S and physical parameter m determine the existence condition for the wind-forced waves. For these values, the limiting states of the wind-forced waves can be discussed as follows:

The maximum wave height for the most stable bounded solution is derived from the extreme case of $k^2 \to 1$ as

$$\left.\begin{aligned} &H_{\max} = 3\sqrt{1-4m}\,/\{1-2\sqrt{1-4m}\}, \\ \text{or}\quad &m = \frac{3}{4}\frac{(1+H_{\max})(3+H_{\max})}{(3+2H_{\max})^2}. \end{aligned}\right\} \tag{4.141}$$

The lower bound of m given by Eq. (4.136) is found to be a singular point of the maximum wave height. The maximum wave height of progressive waves of permanent type without wind effects can reach $H_{\max} \fallingdotseq 0.83$, so the wind-forced waves will take on this value as the maximum wave height, more or less. If the restriction $0 < H_{\max} < 1$ for $k^2 \to 1$ is imposed, the range of m becomes

$$6/25 < m < 1/4. \tag{1.142}$$

Fig. 4.13 shows that the maximum wave height decreases monotonically with respect to the increase in m; when $m \to 1/4$, that is, when the quadratic equation (4.39) has an equal root, the wave height tends to vanish. In

Figs. 4.9, 4.10, and 4.11, broken lines are for the lower bound $m = 6/25$. The limiting values of hydraulic quantities are given by

$$\left.\begin{aligned} c^2 &= 3(1+S)\frac{1+H_{\max}}{3+2H_{\max}}, \\ U_c &= \frac{1}{2}\frac{3S+4H_{\max}}{3+2H_{\max}}, \\ \bar{Q} &= \frac{3}{2}(2-S)\frac{1+H_{\max}}{3+2H_{\max}}, \\ U_m &= \frac{3(1+H_{\max})S-2H_{\max}}{2(3+2H_{\max})}, \\ U_w &= \frac{S}{2}. \end{aligned}\right\} \tag{4.143}$$

Fig. 4.14 shows the relations between the external force S and hydraulic quantities given by Eq. (4.143). When $S \to 0$, for finite wave heights,

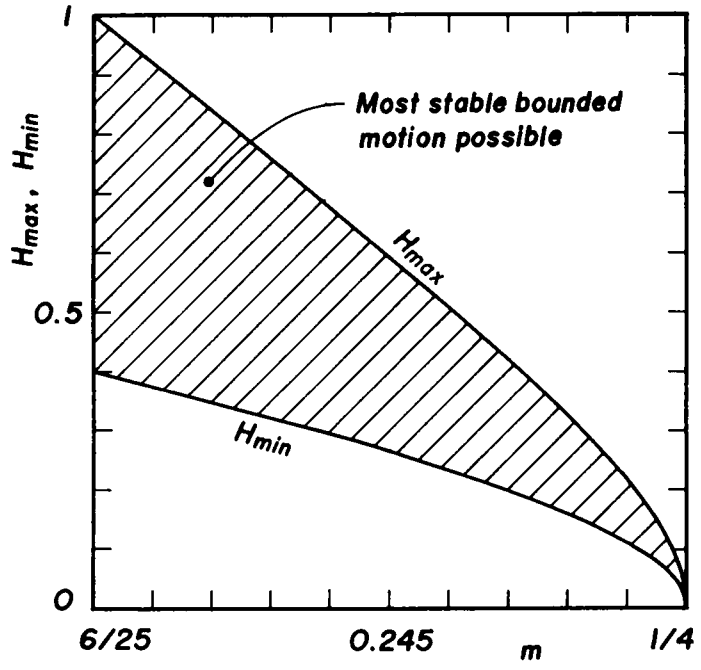

Fig. 4.13 The maximum and minimum wave heights as functions of the parameter m.

the progressive discharge $\overline{Q}$ takes on values greater than unity and the mass transport velocity becomes negative. The situation is, of course, unsuitable physically. Therefore, an additional condition for the external force,

$$S > \frac{2}{3}\frac{H_{max}}{1+H_{max}} = 2\sqrt{1-4m}/\{1+\sqrt{1-4m}\} \qquad \text{when } k^2 \to 1, \qquad (4.144)$$

should also be applied to exclude the broken lines in **Figs. 4.14(1)** and (2).

Fig. 4.14(1) indicates that even in the limiting case of $H_{max} \to 0$, there exist finite values of wave velocity because of the presence of shear stress from wind. When $S \to 2$, the average velocity at a wave crest becomes equal to unity, so the progressive discharge, of course, vanishes independently of wave height. Since the state of $H_{max} \to 0$ corresponds to that for the existence of a wind-induced current with no wave, the mass transport velocity diminishes slightly when waves are generated. The average velocity and water surface displacement at the wave trough are respectively given by $U_t = U_m$ and $\eta_t = 0$ as $k^2 \to 1$.

On the other hand, the modulus of the most stable wave motion for the limiting state of $k^2 \to 0$ becomes

$$k^2 \fallingdotseq (2/3)^{3/2}(2-S)\sqrt{1-4m}/\{S+(2-S)\sqrt{1-4m}\}, \qquad (4.145)$$

because $X_2 \to 0$. Furthermore, the relation between $\varepsilon_1/\varepsilon_2$ and k^2 is given by

$$\left.\begin{aligned} &k^2 \fallingdotseq -(\varepsilon_1/\varepsilon_2)\{1-(7/16)(\varepsilon_1/\varepsilon_2)\}, \\ \text{or}\quad &\varepsilon_1/\varepsilon_2 \fallingdotseq -k^2\{1-(7/16)k^2\}. \end{aligned}\right\} \qquad (4.146)$$

Eqs. (4.145) and (4.146) give hydraulic quantities for $k^2 \to 0$ as

$$\left.\begin{aligned} &H_{min} = 2\sqrt{(2/3)(1-4m)}/\{1-2\sqrt{(2/3)(1-4m)}\}^{1/2}, \\ \text{or}\quad &m = (1/4)\{1-(3/32)H_{min}^2\{\sqrt{H_{min}^2+4}-H_{min}\}^2\}, \end{aligned}\right\} \qquad (4.147)$$

and

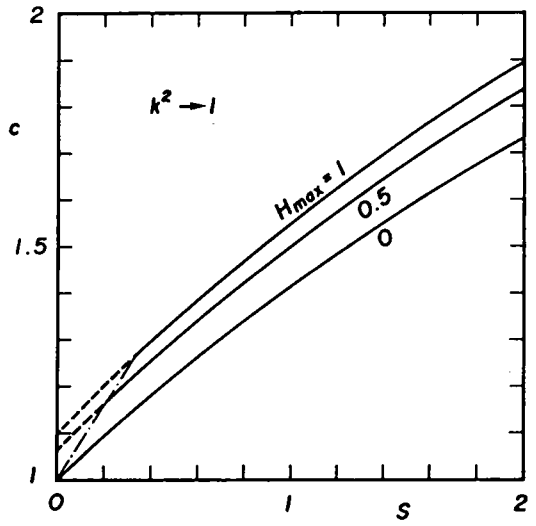

(1) Wave velocity

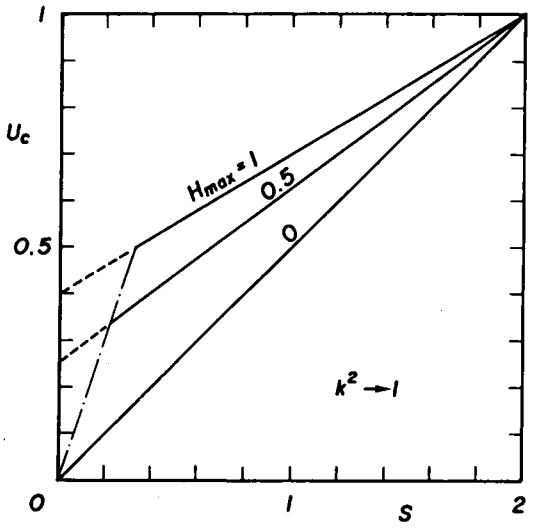

(2) Average velocity at the wave crest

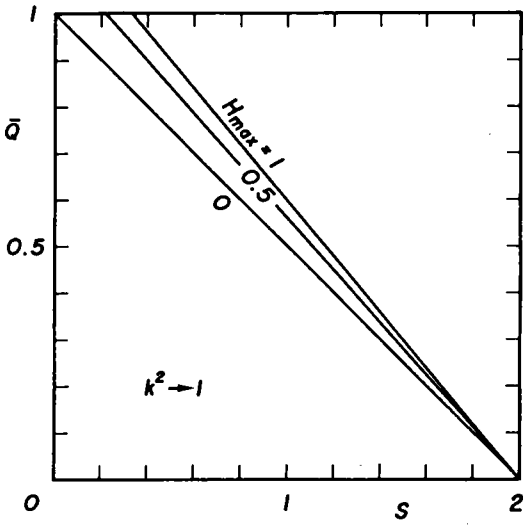

(3) Progressive discharge

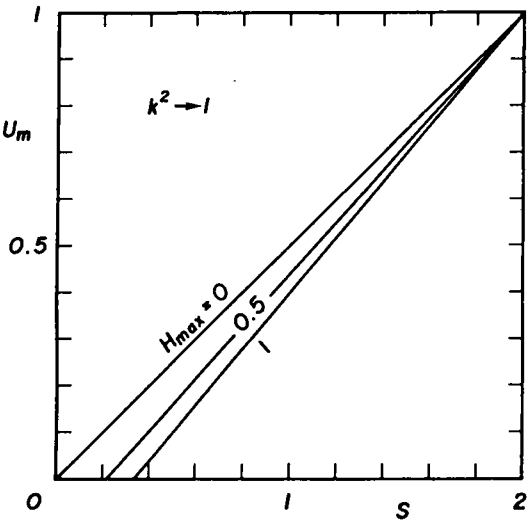

(4) Mass transport velocity

Fig. 4.14 Limiting values of hydraulic quantities in relation to the external force S.

$$\left.\begin{aligned}
&\bar{Q} = O(k^2) \to 0,\\
&c^2 = O(\bar{Q}) \to 0,\\
&U_c = U_m = U_t \to 1,\\
&U_w = 0,\\
&\eta_c = \{1 - 2\sqrt{(2/3)(1 - 4m)}\}^{-1/2} - 1,\\
&\eta_t = \{1 - 2\sqrt{(2/3)(1 - 4m)}\}^{1/2} - 1.
\end{aligned}\right\} \qquad (4.148)$$

Similar to Eq. (4.142), the range of m becomes

$$(7 + 3\sqrt{5})/64 < m < 1/4 \qquad (4.149)$$

for $0 < H_{min} < 1$.

The variations in minimum wave height are also drawn in **Fig. 4.13**. Therefore, the wind-forced waves in the most stable state exist within the region enclosed by Eqs. (4.141) and (4.147). The wave velocity, progressive discharge, and wind-induced current all vanish when $k^2 \to 0$. The velocity components given by the third of Eq. (4.148) are non-dimensionalized by the wave velocity, therefore these components also vanish. Since the condition that $m \to 1/4$ must be held for η_c and η_t to vanish, as indicated in **Fig. 4.12(1)**, the external force S should take on values very close to 2 for waves of $k^2 \fallingdotseq 0$ to exist.

4.4 Wind Stresses

The hydraulic quantities presented above depend fundamentally both on the friction at the sea bottom and on wind stresses exerting on wave surfaces through the parameters m and S. The wind stresses can be derived from Eqs. (4.32), (4.33), (4.42), and (4.130) as

$$\bar{\sigma}_\tau/s = S/(\delta_1 - 1), \qquad (4.150)$$

$$(1 + m_b)(\tau_s/s) = (\sigma_\tau/s)(1 + \delta_1\eta), \qquad (4.151)$$

$$\bar{\sigma}_p/s = \{(4/s\bar{R}) - (\varepsilon_1/s)\}/\bar{Q}, \qquad (4.152)$$

where

$$\varepsilon_2/s = 1/[\overline{Q}\{1 + 2(\overline{Q}/c^2)\}], \tag{4.153}$$

and $\varepsilon_1/\varepsilon_2$ can be determined as the function of the modulus k from the definition for the most stable wave motion, explained in Section 4.3(4). Furthermore, the shear stress required to cause a wave to break in the presence of surface drift, mentioned previously in Chapter 2, is given by

$$(\tau_s/s)_c = \frac{\lambda^2}{sRe}\sqrt{\tilde{B}^2 - 2Re\,\tilde{A}} \fallingdotseq \sqrt{(\lambda/sR)(\sigma_p/s)(-2\kappa_s)}, \tag{4.154}$$

in the notation there, for the kinematic boundary condition at the wave surface, $\partial\eta/\partial\xi = W/(U-1)$, can be satisfied exactly with the aid of Eqs. (4.106), (4.109), and (4.111). If the average velocity of a wind-forced wave is taken as the water particle velocity at a wave crest, the effect of the vertical distribution of water particle velocity $\tilde{B}$ can be negligible, but the resultant shear stress might be overestimated due to the underestimation of the water particle velocity.

It is clear that the effect of friction at the sea bottom on the shear stresses σ_τ and $(1 + m_b)\tau_s$ can be excluded by the adoption of the ratios of stresses to bottom friction, and that these ratios are also independent of the Reynolds number, as seen in Eqs. (4.150) and (4.151). The pressure σ_p/s and additional shear stress $(\tau_s/s)_c$, on the contrary, depend both on the bottom friction and on the Reynolds number.

4.5 Quantitative Character of Wind-Forced Waves

The physical quantities of the wind-forced waves can be determined for the five quantities given, the Reynolds number R, the friction at the sea bottom s, the wind stresses σ_p and σ_τ, and the unknown coefficient δ_1; the first two are the flow field quantities, while the others are unknown variables and it is difficult to give these three quantities theoretically

in advance. However, the parameters S, $\varepsilon_1/\varepsilon_2$, and m can respectively take on the roles of wind stresses σ_τ, σ_p, and the coefficient δ_1 through the second of Eq. (4.130), the first and second of Eq. (4.42), and Eq. (4.138). Then, with the aid of these relations, two of the three parameters can be eliminated. Moreover, if Manning's roughness coefficient n is used, the relation between h and s is given by

$$s = g \cdot n^2 \cdot h^{-1/3}, \qquad h = h(\nu, R). \tag{4.155}$$

Accordingly, the wind-forced waves for a given water depth and Manning's roughness coefficient n are formulated as a one parameter family of S or m or $\varepsilon_1/\varepsilon_2$. Hereafter, the kinetic viscosity ν = 0.01 cm^2/sec and Manning's roughness coefficient n = 0.02 $sec \cdot m^{-1/3}$ are used to represent the quantitative character of the wind-forced waves.

(1) **Hydraulic quantities**

Among the hydraulic quantities of wind-forced waves, the wave height and wave period are easily observable. In addition, as the parameter S relates directly to the shear stress exerting on waves, it is chosen as the main parameter and the diagrams are given as functions of the wave period for the required wave height.

Fig. 4.15 shows the changes in wave velocity with respect to the wave period for H = 0.3, 0.5, and 0.7. The lowest wave periods of the curves for given values of S were determined from Eq. (4.140) and the greatest wave periods for small values of S were determined to satisfy the condition that $\overline{Q}$ = 1. Chain and broken lines in the figure show the relation between the wave velocity and wave period given by finite amplitude wave theories, the Stokes third order wave theory(S-3)[13] and the cnoidal wave theory of the third order approximation(NC-3)[14], neglecting wind effects. The lowest values for S-3 were also decided using the Rankine-Stokes breaking

condition[15]. There exists an envelope, the upper bound of the wave velocity, for a given wave height. Note that the wind-forced waves exist in the region where the wave velocities are nearly equal to or greater than those determined by the finite amplitude wave theories above, and also that the changes are more sensitive to the external force S rather than to the wave height.

Similarly, changes in wind-induced current, in mass transport velocity, in progressive discharge, and in average velocity at the wave crest are shown in Figs. 4.16, 4.17, 4.18, and 4.19, respectively. Fig. 4.16 shows that the wind-induced current increases sharply with respect to the wave period and is asymptotic to the limiting value of $S/2$, as given in Eq.

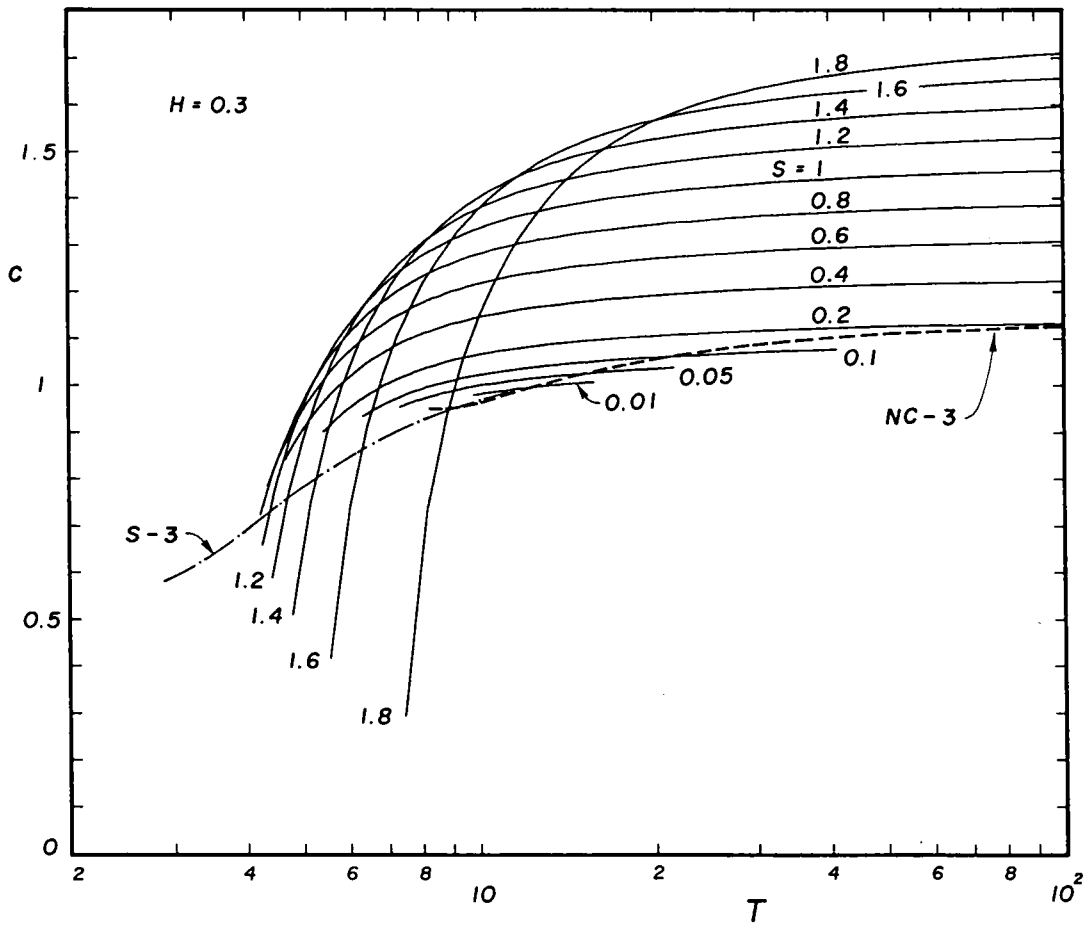

(1) H = 0.3

Fig. 4.15 Wave velocity of the wind-forced waves.

(4.143). Moreover, the mass transport velocity can be approximated by $U_m \fallingdotseq 1 - \overline{Q}$, comparing **Fig. 4.17** with **Fig. 4.18**, but the difference in approximation becomes comparatively great both for smaller wave periods and for greater wave heights. The reason can be explained as follows: from Eq. (4.36)

$$U_m = 1 - \overline{Q} - (1/L)\int_0^L U\eta \, d\xi, \tag{4.156}$$

so the nonlinear interaction between the water surface displacement and average velocity is, in effect, the same as in nonlinear wave theories without wind effects[14),15),16)].

Evidently from Eq. (4.36), for a great progressive discharge, the

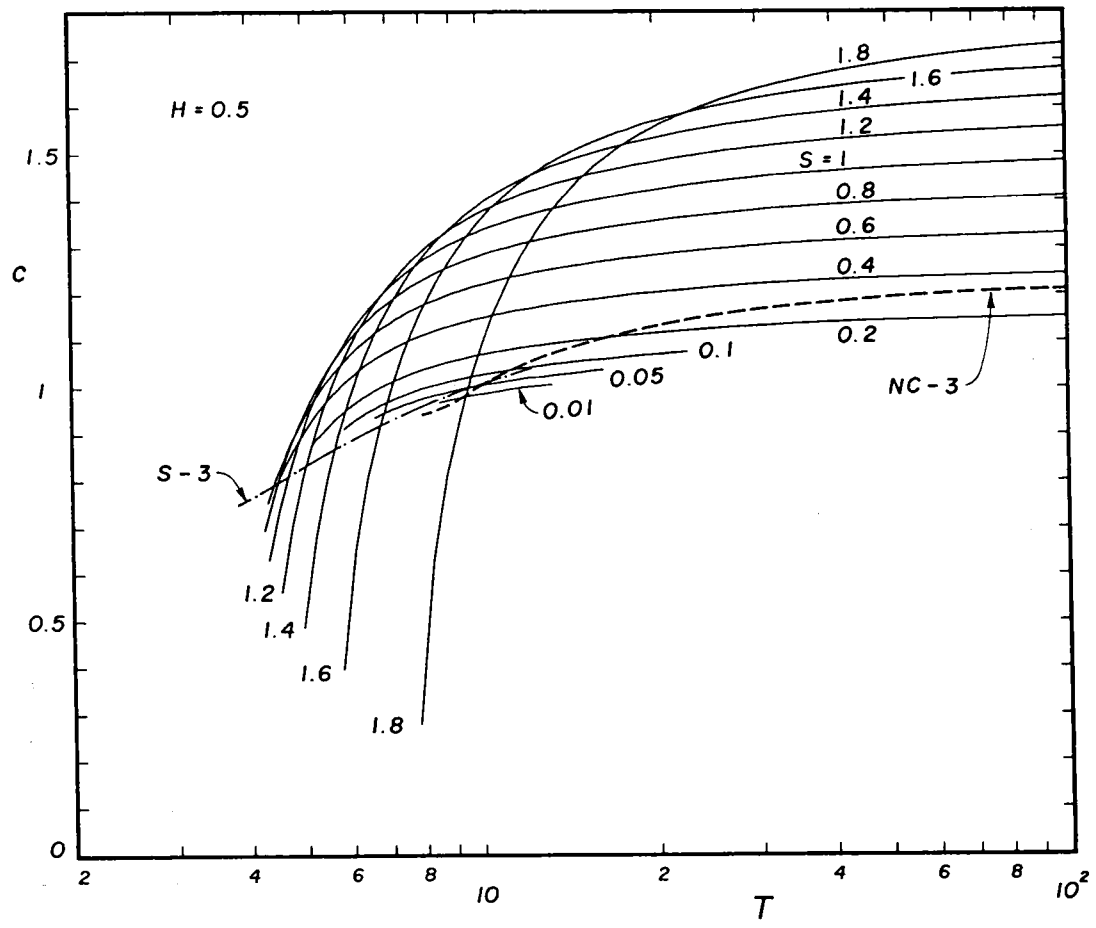

(2) $H = 0.5$

Fig. 4.15 Continued.

average velocity at the wave crest takes on a small value, while this velocity approaches unity as the external force S tends toward 2 as shown in Fig. 4.19, which corresponds to the Rankine-Stokes breaking condition in a certain sense. However, the velocity is averaged over the water depth, so the horizontal component of water particle velocities is underestimated, and, furthermore, the surface drift due to the vortical wind-drift layer at the air-sea interface may cause the average velocity to take on a value smaller than unity at just breaking. In this case, the wind-forced waves would break before the external force S reached to 2, that is, there may exist an upper restriction for S in practical applications.

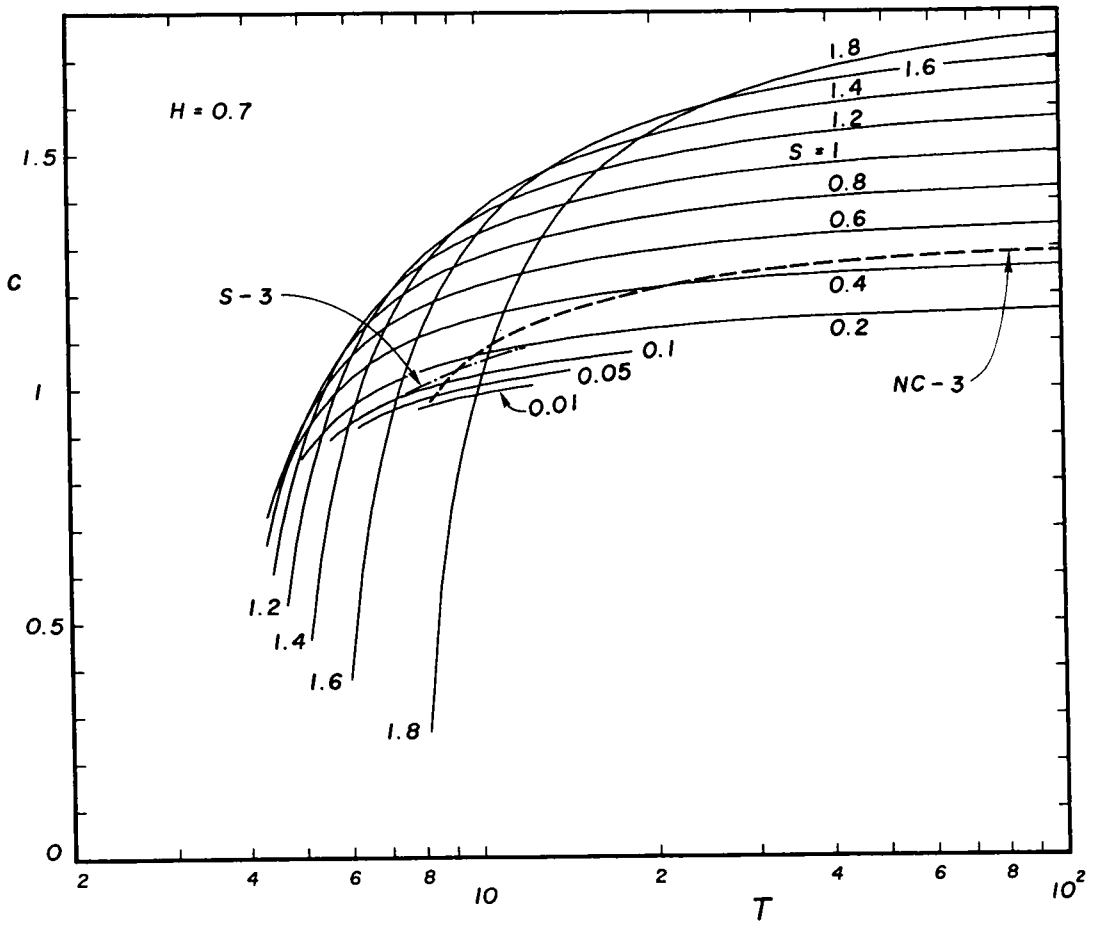

(3) H = 0.7

Fig. 4.15 Continued.

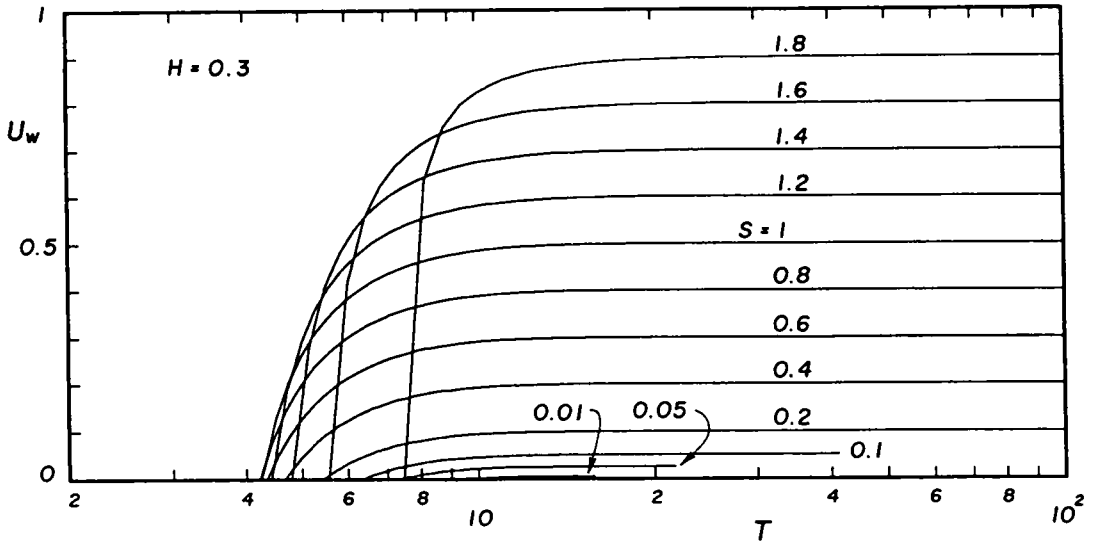

(1) H = 0.3

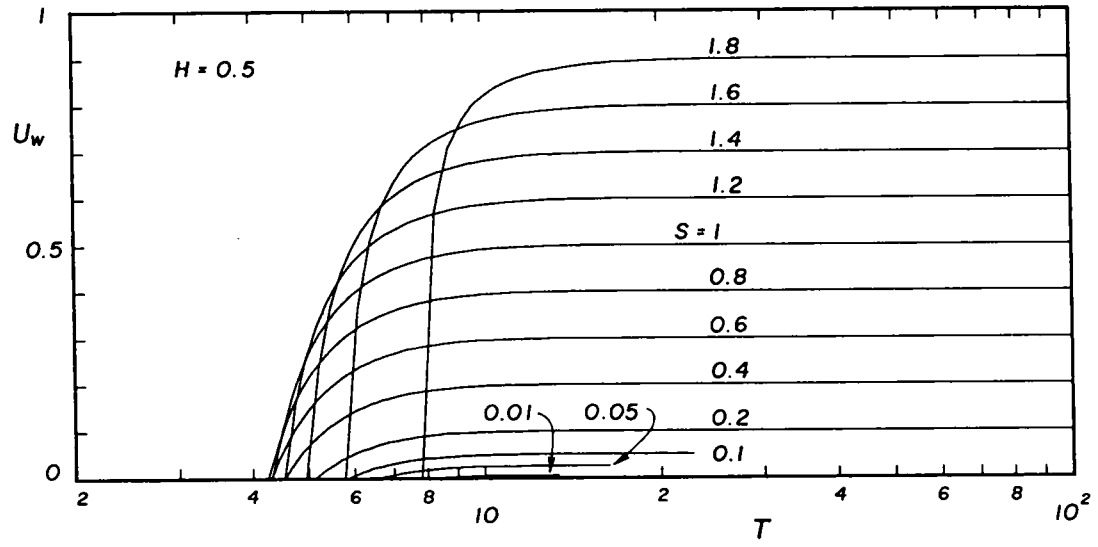

(2) H = 0.5

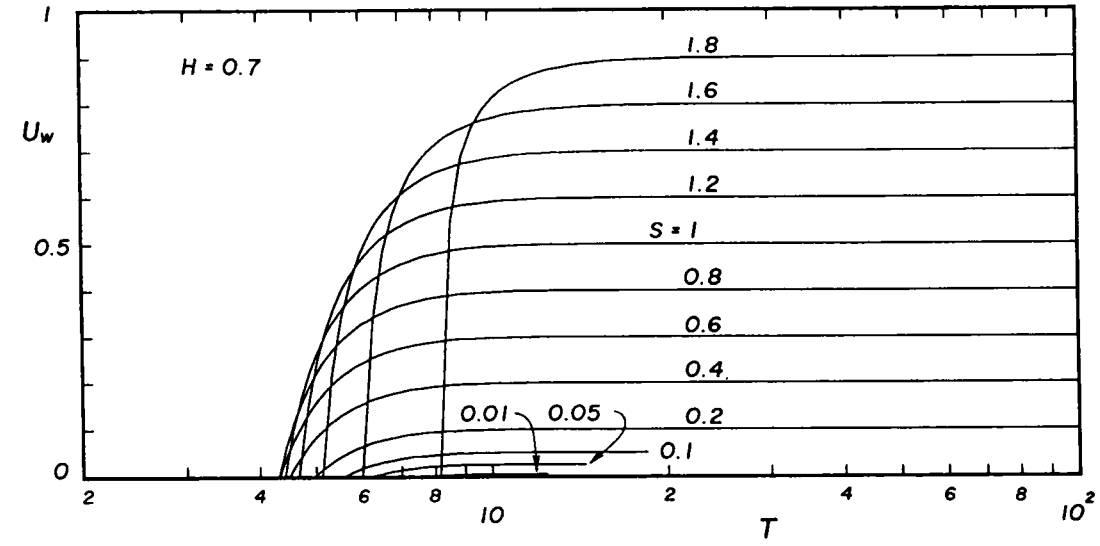

(3) H = 0.7

Fig. 4.16 Wind-induced current in the wind-forced waves.

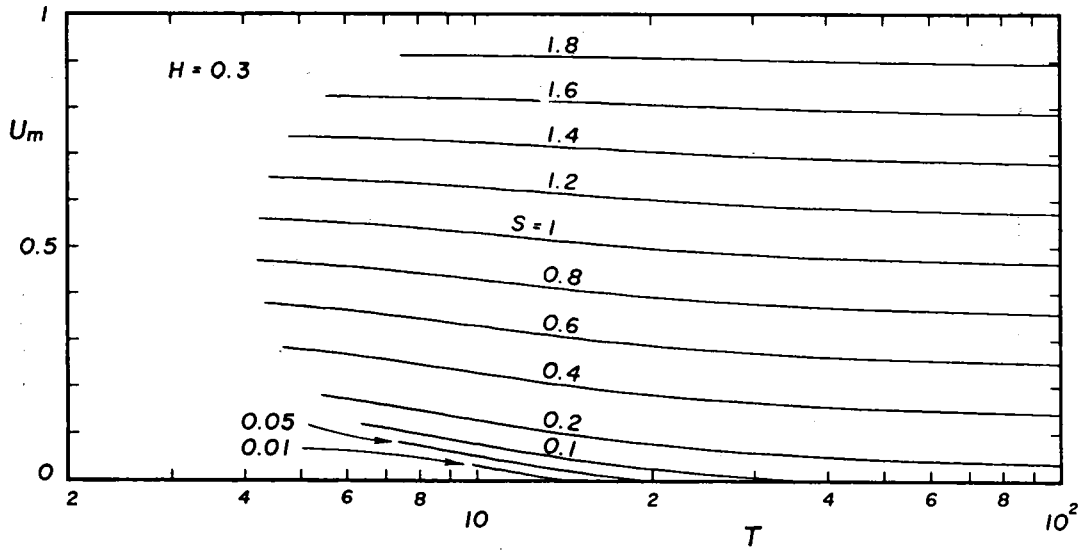

(1) H = 0.3

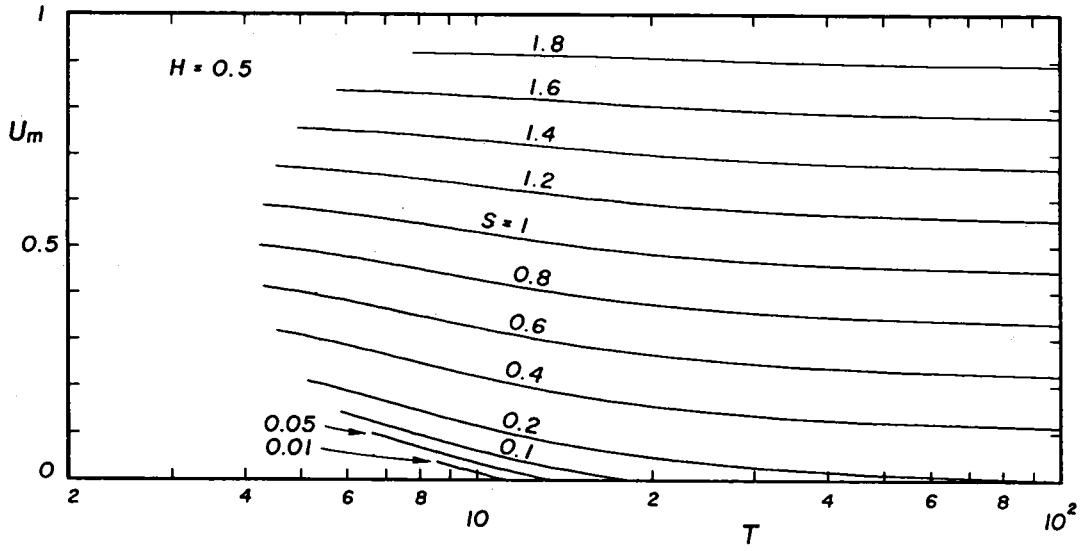

(2) H = 0.5

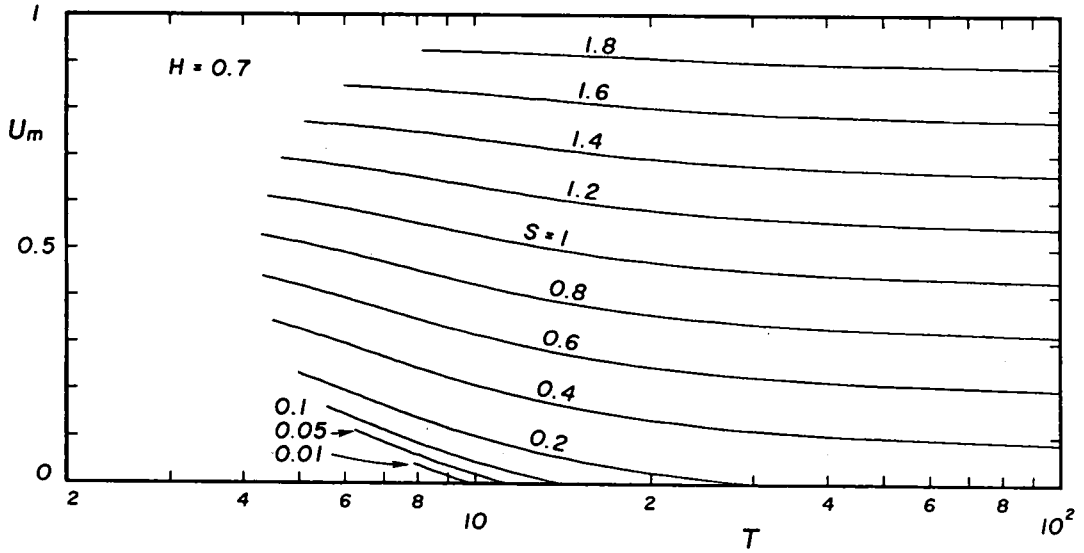

(3) H = 0.7

Fig. 4.17 Mass transport velocity of the wind-forced waves.

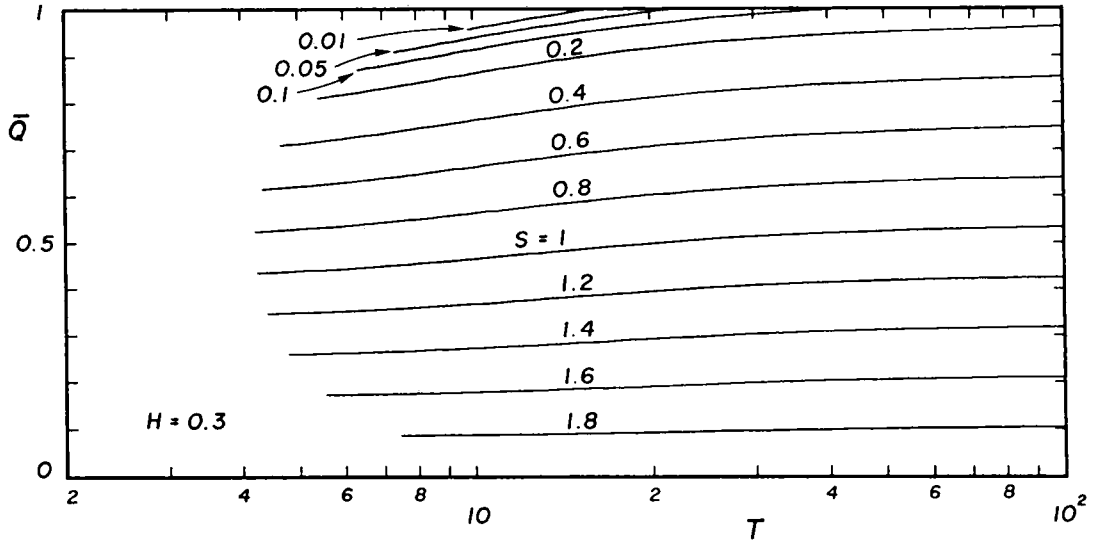

(1) H = 0.3

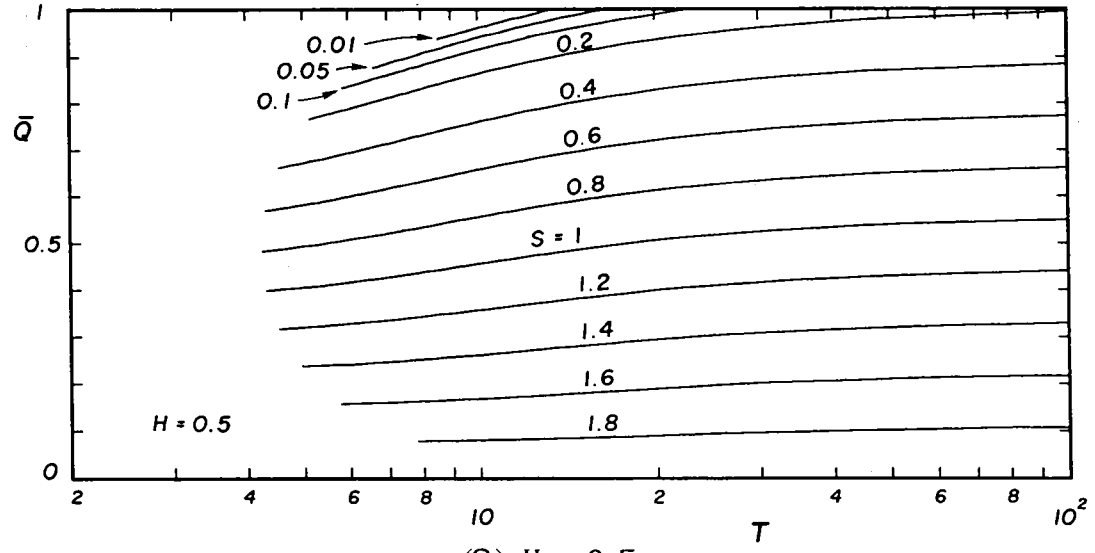

(2) H = 0.5

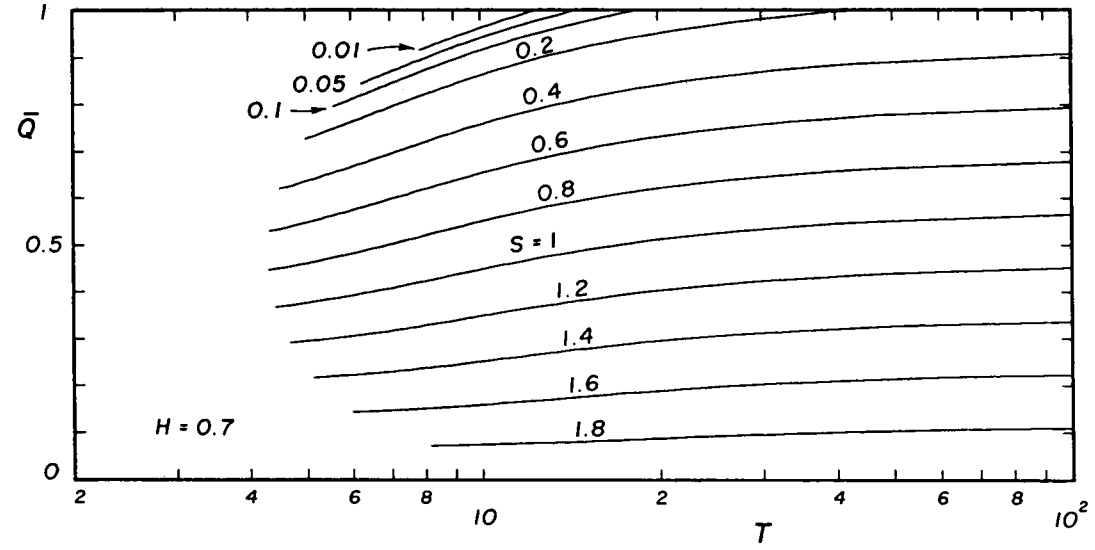

(3) H = 0.7

Fig. 4.18 Progressive discharge of the wind-forced waves.

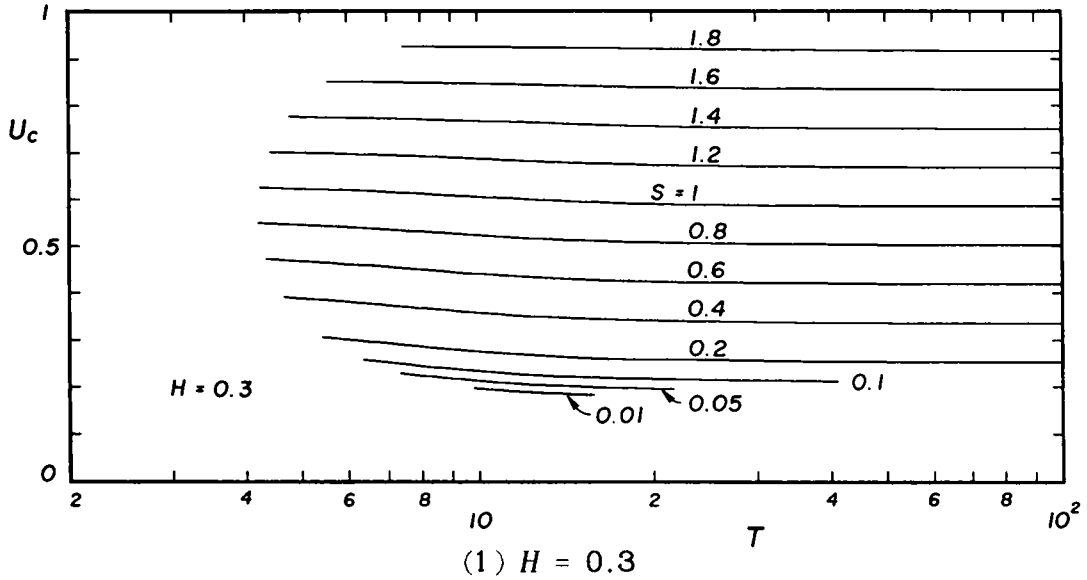

(1) H = 0.3

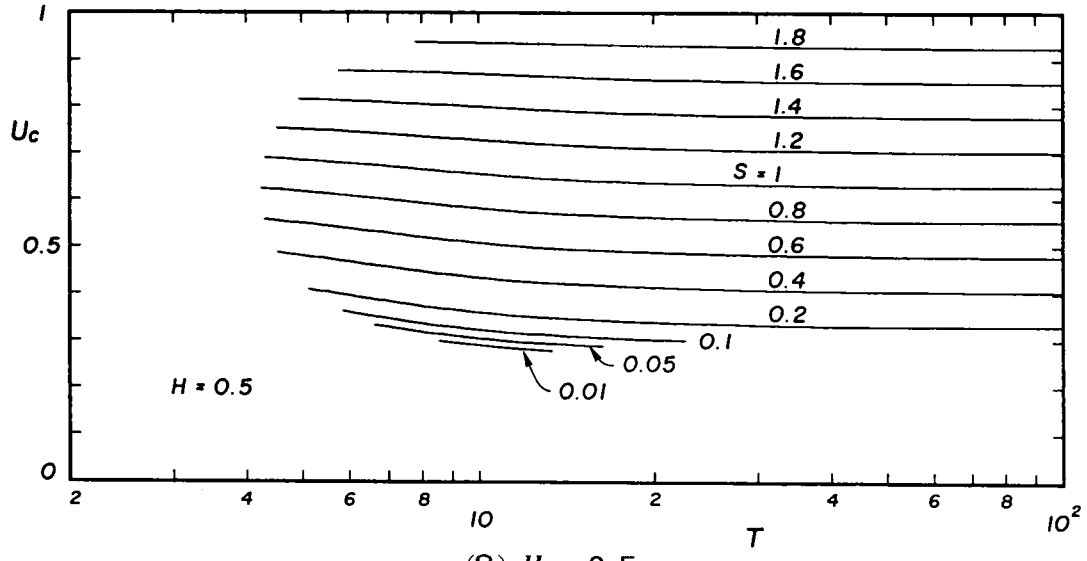

(2) H = 0.5

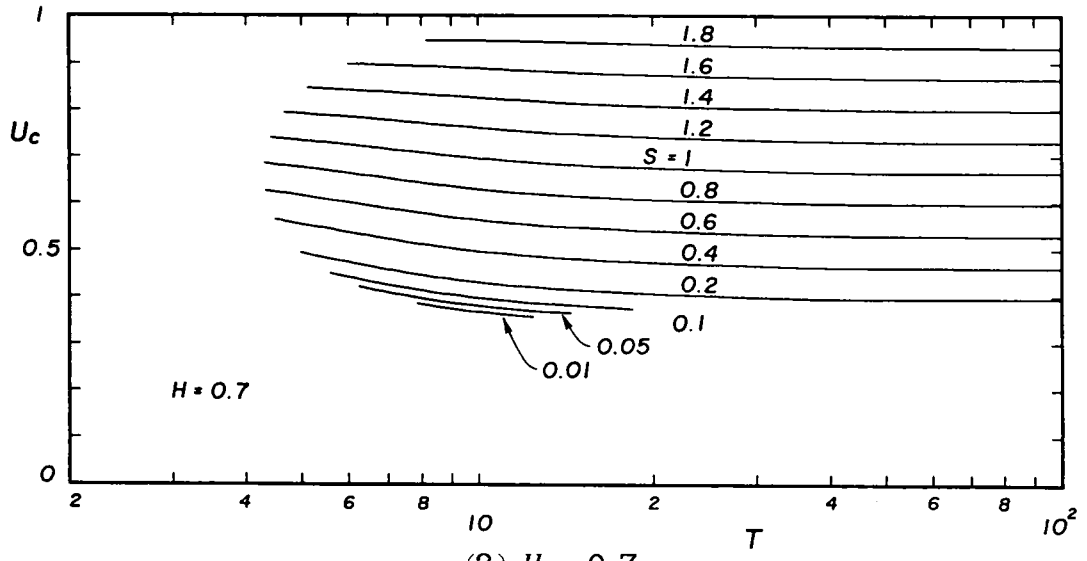

(3) H = 0.7

Fig. 4.19 Average velocity at the cests of the wind-forced waves.

(2) Wind Stresses

Figs. 4.20 and **4.21** show the changes in shear stresses σ_τ/S and $(1+m_b)(\tau_s/S)_c$ at the wave crest, they being independent of the Reynolds number and bottom friction. The increase in these shear stresses with respect to the wave height for small values of S is remarkable compared with that for great values of S. It can also be noted that there exist maxima at certain wave periods both in the shear stress σ_τ/S for all S and in the shear stress at the wave crest $(1+m_b)(\tau_s/S)_c$ for moderately small values of S, but this second shear stress $(1+m_b)(\tau_s/S)_c$ increases sharply with respect to the wave period for great values of S, while the maxima, on the contrary, disappear. Nearly constant values for shear stresses indicate that they may be in a saturation state. This suggests the existence of optimum wave heights and wave lengths for the generation of shear stress by wind-wave interaction; namely, as the wave length becomes moderately long for great values of S, the roughness caused by the water surface displacement has less effect on the shear stress. Since the shear stress σ_τ/S can be regarded as a quantity at the mean water level, the distribution of shear stress in phase with a given wave elevation governs the shear stress values.

On the other hand, the pressure depends on the Reynolds number and on the friction at the sea bottom and it changes as shown in **Fig. 4.22.** Slight differences in pressure for $R = 10^5$ and $R = 10^6$ occur only near a region of small T and of great S, but the pressure for $R > 10^6$ is indistinguishable from that for $R = 10^6$. For the conditions $R = 10^5$ and 10^6, the water depths are $h \fallingdotseq 10.1$ cm and 46.7 cm for $\nu = 0.01\text{cm}^2/\text{sec}$, respectively, so the effect of the Reynolds number on the pressure is negligible in the deeper region for almost all wind-forced waves except for ones with small T and great S. Similar to the changes in shear stress σ_τ/S, the pressure takes on

local maximum values and approaches the saturation point, depending on the effect of the distribution of pressue in phase with a given wave slope.

Comparison of **Fig. 4.20** with **Fig. 4.22** shows that for small S the pressure is always greater than the shear stress, but the pressure becomes smaller than the shear stress, where values of T are small, with respect to the increase in S. Therefore, at the outset where the wind-induced current increases sharply for great S, as shown **Fig. 4.16**, the shear stress has a primary role in the wave generation, but after that, the fully developed wind-forced waves are maintained chiefly by the pressure.

Fig. 4.23 gives the total wind stress $\sqrt{\sigma_\tau^2+\sigma_p^2}/S$ exerting on wave surfaces. The Reynolds number has much less effect for the same reasons explained just above. The total wind stress takes on the maximum value at certain wave periods as does the pressure. It can be conclusively noted that Burgers' term, the first term in the right-hand side of Eq. (4.37), as well as the shear stress term, has significant effect on the generation of the wind-forced waves.

The shear stress at just breaking $(\tau_s/S)_c$, given by Eq. (4.154), is also dependent on the Reynolds number and on the bottom friction. The effects of the Reynolds number on this shear stress for the three wave heights H = 0.3, 0.5, and 0.7 are shown in **Fig. 4.24**, where the values for pressure from **Fig. 4.22** are evaluated. This figure, then, gives the values for shear stress at the wave crest which will cause the wind-forced waves to break. Their orders are naturally less than that for the wind-forced waves given in **Fig. 4.21**. The typical feature is that the shear stress $(\tau_s/S)_c$ takes on local maximum values at certain wave periods, similar to σ_τ/S and σ_p/S, and begins to increase sharply for all Reynolds numbers. In Eq. (4.154), for given H and S, the terms λ/SR and σ_p/S are slowly varying functions in the region of great T as shown in **Figs. 4.19** and **4.22**, thus the sharp increase in shear stress can be attributed to that of the curva-

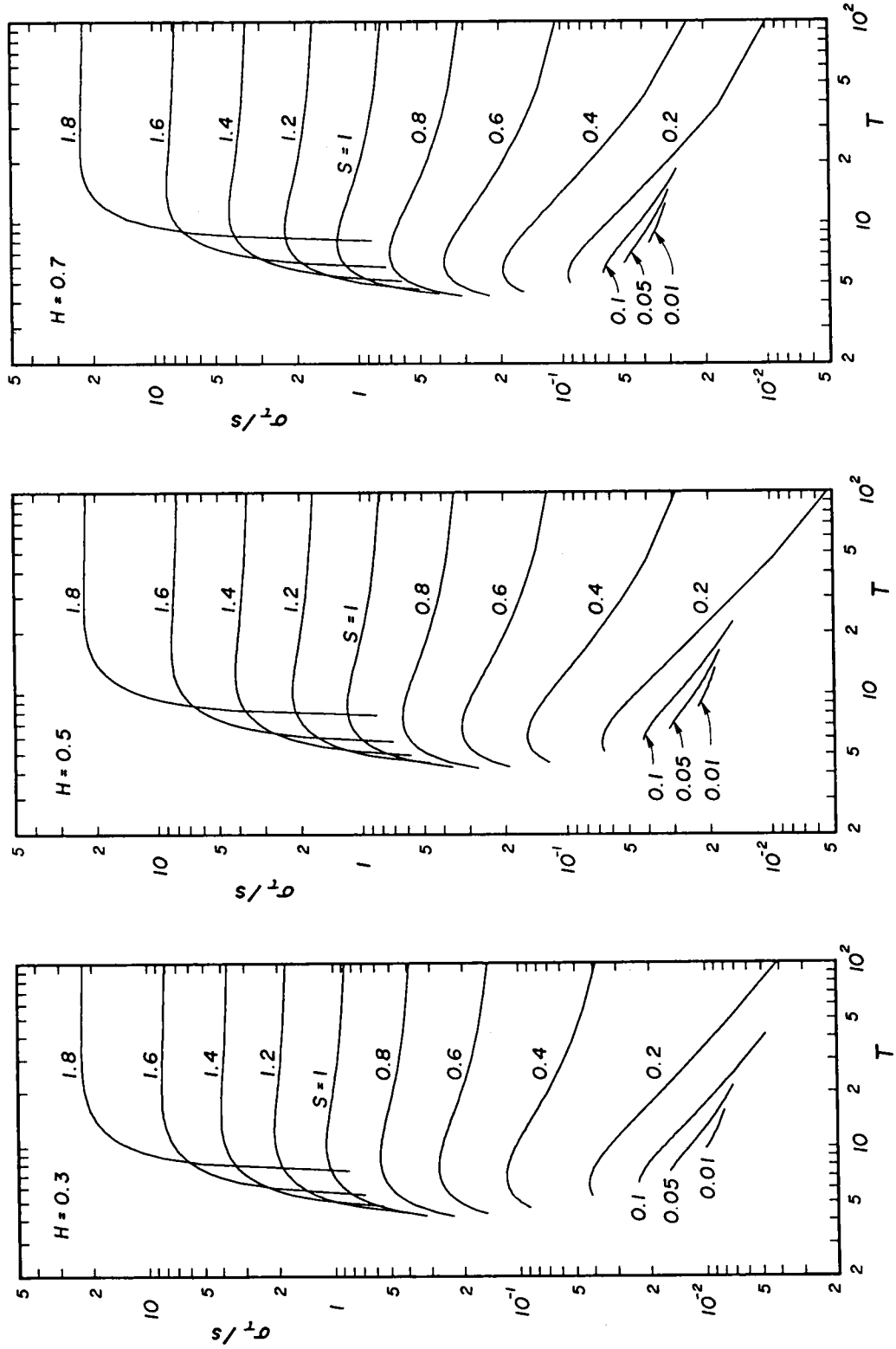

(1) $H = 0.3$ (2) $H = 0.5$ (3) $H = 0.7$

Fig. 4.20 Shear stress exerting on the wind-forced waves.

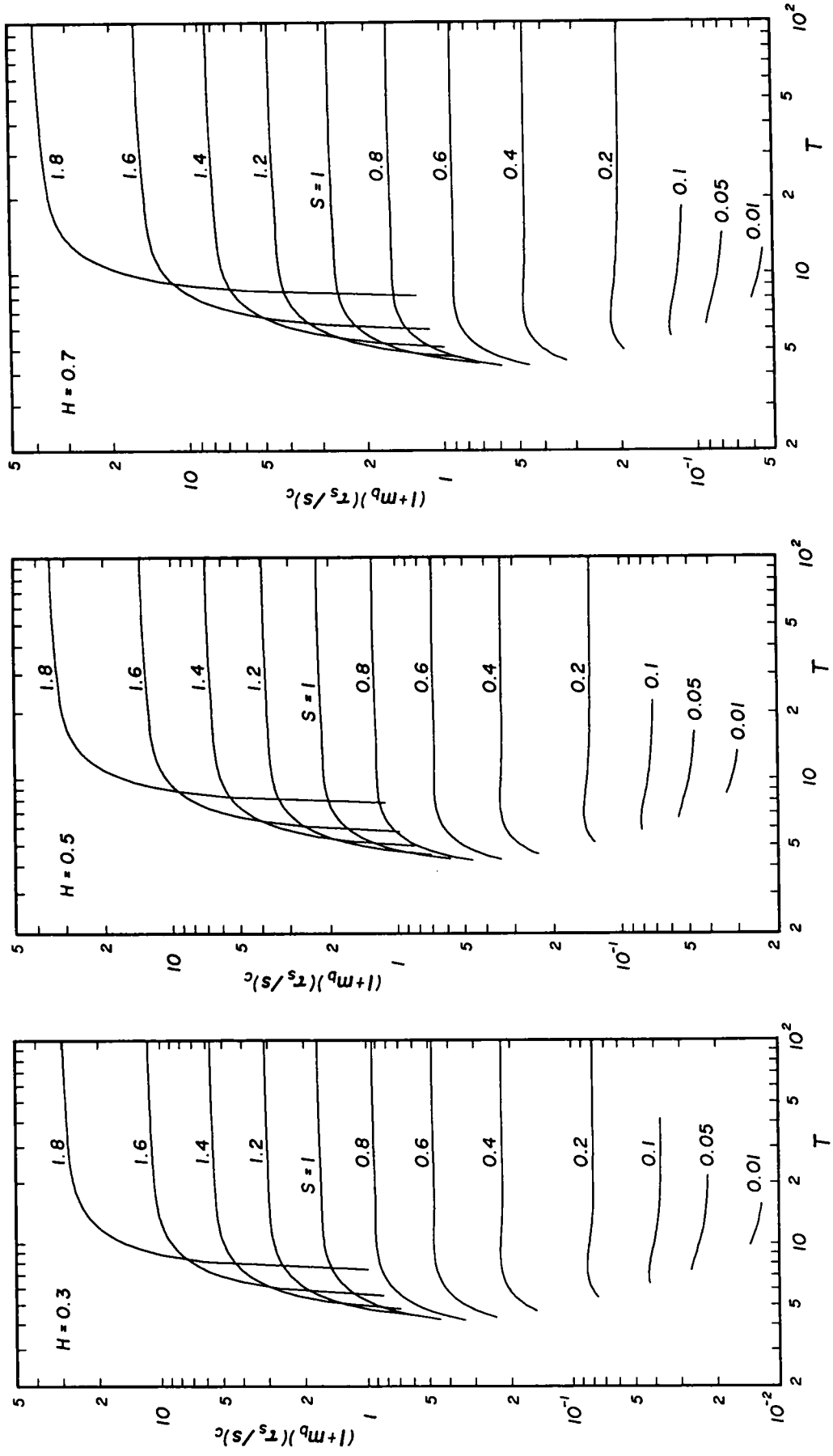

(1) $H = 0.3$ (2) $H = 0.5$ (3) $H = 0.7$

Fig. 4.21 Shear stress exerting on the crests of the wind-forced waves.

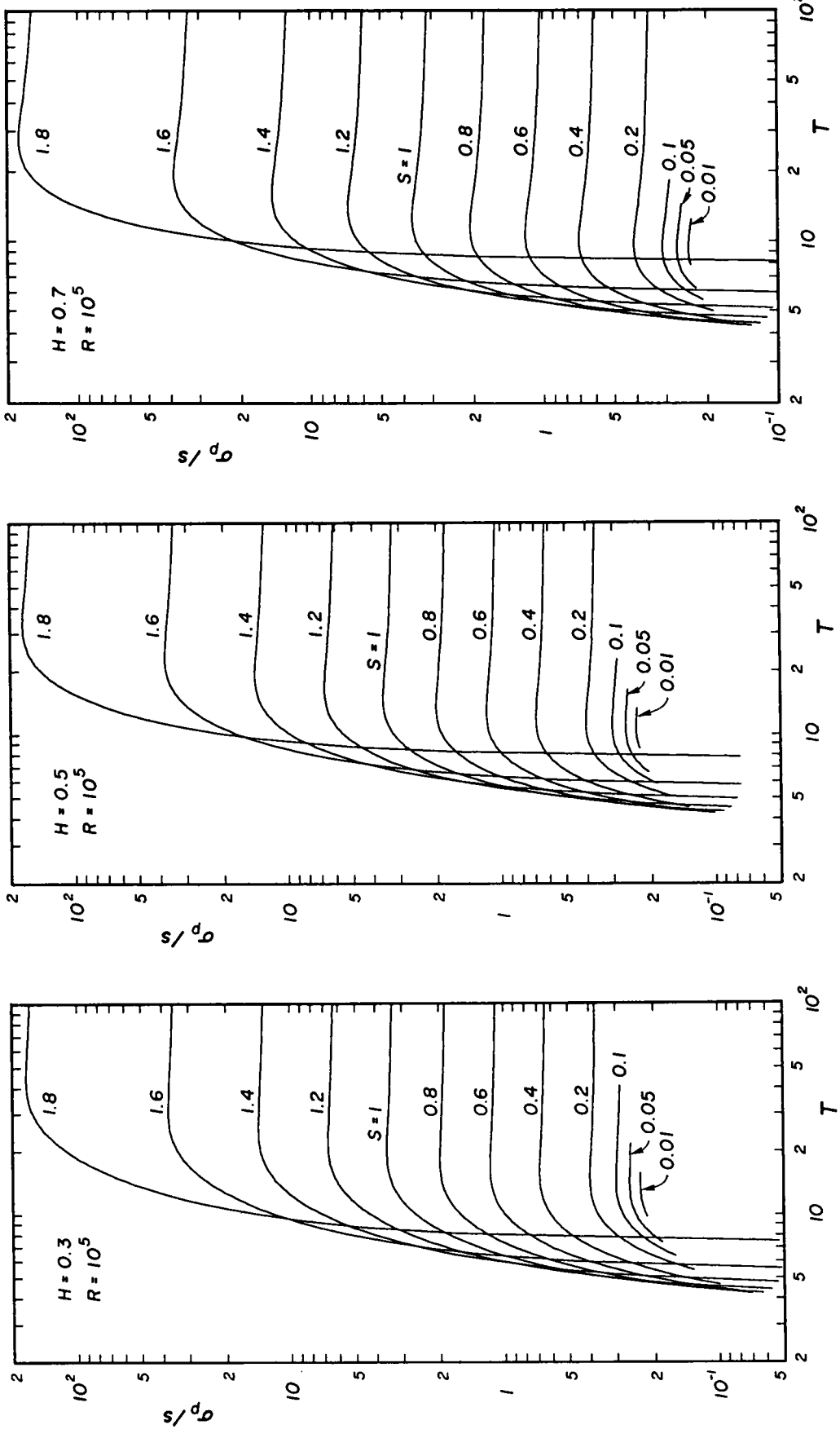

(1) $H = 0.3$ (2) $H = 0.5$ (3) $H = 0.7$

Fig. 4.22 Pressure exerting on the wind-forced waves ($R = 10^5$).

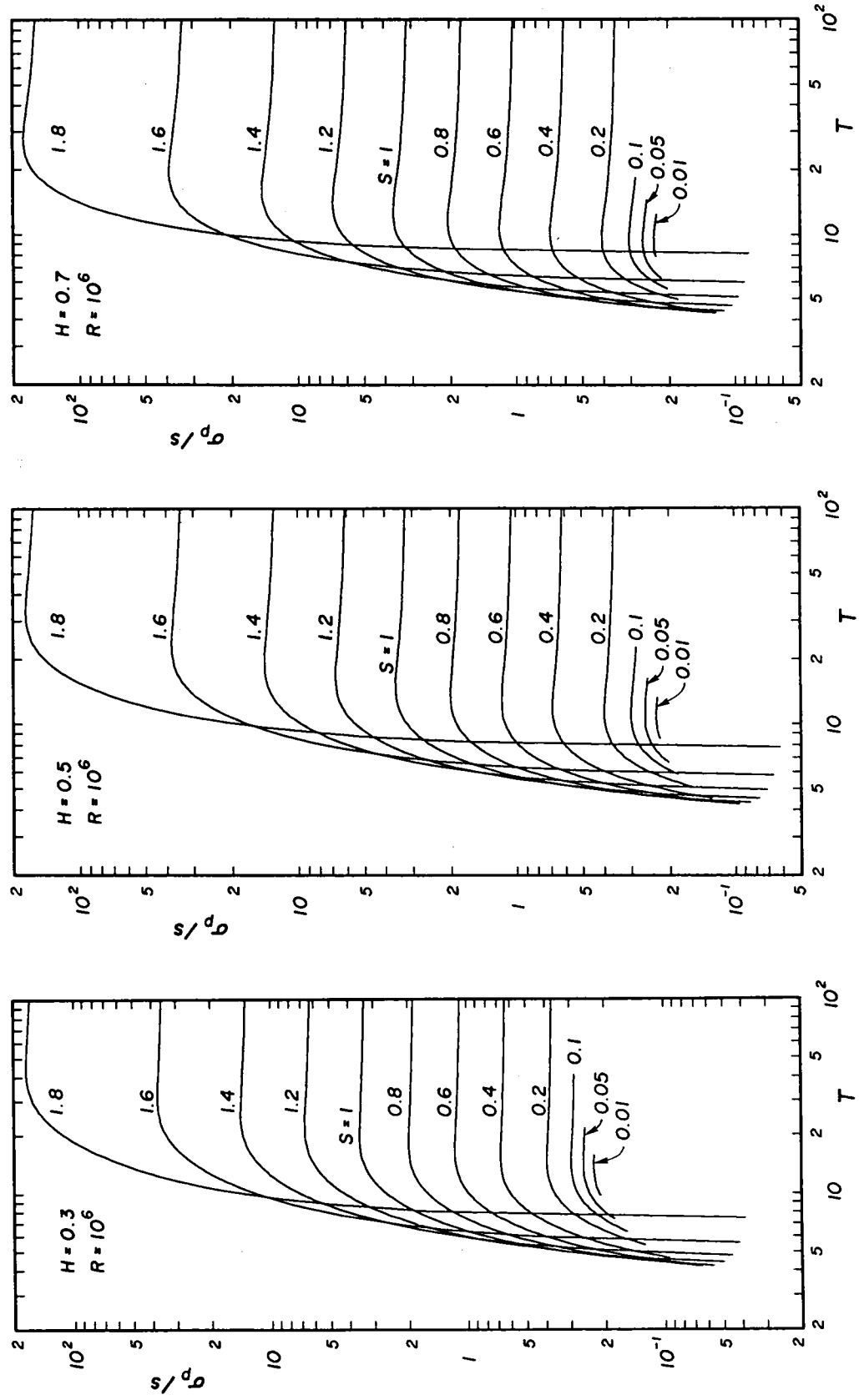

(1) $H = 0.3$ (2) $H = 0.5$ (3) $H = 0.7$

Fig. 4.22 Continued ($R = 10^6$).

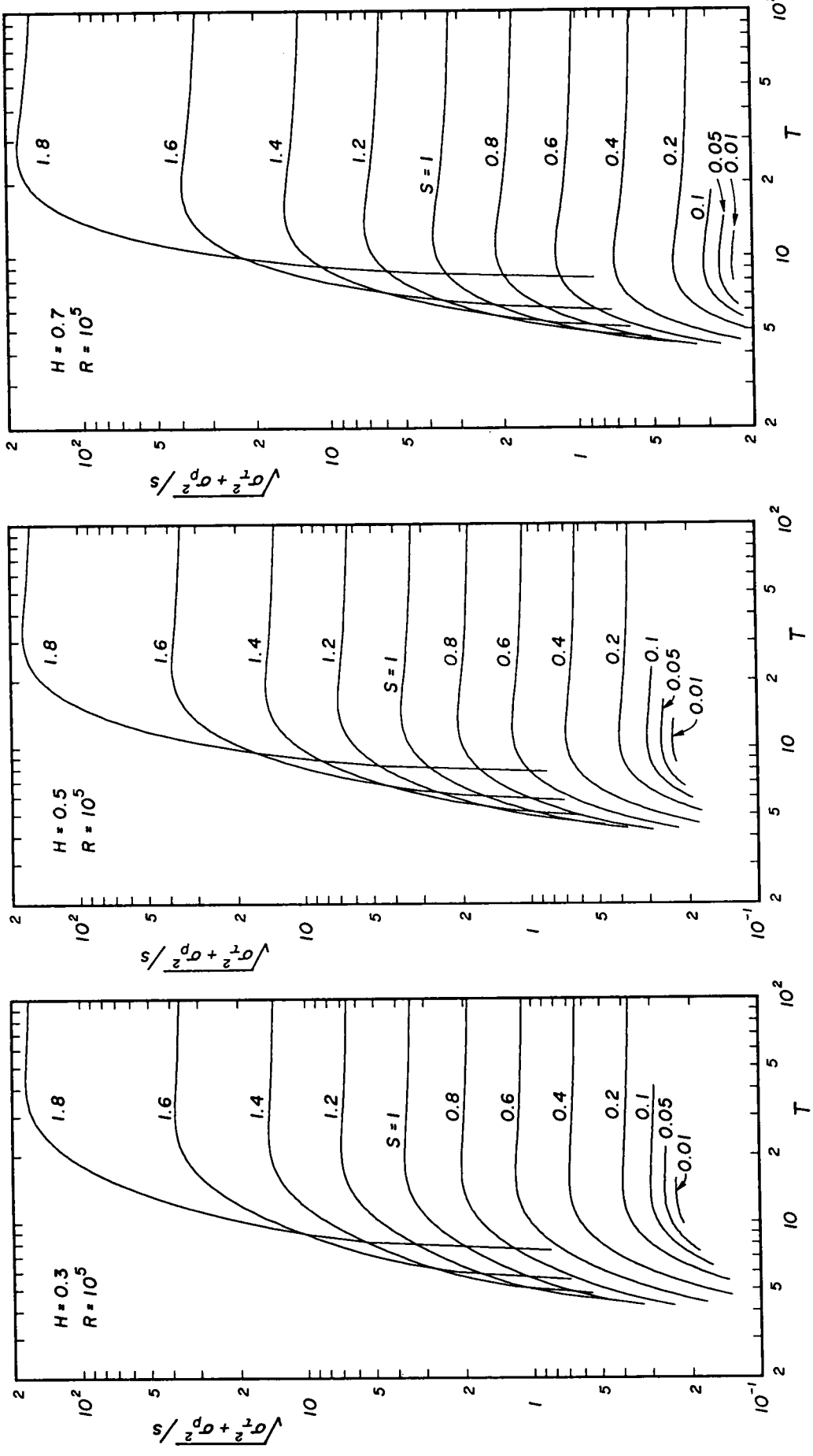

(1) $H = 0.3$ (2) $H = 0.5$ (3) $H = 0.7$

Fig. 4.23 Total wind stress exerting on the wind-forced waves ($R = 10^5$).

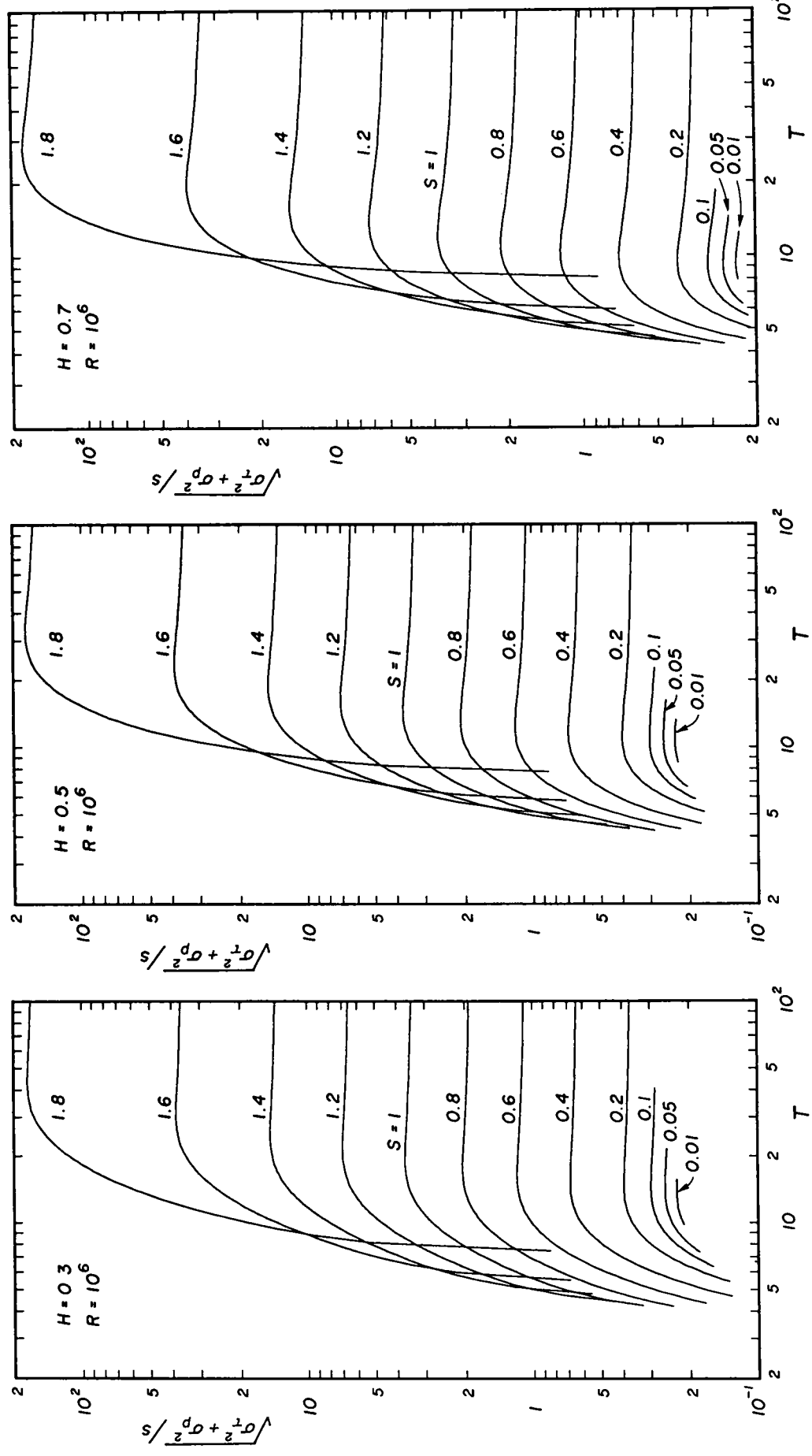

(1) $H = 0.3$ (2) $H = 0.5$ (3) $H = 0.7$

Fig. 4.23 Continued ($R = 10^6$).

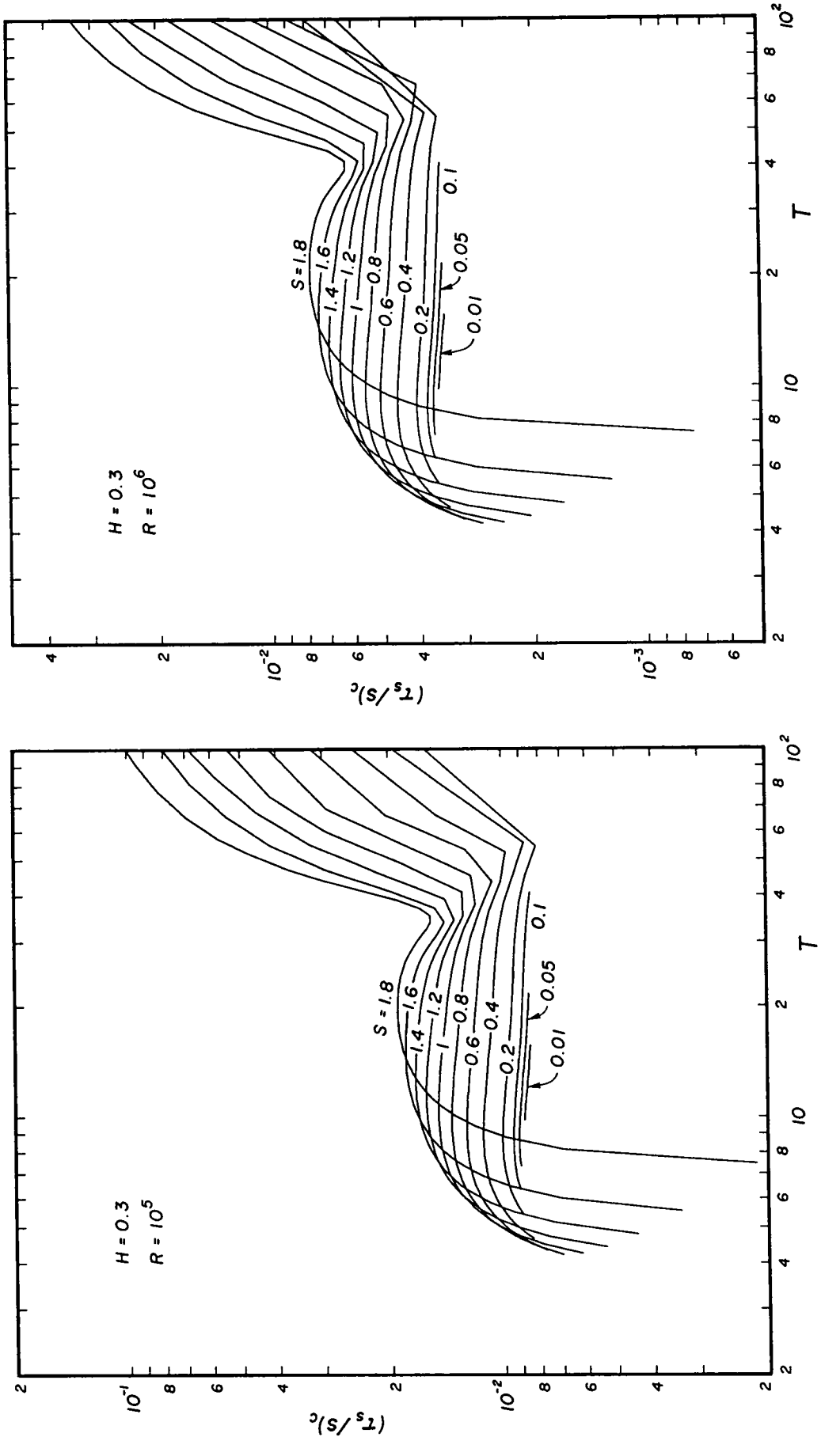

(1) $R = 10^5$ (2) $R = 10^6$

Fig. 4.24 Shear stress at the crests of the wind-forced waves in the presence of surface drift ($H = 0.3$).

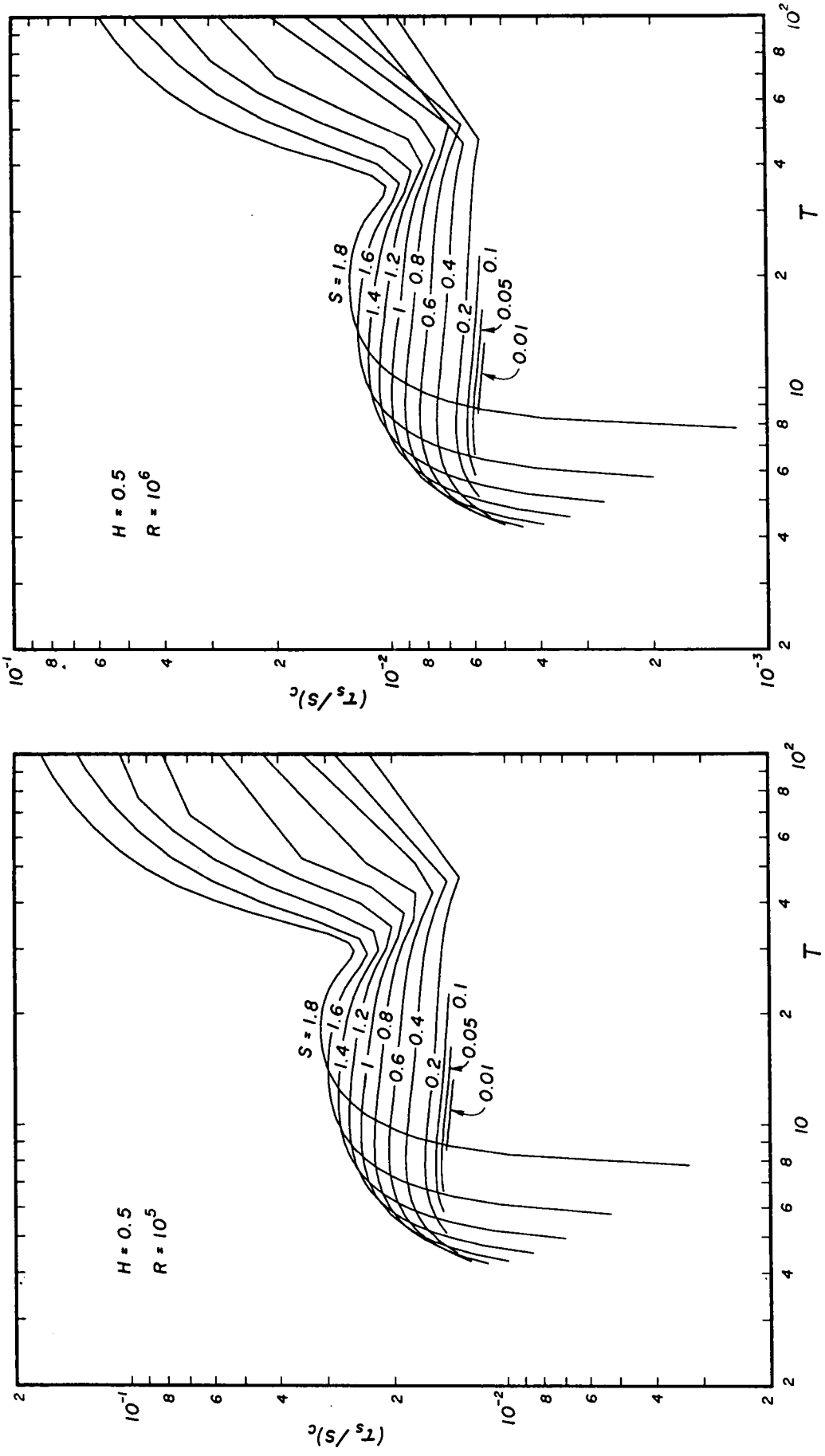

(2) $R = 10^6$

(1) $R = 10^5$

Fig. 4.24 Continued ($H = 0.5$).

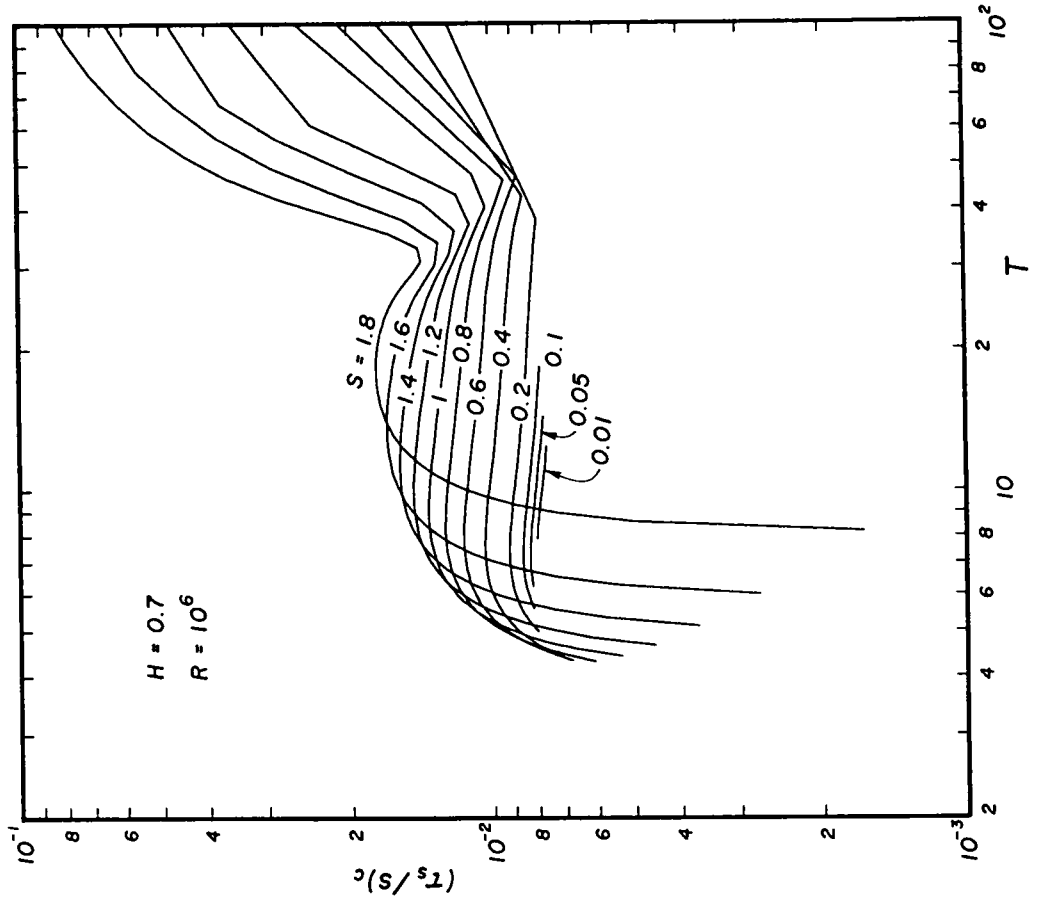

(2) $R = 10^6$

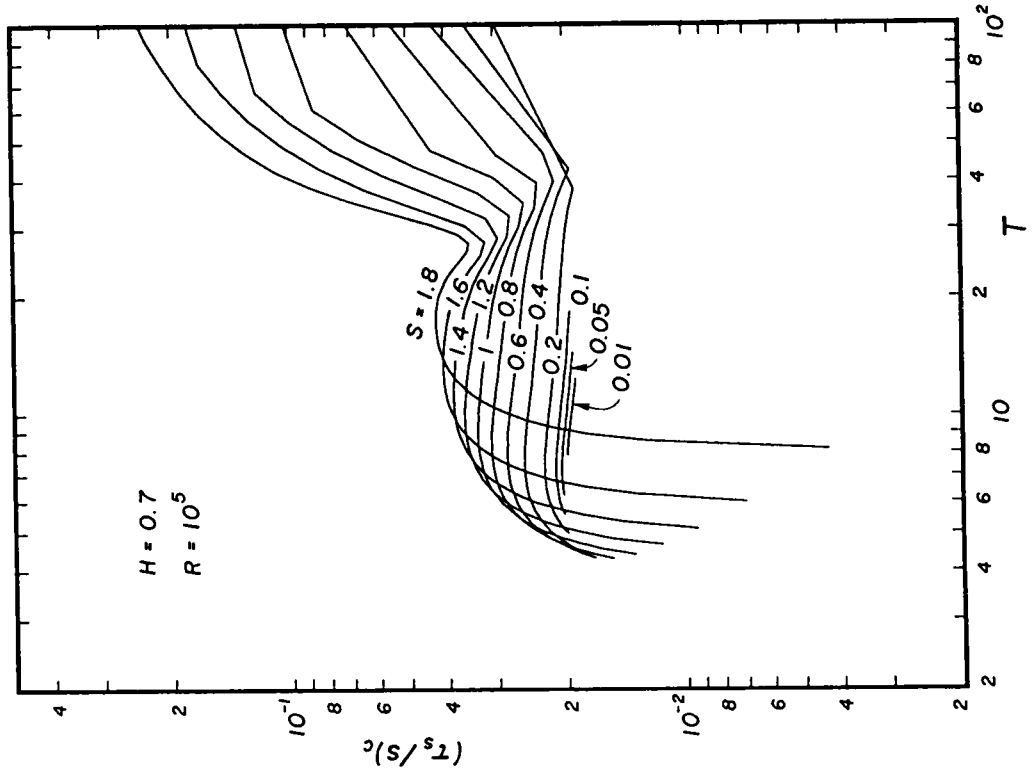

(1) $R = 10^5$

Fig. 4.24 Continued ($H = 0.7$).

ture k_s at the wave crest. This may greatly affect wave breaking, but, unfortunately, how the shear stress is partitioned to generate the wind-forced waves and to produce surface drift is unknown in the present analysis, so the breaking condition cannot be formulated.

These diagrams presented above can be used practically to obtain physical quantities for wind-forced wave. First, for the flow field quantities given, R and s, detemine the wave height and wave period, for instance, the significant wave height and wave period because the wave field can be characterized by these wave quantities. Secondly, determine the physical parameter S from **Fig. 4.20** for the required σ_τ/s if the shear stress σ_τ is known. Consequently, physical quantities for the wind-forced waves can be obtained.

(3) Wave Profiles and Distributions of Average Velocity and Shear Stress with Respect to the Phase of Waves

Fig. 4.25 to **Fig. 4.30** show the representative wave profile η and distribution of average velocity U together with the phase shift ξ_0/L. The values for $1 - U$ and the inverse of the wave velocity $1/c$ are also shown in the figures. The physical parameter is temporarily fixed to be $m = 0.242$ in these figures to clarify the effects of the Reynolds number and the bottom friction on wave profiles and velocity fields of developing wind-forced waves, so the Reynolds number takes on three values of $R = 10^6$, 10^7 and 10^8 for the same waves given in **Table 4.1.**

For small wave heights, the wave profiles remain nearly symmetric but become asymmetric as the waves grow. The smaller the Reynolds number and progressive discharge, (namely, the shallower the water depth and the greater the average velocity,) the more remarkable the asymmetry, as the friction at the sea bottom for a small Reynolds number is greater than that

for a large Reynolds number; consequently, the phase shift is great, and also, for smaller progressive discharge, the shear stress is great compared with the bottom friction, as shown in **Fig. 4.20**. Moreover, when the wave profiles become asymmetric, slight secondary waves occur at the windward sides of wave crests, as indicated in **Fig. 4.25(4)**.

As to the velocity field, when the progressive discharge is great, that is, when the water particle velocity is small, the two curves $1 - U$ and $1/c$ intersect at some phases, and then the phases become nearly equal to the mean water level as the wave grows. At intersections of the curves $1 - U$ and $1/c$, the equality $c - \bar{u} = 1$ holds in the frame of reference moving with the wave. In this situation, it follows that $c - \bar{u} > 1$ near the phase of the wave crest, thus the velocity field within these phases is, hydraulically speaking, subcritical and in the other phases, supercritical. For another m and R or s the same properties can be obtained.

Fig. 4.31 shows the distribution of normalized shear stress $\tau_s/\tau_{sc} = (1 + \delta_1\eta)/(1 + \delta_1\eta_c)$ exerting on waves given in **Table 4.1**, where τ_{sc} is the shear stress at the wave crest. The shear stress distributes similar to the wave profile and average velocity but is positive even at the wave trough. For a small progressive discharge, great average velocity and wind-induced current, the shear stress at the wave trough also becomes great, therefore the shear stress term in the right-hand side of Eq. (4.34) always acts like a positive external force.

Similar configurations of the asymmetric wave profile and water particle velocity may be seen in waves generated by strong wind in shallow water near a coastal zone. Therefore, the present analysis can help understand this phenomenon; the analysis, however, depends chiefly on the evaluation of the friction at the sea bottom, which affects the phase directly. At this stage, an example for a reasonably great value of bottom friction is needed to show how the asymmetry occurs. **Fig. 4.32** shows examples for when

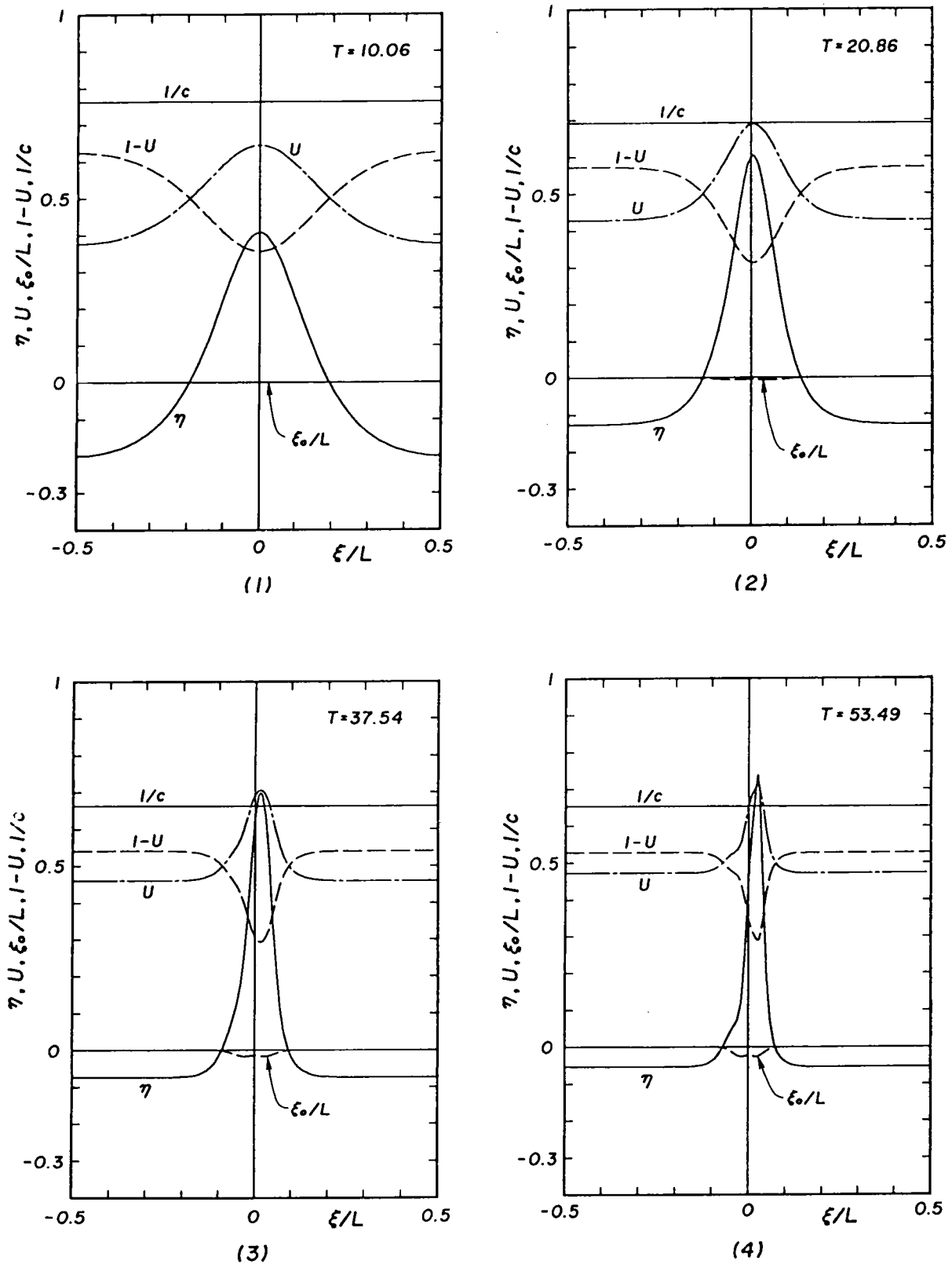

Fig. 4.25 Wave profiles and distributions of average velocity with respect to the phase of waves ($\bar{Q}$ = 0.5, R = 10^6, s = 0.00505).

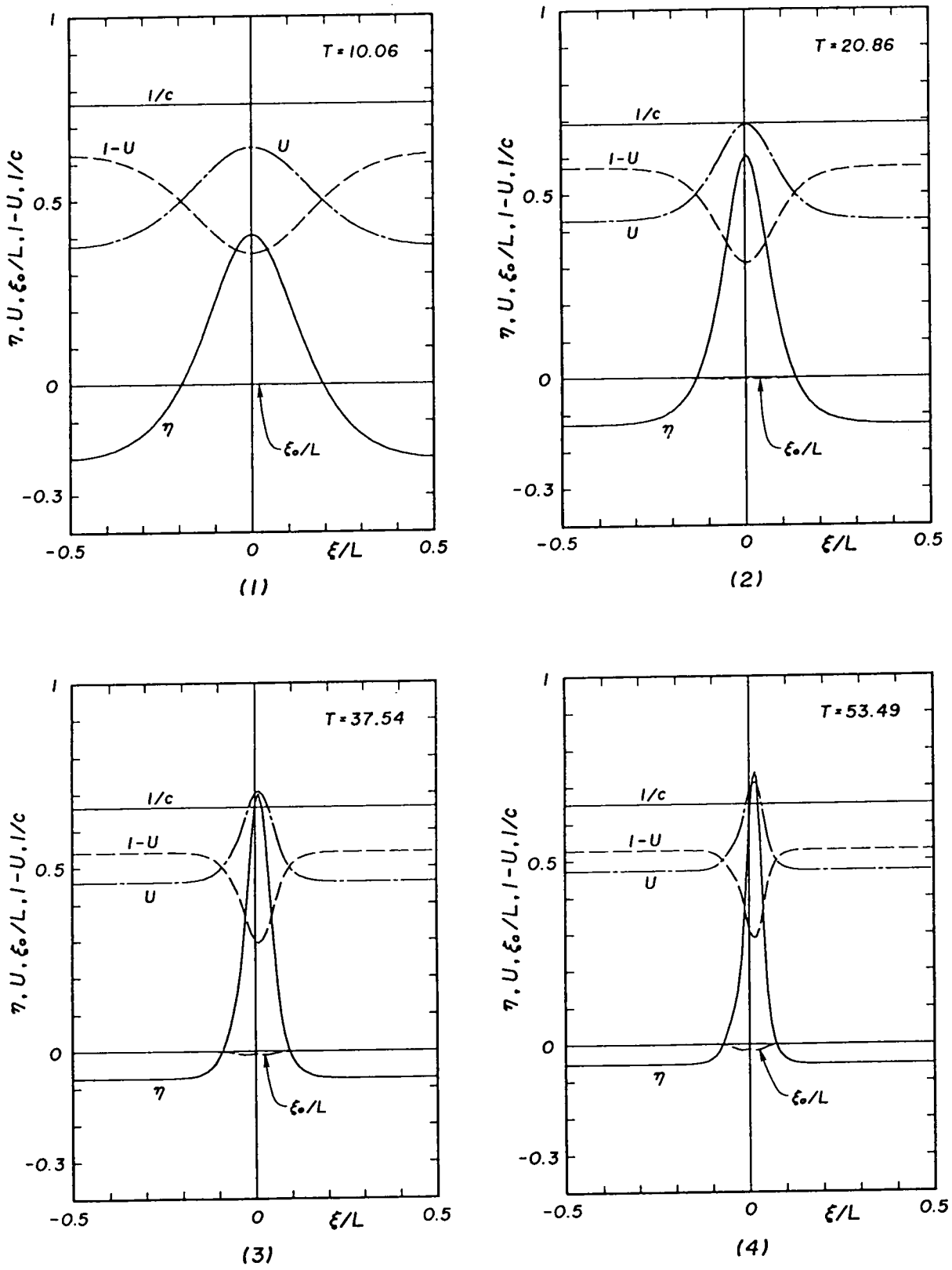

Fig. 4.26 Wave profiles and distributions of average velocity with respect to the phase of waves ($\bar{Q}$ = 0.5, R = 10^7, s = 0.00303).

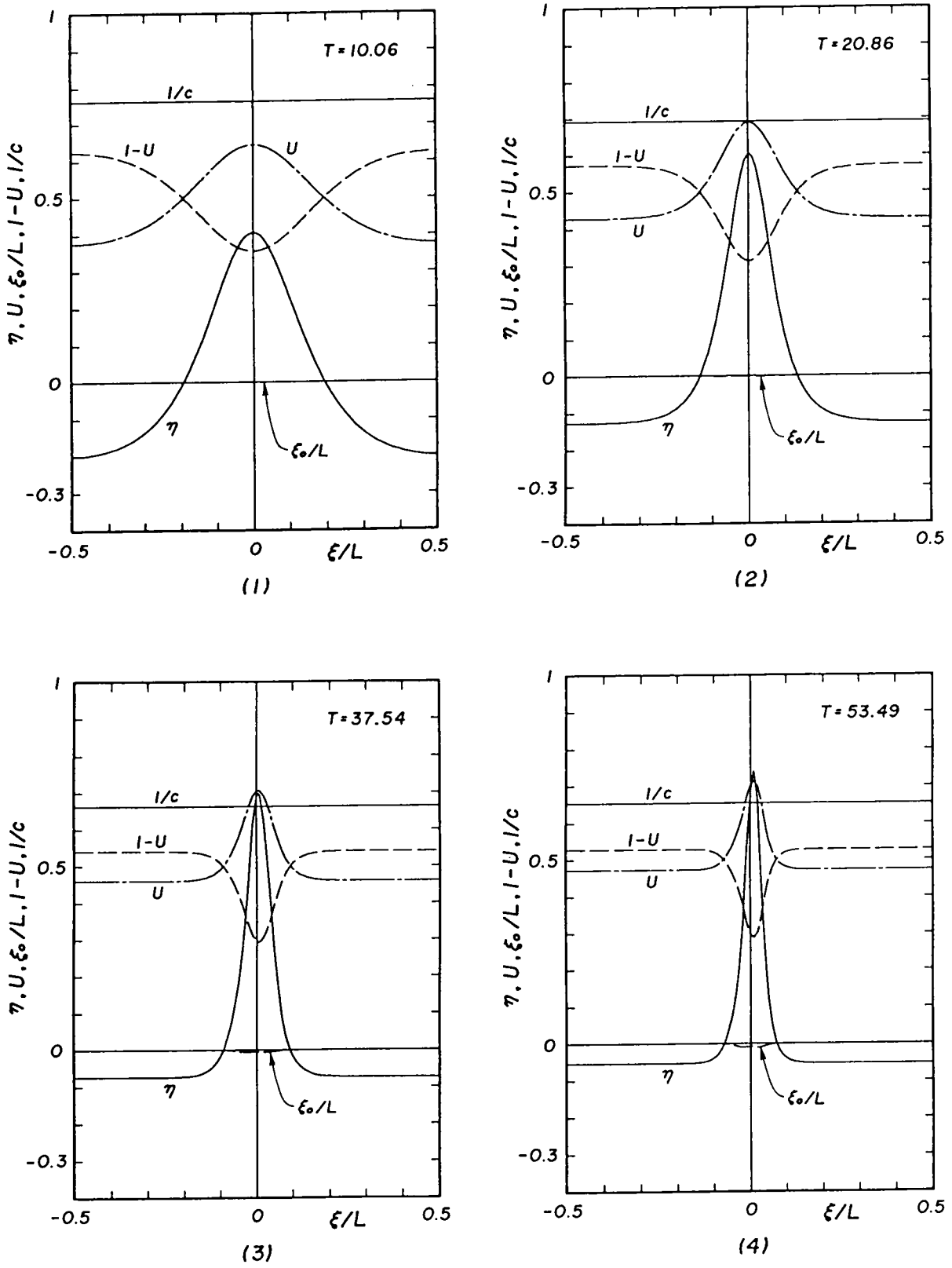

Fig. 4.27 Wave profiles and distributions of average velocity with respect to the phase of waves ($\bar{Q}$ = 0.5, R = 10^8, s = 0.00182).

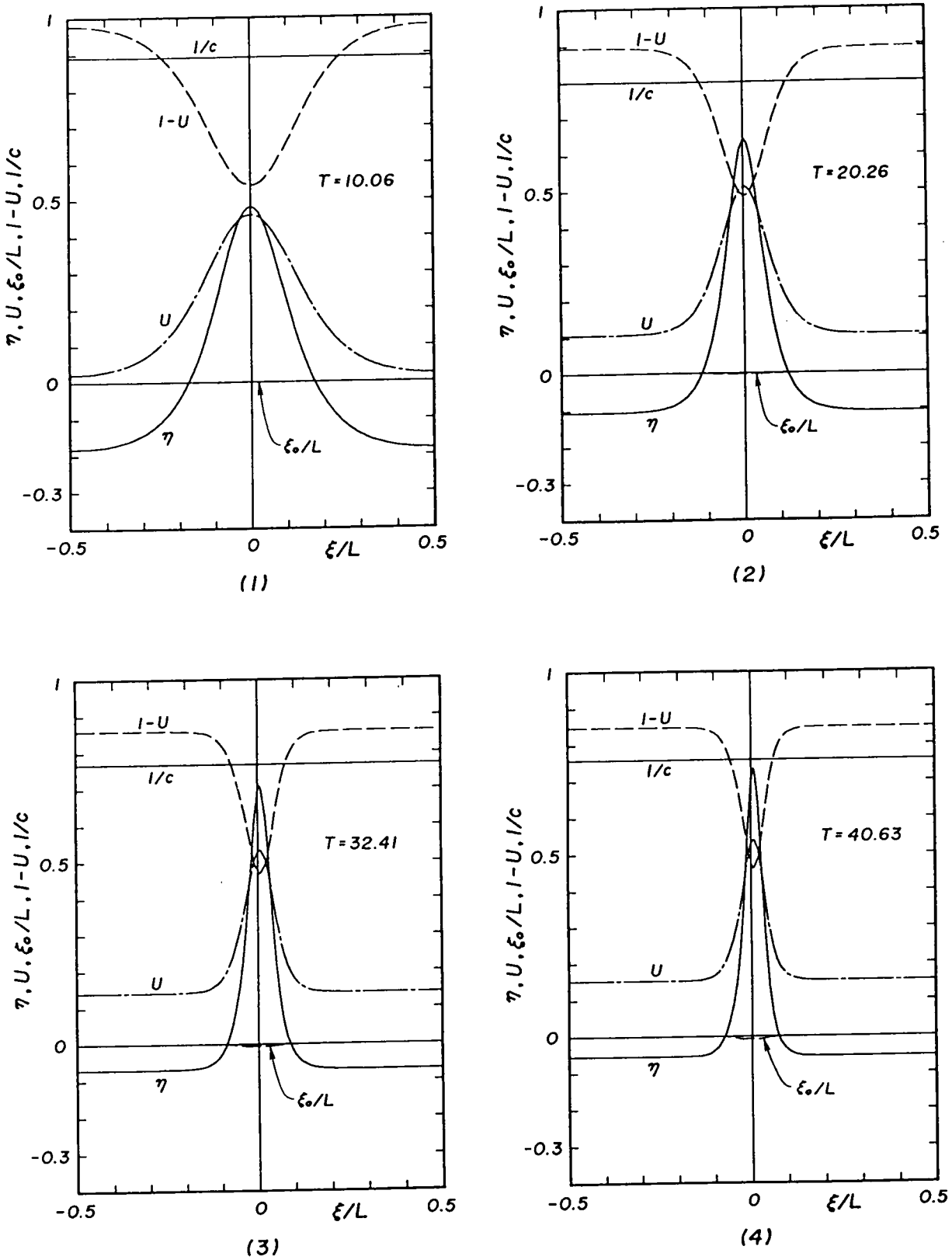

Fig. 4.28 Wave profiles and distributions of average velocity with respect to the phase of waves ($\bar{Q}$ = 0.8, R = 10^6, s = 0.00505).

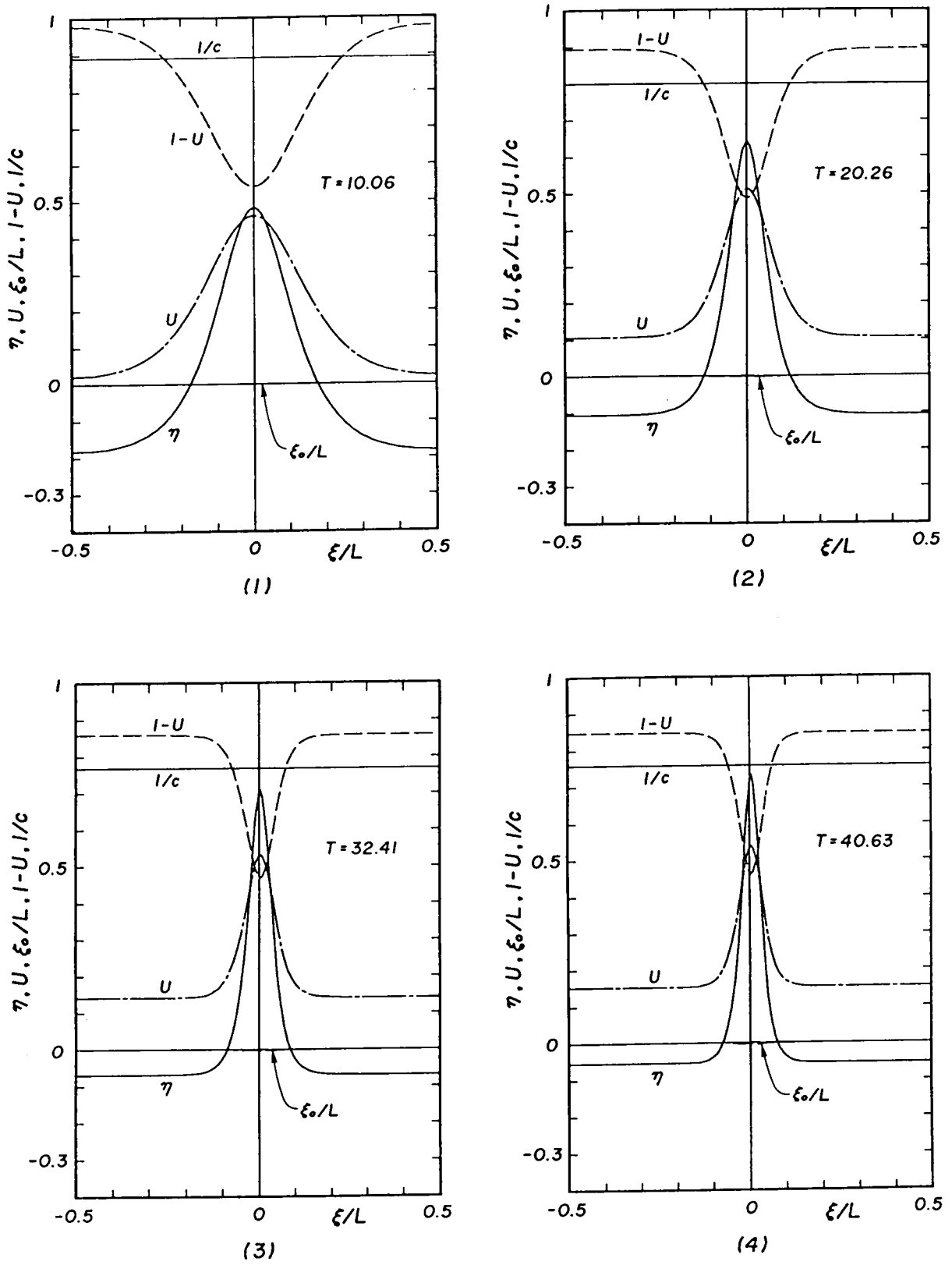

Fig. 4.29 Wave profiles and distributions of average velocity with respect to the phase of waves ($\bar{Q} = 0.8$, $R = 10^7$, $s = 0.00303$).

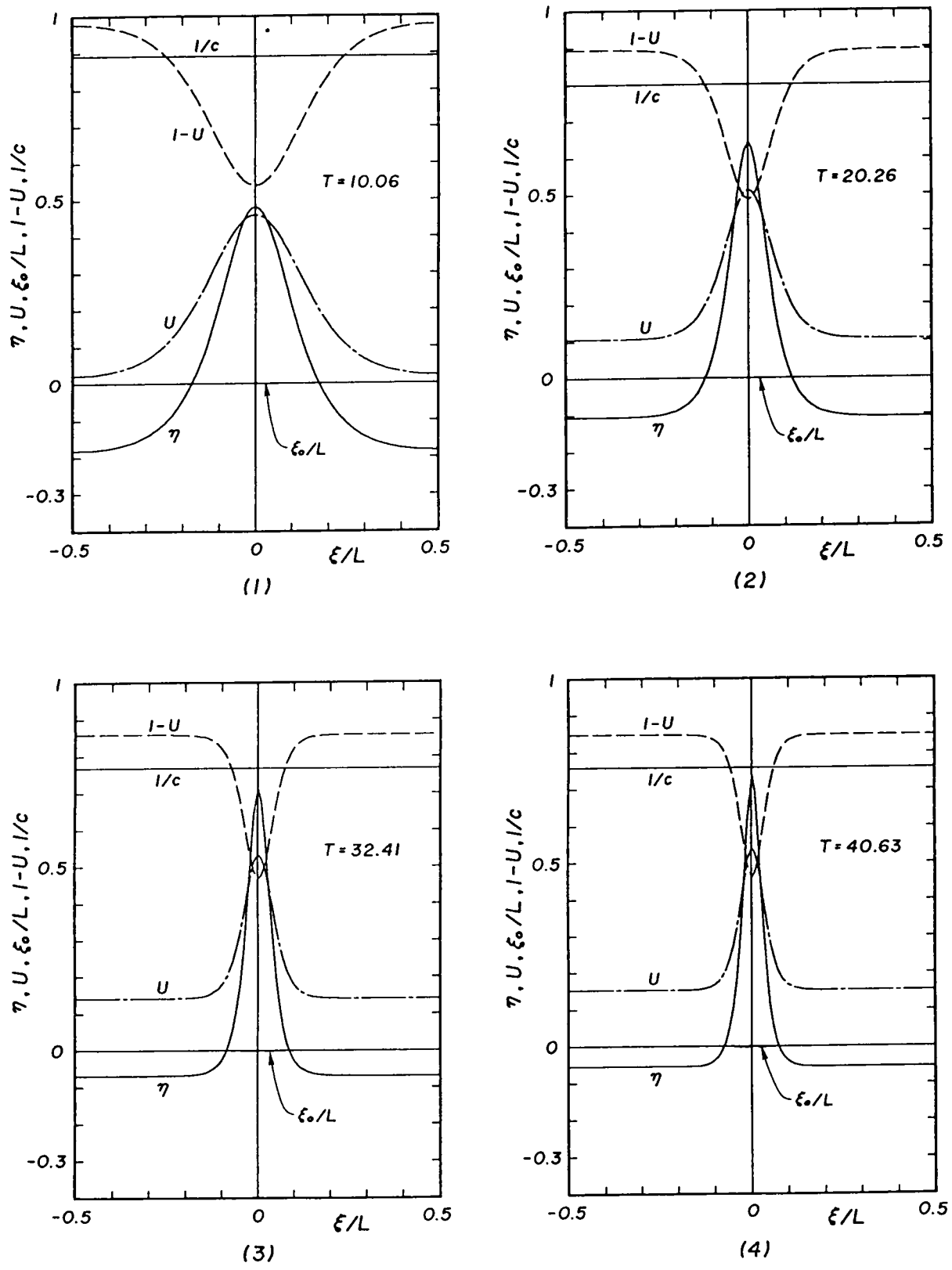

Fig. 4.30 Wave profiles and distributions of average velocity with respect to the phase of waves ($\overline{Q}$ = 0.8, R = 10^8, s = 0.00182).

Table 4.1 Physical quantities for the wind-forced waves, shown in Fig. 4.25 to Fig. 4.32.

No.	T	H	c	U_m	U_w	$\bar{Q}$	n	s	R	Fig. No.
1	10.06	0.605	1.311	0.481	0.448	0.5	0.02	0.505×10^{-2}	10^6	Fig. 4.25
2	20.86	0.730	1.446	0.483	0.514			0.303	10^7	Fig. 4.26
3	37.54	0.773	1.508	0.489	0.542			0.182	10^8	Fig. 4.27
4	53.49	0.791	1.532	0.492	0.552					
1	10.06	0.663	1.122	0.168	0.160	0.8	0.02	0.505	10^6	Fig. 4.28
2	20.26	0.748	1.251	0.177	0.242			0.303	10^7	Fig. 4.29
3	32.41	0.778	1.302	0.184	0.271			0.182	10^8	Fig. 4.30
4	40.63	0.789	1.319	0.186	0.281					
1	10.06	0.663	1.122	0.168	0.160	0.8	——	12.63	10^6	Fig. 4.32
2	15.45	0.723	1.210	0.172	0.217					
3	20.26	0.748	1.251	0.177	0.242					
4	27.04	0.768	1.284	0.181	0.261					

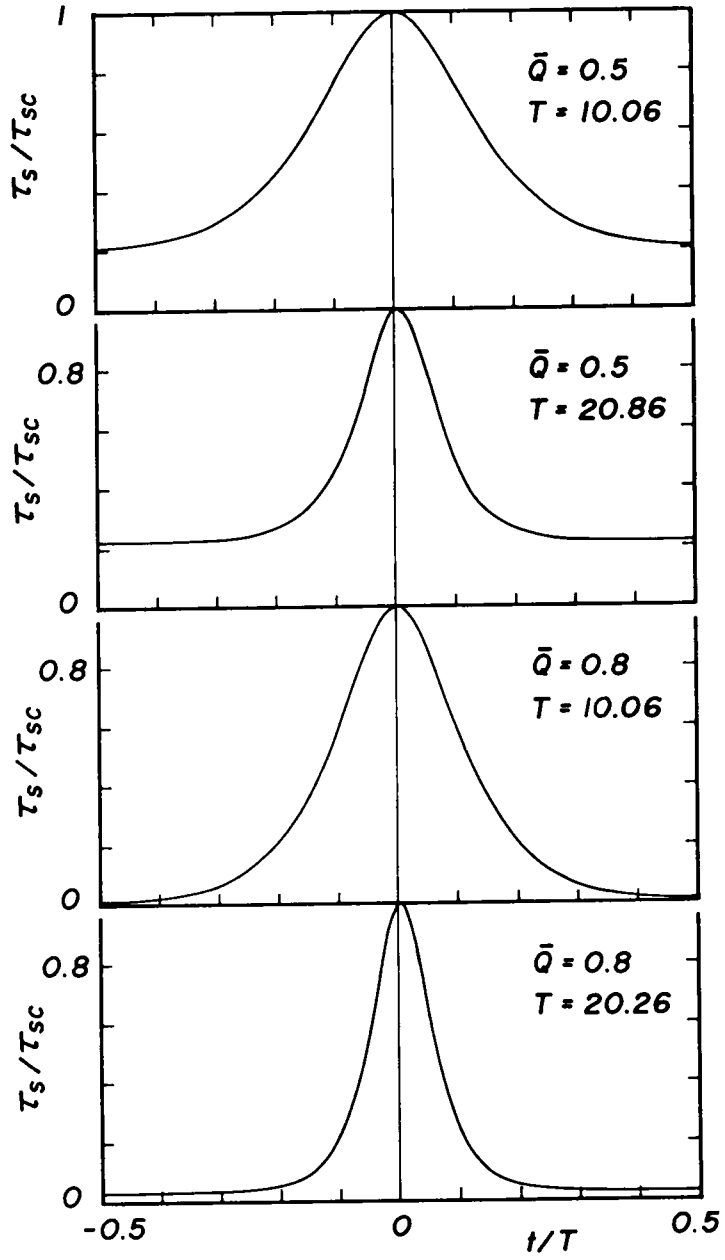

Fig. 4.31 Distributions of shear stress with respect to the phase of waves.

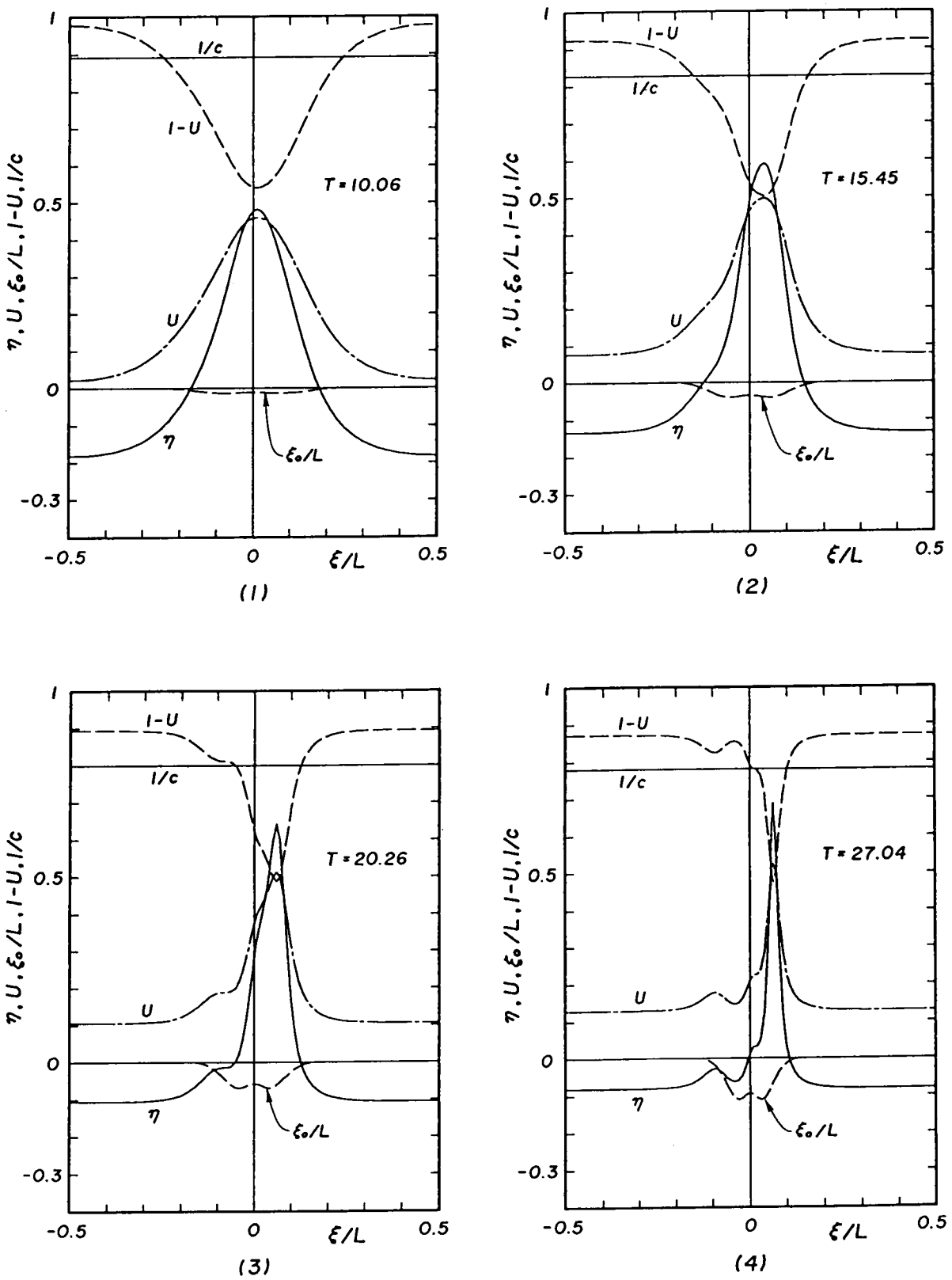

Fig. 4.32 Representative wave profiles and distributions of average velocity with respect to the phase of waves for great friction at the sea bottom ($\bar{Q} = 0.8$, $R = 10^6$, $s = 0.1263$).

the bottom friction is enlarged 25 times independently of Eq. (4.155), whose physical quantities are also given in the last column of Table 4.1. The fundamental characteristics are the same as for Fig. 4.25 to Fig. 4.30, but the asymmetry accompanied by the increases in phase shift and the occurrence of secondary waves in the windward sides of the wave crests are clearly represented; even if the wave period is small, asymmetry of wave profile can be attained if the friction at the sea bottom is great. Fig. 4.32(4) shows well that the secondary wave is almost completely split as a soliton. The phase shift is always negative near the wave crest and positive though extremely small near the wave trough. This is the reason the asymmetry occurs.

In concluding this section, the significance of the evaluation of the friction at the sea bottom merits paticular attention in attempting to understand the character of wind-forced waves. The friction at the sea bottom may apparently be excluded from the obtaining of hydraulic quantities of waves except for waves with small wave periods and great progressive discharge because the product of the bottom friction and Reynolds number, sR, is only important in evaluating the pressure exerting on waves, as given in Eq. (4.152). However, wave profiles and water particle velocities are almost completely dependent on the bottom friction through the phase shift. Accurate information about the bottom friction is, therefore, necessary for practical applications.

4.6 Some Verifications for Wind-Forced Waves

In this section a laboratory experiment and field observation are described to verify the analytical characteristics of wind-forced waves. The laboratory experiment is concerned with breaking wave trains, a special type of wind-forced wave, in which successive spilling regions are fromed

ahead of the wave crests. The aim of the field observation is to discover the characteristics of actual wind-forced waves generated by strong wind. First, primary characteristics are discussed, then the analytical results of the wind-forced waves are verified in comparison with these experimental and field data.

Note that all variables in this section are dimensional ones.

(1) Simulation of Breaking Wave Trains

a. Experimental Apparatus and Procedures

i) Wind wave simulator

The wind wave tank used was recirculating-type as illustrated in **Fig. 4.33**, belonging to the Ujigawa Hydraulic Laboratory, Disaster Prevention Research Institute, Kyoto University. This tank has two parallel straight sections joined at the ends by two semicircular sections, forming an oval. Wind waves generated by a blower circulate in the tank by closing a wave direction controller, installed at one corner between straight and semicircular sections of the tank, corner (V) in **Fig. 4.33.** According to preliminary experiments, wind-induced currents at high wind speeds were reasonably great, so a weak lateral oscillation was observed due to meandering of wind waves, probably caused by the curvature of the semicircular parts of the tank; consequently, a wave direction control plate was installed to prevent this oscillation.

In a straight wind wave tank, the fetch is limited by the length of the tank, so reversal of wind-induced currents occurs in lower zones of the water as in storm surges. On the other hand, this current reversal does not occur in the recirculating wind wave tank. Therefore, if the duration is long enough, wind waves on the fully developed currents can be generated. This is an advantage of this wind wave tank, but on the other hand the wave

field may differ from that for an infinite fetch. According to Tsuchiya and Yamaguchi's investigation[17] on wind waves using this recirculating wind wave tank, however, the properties of power spectra for wind-generated waves resemble statistically those for field observations, so that wind waves in this tank were found to be nearly identical to those with an infinite fetch.

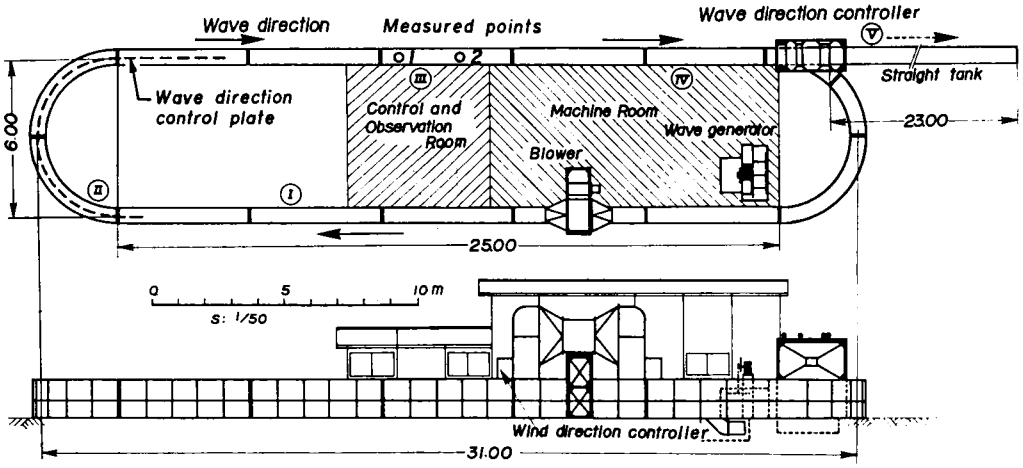

Fig. 4.33 Recirculating wind wave tank.

ii) **Measurements of wind**

Wind speeds over wind waves were measured with Robinson's cup anemometer with 5 cm intervals.

iii) **Measurements of wave profiles and wave velocities**

Wave gauges were set up at two points 2.24 m apart in the straight part of the tank, marked by 1 and 2 in **Fig. 4.33**. Wave velocities were determined from the travel-time of waves between these two points.

iv) **Measurements of water particle velocities**

In the present work, a current meter(2 cm in diameter) was used for measurements of water particle velocities due to several experimental considerations: 1) the reversal of wind-induced currents might not occur in the preliminary experiments and the horizontal component of the current u

predominated over the vertical one w, so the current meter would register values of $\sqrt{u^2+w^2} \fallingdotseq u$, 2) since measurement with hot-wire or hot-film was strongly affected by water characteristics, such as a temparature, this method was unsuitable for the experiments in long run, and 3) a tracer method was also deemed unsuitable because the flow field in wind waves might be turbulent and the type of wave to be measured was never decided *a priori*.

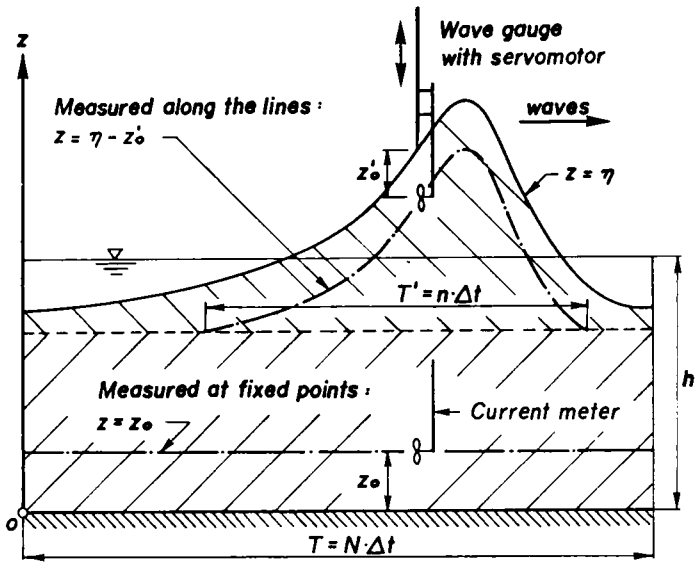

Fig. 4.34 Measurement procedure for water particle velocities.

The measurement procedure for water particle velocities is illustrated in **Fig.4.34**, where the coordinate origin is taken at the bottom of the wave tank and the wave surface is referred to as $z = \eta$. Water particle velocities under wave troughs are measured at a point $z = z_0$, and the velocities between wave crests and wave troughs are measured as follows: the current meter is fixed to a wave gauge, which can follow wave profiles by surbo-control, and records velocities on a line $z = \eta - z_0'$, i.e. along a line at a constant depth below the wave surface. This procedure was carried out at measuring point 2, changing z_0 at intervals of 2 cm and z_0' at intervals of 0.5 cm.

It was hoped that the self-induced velocity due to vertical motion of the current meter was negligibly small compared with wind-induced currents. This velocity was less than 3 cm/sec, the minimum value of measurement ability of the current meter, when measured in still water.

b. Wave and Wind Properties

Fig. 4.35 shows the time history of power spectra based on the FFT method, where the record length is about 100 sec and the time lag is 0.06 sec. The peak frequencies are about 1 Hz for both Runs 1 and 2 after t = 100 min, the beginning time of measurements. Power spectra in the high frequency region for both Runs 1 and 2 agree well with Phillips' law[18] of f^{-5}, and bi-frequency components occur at about 2 Hz. Values of power spectra in the lower frequency region, less than peak frequencies, may be reasonably greater than that of field observations due to the presence of long wave components in the wave tank, generated by the interaction between wind-induced currents and wind waves. Furthermore, in these lower frequency regions, power spectra have local maxima resulting from the slight meandering of waves, as mentioned above.

Fig. 4.36 shows the changes in depression of the mean depth of water $-\Delta h$, in mean wave height H_m, in significant wave heights $H_{1/3}$ and $H_{1/10}$, in maximum wave height H_{max}, in mean wave period T_m, and in occurrence ratio for wave breaking α_b. The occurrence ratio for wave breaking is defined by $\alpha_b = \alpha_{b1}+\alpha_{b2}$, in which α_{b1} is the ratio of the numnber of waves completely broken with decreased wave height to the total wave mumber, and α_{b2} is the ratio of the number of waves partially broken near the wave crests without deformation of wave profile to the total wave mumber.

The depression of the mean depth of water $-\Delta h$ gradually increases with respect to the duration and becomes nearly constant. The mean wave height H_m and significant wave heights $H_{1/3}$ and $H_{1/10}$ are roughly constant after 50

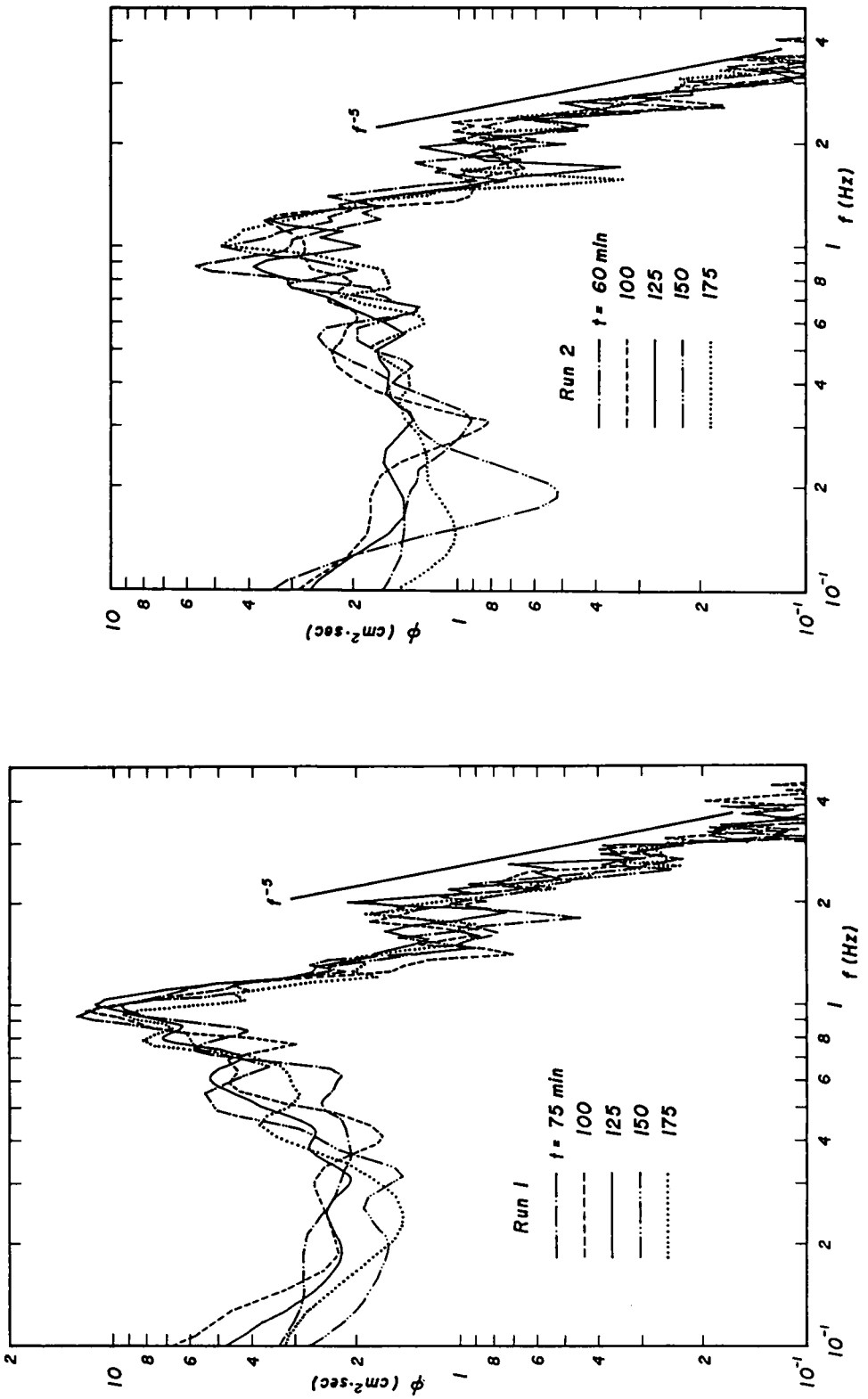

(2) Run 2

(1) Run 1

Fig. 4.35 Time history of power spectra of wind waves on wind-induced currents.

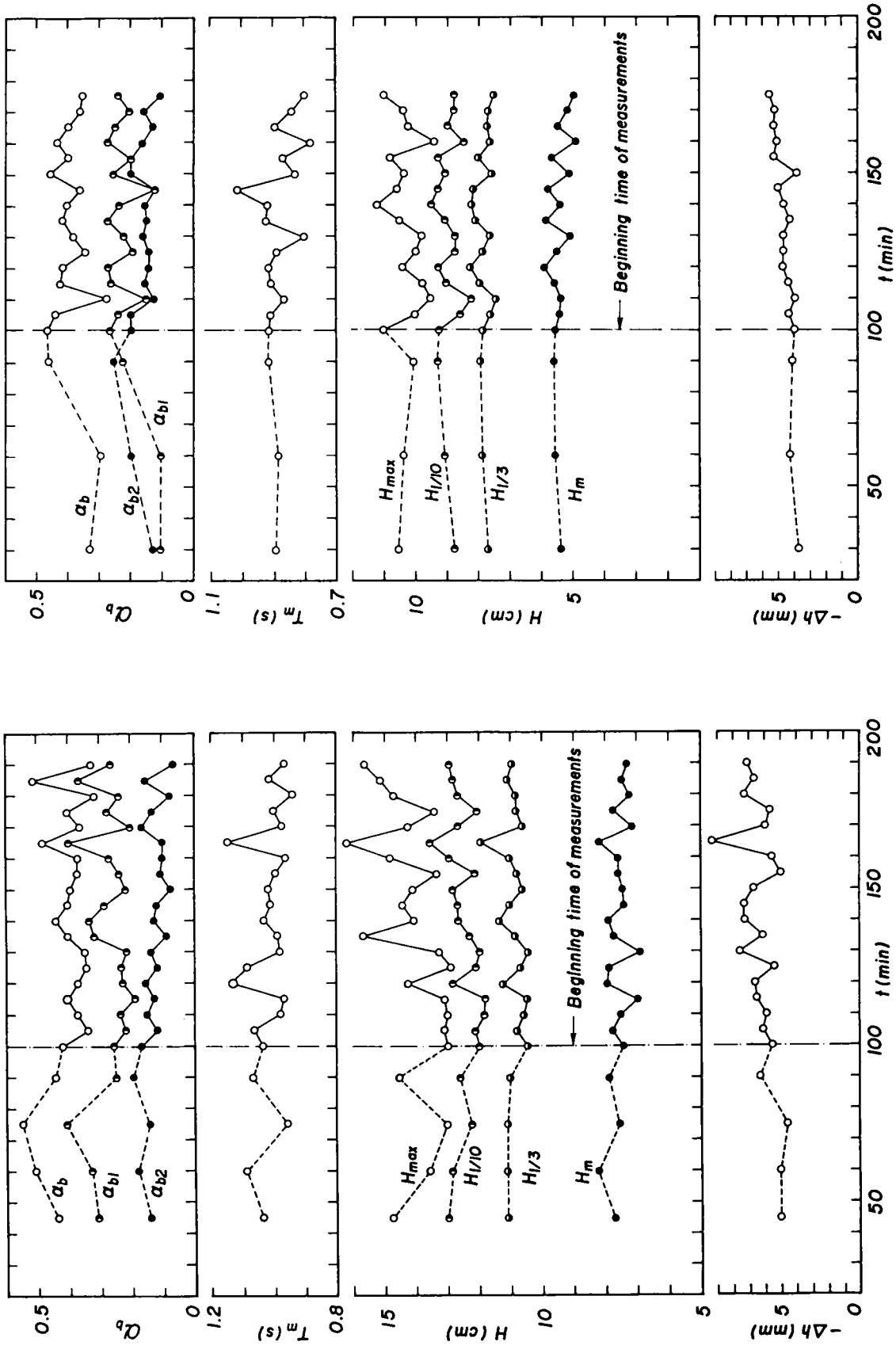

Fig. 4.36 Time history of the changes in mean depth of water, in wave height, and in occurrence ratio for wave breaking.

min, while the maximum wave height H_{max} is strongly affected by the duration. The mean wave period T_m often takes on great values and varies with respect to the duration, being related to the breaking wave heights and corresponding wave periods. The ocurrence ratio α_b also varies with the duration but can be considered nearly constant after the beginning time of measurements.

Fig.4.37 shows the comparison of the wave heights with Longuet-Higgins' theory[19]. All values measured for wave height are smaller than his theoretical ones. This is in accordance with Tsuchiya and Yamaguchi's observation[17] for non-breaking wind waves and is one of the characteristics of waves generated in the recirculating wind wave tank.

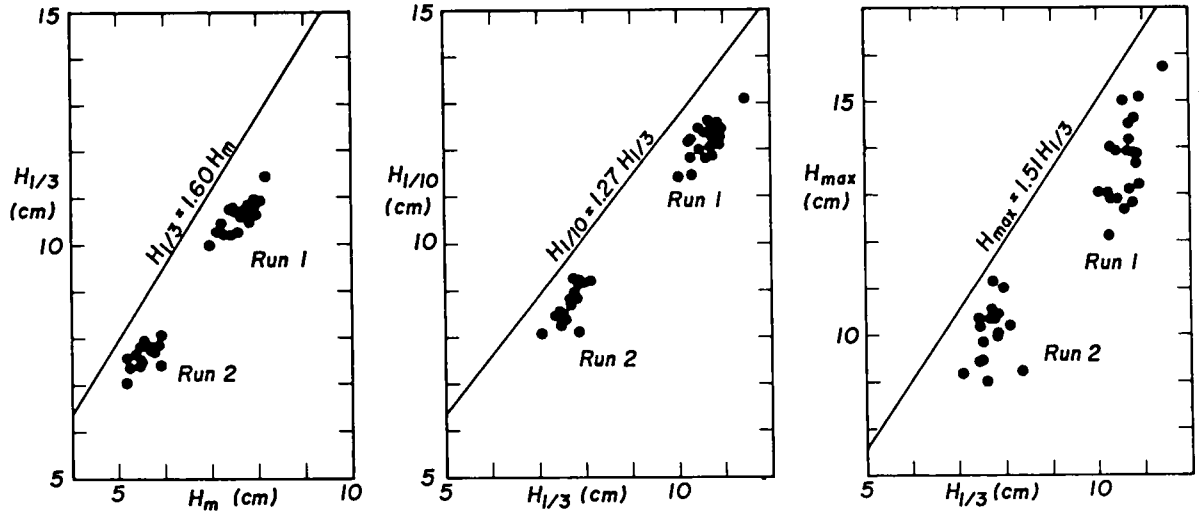

Fig. 4.37 Comparison of wind wave heights with Longuet-Higgins' theoretical curves.

Breaking wave trains can, now, be defined such that the successive spilling regions are formed ahead of the wave crests and the wave profiles are, then, partly deformed only near the wave crests; accordingly, they were observed by the ratio of α_{b2}.

Examples of wave profiles and water particle velocities for the break-

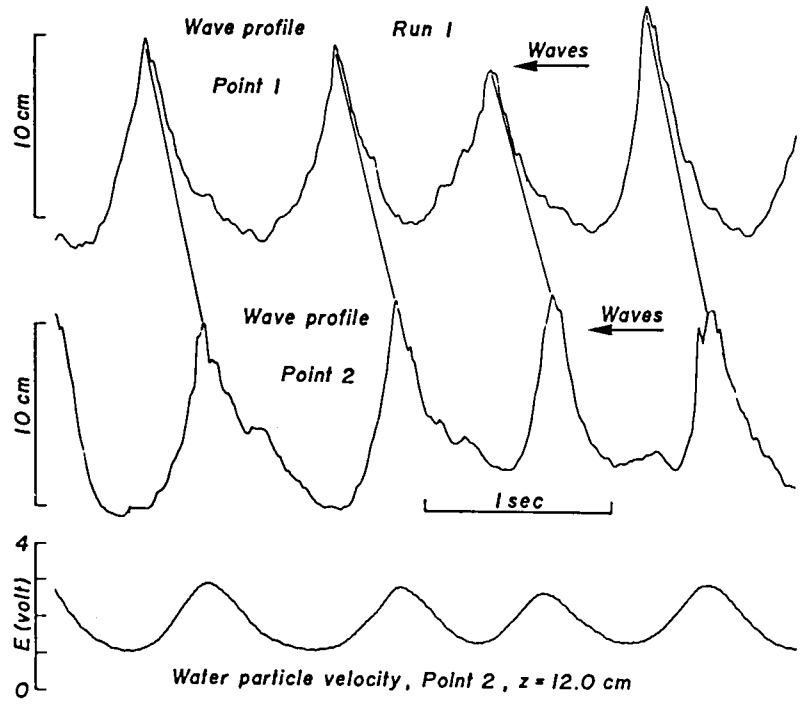

(1) Run 1

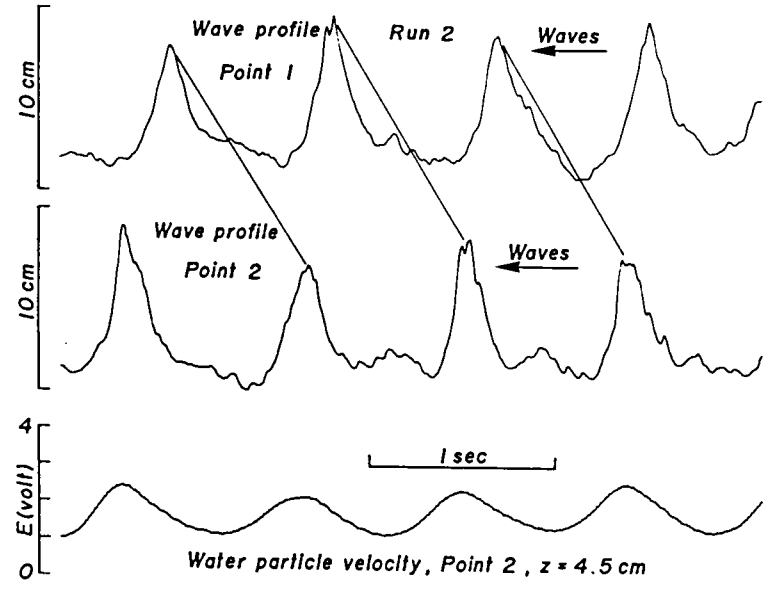

(2) Run 2

Fig. 4.38 Examples of wave profiles and water particle velocities for the breaking wave trains.

Table 4.2 Physical quantities for the representative breaking wave trains.

Run	h(cm)	$T\sqrt{g/h}$	H/h	$c/\sqrt{gh}$	$W_{10}/\sqrt{gh}$
1	24.1	6.89	0.458	1.28	11.48
2	19.7	6.78	0.408	1.27	10.93

ing wave trains are shown in **Fig. 4.38**. Short waves, or wavelets disturbed by wave breaking, clearly occur in the wave trough phase. The measured water particle velocities indicate that reversal of the velocities never occurs in the wave trough phase, that is, the wind-induced currents are greater than the water particle velocities due to the wave motion.

Table 4.2 gives physical quantities for the breaking wave trains, which were determined as the mean values for waves of more or less the same wave profile, wave height, and wave period. From comparison of **Figs. 4.35** and **4.36** with **Table 4.2**, the wave periods of the breaking wave trains correspond to those at the peak frequencies of power spectra, and the wave heights are also nearly the same as the significant wave heights $H_{1/3}$. The relation between the wave heights and wave periods is shown in **Fig. 4.39**, where waves with wave heights within the significant wave height ± 10 %

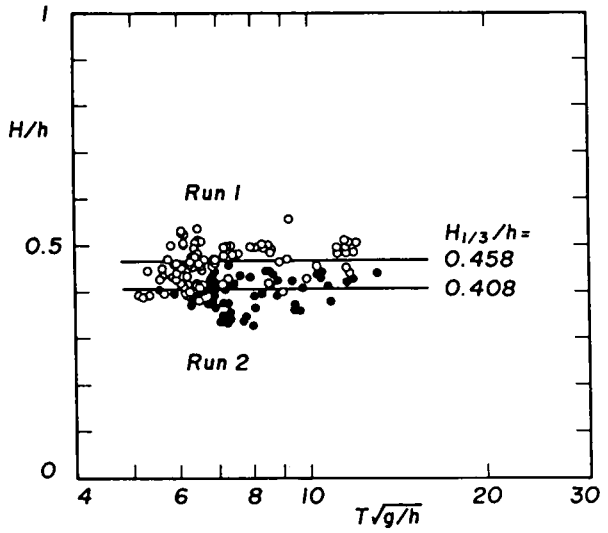

Fig. 4.39 Wave periods of the breaking wave trains corresponding to the significant wave heights.

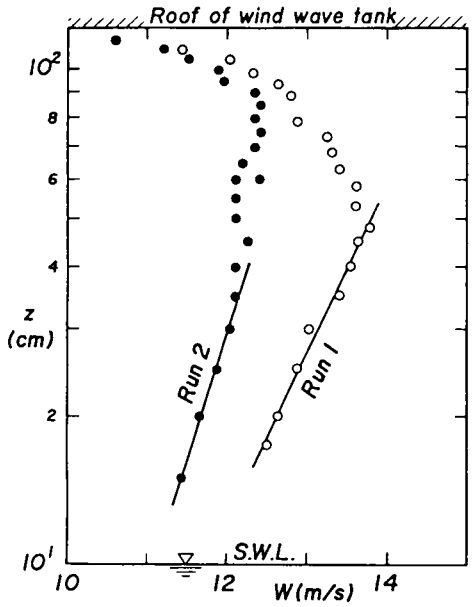

Fig. 4.40 Vertical distribution of wind over waves.

were selected. Most wave periods are close to the significant wave periods, but there are waves with wave periods somewhat longer than the significant wave periods both in Runs 1 and 2 because the power spectra have low-frequency components slightly greater than usual, as seen in **Fig. 4.35.**

Fig. 4.40 shows that the universal logarithmic law of vertical distribution of wind speed is well satisfied for breaking waves. If the distribution of wind speed is assumed as

$$(W_a - c)/W_* = (1/k)\log_{10}(Z/Z_0), \tag{4.157}$$

where the coordinate Z is measured upward from the mean water level, the charateristic values of wind can be evaluated as given in **Table 4.3**, in which W_{10} is the wind speed at Z = 10 m, W_* the friction velocity, c the wave velocity for the breaking wave trains, Z_0 the relative roughness, and k Kármán's constant.

Table 4.3 Characteristic values of wind.

Run	W_{10}(m/s)	W_*(cm/s)	Z_0(cm)	C_d	$R^*_{e2}=W_*H/\nu$
1	17.65	51.4	0.005	1.07×10^{-3}	3830
2	15.18	35.8	0.0003	0.712	1877

Fig. 4.41 shows the relation between the drag coefficient C_d and roughness Reynolds number[20] $Re_2^* = W_* H/\nu$, where H is the wave height for the breaking wave trains. This figure indicates that the breaking wave trains are in the region $Re_2^* > 10^3$ where wave breaking occurs constantly, but the drag coefficient C_d is about half of Toba and Kunishi's[20] and Kunishi and Imasato's[21]. The discrepancy in C_d results from a fundamental difference in experiments, that is, current reversal would occur in their experiments, while it does not in the present work, as mentioned already.

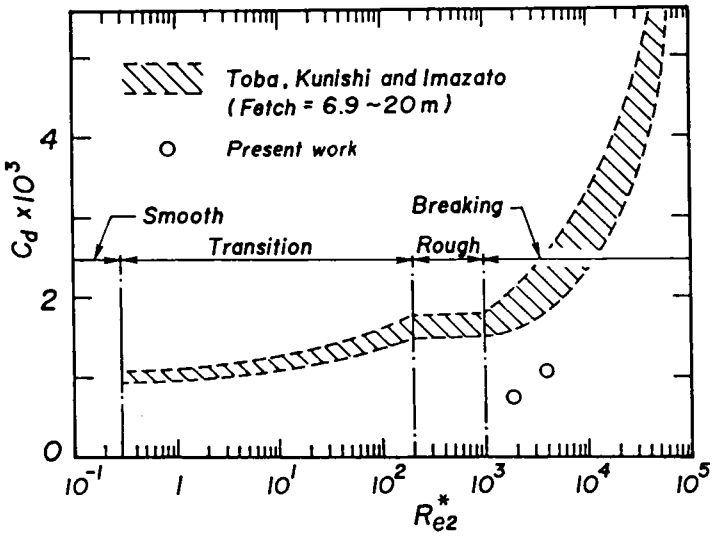

Fig. 4.41 Relation between the coefficient of friction and roughness Reynolds number.

Fig. 4.42 also shows the relation between the occurrence ratio for wave breaking and the roughness Reynolds number. The occurrence ratios by Toba *et al.* increase with Re_2^*, but the ratios in the present work are nearly constant. These results, as before, strongly depend both on the fetch and on the types of wind wave tanks, that is, whether the wind wave tank has ends or not.

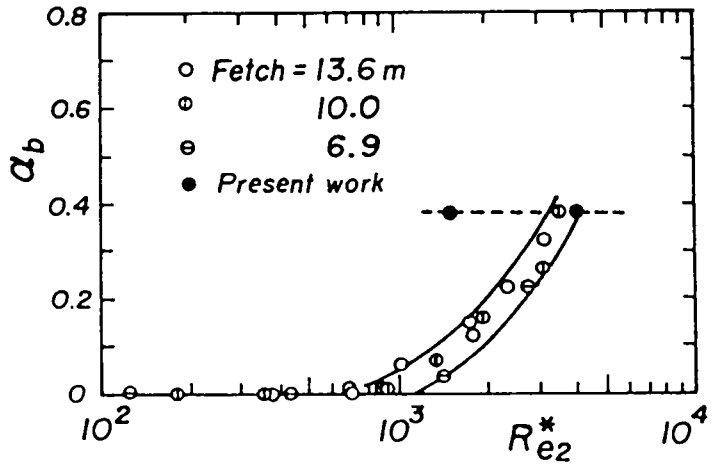

Fig. 4.42 Relation between the occurrence ratio for wave breaking and roughness Reynolds number.

c. Characteristics of the velocity field

i) Existence of the Critical Depth

The representative vertical distributions of water particle velocity in the breaking wave trains in Runs 1 and 2 are presented in **Figs. 4.43** and **4.44**, respectively, where the curves are experimental ones. In both Runs 1 and 2, great surface drift occurs in the leeward side of wave crests $t/T \leqq 0$ but decreases gradually with respect to the phase of waves, and water particle velocities distribute uniformly over the whole water depth, while, for $t/T > 0$, the surface drift decreases sharply. Therefore, the surface drift in the leeward side of wave crest is chiefly produced by wave breaking and there possibly exists a sheltered region there.

The average velocity, defined by

$$\bar{u} = \frac{1}{\eta}\int_0^{\eta} u \, dz, \tag{4.158}$$

can be evaluated from the vertical distributions of water particle velocity shown in **Figs. 4.43** and **4.44**. Accordingly, **Fig. 4.45** shows examples of the average velocity minus the wave velocity, $\bar{u} - c$, together with the wave profile in the frame of reference moving with the wave velocity c. There

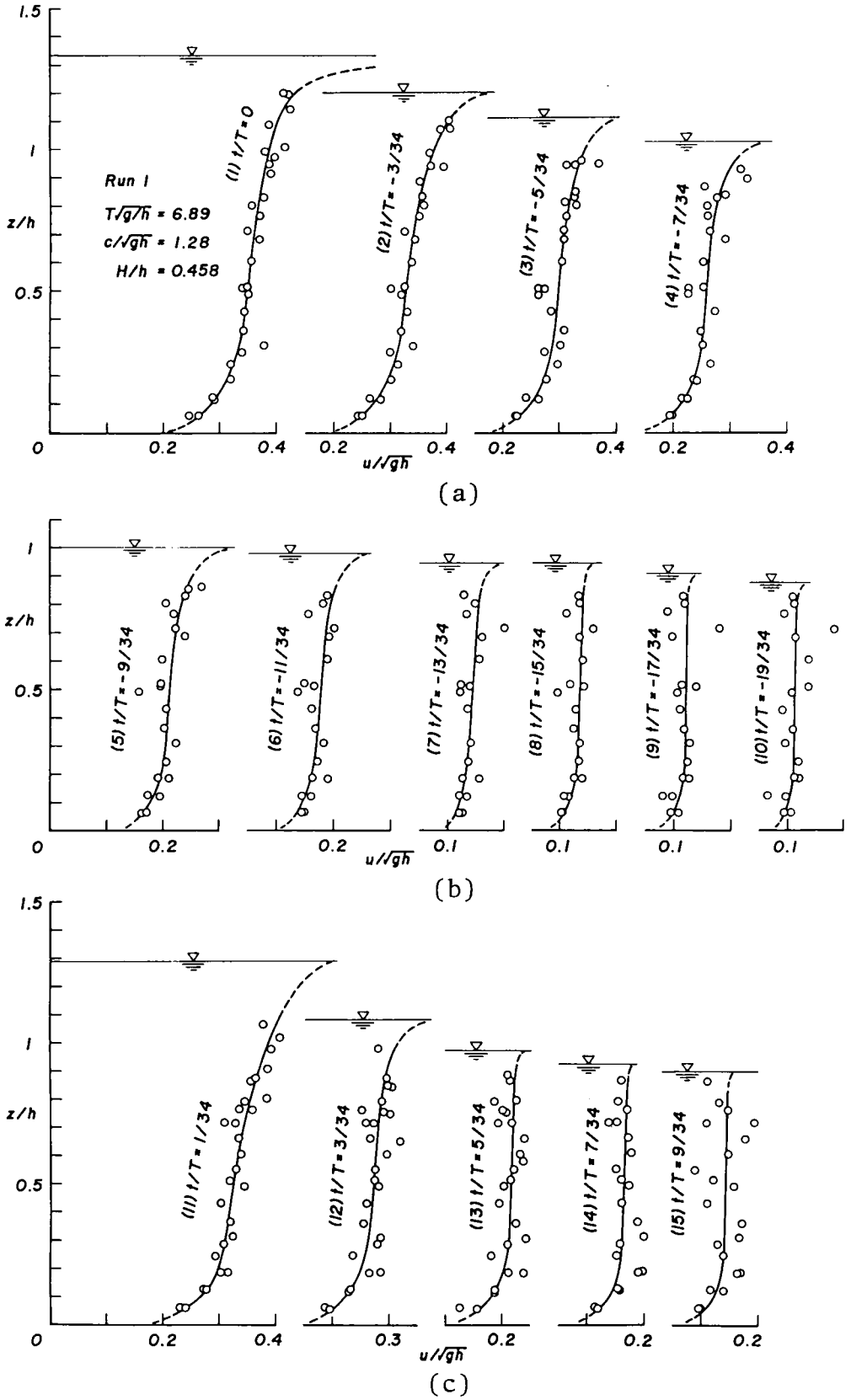

Fig. 4.43 Vertical distribution of water particle velocity in the breaking wave trains (Run 1).

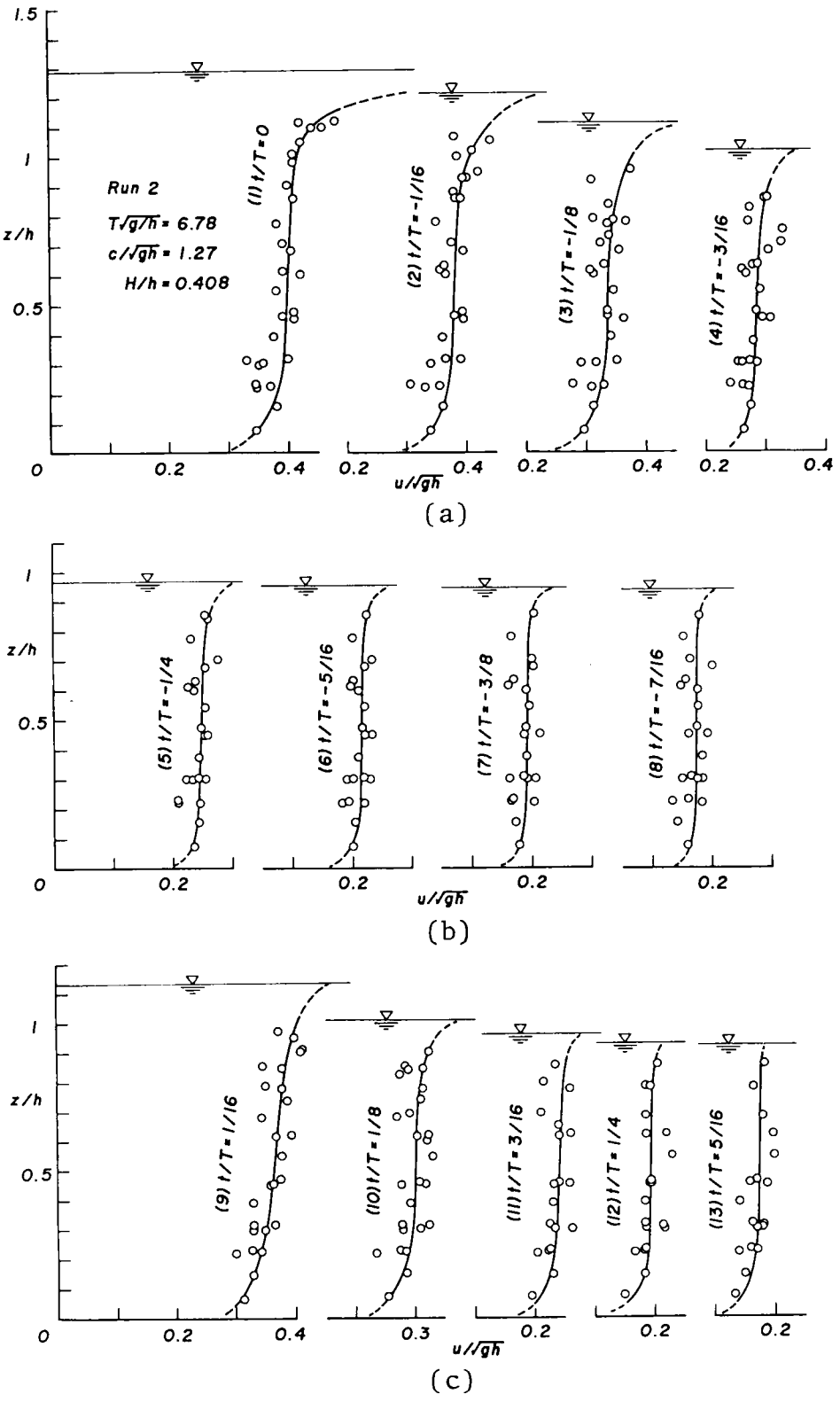

Fig. 4.44 Vertical distribution of water particle velocity in the breaking wave trains (Run 2).

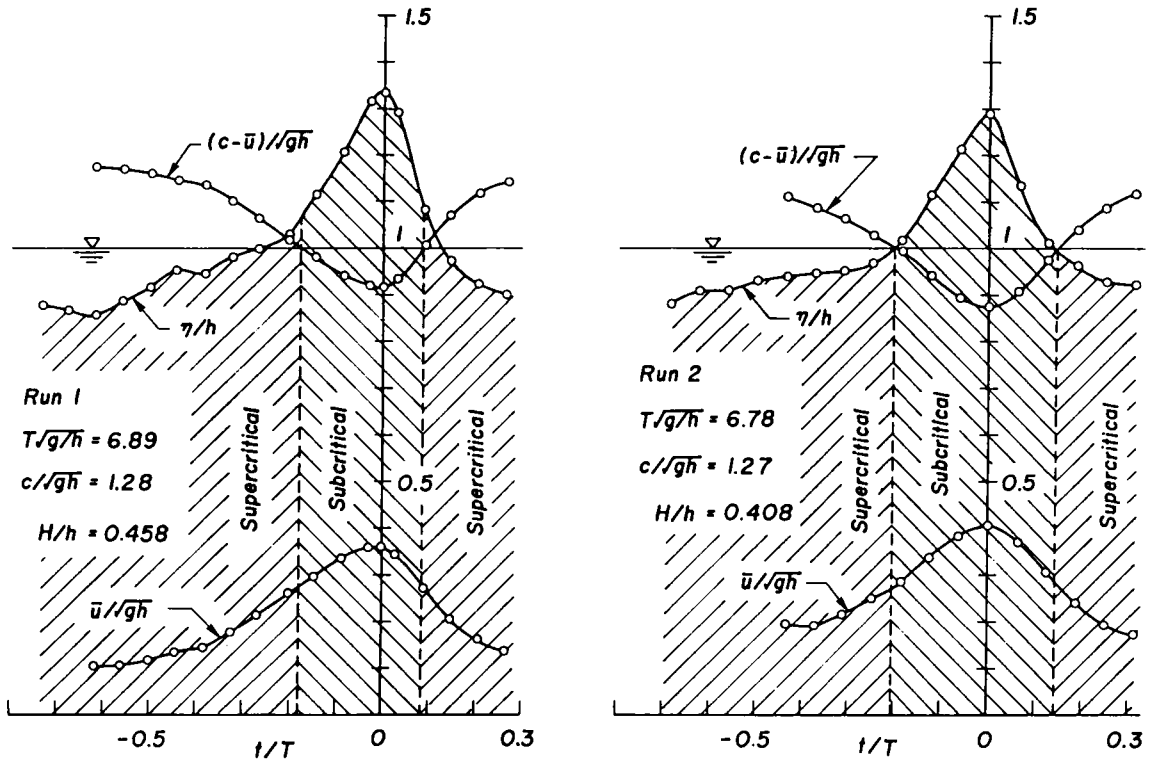

(1) Run 1 (2) Run 2

Fig. 4.45 Existence of the critical depth in the breaking wave trains.

exist points $(c-\bar{u})/\sqrt{gh} = 1$ near the mean water level, so the flow near the wave crest is, hydraulically speaking, subcritical and supercritical near the wave trough in this steady flow system. This fact is similar to the analytical results for the wind-forced waves, as mentioned in Section 4.5(3), and also for the roll-waves[11] which occur when a liquid flows downward on a steep open channel with bottom friction.

ii) **Wind-Induced Current and Mass Transport**

The vertical distribution of mean velocity in the measured time T_{total}, defined by

$$u_w = (1/T_{\text{total}})\int_0^{T_{\text{total}}} u\,dt, \tag{4.159}$$

is shown in **Fig. 4.46.** These mean velocities can give values of wind-induced currents by strong wind as the Frouds number $u_w/\sqrt{gh} \fallingdotseq 0.2$, though the velocity components due to waves are, of course, contained, too.

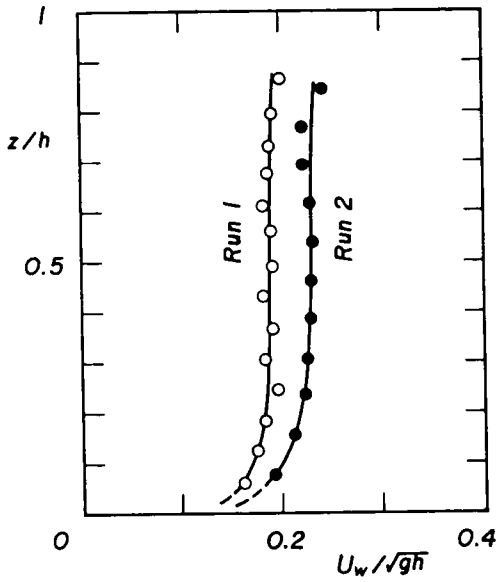

Fig. 4.46 Vertical distribution of wind-induced current.

The mass transport velocity can be defined as follows:

(a) In the region under wave troughs (on $z = z_0$)

$$u_m = (1/T)\int_0^T u\,dt = (1/N)\sum_{j=1}^{N} \Delta u_j . \tag{4.160}$$

(b) In the region between wave crests and troughs (on $z = \eta - z_0'$)

$$u_m' = (1/T')\int_0^{T'} u\,dt = (1/n)\sum_{j=1}^{n} \Delta u_j . \tag{4.161}$$

If u_m' is expressed as the mean value per unit wave period, Eq. (4.161) becomes

$$u_m' = (1/T)\int_0^{T'} u\,dt = (T/T')u_m = (n/N)u_m . \tag{4.162}$$

In these equations, N and n are the sequence numbers of measured time, defined by

$$T = N\Delta t, \qquad T' = n\Delta t, \tag{4.163}$$

respectively, as shown in **Fig. 4.34**, and Δu_j is a corresponding water particle velocity.

Fig. 4.47 shows the vertical distribution of mass transport velocity.

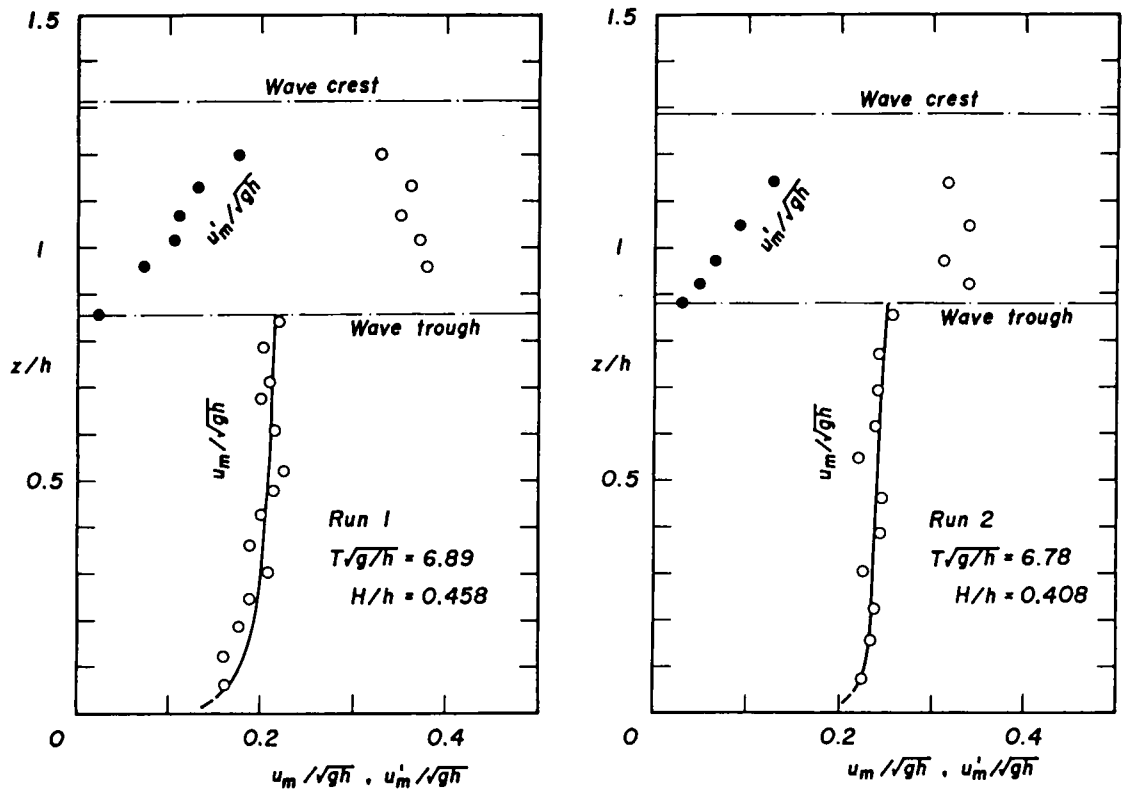

(1) Run 1 (2) Run 2

Fig. 4.47 Vertical distribution of mass transport velocity in the breaking wave trains.

in which the values in the region between wave crests and troughs are, for brevity, plotted at the phases of wave crests $z = \eta_{crest} - z_0$'. The mass transport velocities under troughs are slightly greater than the wind-induced currents shown in **Fig. 4.46**. The great part of the mass transport induced by the breaking wave trains is, then, due to wind-induced currents, though surface drift, of course, affects mass transport in the region between wave crests and troughs, as shown in **Figs. 4.43** and **4.44**. Dimensionless periods in the present experiment are nearly equal to $T\sqrt{g/h}$ = 6.89 and 6.78. However, Run 2 gives slightly greater mass flux than Run 1, in which the former has a smaller value of H/h than the latter. Mass flux deeply depends on wind-induced currents and on the foundamental properties of the breaking wave trains, therefore it is necessary to investigate the relations more in detail.

(2) Field Observation for Wind-Forced Waves

a. Coastal and atmospheric environments

A field observation[22] was carried out using an observational pier at the Ogata Wave Observatory in Ogata-Cho, Niigata, belonging to the Disaster Prevention Research Institute, Kyoto University. The pier is about 315.4 m in length and nearly perpendicular to the shore line as illustrated in **Fig. 4.48**. The water depth along the pier varies as is also shown in the figure. Four wave gauges of ultra-sonic type were set up at the top of the pier and a linear wave-probe array along the pier was made up of eight wave gauges of capacitance type, wave data being chiefly observed by this array. Wind speeds and their directions were taken by a wind vane and anemometer.

The storm measured was a low atmospheric pressure which ran through the Japan Sea from Tsushima, Nagasaki (at 3 a.m., 14 March 1981) to Otaru, Hokkaido (at 3 a.m., 15 March 1981). The observation was carried out con-

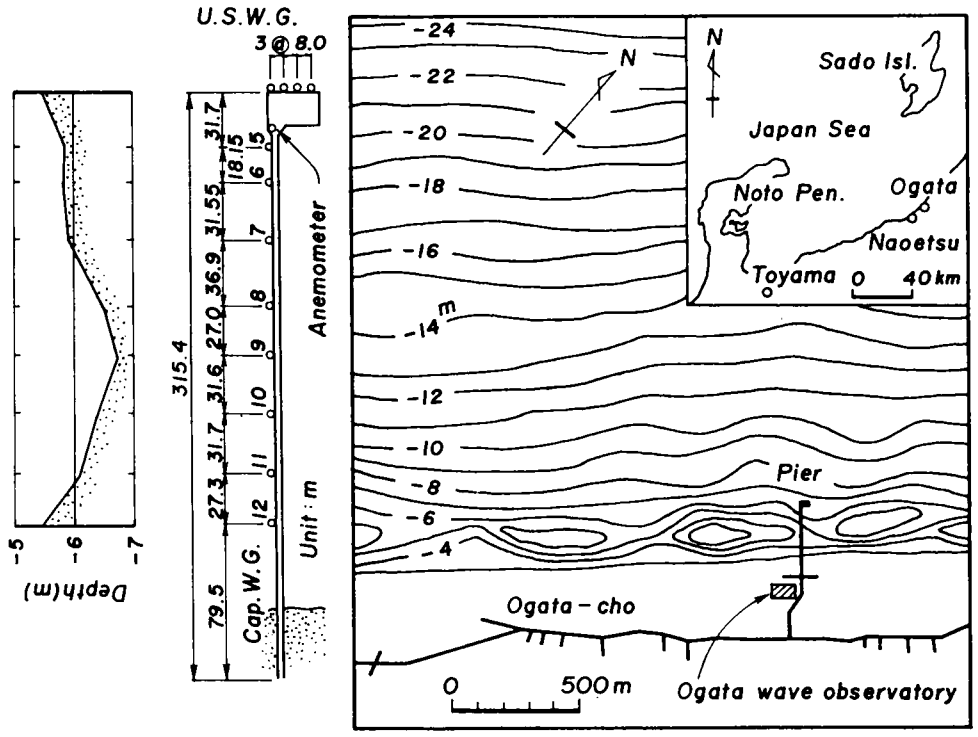

Fig. 4.48 Environments of a observational pier and linear wave-probe array.

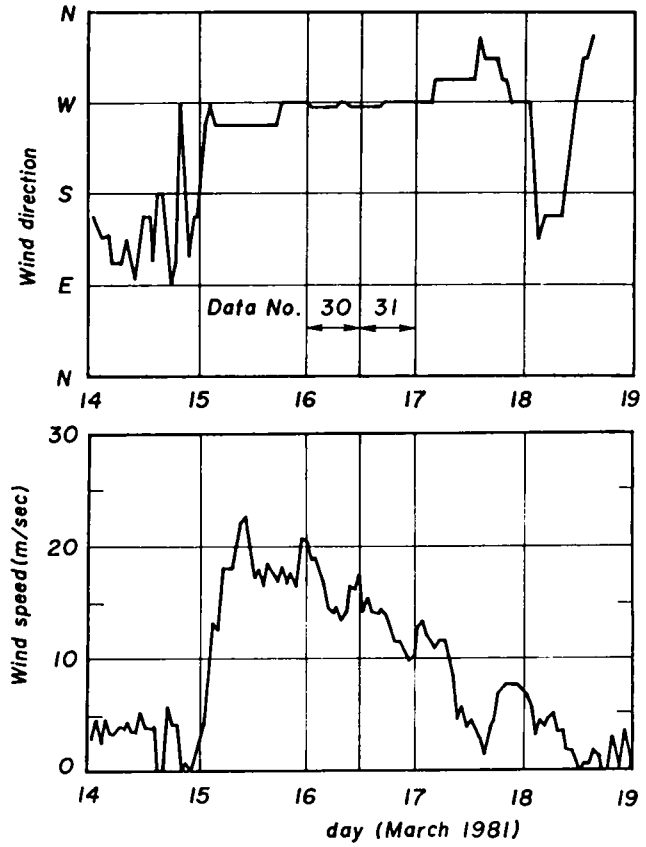

Fig. 4.49 Wind directions and wind speeds at Ogata coast, March 1981.

stantly from 7-31 March 1981 at intervals of 1 hour during the storm. Wave data used in the present analysis are Data No. 30(1-6 a.m., 16 March) and Data No. 31(7-11 a.m., 16 March), which were nearly the peak time of the storm. The time histories of the wind speed and wind direction are shown in **Fig. 4.49**, indicating that the mean wind speeds were about 16 m/sec for Data No. 30 and 13 m/sec for Data No. 31, respectively, and that the wind blew steadily from the west.

b. Statistical Properties of Wind-Waves

Representative wave data used are shown in **Fig. 4.50**, where the record length is about 655 sec and the time lag is 0.16 sec. Since wave data contained a trend caused by low-frequency components of waves, the trend was excluded by the running average method with a low-pass filter of 32 sec

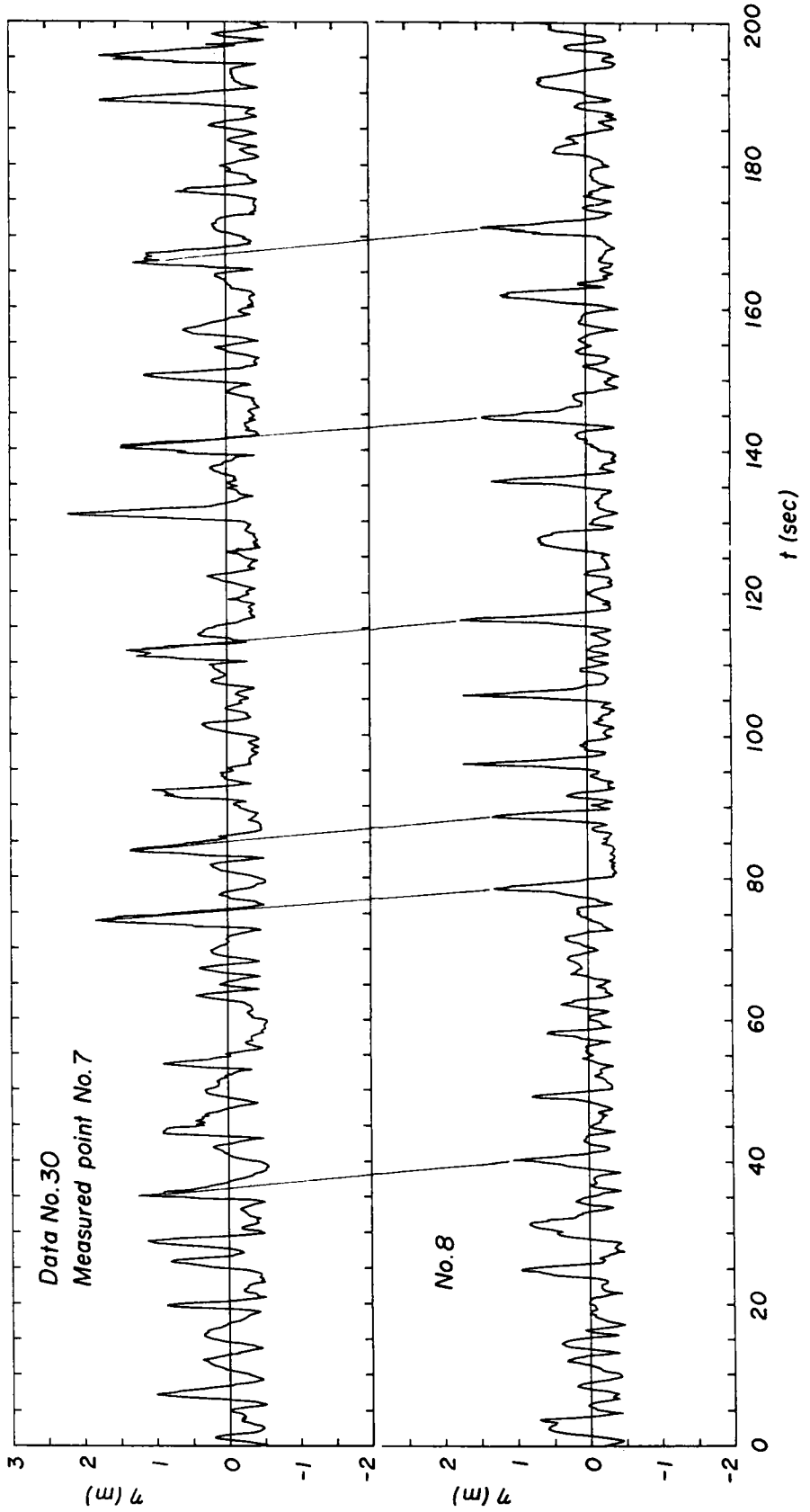

(1) Data No. 30

Fig. 4.50 Adjusted wave records at Ogata coast, March 1981.

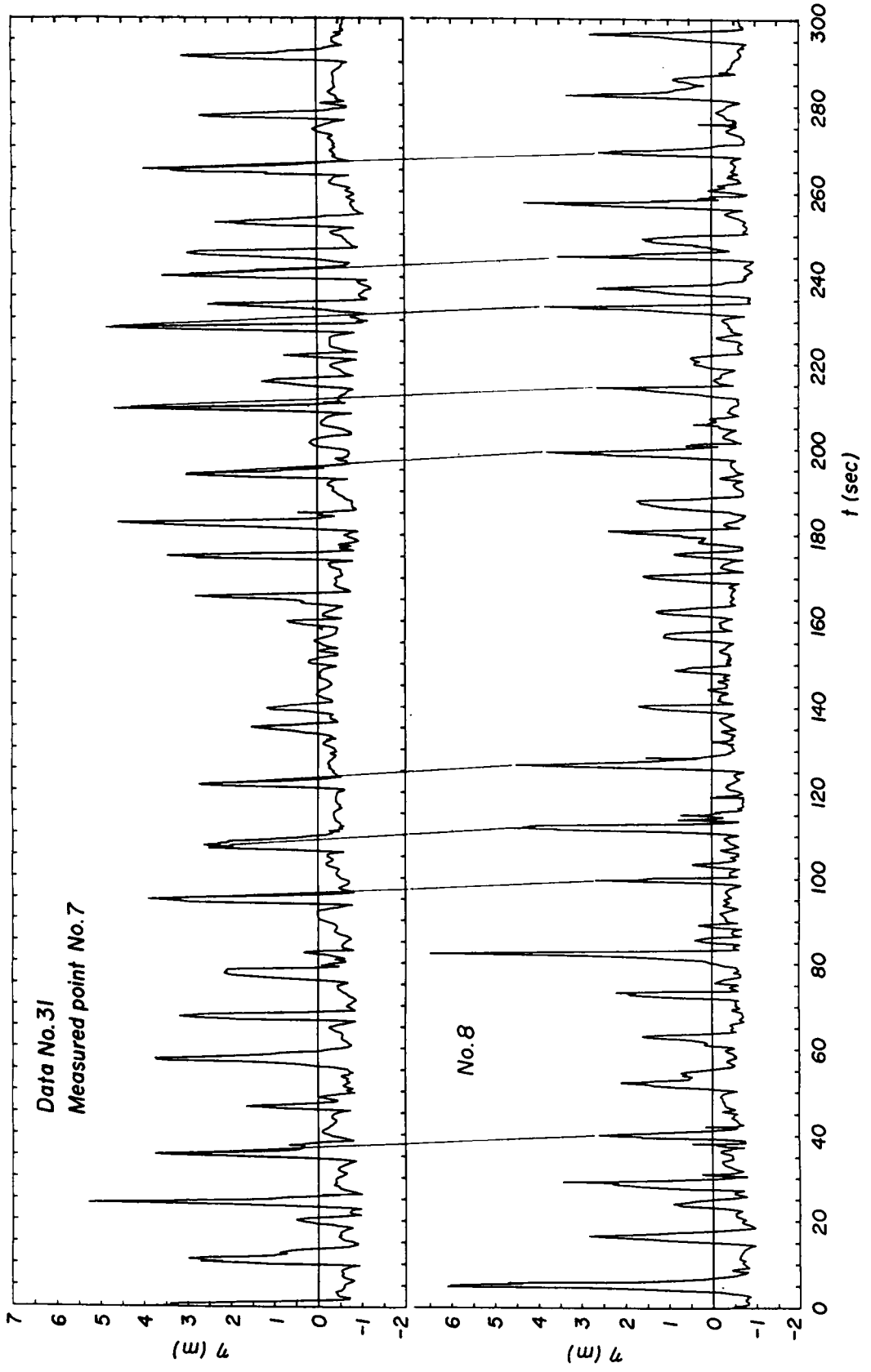

(2) Data No. 31

Fig. 4.50 Continued.

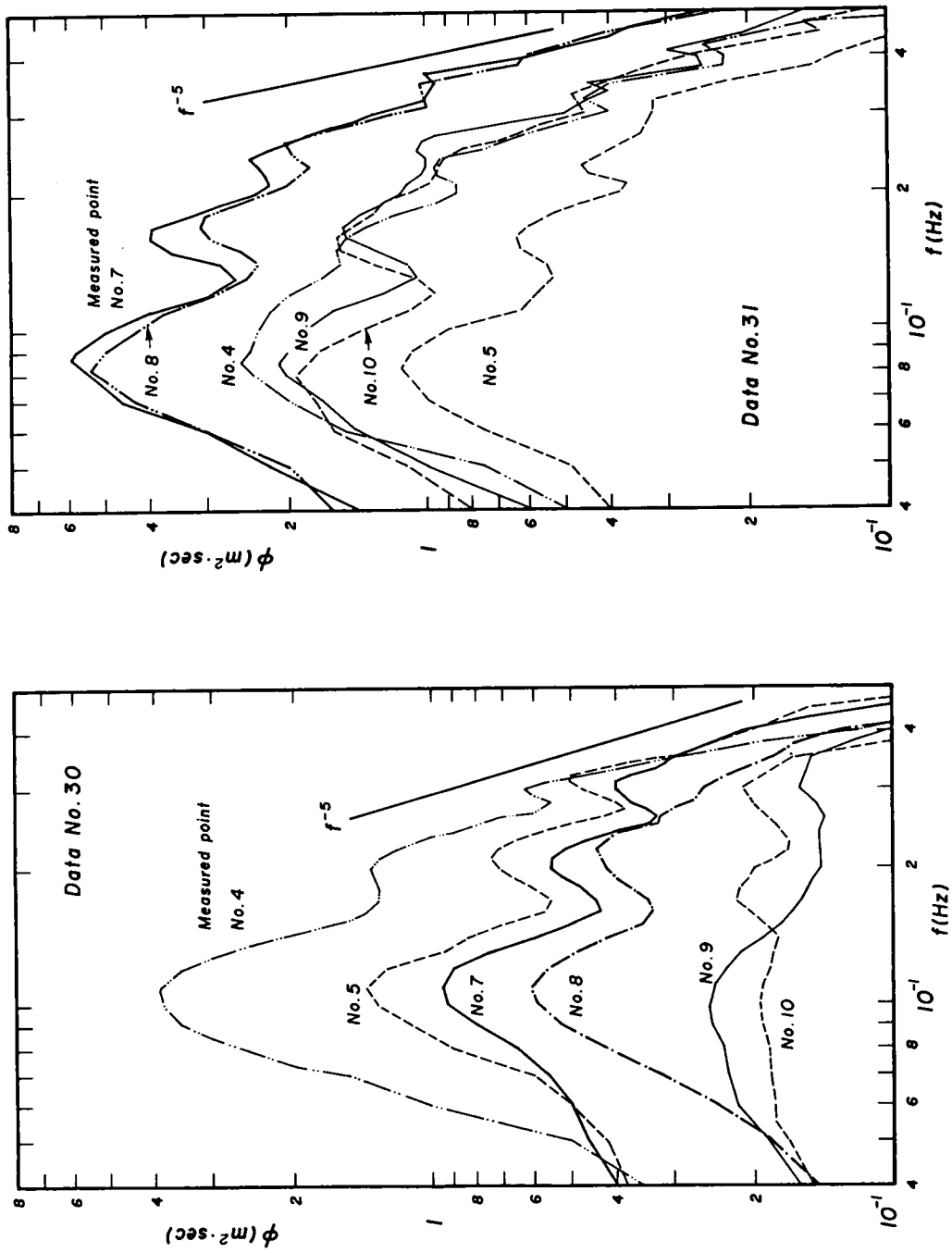

(1) Data No. 30 (2) Data No. 31

Fig. 4.51 Power spectra along the observational pier.

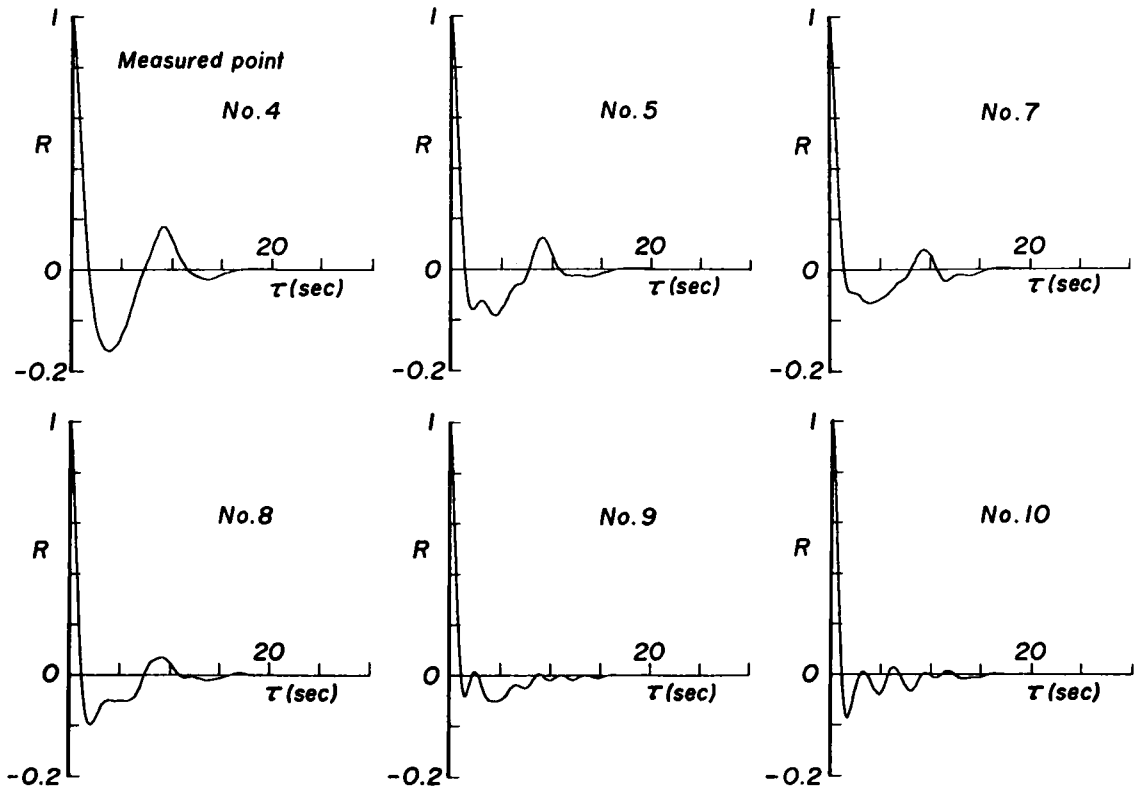

(1) Data No. 30

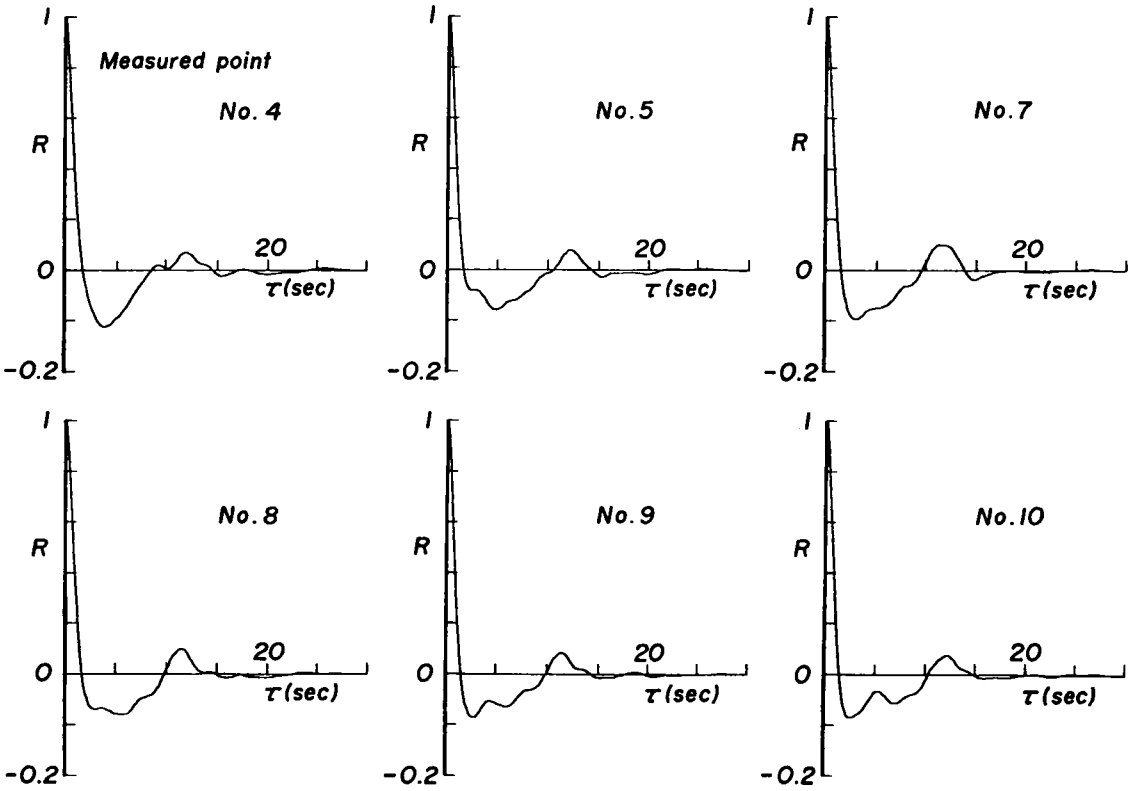

(2) Data No. 31

Fig. 4.52 Auto-correlations along the observational pier.

in band-width. Wave properties, such as wave height and wave period, were determined based on the zero-up cross method using the adjusted data above.

Fig. 4.51 shows power spectra by the FFT method along the observational pier for Data No. 30 and No. 31. The maxima of power spectra decrease clearly during the waves travel from measuring points 4 to 5 and from points 8 to 9, and bi-frequency components become strong near point 5. Fig. 4.52 shows the changes in auto-correlation along the pier. At points 9 and 10 for Data No. 30, there are no longer distinct peak frequencies. It can also be seen from Data No. 31 that bi-frequency components are more remarkable at points 9 and 10 in comparison with those at points 7 and 8. When waves break, power spectra may decrease sharply, so there might be breaking points near points 5 and 9 or 10. This fact was supported by visual observation.

In the following analysis, wave data at measuring points 7 and 8 are used because they have the nearly same power spectra. Table 4.4 gives mean values for significant wave heights and corresponding wave periods at points 7 and 8 for Data No. 30 and No. 31. Note that significant wave periods are nearly equal to those for bi-frequency components and not to those for peak frequencies of power spectra. According to the laboratory experiments on breaking wave trains, the significant wave period corresponds to the peak frequency of power spectra, but the bi-frequency component is not conspicuous compared with the peak frequency. Therefore, these differences in the experimental and field data may result from a strong occurrence of bi-frequency components as seen in Fig. 4.51, for

Table 4.4 Significant wave heights and periods in field measurements.

Data No.	$H_{1/3}/h$	$T_{1/3}\sqrt{g/h}$
30	0.282	6.77
31	0.633	9.95

instance, in a fully developed soliton separation due to wave shoaling, as predicted by Tsuchiya and Yasuda *et al.*[23].

c. Wave Properties of Wind-Forced Waves

Waves at point 7 and corresponding waves at point 8 were determined from wave records shown in **Fig. 4.50**, and the wave velocities were determined from the travel-time of waves between these two points. Among them, the waves, having wave heights within the significant wave height ±10 %, were selected because a wave field can be characterized by its significant wave. **Fig. 4.53** shows the relation between these selected wave heights and wave periods, where the values are mean values at points 7 and 8 using the mean water depth at these two points. The dimensionless wave periods for the peak and bi-frequencies obtained from the power spectra are respectively $T\sqrt{g/h} \fallingdotseq 11.4$ and 5.97 for Data No. 30, and $T\sqrt{g/h} \fallingdotseq 14.8$ and 7.38 for Data No. 31. Therefore, it is to be noted that dimensionless wave periods of the wind-forced waves cover the region containing these two wave periods and that this fact depends on the strong occurrence of bi-frequency components, as pointed out for the power spectra.

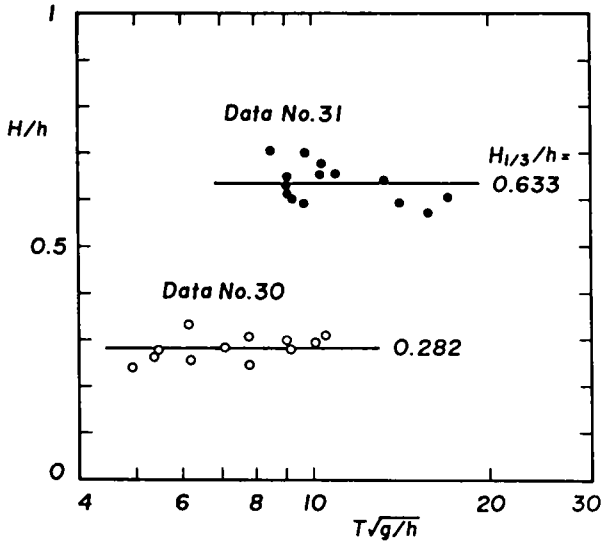

Fig. 4.53 Wave periods of the wind-forced waves corresponding to the significant wave heights.

(3) Discussion

To verify the analytical characteristis of the wind-forced waves, the physical parameter S needs to be estimated.

First, **Fig. 4.54** shows a comparison of experimental wave velocities for the breaking wave trains, having wave heights within the significant wave height $\pm 10\%$, with theoretical wave velocities shown by solid lines. In Run 1, experimental wave velocities at wave periods less than the significant wave period are greater than the theoretical wave velocities by about 10 %, but measured wave velocities, as a whole, can be considered to be in the theoretically estimated regions. Experimental wave velocities for the significant waves are near the upper bounds of theoretical ones, and the parameter S takes on values from 0.6 to 1.0 for both Runs 1 and 2.

Wind-induced currents predicted in **Fig. 4.46** and mass transport velocities in the Eulerian coordinates presented in **Fig. 4.47** are compared with the theoretical results in **Figs. 4.55** and **4.56**, respectively. These figures, on the contrary, indicate that the values of S may be within from 0.2 to 0.4 for both Runs 1 and 2. Moreover, the values of σ_τ/s are plotted in **Fig. 4.57**, where the bottom friction s was evaluated based on Manning's empirical friction law, Eq. (4.155), and the shear stress σ_τ was estimated by Eq. (4.33) using the drag coefficients given in **Table 4.3** from the laboratory measurements and those by Mitsuyasu and Honda's experimental formula[24]. Manning's roughness coefficient n can take on two values of 0.01 and 0.015 because the bottom of the wind wave generator is made of a steel plate. Furthermore, the coefficient m_b in Eq. (4.33) was assumed to be 0.1; in the numerical simulations of storm surges, m_b is generally about 0.25, but this coefficient is considered to vary from 0.1 to 0.5 according to the flow conditions, either turbulent or laminar, so the flow in the breaking wave trains was assumed to be nearly turbulent. **Fig. 4.57** also

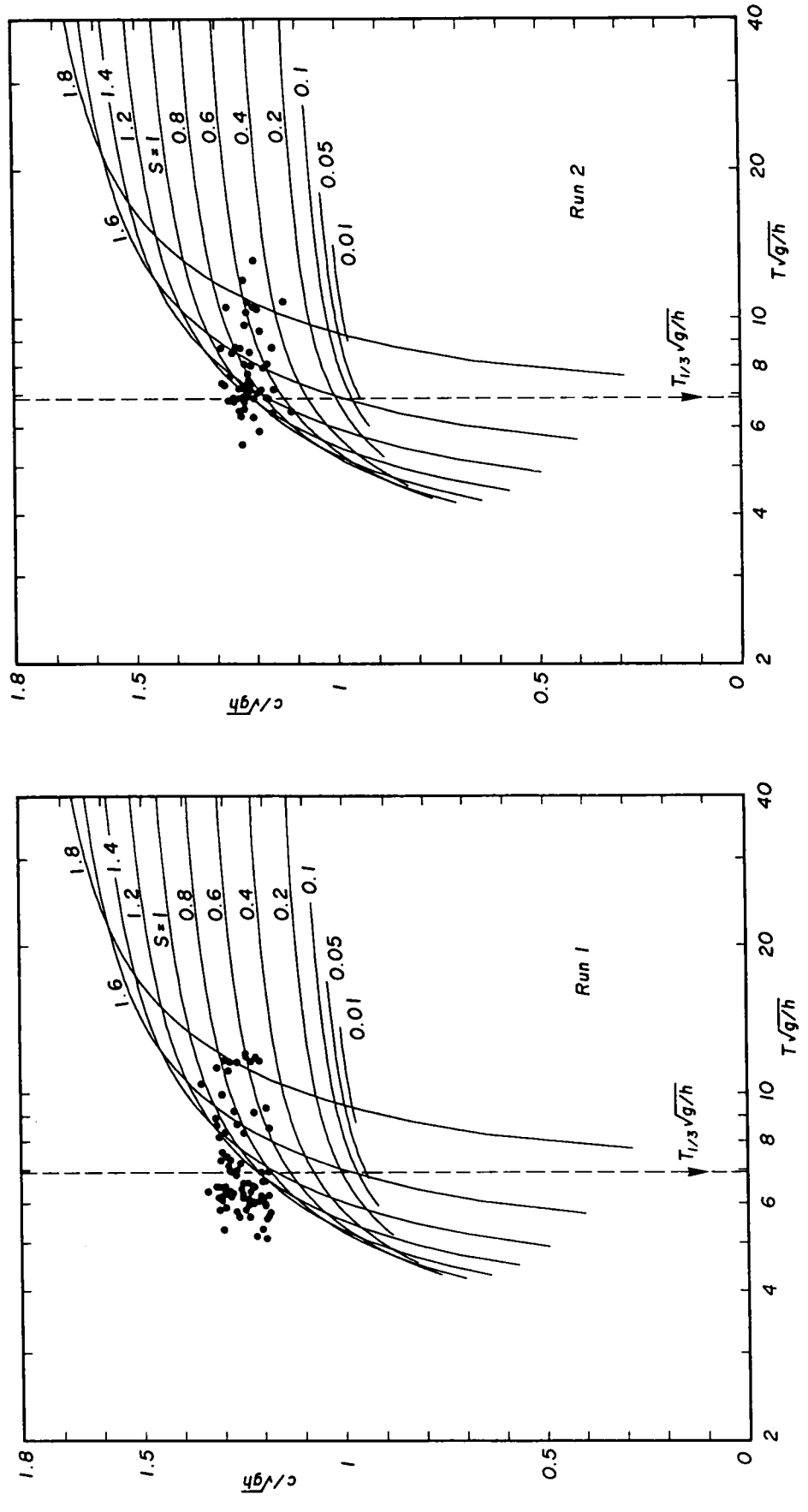

(1) Run 1　　(2) Run 2

Fig. 4.54 Wave velocity of the breaking wave trains with wave heights within the significant wave height ±10%.

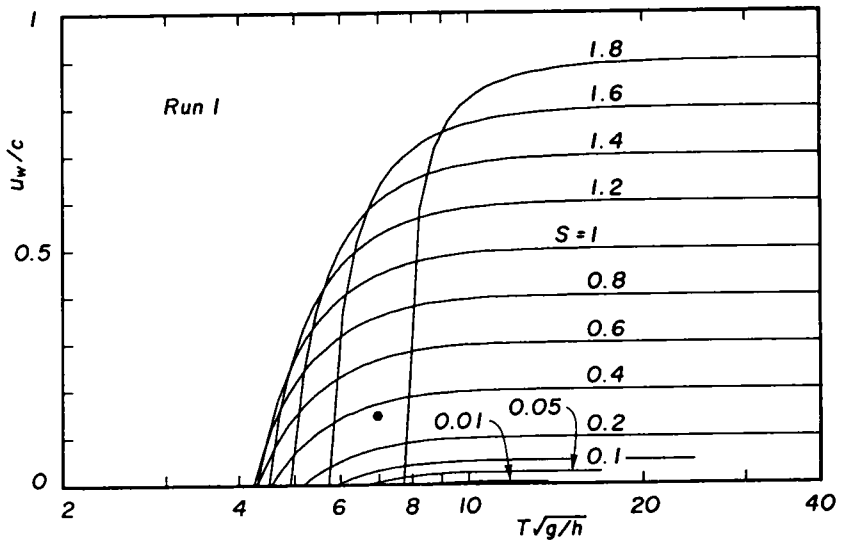

(1) Run 1

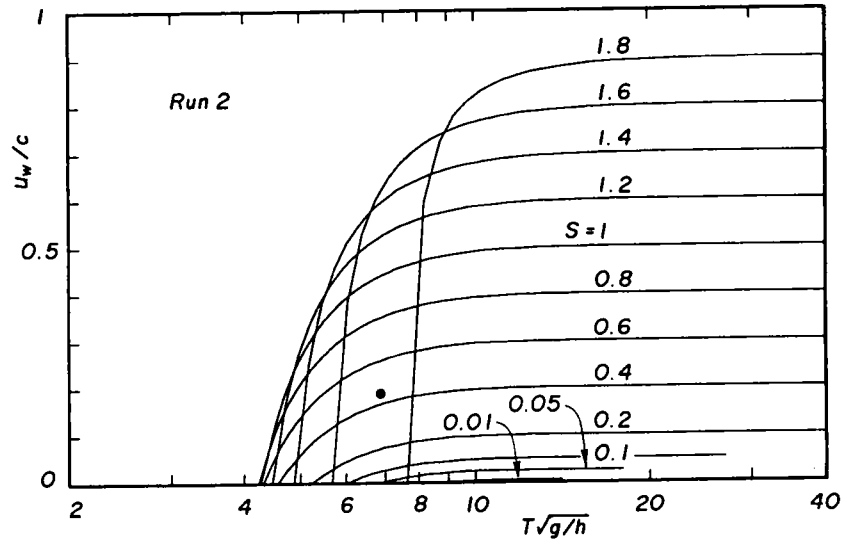

(2) Run 2

Fig. 4.55 Wind-induced current in the breaking wave trains.

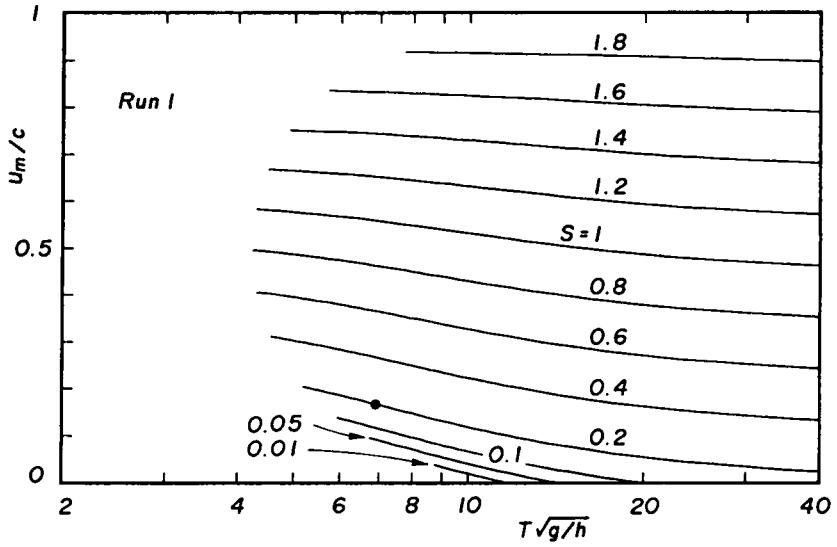

(1) Run 1

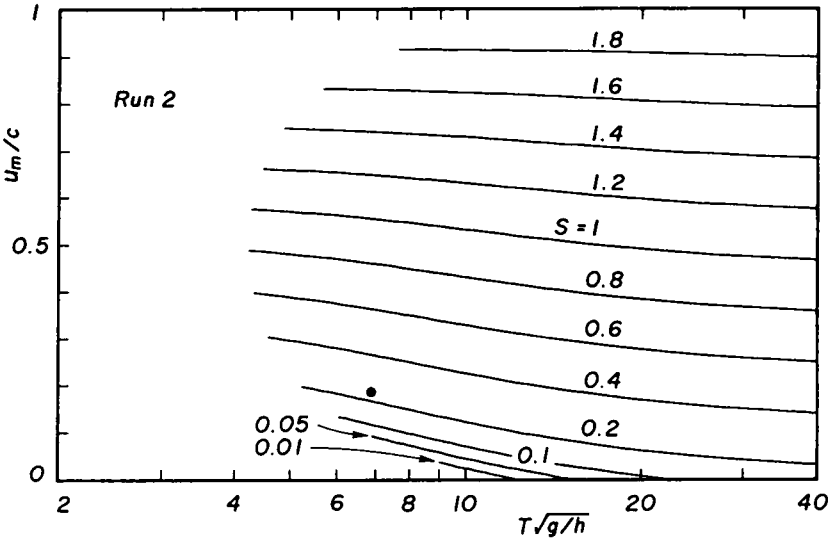

(2) Run 2

Fig. 4.56 Mass transport velocity of the breaking wave trains.

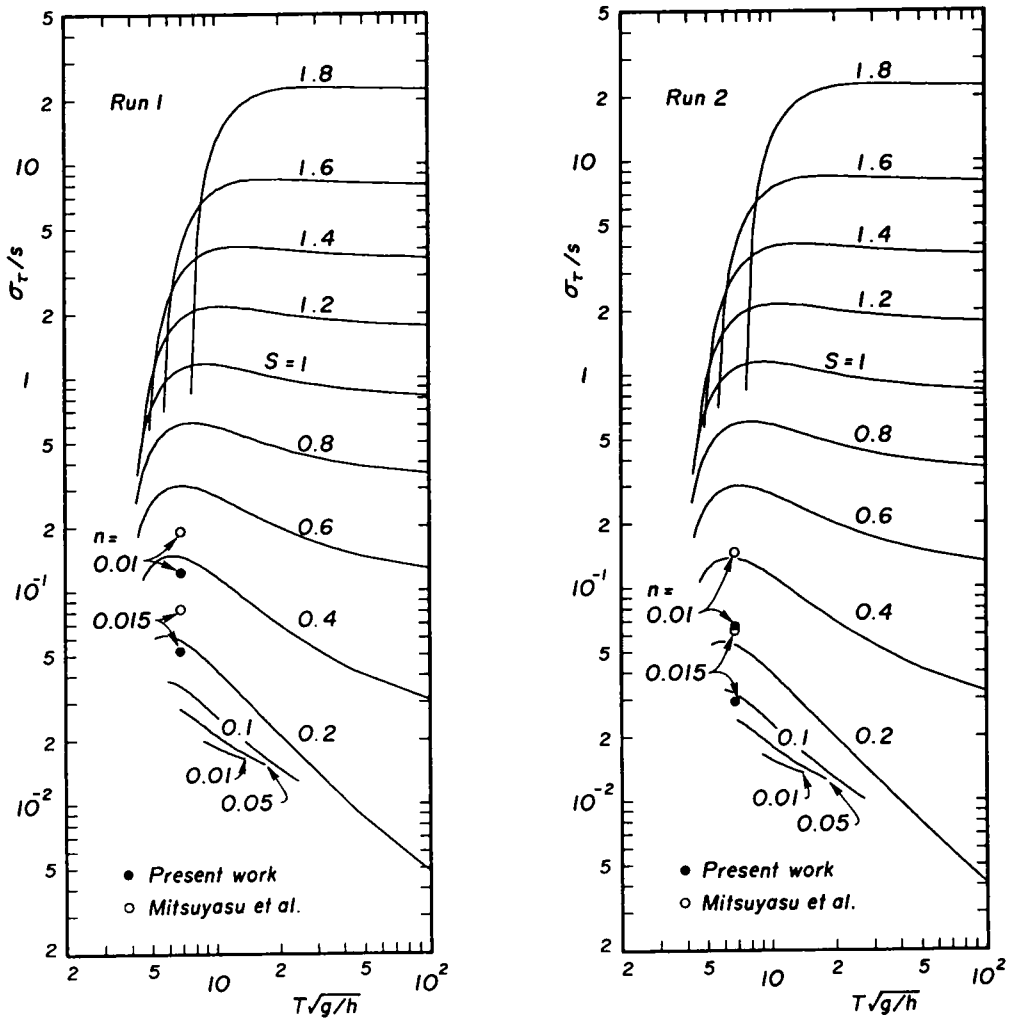

(1) Run 1 (2) Run 2

Fig. 4.57 Values of σ_τ/s, evaluated based on Manning's empirical friction law.

indicates that the parameter S changes from 0.2 to 0.5 for Run 1 and from 0.1 to 0.4 for Run 2, respectively.

Summing up these results, only **Fig. 4.54** gives slightly greater values of S than the others. However, since the breaking wave trains surely accompany strong wind-induced currents, it may be preferable that the parameter S be chosen for the theoretical velocity field to nearly coincide with the experimental velocity field. It should be noted that the wind-induced currents in the breaking wave trains shown in **Fig. 4.46** include velocity components due to the presence of waves, so give rather large

values of S, and also that the mass transport velocities shown in Fig. 4.47, on the contrary, indicate rather small values of S because water particle velocities very close to wave surfaces were not measured. Therefore, the roughly estimated values of S and Manning's roughness coefficient n are respectively taken to be 0.3 and 0.012 for Runs 1 and 2, in the following discussion.

This judgment is supported by Fig. 4.58. The figure shows a comparison of the distribution of average velocity with respect to the phase of waves, where the experimental values are evaluated from Figs. 4.43 and 4.44. The theoretical and experimental average velocities agree fairly well except that the latter distributes asymmetrically and takes on rather large values in the wave trough phase, which may be caused by short period waves riding on the breaking wave trains.

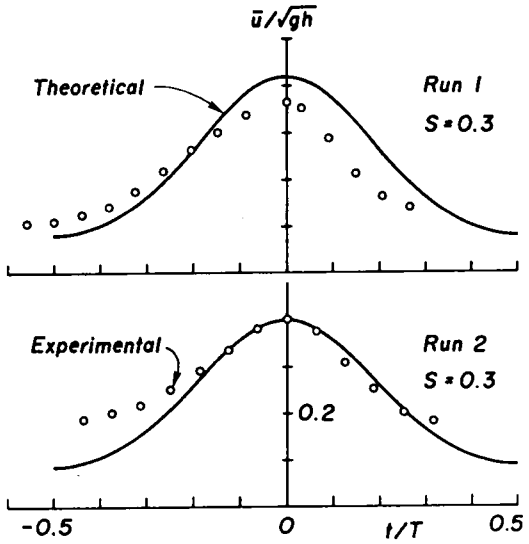

Fig. 4.58 Comparison of the distribution of average velocity in the breaking wave trains with theoretical ones.

Figs. 4.59 and 4.60 show experimental wave profiles of the breaking wave traines corresponding to the significant waves. Note that experimental wave heights are within the significant wave height ±10 %, but theoretical wave heights are fixed to be those for significant waves, i.e. H/h =

$H_{1/3}/h$ = 0.458 and 0.408 for Runs 1 and 2, respectively, thus there exists a discrepancy in wave height of about 10 %. The representative feature is that experimental wave profiles of the breaking wave trains are more asymmetric and steep compared with theoretical ones. However, surface slopes on the windward sides of the waves seem to agree comparatively well with theoretical ones.

Secondly, **Fig. 4.61** shows a comparison of wave velocities from field measurements, where waves with heights within the significant range were selected in a manner similar to that used for **Fig. 4.54**. The observed wave velocities exist near the lower bounds of theoretically estimated regions and have variances of about 10 %. The present observation did not measure quantities related to the velocity field in waves, thus the parameter S must be estimated from this figure. Though the wave velocities observed are sometimes under the theoretically estimated curves, the parameter S at the significant wave periods, at this stage, still can be assigned 0.1 as the mean value for both Data No. 30 and No. 31.

Furthermore, the friction coefficient at the sea bottom s is also unknown in the present observation, while the successive field measurements at Ogata coast using the same observational pier have been carried out by Kakinuma *et al.*[25),26),27),28)]. According to their results for bottom friction, the usual relation between the friction coefficient and wave Reynolds number is well satisfied in the offshore region, but the friction coefficient in the nearshore region takes on large values. The wave Reynolds numbers at measuring points 7 and 8 are about 4×10^7 in the present measurements, thus the bottom friction s can be assumed to be about 0.04 from their investigations.

Similar to **Figs. 4.59** and **4.60**, comparisons of wave profiles for Data No. 30 and No. 31 are shown in **Figs. 4.62** and **4.63**, respectively. As the significant wave periods are smaller than those for spectral peaks, as

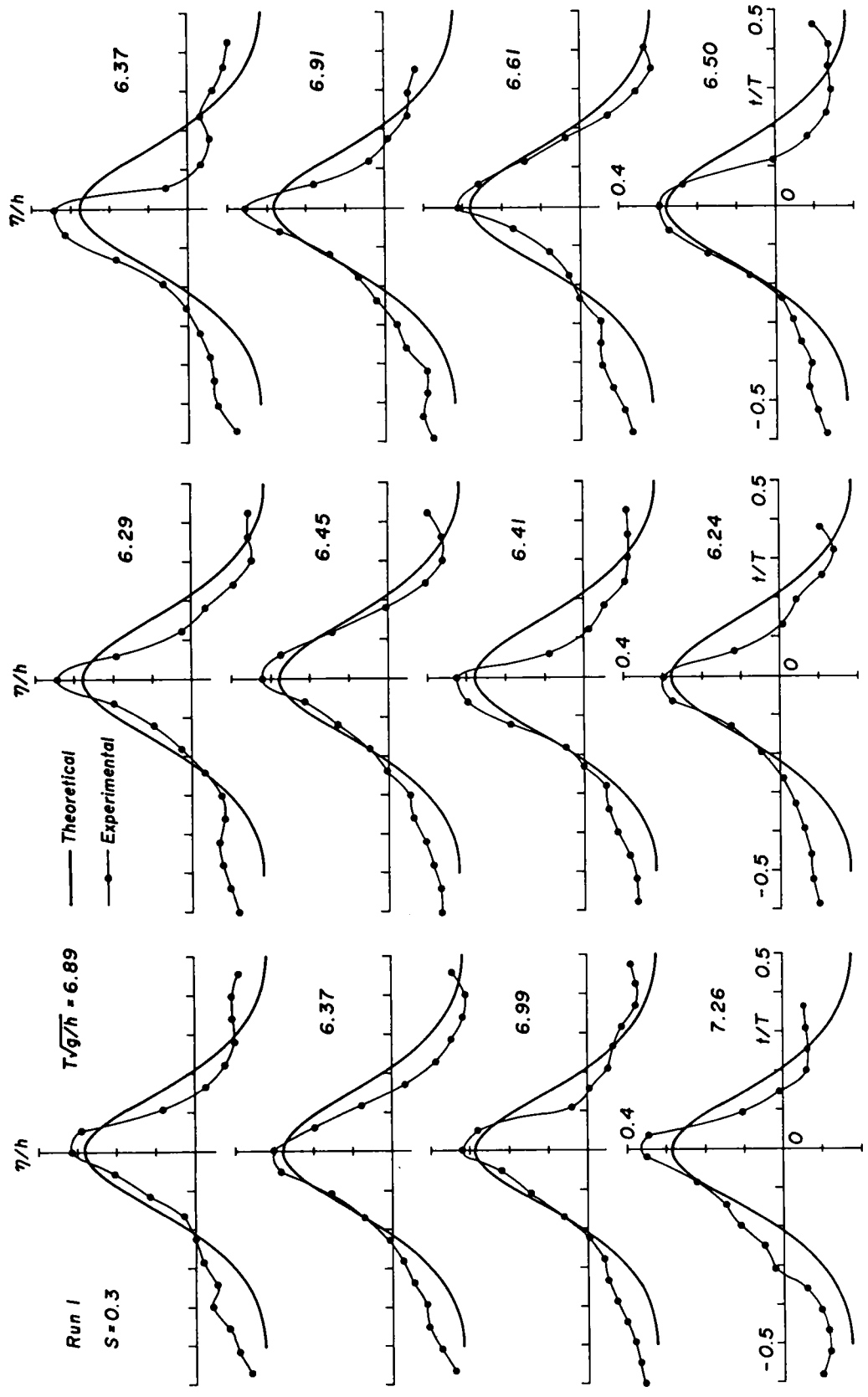

Fig. 4.59 Comparison of wave profiles of the breaking wave trains with theoretical ones (Run 1).

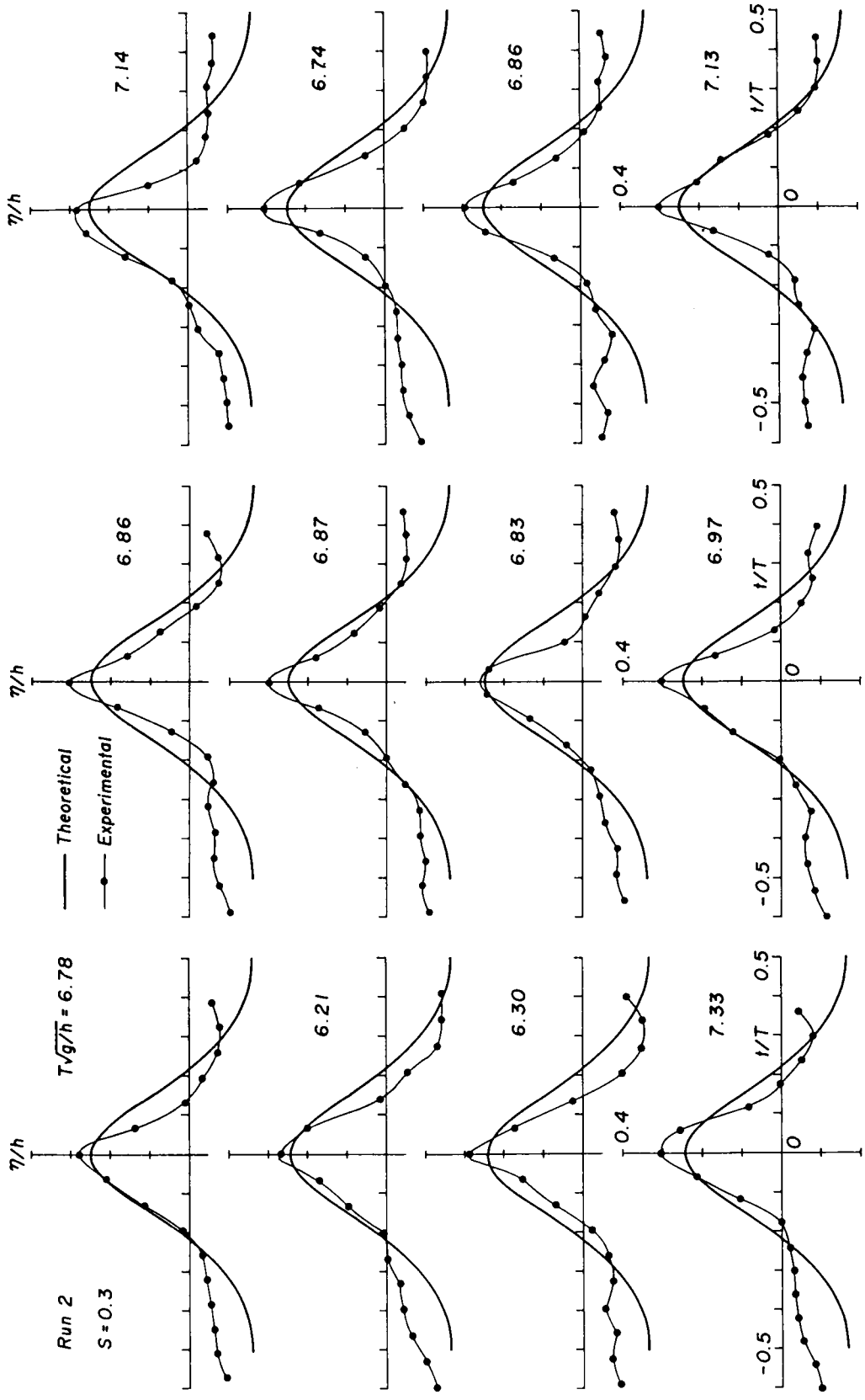

Fig. 4.60 Comparison of wave profiles of the breaking wave trains with theoretical ones (Run 2).

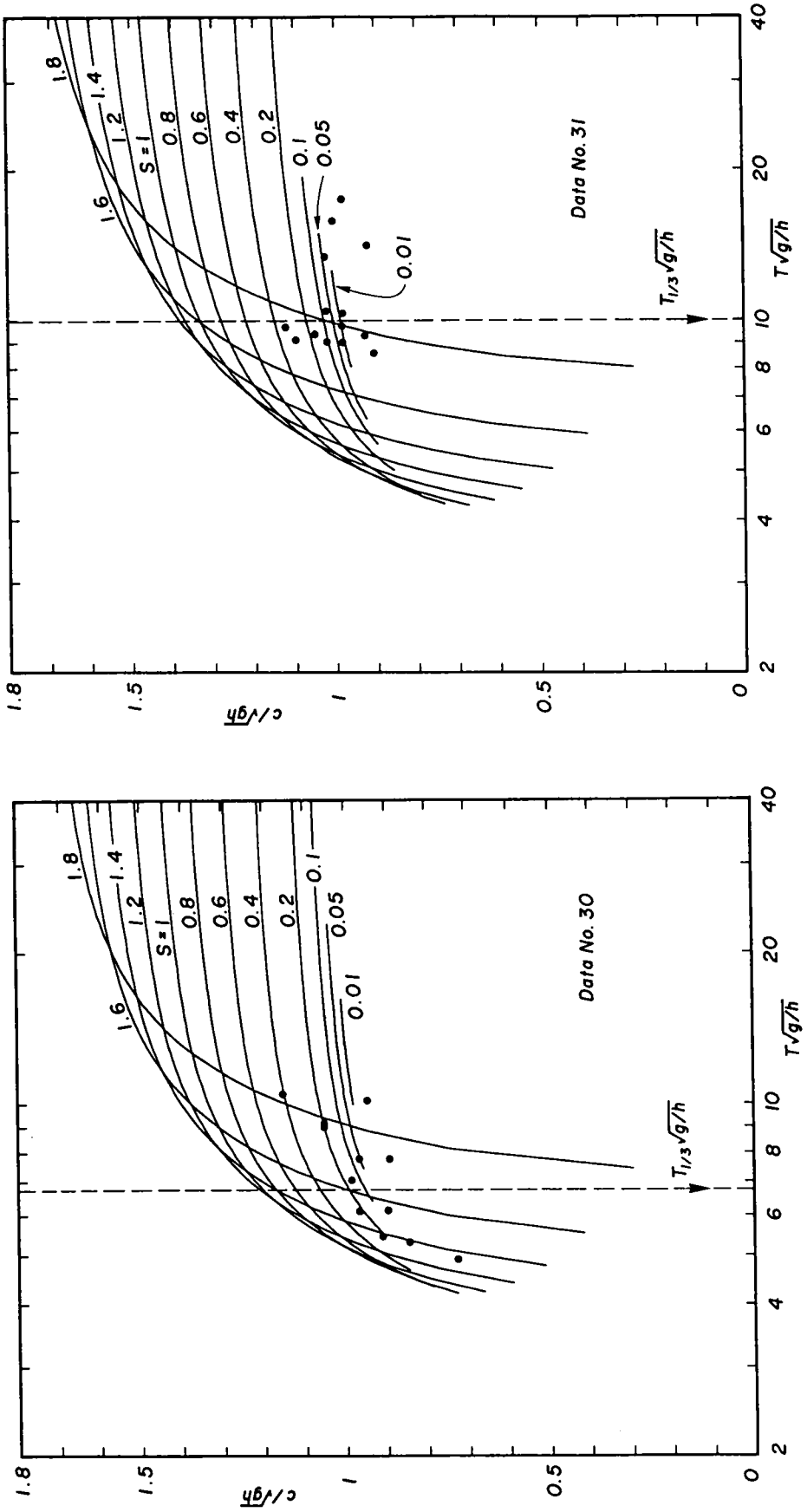

(1) Data No. 30

(2) Data No. 31

Fig. 4.61 Wave velocity of the wind-forced waves with wave heights within the significant wave height ±10%.

mentioned above, the wave profiles for spectral peaks are also shown on the right-hand side of each figure. Fundamental properties are the same as for the laboratory simulation of the breaking wave trains, therefore the experiment using the recirculating wind wave generator may be suitable for the simulation of wind-forced waves generated by strong wind, accompaning reasonably great wind-induced currents. However, the asymmetry of wave profiles in field data is stronger compared with experimental wave profiles for the breaking wave trains, and this may be natural as the observed wave profiles in the nearshore region are surely subject to asymmetric deforma-

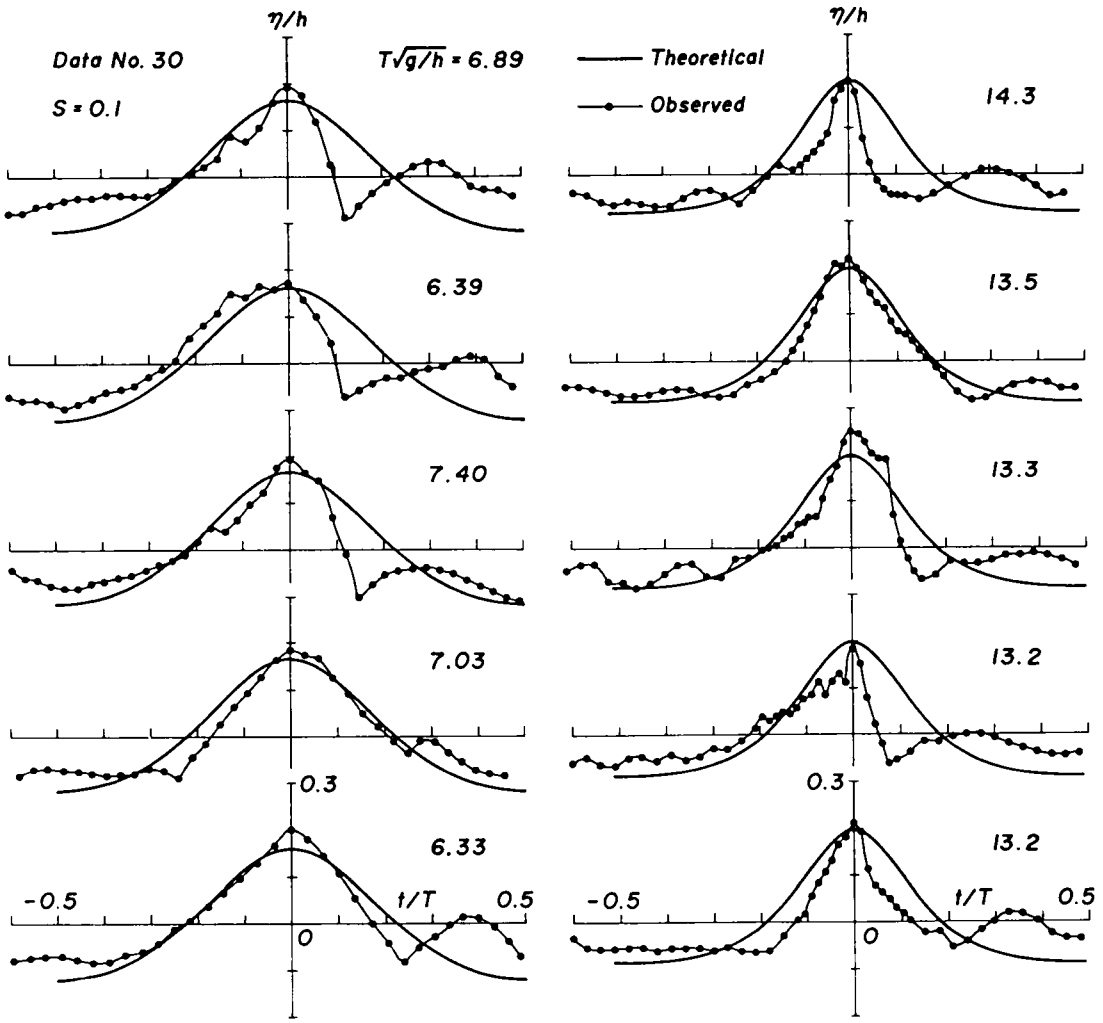

Fig. 4.62 Comparison of wave profiles of the wind-forced waves with theoretical ones (Data No. 30).

tion of waves due to wave shoaling. The occurrence of short period waves in wave trough phases is also remarkable.

Fig. 4.64 shows the corresponding velocity fields in the wind-forced waves together with wave profiles, estimated by the present model. Figs. 4.64(2) and (4) are those for spectral peaks. In case of Fig. 4.64(1), since the wave velocity is less than unity, the whole velocity field is

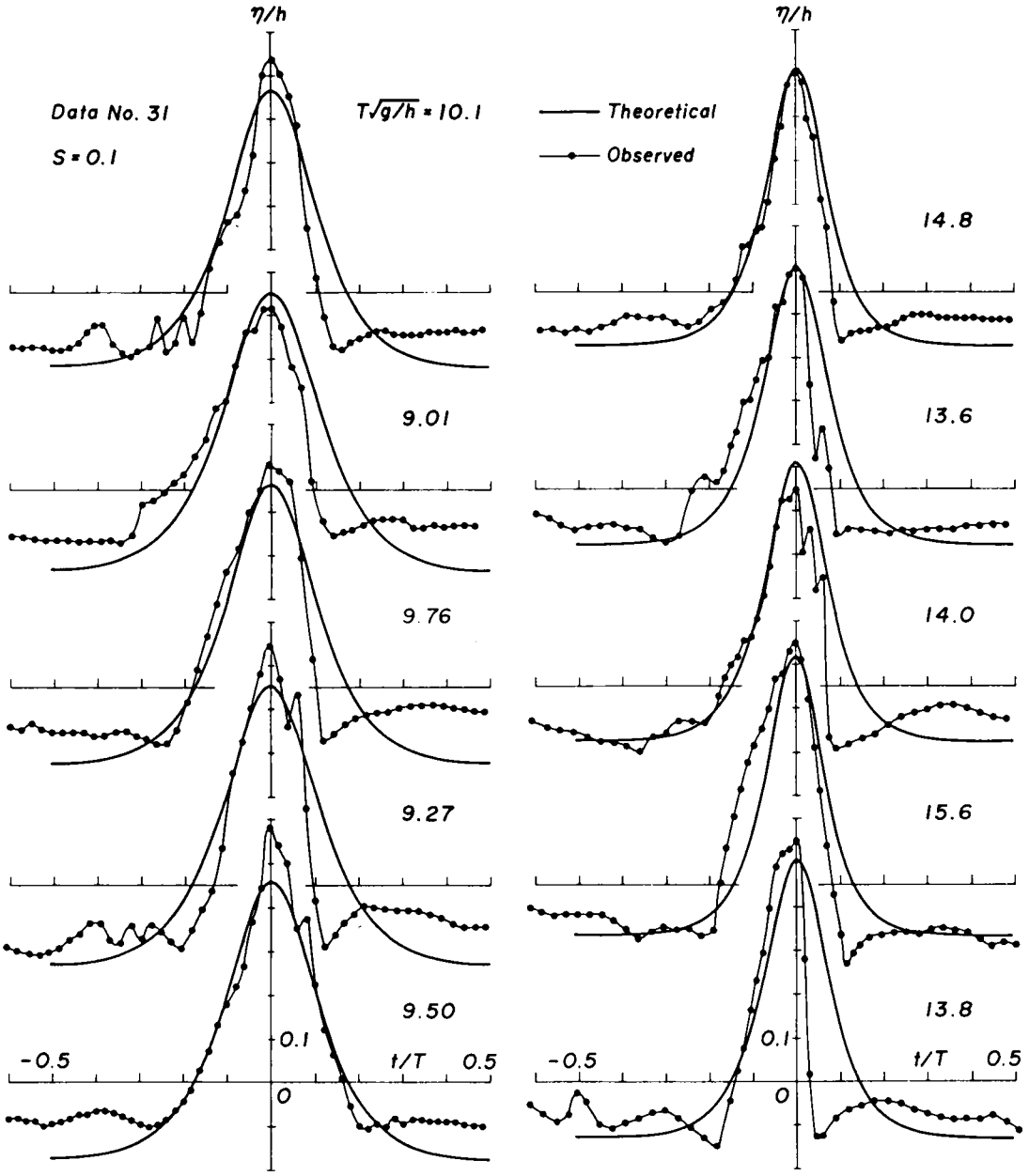

Fig. 4.63 Comparison of wave profiles of the wind-forced waves with theoretical ones (Data No. 31).

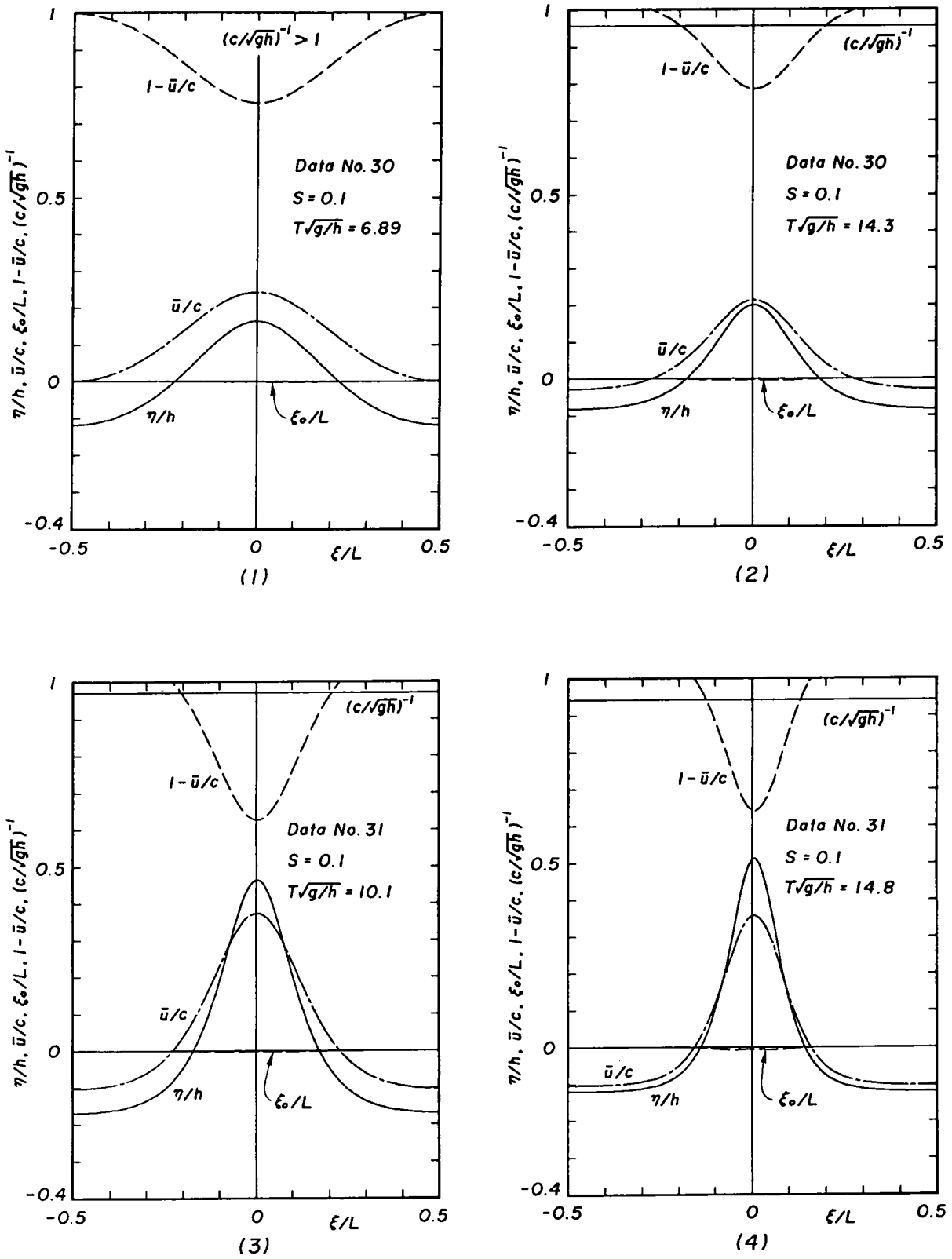

Fig. 4.64 Representative wave profiles and distributions of average velocity with respect to the phase of waves, corresponding to the significant waves and waves for the spectral peaks.

subcritical in the frame of reference moving with the wave. In the others, the regions near the wave crests are subcritical and near the wave troughs, supercritical in this steady flow system. The wind-induced current for the wind-forced waves from field measurements can be estimated as $u_w/\sqrt{gh} \fallingdotseq S/2 = 0.05$, and wave breaking seems to occur, as seen in Figs. 4.62 and 4.63; this value is, however, about one-third of those for the breaking wave trains. A reason may be attributed to the restraint of mass transport in the wind-forced waves by the presence of the shore.

Judging from the investigations above, it can be conclusively noted that the gross features of the wind-forced waves can be simulated satisfactorily by the present model. As to bottom friction and surface shear stress, our knowledge, however, is far from satisfactory which obstructs a better understanding of the present problem. Therefore, more thorough knowledge about bottom friction and surface shear stress, which interact each other in nearshore regions, is needed.

4.7 Conclusion

This chapter has developed formulas for wave motion generated by strong wind in shallow water. General partial differential equations governing wave motion subject to the surface wind stresses and bottom friction have been formulated, which turn into the generalization of the Korteweg-deVries-Burgers equation. The governing equations contain all physical and mathematical terms to be taken into account for, such as nonlinearity and dispersion of waves, dissipation in water, external wind stresses, and bottom friction. Wind-forced waves could occur in the equilibrium state of these internal and external forces. The equation has been analyzed using the method of averaging as for the nonlinear oscillations, where wind stresses have been assumed to vary along the same lines as in Section 2.4.

that is, the shear stress varies in phase with the wave elevation, and the pressure, in phase with the surface slope. The most stable wave motion has also been defined by introducing the physical motion. The fundamental physical quantities of the wind-forced waves have been formulated as one parameter family for a required wave height and wave period together with flow field quantities, such as friction at the sea bottom and Reynolds number, in which the parameter is deeply related to the surface shear stress. Laboratory experiments and field measurements have given some verifications for the wind-forced waves.

Chief characteristics of the wind-forced waves are concluded to be as follows: 1) Mathematically, Burgers' term, namely, the pressure caused by wind, has a significant role in the generation of the wind-forced waves as does the shear stress. 2) The wind-forced waves accompany strong wind induced currents and mass transport in comparison with the progressive waves investigated by the usual nonlinear finite amplitude wave theories without wind effects; thus, their wave velocities are nearly the same or greater. 3) The critical depth in the frame of reference moving with the wave can occur if the water particle velocity is small compared with the wave velocity. 4) Wave profiles can also become asymmetric due to the increase in bottom friction.

Regarding the wind stresses needed to generate the wind-forced waves, both the shear stress and pressure take on local maximum values at certain wave periods, and if the wind-forced waves accompany strong currents, the wind stresses become nearly constant for long period waves. This suggests the existence of a saturation state of wind stresses; namely, when the wave length surpasses a certain threshold length, the roughness caused by the water surface displacement has less effect on the generation of wind stresses. It is, furthermore, noted that if the wind-induced current becomes great, the shear stress has a primary role in generation of the

short period wind-forced waves, and the fully developed long period waves are chiefly maintained with the aid of the pressure by wind.

In practical applications, once a design storm, with its significant wave, surface shear stress, and bottom friction, has been determined, the model will permit an estimate of wind-forced waves and supply design data for various coastal engineering works. However, the model depends heavily both on the bottom friction and on the surface shear stress by wind. It is, therefore, necessary to clarify the interrelation between these two external forces more in detail.

References

1) Korteweg,D.J. and G.deVries: On the changes of form of long waves advancing in a rectangular channel, and on a new type of long stationary waves, Phil. Mag., Ser.39, 1895, pp.422-443.
2) Keller,J.B.: The solitary wave and periodic waves in shallow water, Comm. Appl. Math., Vol.1, 1848, pp.323-339.
3) Boussinesq,J.: Théorie de l'intumescence liquide appelée onde solitaire ou de translation se propageant dans un canal rectangulaire, Comptes Rendus, Vol.72, 1871, pp.755-759.
4) Johnson,R.S.: Shallow water waves on a viscous fluid-The undular bore, Phys. Fluids, Vol.15, 1972, pp.1693-1699.
5) Ursell,F.: The long-wave paradox in the theory of gravity waves, Proc. Camb. Phyl. Soc., Vol.49, 1953, pp.685-694.
6) Chester,W.: Resonant oscillations of water waves. I. Theory, Proc. Roy. Soc. Lond., A.306, 1968, pp.5-12.
7) Peregrine,D.H.: Long waves on a beach, Jour. Fluid Mech., Vol.27, 1967, pp.815-827.
8) Stewartz,R.W.: Mechanics of the air-sea interface, Phys. Fluids, Suppl., Vol.10, 1967, S47-S55.
9) Longuet-Higgins,M.S.: Action of a variable stress at the surface of water waves, Phys. Fluids, Vol.12, 1969, pp.737-740.
10) Yamada,H. and J.Okabe: On the resonance effect in a storm surge(Part II), Bull. Disas. Prev. Res. Inst., Kyoto Univ., Vol.15, Part 2, 1965, pp.59-74.
11) Dressler,R.F.: Mathematical solution of the problem of roll waves in inclined open channel, Comm. Pure Appl. Math., Vol.2, 1949, pp.149-194.
12) Byatt-Smith,J.G.B.: Effects of empirical dissipation terms in the solution of the undular bore, Quart. Appl. Math., 1971, pp.499-515.
13) Skjelbreia,L.: Gravity waves, Stokes' third order approximation, Tables of functions, Council on Wave Reseach, The Engineering Foundation, ASCE, 1959, 337p.
14) Tsuchiya,Y. and T.Yasuda: A study on the new cnoidal wave theory, Proc. 21th Japanese Conf. on Coastal Engrg., JSCE, 1974, pp.65-71(in Japanese).
15) Stokes,G.G.: On the theory of oscillatory waves, Trans. Camb. Phil. Soc., Vol.8, 1847, pp.441-455.

16) Tsuchiya,Y. and T.Yasuda: Quasi-Stokes wave theory by the reductive perturbation method, Proc. 25th Japanese Conf. on Coastal Engrg., JSCE, 1978, pp.6-9(in Japanese).
17) Tsuchiya,Y. and M.Yamaguchi: Recirculating random wave generator (shallow water ocean wave simulator) using a wind wave tank and its characteristics, Bull. Disas. Prev. Res. Inst., Kyoto Univ., No.14, B, 1971, pp.391-406(in Japanese).
18) Phillips,O.M.: The equilibrium range in the spectrum of wind-generated waves, Jour. Fluid Mech., Vol.14, 1958, pp.426-434.
19) Longuet-Higgins,M.S.: On the statistical distribution of height of sea waves, Jour. Mar. Res., Vol.11, 1952, pp.245-266.
20) Toba,Y. and H.Kunishi: Breaking of wind waves and the sea surface wind stress, Jour. Oceanogr. Soc. Japan, Vol.26, 1970, pp.71-80.
21) Kunishi,H. and T.Imazato: On the wave growth in a recirculating random wave generator, Bull. Disas. Prev. Res. Inst., Kyoto Univ., No.9, B, 1966, pp.1-10(in Japanese).
22) Tsuchiya,Y., Y.Kawata, T.Shibano, T.Yamashita, and M.Kobayashi: Characteristics of water surface displacements in time and in space at a real coast, Proc. 29th Japanese Conf. on Coastal Engrg., JSCE, 1982, pp.26-30(in Japanese).
23) Tsuchiya,Y., T.Yasuda, T.Yamashita, and Y.Takeyama: Representation of wind-generated sea in terms of the soliton spectrum, Proc. 29th Japanese Conf. on Coastal Engrg., JSCE, 1982, pp.41-45(in Japanese).
24) Mitsuyasu,T and T.Honda: Experimental investigations on the wind action exerting on the water surface, Proc. 27th Japanese Conf. on Coastal Engrg., JSCE, 1980, pp.90-93(in Japanese).
25) Kakinuma,T., A.Ishida, and T.Moji: A wave prediction at Ogata coast, Proc. 15th Japanese Conf. on Coastal Engrg., JSCE, 1968, pp.69-72(in Japanese).
26) Iwagaki,Y., T.Kakinuma, and T.Moji: On the deformation of wind waves at Ogata coast, Proc. 16th Japanese Conf. on Coastal Engrg., JSCE, 1969, pp.69-73(in Japanese).
27) Kakinuma,T., T.Futatsuya, and S.Kawai: On the deformation of wind waves at Ogata coast (2), Proc. 20th Japanese Conf. on Coastal Engrg., JSCE, 1973, pp.535-538(in Japanese).
28) Kakinuma,T. and M.Ifuku: On the deformation of wind waves at Ogata coast (3), Proc. 23th Japanese Conf. on Coastal Engrg., JSCE, 1976, pp.302-307(in Japanese).

CHAPTER 5

CONCLUSION

This study has dealt with the two types of breaking phenomena of progressive gravity waves, when wave motion can be assumed to be irrotational and when wind blows over waves, and also with wave motion generated by strong wind which may accompany wind-induced currents.

In Chapter 2 a breaking model was proposed to show what kind of mathematical equation could describe the symmetric "peaking" of the wave crests with a finite angle, such as Stokes' crested configuration, as well as smooth wave profiles. The customary basic equations of wave motion were transformed into the Hamiltonian systems by using the reductive perturbation method and through the variational principle. The resultant Hamiltonian coincided with the first integral for the Korteweg-deVries equation in the lowest order of approximations and had singularity as the "breaking operator" to initiate wave breaking. Thus, the Hamiltonian was converted into a more preferable form based on Thom's catastrophe theory. The resulting breaking model was for cnoidal wave trains, and could describe the whole wave history from non-breaking to desired peaking. According to the model, at just breaking, the wave profile ceases to be rounded and attains "peaking" with a crested angle, while holding the Rankine-Stokes breaking condition. The breaking inception under the shallow water assumptions agrees fairly well with that previously estimated by finite amplitude wave theories.

Also in Chapter 2 was the clarification of the breaking condition in the presence of surface drift generated by wind. The distribution of surface drift in a vortical wind-drift layer, formed at and just below a

wave surface, was determined based on intrinsic equations, derived from the Navier-Stokes equations of motion with boundary layer approximations, in connection with the underlying velocity field, being, in essence, irrotational. The pressure and shear stress from wind were assumed to vary in phase with the surface slope and wave elevation, respectively. The pressure acts like suction near the wave crest. The shear stress and surface drift change sign and become negative in the leeward side of the wave crest, indicating the separation of air-flow on the downstream side or causing a shelterd region in the usually understood sense. The breaking inception in relation to surface drift was also presented with the use of the Rankine-Stokes breaking condition. These breaking conditions, however, are for small scale breaking phenomena which occur near the wave crest at just breaking. Doubtless another significant phenomena might occur in breaking waves, which relate to all the wave properties and may give internal breaking conditions.

In Chapter 3 experiments on the breaking of progressive waves was described not only to confirm usual local breaking conditions but also to discover the internal breaking conditions in reference to the imbalance in the partition rate of wave energies. The local breaking conditions, such as the Rankine-Stokes breaking condition and the breaker index, were found to be satisfied by breaking waves. Furthermore, the fact that the behaviour of water particles in breaking waves is more active than that estimated by the usual wave theories implies the existence of internal breaking conditions. Ever-changing wave energies should be estimated based on the conservation law of energy flux. Among them, only the potential energy can be evaluated from measured water surface displacements. The potential energy begins to decrease at a certain point in front of the breaking point, near the point where the changes in radiation stress take on a maximum value, while the kinetic energy increases sharply and predominates in the partition of wave

energies. As a result, waves fall into an unstable state as a whole. These are premonitory phenomena in breaking waves and may finally lead waves to the breaking.

In the study of coastal phenomena, most wave properties for wind-generated waves are usually estimated by using of finite amplitude wave theories with wind effects neglected. It is necessary to develop a new wave theory which includes the wind effects because fundamental characteristics of waves surely change due to wind effects. The ocean surface waves are formed by the superposition of many wave trains with different wave height and frequency. Among them, large scale "carrier" waves, termed the "wind-forced waves", are important as they characterize the wave field in a shallow coastal zone when strong wind blows.

In Chapter 4 the dynamics of the wind-forced waves were developed. The governing equations were derived from the Navier-Stokes equations of motion based both on the perturbation method with the shallow water assumptions and on a one-dimensional analysis. The equations contain all the physical and mathematical terms to be accounted for, namely, nonlinearity and dispersion of waves, dissipation in water, wind stresses exterting on the wave surface, and friction at the sea bottom. In other words, the equations are an extension of the Korteweg-deVries-Burgers equation. Wind stresses were assumed along the same lines as in Chapter 2 and the bottom friction was treated as an empirical friction law like Chézy's law. Wind-forced waves can occur in the equilibrium state of these internal and external forces. The governing equations were analyzed by the method of averaging to show that the steady wind-forced waves on water of uniform depth are possible, which resulted in a cnoidal solution. The stability condition, furthermore, gave the definition for the most stable wave motion by introducing a physical motion. The physical quantities of the wind-forced waves can now formulate as a one parameter family of the shear stress parameter

if the wave height and wave period are given together with the flow field quantities, the Reynolds number and the friction at the sea bottom. As to the wave profiles, they become asymmetric due to the phase shift in the wave for reasonably great values of bottom friction, and the waves accompany wind-induced currents, which cannot be estimated by the usual wave theories. The wind stresses, shear stress and pressure, needed to generate wind-forced waves, have been clarified; for most wind-forced waves, the pressure, i.e. Burgers' term, has a primary role as does the shear stress, always acting as a positive external force. These wind stresses for certain wave heights take on maximum values and become nearly constant after certain wave periods. This indicates that the surface roughness, caused by the water surface displacements of long period waves, has little effect on the generation of wind stresses, even if the wave length is very long. In this situation, the pressure predominates over the shear stress, so the shear stress has the chief role in the generation of short period waves, while the pressure maintains long period waves. The laboratory experiment and field observation have shown that the gross features of the wind-forced wave can be estimated by the present theory.

As to further investigations, the wind-forced waves depend strongly on the evaluation both of the friction at the sea bottom and of the shear stress by the exertion of wind, and they interact with each other as in storm surges, therefore the interrelation between these external forces needs to be thoroughly investigated.